

FINAL REPORT

Large-Scale Physical Models of Thermal Remediation of DNAPL Source Zones in Aquitards

SERDP Project ER-1423

MAY 2009

Ralph S. Baker
TerraTherm, Inc.

Uwe Hiester
University of Stuttgart

This document has been approved for public release.
Distribution is unlimited.



Strategic Environmental Research and
Development Program

Report Documentation Page			Form Approved OMB No. 0704-0188		
Public reporting burden for the collection of information is estimated to average 1 hour per response, including the time for reviewing instructions, searching existing data sources, gathering and maintaining the data needed, and completing and reviewing the collection of information. Send comments regarding this burden estimate or any other aspect of this collection of information, including suggestions for reducing this burden, to Washington Headquarters Services, Directorate for Information Operations and Reports, 1215 Jefferson Davis Highway, Suite 1204, Arlington VA 22202-4302. Respondents should be aware that notwithstanding any other provision of law, no person shall be subject to a penalty for failing to comply with a collection of information if it does not display a currently valid OMB control number.					
1. REPORT DATE MAY 2009		2. REPORT TYPE N/A		3. DATES COVERED -	
4. TITLE AND SUBTITLE Large-Scale Physical Models of Thermal Remediation of DNAPL Source Zones in Aquitards				5a. CONTRACT NUMBER	
				5b. GRANT NUMBER	
				5c. PROGRAM ELEMENT NUMBER	
6. AUTHOR(S)				5d. PROJECT NUMBER	
				5e. TASK NUMBER	
				5f. WORK UNIT NUMBER	
7. PERFORMING ORGANIZATION NAME(S) AND ADDRESS(ES) TerraTherm, Inc.				8. PERFORMING ORGANIZATION REPORT NUMBER	
9. SPONSORING/MONITORING AGENCY NAME(S) AND ADDRESS(ES)				10. SPONSOR/MONITOR'S ACRONYM(S)	
				11. SPONSOR/MONITOR'S REPORT NUMBER(S)	
12. DISTRIBUTION/AVAILABILITY STATEMENT Approved for public release, distribution unlimited					
13. SUPPLEMENTARY NOTES The original document contains color images.					
14. ABSTRACT					
15. SUBJECT TERMS					
16. SECURITY CLASSIFICATION OF:			17. LIMITATION OF ABSTRACT SAR	18. NUMBER OF PAGES 250	19a. NAME OF RESPONSIBLE PERSON
a. REPORT unclassified	b. ABSTRACT unclassified	c. THIS PAGE unclassified			

This report was prepared under contract to the Department of Defense Strategic Environmental Research and Development Program (SERDP). The publication of this report does not indicate endorsement by the Department of Defense, nor should the contents be construed as reflecting the official policy or position of the Department of Defense. Reference herein to any specific commercial product, process, or service by trade name, trademark, manufacturer, or otherwise, does not necessarily constitute or imply its endorsement, recommendation, or favoring by the Department of Defense.

Table of Contents

1.	Acknowledgements	1
2.	Executive Summary.....	2
3.	Objectives	7
4.	Background	10
5.	Materials and Methods	13
5.1	Batch/1-D tests to select and characterize sandy / silty soils for large-scale physical model experiments (Task 1.1)	13
5.2	Small-scale 2-D heat transfer experiments (Task 1.2).....	13
5.3	Large-scale 3-D heat transfer experiments (Task 1.3).....	14
5.4	Small-scale 2-D remediation experiments (Task 3.1).....	14
5.5	Design and installation of new large-scale containers for heat transport and remediation experiments (Task 3.2).....	17
5.6	Experiment-specific adjustments of chemical analytical methods (Task 3.3).....	25
6	Results and Accomplishments.....	27
6.1	Task 1.1: Batch/1D tests to select and characterize sandy / silty soils for large-scale physical model experiments.....	27
6.2	Task 1.2: Small-scale 2-D heat transfer experiments	30
6.2.1	Introduction	30
6.2.2	Homogeneous heating experiments.....	30
6.3	Task 1.3: Large-scale container heat transport experiments.....	32
6.4	Selection of representative DNAPL.....	35
6.5	Task 3.1 - Visualized 2-D remediation experiments:	44
6.6	Conclusions from 2-D experiments and associated numerical simulations.....	48
6.7	Task 4.1: 3-D Heat transport experiment in the large container 1 (smaller tank).....	49
6.7.1	Phases of operation.....	49
6.7.2	Results	50
6.8	Task 4.2: Heat transport experiment in the large-scale container 2 (larger tank).....	58
6.8.1	Phases of operation.....	58
6.8.2	Results	59
6.9	Comparison and conclusions of the two heat transport experiments.....	62
6.10	Task 4.3: Remediation experiment in the small tank.....	67
6.10.1	Phases of operation.....	67
6.10.2	Results	69
6.11	Task 4.4: Remediation experiment in the large tank	82
6.11.1	Phases of operation.....	82
6.11.2	Results	83
6.12	Comparison and conclusion of the two remediation experiments	92
7	Simulation Modeling	94
7.1	Need for more reliable numerical simulations	94

7.2	General description of STARS	95
7.2.1	Application of STARS to simulation of processes during TCH remediation in the saturated zone.....	96
7.2.2	Open questions to improve the reliability of the simulated results	96
7.3	Modeling methodology and results.....	97
7.4	Lessons learned from the current research.....	97
7.4.1	Validation of the numerical model with 2D-experimental data	97
7.4.2	Application of the numerical model to analyze the 3D heat transport processes	98
7.5	Summary of the numerical model validation.....	102
7.6	Application of the numerical model to predict the remediation behavior in the large container remediation experiments	105
7.7	Context of the additional large-scale container heat transfer experiments	107
7.8	Proposed additional simulations and data.....	107
7.9	Need for additional experimental data to improve the process understanding and validation of the numerical model	108
7.10	Additional large-scale container experiments and outcome of the simulation work	108
7.11	Conclusions of the simulation modeling.....	109
8	Technology Transfer and Applicability Generalizations	111
8.1	Background and Historical Context of the Study	111
8.2	How were the study conditions selected, and how do they relate to the field-scale?	113
8.3	What have we learned, and with what limitations?	115
8.3.1	General Observations and Caveats.....	115
8.4	TCH Applicability Generalizations and Design Guidance	116
8.4.1	Delineation of the DNAPL Source and Target Treatment Zone.....	116
8.4.2	Selection of the Most Appropriate Heating Technology for a Site	117
8.4.3	Prevention of DNAPL Condensation in Unwanted Places	118
8.4.4	Utility and Economic Feasibility.....	120
9	Conclusions	121
10	References	124
	Appendix A: Supporting Data: Mark, 2005 Thesis	A-1
	Appendix B: Supporting Data: MKTS, 2009 Simulation Modeling Report	B-1
	Appendix C: List of Technical Publications:.....	C-1

List of Acronyms

Ant	Anthracene
BP	boiling point
CHC	chlorinated hydrocarbon
CBz	Chlorobenzene
CP	center point
CVOC	Chlorinated Volatile Organic Compound
DCBz	Dichlorobenzene
DNAPL	Dense Nonaqueous Phase Liquid
DoD	Department of Defense
DOE	Department of Energy
ERD	Enhanced Reductive Dechlorination
ERH	Electrical Resistance Heating
FSG	German for “fine grained mixture”
GC-PID	gas chromatography/photoionization detector
GEBA	German for “fine quartz flour”
GW	groundwater
HDPE	High Density Polyethylene
HE	Heater element
HPLC	High Performance Liquid Chromatography
HTC-TDR	High Temperature- and Corrosion-resistant Time Domain Reflectometry
HTE	Heat Transport Experiment
ISCO	In Situ Chemical Oxidation
ISTD	In Situ Thermal Desorption
ISTR	In-Situ Thermal Remediation
LPL	Lower Permeability Layer
Merc	Mercury
Nap	Naphthalene
NAPL	Nonaqueous Phase Liquid
PAH	Polycyclic Aromatic Hydrocarbon
PCE	Perchloroethylene (i.e., Tetrachloroethylene)
SEE	Steam-Enhanced Extraction
SVE	Soil Vapor Extraction
SVE/IAS	Soil Vapor Extraction/In Situ Air Sparging
TCA	trichloroethane
TCH	thermal conduction heating
TCM	Trichloromethane
TeCM	Tetrachloromethane
TESVE	Thermally Enhanced Soil Vapor Extraction
TTZ	Treatment Target Zone
VEGAS	Research Facility for Subsurface Remediation, Universität Stuttgart

List of Figures

Figure 1.	Front side of the 2-D flume.....	13
Figure 2.	Plan view and side view of the existing large container (3-D heat transfer experiment for task 1.3). Red indicates heater elements.....	14
Figure 3.	Experiment setup for the first 2-D remediation experiment. The blue-green rectangles indicate the locations of the two heaters. The red rectangle is the DNAPL release lens.....	15
Figure 4.	Close up of PCE emplaced in coarse sand lens.	16
Figure 5.	Experiment setup for the second 2-D remediation experiment. The blue rectangle indicates the location of the diagonal heater. The red rectangle is the DNAPL release lens.....	17
Figure 6.	Impressions from excavation of old large container: removal of measurement devices (a), wells (b) and soil (c).	17
Figure 7.	(a) Part of the soil material, (b) first layer within the smaller large-scale container, (c) installation of heater pipes and measurement devices (thermocouples) in the smaller large-scale container.	19
Figure 8.	(a) Example of the installation of thermocouples, and (b) installation of HTC-TDR sensors between the heater pipes.	19
Figure 9.	(a) Installation of the DNAPL release lens (coarse sand) in the LPL between the heater pipes, and (b) DNAPL Diffusor inside the DNAPL release lens. After being filled with coarse sand, the temporary forms were removed.....	20
Figure 10.	Plan view of the smaller 3-D tank 1.....	21
Figure 11.	Side view of the smaller 3-D tank 1.....	22
Figure 12.	Plan view of the larger 3-D tank 2.	23
Figure 13.	Side view of the larger 3-D tank 2.	24
Figure 14.	Dual-phase sampling system.....	26
Figure 15.	Grain size distribution of Mixtures B and M2.	27
Figure 16.	Permeability – dry density - relation of lower permeability soil from batch-scale experiments.	27
Figure 17.	Permeability – dry density - correlation of low permeable soil in both large-scale containers.	28
Figure 18.	Permeability distribution of low permeability soil layers, implemented in large –scale containers.	29
Figure 19.	2-D experimental setup – homogeneous heating. Colored vertical line indicates position of the heating element.	30

Figure 20.	Measured temperature distribution, homogeneous heating in 2-D flume with high power input (1200 W).	31
Figure 21.	Measured temperature distribution, homogeneous heating in 2-D flume with low power input (240 W).	31
Figure 22.	Progression of temperature and saturation measured in profile 2 (just outside the square heater pattern, at the position shown in Figure 2). The groundwater table was measured at the side of the large container in the coarse sand. LPL = lower permeability layer.	33
Figure 23.	Progression of temperature and saturation measured in profile 4 (center profile midway between the four heaters, at the position shown in Figure 2). The groundwater table was measured at the side of the large container in the coarse sand. LPL = lower permeability layer.	34
Figure 24.	Temperature dependent vapor pressures (absolute and relative to 10°C) of different contaminants.	36
Figure 25.	Temperature dependent Henry's Law coefficients (absolute and relative to 10°C) of different contaminants.	37
Figure 26.	Temperature dependent solubility of different contaminants.	38
Figure 27.	Temperature dependent viscosity (absolute and relative to 10°C) of different contaminants.	39
Figure 28.	Temperature dependent surface tension (absolute and relative to 10°C) of different contaminants.	40
Figure 29.	Temperature dependent density (absolute and relative to 10°C) of different contaminants.	41
Figure 30.	Temperature dependent Ratio of relative Henry's Law Constant to relative vapor pressure.	42
Figure 31.	Visualization, and temperature measurements during the first 2-D remediation experiment.	45
Figure 32.	PCE recovery curve and PCE flux curve from the first 2-D remediation experiment.	46
Figure 33.	PCE distribution after the first 2-D remediation experiment. The PCE remaining in the soil totaled less than 1 g, relative to 320 g infiltrated initially.	46
Figure 34.	Results of the second 2-D remediation experiment.	47
Figure 35.	PCE distribution after the second 2D remediation experiment. The PCE remaining in the soil totaled less than 2 g, relative to 200 g infiltrated initially.	48

Figure 36. Temperature development of the HTE in the small container (time-variation curves). Top: central profile j, located equidistant from the heaters (center point profile); Center: Profile g, located between the heaters at the boundary of the TTZ; Bottom: Profile e, located 0.5 m outside the TTZ.....	54
Figure 37. Temperature distribution of the the HTE in the small container (spatial interpolation of the measured data). Top: Groundwater inflow during the HTE Middle: Profile j, located equidistant from the heaters (center point profile); bottom: Profile g, located between the heaters at the boundary of the TTZ.	55
Figure 38. Steam Saturation of the HTE in the small container (spatial interpolation of the measured data). Top: Profile A, located equidistant from the heaters (center point profile); Center: Profile B, located between the heaters but inside the TTZ; Bottom: Profile C, located between the heaters but outside the TTZ.....	56
Figure 39. Steam saturation of the HTE in the small container (spatial interpolation of measured data of profiles A to F). Presented in order of increasing groundwater flux. HE = Heater Element; CP = Center Point.	57
Figure 40. Temperature development of the second HTE in the large container (time-variation curves). Top: central profile j, located equidistant from the heaters; Center: Profile g, located between the heaters at the boundary of the TTZ; Bottom: Profile e, located 0.5 m outside the TTZ.	61
Figure 41. Temperatures of the second HTE in the large container (spatial interpolation of measured data). Top: central profile j, located equidistant from the heaters; bottom: Profile g, located between the heaters at the boundary of the TTZ.....	62
Figure 42. Correlation between groundwater flux and steady state temperatures during the experimental phases observed at the central profile “j” at 155 and 190 cm above base within the lower permeability layer, and 140 cm above base within the underlying aquifer.....	63
Figure 43. Temperature distribution (left-hand side and middle part) and steam front propagation for each layer in both tanks (right hand side, with different permeabilities). TTZ = Target Treatment Zone. Layer 295 was just above the upper DNAPL-release lens, while layer 190 was just beneath the lower DNAPL-release lens.	66
Figure 44. Temperatures during the first remediation experiment. Top: central profile j, equidistant from the heaters; Center: Profile g, located between the heaters at the boundary of the TTZ; Bottom: Profile e, located 0.5 m outside the TTZ.....	71
Figure 45. Temperatures during the first remediation experiment (spatial data interpolation along a cross-section through the centerline of the tank from	

	profile “j” to “a”, which are indicated in Figure 10 as “J” and “A”). The positions of the heaters are shown by projection. Top: end of Phase 0 and end of Phase 1;.....	72
Figure 46.	Concentrations of PCE and tracer compounds recovered via SVE [mg/m ³] and GW outflow [mg/l]. 1,4-DCBz tracer added to top NAPL-release lens; 1,2-DCBz tracer added to bottom NAPL-release lens.	74
Figure 47.	Total PCE and Tracer Recovery via SVE and GW outflow (cumulative curve) 1,4-DCB tracer added to top NAPL-release lens; 1,2-DCB tracer added to bottom NAPL-release lens.	75
Figure 48.	Set-up of the smaller tank 1. Left: Plan view; right: side view. Refer to Figures 10 and 11 for greater detail.	77
Figure 49.	Interpolated PCE concentrations per layer at different time steps. See text for explanation.	80
Figure 50.	Temperatures during the 2 nd remediation experiment (Temperature development vs. time). The groundwater flux was constant. Vertical bars indicate intermittent heater shut-down events. Top: central profile j, located equidistant from the heaters; Center: Profile g, located between the heaters at the boundary of the TTZ; Bottom: Profile e, located 0.5 m outside the TTZ.....	85
Figure 51.	Temperature distribution (spatial interpolation of the measured data across a vertical cross-section through the center line from profile “j” to profile “a”, which are indicated in Figure 12 as “J” and “A”). The positions of the heaters are shown by projection. Top left hand side: beginning of the experiment (heat-up period); Top right hand side: end of the experiment; Bottom: The end of phase 4 of first remediation experiment, shown for comparison.	86
Figure 52.	Interpolated steam front shape isotherms of the large tank experiment (container 2) reaching upper lens (left side) and completing steaming of upper lens (right side).	87
Figure 53.	Interpolated steam front shape isotherms of the large tank experiment (container 2) reaching bottom lens (left side) and completing steaming of bottom lens (right side).	87
Figure 54.	PCE and Tracer Extraction with SVE [mg/m ³] in the second remediation experiment. 1,4-DCB tracer added to top NAPL-release lens; 1,2-DCB tracer added to bottom NAPL-release lens. Vertical bars indicate intermittent heater shut-down events.....	88
Figure 55.	Total PCE and Tracer Extraction with SVE and groundwater (summation curve). 1,4-DCB tracer added to top NAPL-release lens; 1,2-DCB tracer	

	added to bottom NAPL-release lens. Vertical bars indicate intermittent heater shut-down events.....	89
Figure 56.	Set-up of the larger tank 2. Left: Plan view; right: side view. Refer to Figures 12 and 13 for detailed views.	90
Figure 57.	PCE concentrations in the large container experiment, interpolated in layers at different time steps; top: day -1.94 and day 4.06, bottom: day 11.2 and day 25.18. See text accompanying Figure 49 for explanation of how to interpret figures.....	91
Figure 58.	PCE concentrations in the large container experiment, interpolated within layers at different times; top: day 52.93 and day 81.06, bottom: day 102.06. See text accompanying Figure 49 for explanation of how to interpret figures.....	92
Figure 59.	Correlation between time generating a steam space in a lens and the generated contaminant output.	93
Figure 60.	Temperature in the 2D, Fine Sand (3×10^{-2} cm/s) Heat Transfer Experiment at 21 Hours, 240 W, $K_h/K_v=4.0$. Physical Model is at left; Simulation at right.	98
Figure 61.	Early Temperature Prediction for 4.5-m 3D Heat Transfer Experiment in the Original Setup.	98
Figure 62.	Progression of Temperature Data Recorded in 4.5-m 3D Heat Transfer Experiment in the Original Setup (at Profile 2, just outside the square heater pattern). LPL = Lower Permeability Layer, here a fine sand.	99
Figure 63.	3D Cross-Sectional View of the Temperature Distribution at 63 Days in the 3D Heat Transfer Experiment in the Original Setup, with Gas-Velocity Vectors. “SVE Wells in Original Vadose Zone” Refers to the Conditions Studied by Hiester et al. 2002.	101
Figure 64.	Comparison of the Measured Temperature at Thermocouple T4240 with an Early Simulation (“Initial” Prediction) and the Result from the Validated Model (“Current” Prediction) for the 3D Heat Transfer Experiment in the Original Setup.	101
Figure 65.	Water Saturation Distribution, Initially and after 10 Weeks of Heating in the 3D Heat Transfer Experiment in the Original Setup.....	102
Figure 66.	Milligrams of TCE Remaining after 20 Days in 3D Aquifer Influx Simulation in the Original Setup. “SVE Wells in Original Vadose Zone” refers to the conditions studied by Hiester et al. 2002, not to the water level conditions examined during the simulation.	107
Figure 67.	Generalized site conceptual model of TCH used with multiphase extraction to treat DNAPL (purple) within a zone of mixed stratigraphy.	112

Figure 68. Example TCH-SEE Combination used at the Knullen Site in Denmark.....	118
Figure 69. Example TCH Design with Heating Below the Zone of DNAPL Impact (HERON ET AL. 2009).....	119

List of Tables

Table 1.	Summarized Data from both tanks for the heat transport experiments (HTE)	20
Table 2.	Summarized Data from both Tanks for remediation experiments	25
Table 3.	Overview of the selected contaminant and tracers.....	43
Table 4.	Duration and mode of operation of the HTE in the small 3-D container.....	50
Table 5.	Duration and mode of operation of the HTE in the large container	59
Table 6.	Duration and mode of operation of the remediation experiment in the small tank.....	68
Table 7.	Time and duration of heater interruptions during the first remediation experiment in the smaller tank.	68
Table 8.	Duration and mode of operation of the remediation experiment in the large container.....	82
Table 9.	Time and duration of heater interruptions during the second remediation experiment in the large container	83
Table 10.	Effect of Several Variables on Heating and Remediation during TCH.....	103

1 Acknowledgements

This material is based on work supported by the Strategic Environmental Research and Development Program (SERDP) under Contract No. W912HQ-05-C-0019.

The co-authors wish to acknowledge the additional members of their project team for their numerous contributions to this work: Dr. Gorm Heron of TerraTherm, Inc., Keene, CA USA; John LaChance of TerraTherm, Inc., Fitchburg, MA USA; Dr. Hans-Peter Koschitzky and Oliver Trötschler of *VEGAS* at Universität Stuttgart, Germany; Dr. Arne Färber, formerly of the Institut für Wasserbau, Universität Stuttgart, Germany; and Dr. Myron Kuhlman of MK Tech Solutions, Houston TX USA. Furthermore, we extend special thanks to Li Yang for conducting the 2-D experiments. We wish to acknowledge the supervisory roles of Jürgen Laich and Henning Eickhoff for the workshop team as well as Wolfgang Rempp and Steffen Hägele (electronical workshop) and Dr. Norbert Klaas, Tanja Fimpel and Daniel Reineberg (Chemical Lab Team). In addition, Steffen Hetzer and Ferdinand Beck supervised numerous student workers in helping to prepare and conduct the experiments (all Institut für Wasserbau, Universität Stuttgart, Germany). Very special thanks go to the Masters students, Johannes Mark for conducting preliminary experiments with the soil media, Philipp Leube for his essential help with the data post-processing and Martina Müller for her contributions to this final report.

2 Executive Summary

Focus and objectives of the research project. In-Situ Thermal Remediation (ISTR) technologies are receiving increasing attention for remediation of dense non-aqueous phase liquid (DNAPL) source zones in soil and groundwater (GW), and are the subject of a number of related current projects funded by the Strategic Environmental Research and Development Program (SERDP) and the Environmental Security Technology Certification Program (ESTCP). A clear understanding of the primary mechanisms of ISTR is crucial for the U.S. Department of Defense (DoD) and Department of Energy (DOE) to be able to select appropriate sites and effective ISTR technologies for DNAPL source zone remediation. This project in particular was proposed in response to SERDP Statement of Need (SON) for FY 2005 CUSON-05-04 dated November 6, 2003, which sought “fundamental or applied studies to improve our understanding of: (1) the mechanisms of removal and destruction of free phase and residual dense nonaqueous phase liquids (DNAPLs) during in situ thermal treatment, including the reductions in plume loading and plume longevity; and (2) the impact of varying subsurface conditions on overall removal and destruction efficiency during thermal treatment.”

It is noteworthy that a more recent SERDP and ESTCP Expert Panel Workshop identified development of treatment approaches for flow-limited portions of DNAPL source zones as a critical research need (SERDP and ESTCP 2006). An ESTCP SON released in 2008 focused further attention on remediation of aquitards.

Thermal conductive heating (TCH) is an ISTR technology that takes advantage of the invariance of thermal conductivity across a wide range of soil types to effect treatment of DNAPL above and below the water table, particularly in lower-permeability and heterogeneous formations. TCH thereby can complement steam enhanced extraction (SEE), which is generally more applicable to higher-permeability formations below the water table.

The objectives of this project (ER-1423) were to:

1. determine the relative significance of the various contaminant removal mechanisms below the water table (e.g. steam generation, steam stripping, volatilization);
2. assess the DNAPL source removal efficiency and accompanying change in water saturation at various treatment temperatures/durations through boiling; and
3. evaluate the potential for DNAPL mobilization, either through volatilization and recondensation, and/or pool mobilization outside of the target treatment zone (TTZ) during heating.

Background. DNAPL source zones are one of the most complex and difficult types of contaminated sites to be remediated. ISTR is of interest for in-situ remediation of saturated low permeability layers because all other, typically hydraulic in-situ methods are limited by low permeability and subsurface heterogeneity. To overcome these limitations, Thermal Conduction Heating (TCH) is gaining attention for usage even in heterogeneous subsurface settings with layers of low permeability and for contaminants with moderate to high boiling points. Thermal wells contain electrical heating elements operating at 400-700°C and can heat both high and low permeability media by a combination of TCH and thermally-induced convection processes. The vaporized contaminants are mainly extracted by Soil Vapor Extraction (SVE). The combination of thermal wells and SVE is also known as In Situ Thermal Desorption or ISTD (Stegemeier and Vinegar 2001; Baker 2006; LaChance et al. 2006).

A research group composed of TerraTherm (remediation company), VEGAS (research facility for subsurface remediation, and MK Tech Solutions (numerical simulation) investigated TCH in the saturated zone to improve process understanding and to optimize contaminant removal.

Overview of Research. Bench- and larger-scale remediation experiments were conducted at the facilities of VEGAS - the Research Facility for Subsurface Remediation at Universität Stuttgart, Germany. In parallel, MK Tech Solutions' simulation modeling was optimized based on the experiments, enabling numerical simulations to be used to design the 3D large-scale experiments. Several quasi 2D experiments were conducted, examining heat propagation in various soil types. In addition, during an initial round of 3D heat-transfer experiments in large containers (up to 150 m³), the progression of heating to 100°C and accompanying desaturation were monitored using 300 temperature sensors and 35 time domain reflectometry (TDR) probes, respectively, allowing comparisons of the physical experiments and accompanying numerical simulations. Remediation experiments were then conducted in the 2D and 3D large-scale containers, with controlled release of DNAPL into lower permeability layers simulating aquitards beneath the water table.

2D Experiments. A series of small-scale 2D heat-transfer and remediation experiments were carried out at VEGAS. The aim of these experiments was to investigate the principal processes of TCH in layered, saturated materials. The experiments were conducted in a stainless steel two-dimensional flume with the dimensions of 1100 mm [width] x 740 mm [height] x 85 mm [thickness]. The front panel consisted of a steel plate for homogeneous heating experiments, and Pyrex[®] glass for the remediation experiments. The flume was equipped with 100 Pt-100 discrete temperature sensors (10 rows x 10 columns) to measure the temperature distributions while heating to steam distillation temperatures, 100°C. Additionally, an infrared camera was used periodically to obtain continuous temperature distributions during the remediation experiments, in which a known amount of tetrachloroethene (PCE) was released prior to heating. During heating, the mass of contaminant collected in the extracted gas was monitored. Following heating, soil samples were collected to estimate the mass of contaminant remaining in the soil.

The main TCH contaminant removal mechanism within the saturated porous media was steam generation in the former saturated zone, NAPL vaporization and steam distillation. In each of the two 2D remediation experiments, nearly complete DNAPL removal from the source zone was accomplished by this method. No DNAPL mobilization was observed through pool mobilization outside of the target treatment zone during or following TCH.

3D Heat-Transfer Experiments. Following the initial round of 3D heat transfer experiments, the two meter-scale containers were emptied and refilled, and heat-transfer experiments were conducted in each of them. The smaller container was 6 m x 3 m x 4.5 m high (81 m³), with a 1.5-m thick intermediate silty aquitard layer, $K_s = 10^{-5}$ cm/s between upper and lower fine sand layers each 1.5-m thick, $K_s = 10^{-3}$ cm/s, with four 1.5 kW heaters in a square pattern. The larger container was 6 m x 6 m x 4.5 m high (162 m³), with a 1.5-m thick intermediate very fine sand aquitard layer, $K_s = 10^{-4}$ cm/s between upper and lower coarse sand layers each 1.5-m thick, $K_s = 10^{-1}$ cm/s, with four (or eight) 1.5 kW heaters positioned in a square pattern. The aquitard layer within each tank was initially saturated. The GW level was maintained at the top of the aquitard layer. Two (to four, in the larger tank) SVE Wells were operated in the overlying sand layer. Although the GW flux through the underlying sand layer (aquifer) was controlled, no pump-and-treat system was installed to

enhance the aqueous remediation process. Power consumption and SVE fluxes were defined. Hundreds of temperature sensors, high temperature and corrosion resistant TDR sensors for the measurement of water saturation and porous sampling ports in the subsurface were installed to determine characteristic heat transport and multiphase flow parameters in the subsurface. The GW flux imposed upon the lower sandy aquifer was varied in steps including, for example, 0.5, 1.0 and 2.0 m³/d, allowing examination of the effect of heat losses on temperature distribution and steam convection.

The 3D heat-transfer experiments confirmed the ability to thoroughly heat (to 100°C) the TTZ within the lower permeability aquitard layer inside each container. Furthermore, the impact of different GW fluxes was quantified indicating the limitation of steam front expansion under conditions of a high GW flux. The investigations contributed to the specification of the experimental conditions for the subsequent remediation experiments. Numerical simulations had suggested that a successful remediation experiment in any 3D container with these relatively small dimensions would occur only when the water flux conditions in the underlying aquifer were such that undesired migration of the steam front into the aquifer would be prevented. Furthermore, the results of the numerical simulations had indicated that a “sufficiently high” GW flux would be required for a successful remediation, to enable an upward steam migration within the TTZ.

3D Remediation Experiments. The 3D remediation experiments were conducted in the same tanks as the above-mentioned 3D heat-transfer experiments, without refilling the tank contents. For the first of the two remediation experiments, 10 kg of PCE (and 2 kg of a tracer) were infiltrated into each of two DNAPL release lenses. Both lenses were situated inside the heater array, one within the upper portion of the aquitard, and the other within the lower portion of the aquitard. The production of PCE and the two tracers in the aquifer water from the bottom of each tank and the SVE in the vadose zone were monitored. Since one tracer (1,4-DCB) was added to the upper DNAPL release lens and another (1,2-DCB) to the lower lens and the two tracers could be distinguished from each other, the production rates of the two tracers were used to identify the lens from which the tracer and associated PCE originated.

We learned that a significant PCE recovery of more than 90% of the initially infiltrated mass could be achieved from the lower of the two DNAPL release lenses within the aquitard via the SVE system in the unsaturated zone. As shown in the second large container remediation experiment, this result occurred provided that there was a sufficient energy input to enable a relatively rapid steam generation and steam distillation of the DNAPL and water in the steamed zone.

In both of the large 3D remediation experiments, due to their limited scale, contaminant condensation had been predicted by numerical simulations and could indeed be observed in the experiments. As shown with an intermittent operation of the heater in the second 3D remediation experiment, the PCE recovery via SVE increased during each shutdown of the heaters due to the collapse of the steam front and the increased transport of condensate by a heat-pipe effect into the already steamed TTZ. Nevertheless, for the conditions studied during the tank experiments, overall mass recovery was not affected by means of intermittent heater operation, because most of the mass recovery had already occurred prior to its onset.

We were able to observe and identify several important effects. A slowly advancing downwardly propagating steam front does not ensure capture of a DNAPL pool already

below that front. As shown for the bottom lens in the first 3D remediation experiment, a slowly advancing steam front might exacerbate an already existing contaminant migration occurring along preferential flow paths. We also observed that too high a GW flux could negatively affect the remediation success. A combined remedies approach, utilizing a tailored combination of TCH with steam injection is recommended to obviate these effects.

Conclusions. During this research, dominating processes, those of more minor importance, and even small-scale effects could be identified. The process understanding of the application of TCH in the saturated zone was significantly improved. As occurs with application of TCH for remediation of VOCs in the unsaturated zone, steam distillation is the major dominating process. It is helpful that the process of steam distillation (co-boiling of water and NAPL) first occurs at temperatures below 100°C, e.g., below the boiling point of either pure water or pure PCE. Consequently, contaminants present as a separate phase have already vaporized by the time that steam production due to boiling of water in the initially water-saturated aquitard layer begins. Nevertheless, an efficient NAPL recovery from the saturated zone by an overlying SVE system requires not only vaporization of the NAPL but also development of one or more contiguous flow paths via which the gaseous phase can travel towards and reach the unsaturated zone and the SVE recovery wells. It follows that steaming of the water within the aquitard in the given large 3D physical models, which occurs at about 100°C (depending on pressure), is important in enabling the desired migration of gaseous NAPL constituents into and through the unsaturated zone.

The generation of steam at a given location during the experiments was significantly affected by the energy intensity (a function of heater power and spacing), soil permeability, depth below the GW level and the cooling effect caused by the GW flux. Furthermore, the extent of lateral versus vertical steam zone propagation is mainly affected by: (a) site-specific conditions such as anisotropy, presence of preferential flow paths and capillary pressure - saturation relations; (b) heater system design factors such as aspect ratio (i.e., the ratio of heater length to heater spacing), the number of heaters and their lateral and vertical positioning relative to the TTZ, and (c) vapor recovery system design factors such as the position of SVE wells and specifically their filter screens, negative pressure exerted and recovery rate (especially for filter screens in the former saturated zone). The recovery of contaminant vapors emanating from a previously saturated aquitard layer through placement of SVE wells only in the unsaturated zone is possible. For field applications, extension of the SVE recovery system into the LPL (aquitard) is often recommended to accelerate the remediation process, even though energy losses from the LPL will be higher.

Condensation of vaporized contaminants at the steam front results in longer remediation times. To minimize formation of this condensate, the heater array must fully encompass and surround the TTZ. This requires adequate site characterization prior to design. A certain amount of condensate is transported by the so-called Heat-Pipe effect (Udell and Fitch 1985) as liquid phase back into the steamed zone.

For a given level of heater power, the higher the soil permeability the greater will be the cooling effect of GW flux, and thus achieved temperatures will be lower at steady state conditions. For the given power and spacing of the heater wells relative to the position of the NAPL, a high GW flux limits the lower expansion of the steamed zone indicating that NAPL located close to the boundary between water saturated aquitard and aquifer may not be recovered without implementation of combined remedies.

The experimental results indicate that advanced numerical simulations would be very helpful to predict steam front propagation, temperature distribution and DNAPL recovery. The accuracy of input data such as geological / hydrogeological information, soil parameters, and contaminant distribution, however, affect simulation results. In some respects, predictions gleaned from numerical simulations proved of value to process understanding; in other respects they differed from the experimental results.

Advanced simulations are needed to answer very specific questions in detail. Lack of basic knowledge, however, such as the impact of temperature on three-phase parameters prevents numerical results from being of sufficient reliability. Further research is needed to improve the results by a better application of some (small-scale) effects of interest.

Nevertheless, we learned that the model design itself can affect the overall results of the simulations. As an example, recognition of heat transfer within the heater cans and the degree of anisotropy were discovered to have a significant impact on the results, e.g., of the temperature distribution and therefore on all interrelated processes.

To facilitate future simulations, it is useful to bear in mind that many flow, transport and remediation effects can be anticipated with no more than an accurate prediction of the temperature distribution. Therefore, researchers who follow us may do well to focus on the quantification of those factors that affect heat transport. By doing so, reliability of numerical simulations may be improved.

3 Objectives

The objectives of this project (ER-1423) were to:

1. determine the relative significance of the various contaminant removal mechanisms below the water table (stream stripping, volatilization, in situ destruction, enhanced solubilization);
2. assess the percentage of the DNAPL source removal and accompanying change in water saturation at various treatment temperatures/durations through boiling; and
3. evaluate the potential for DNAPL mobilization, either through volatilization and recondensation, and/or pool mobilization outside of the target treatment zone during heating.

Five main tasks were designed to meet these objectives. Task-specific activities and goals are summarized as follows:

1. Soil Selection and Large-Scale Design

1.1. Conduct batch/1-D tests to select and characterize sandy / silty soils for large-scale physical model experiments

The sandy-silty soil mixture to be selected to serve as the source zone for the large scale physical model experiments needed to have a relatively low permeability. After the selection of the specific soil mixture for the large-scale experiments, permeability tests, constitutive relationships, proctor density and other soil mechanical properties of that material were determined.

1.2. Perform 2-D experiments on heat front propagation in different soils

Two-dimensional experiments without contaminants were performed to enable development of process understanding regarding heat front propagation as a function of injected power and soil properties. The aim of this task was to facilitate the transfer of results to a range of soil properties.

1.3. Execute large-scale 3-D physical heat transfer experiments under saturated conditions

At the onset of this project, the large-scale container remained as it had been set up for a previous large-scale experiment of steam-air injection and thermal wells in the unsaturated zone. We then raised the groundwater level and carried out preliminary investigations concerning heat transfer in the existing soil layers of different permeability (coarse sand of $K_h=10^{-1}$ cm/s and finer-grained mixture of $K_h=10^{-3}$ cm/s). Temperature distribution in the subsurface and the energy consumptions were detected by automatic data logging and the results were compared to numerical simulation results. The purpose of these experiments within the saturated zone were to provide data on heat transfer and information about the needed boundary distances to help plan the large-scale remediation experiments.

1.4. Milestone 1 (month 6): Develop design parameters for the heater arrays and instruments to be used in the remediation experiments; and define the large-scale sand-silt mixture.

2. Contaminant Selection and Feasibility Testing

2.1. Select representative DNAPL with respect to temperature dependent sorption and desorption behavior in cohesive soils (literature research)

The relevant DNAPL of interest with respect to temperature dependent sorption and desorption behavior in cohesive soils was selected by conducting literature research. One characteristic CVOC (PCE) was selected for the large-scale experiments.

2.2. Carry out feasibility tests for specific temperature-resistant monitoring techniques in the porous media (e.g. TDR (saturation), fiber sensors (temperature), etc.)

In this task useful measurement technologies were evaluated for the measurement of water saturation on a large-scale under aggressive environmental conditions such as high temperatures and the presence of contaminants. Experience from former research and development was utilized (e.g. temperature resistant time-domain reflectometry (TDR) sensors). Also the methodology for collection of aqueous-phase samples (water, dissolved phase, separate phase) from discrete points during the remediation experiments (e.g., porous sampling discs) was determined. Together with the detailed information from earlier steps, the design of the container setup was finalized.

3. 2-D Experiments and Preparation for 3-D

3.1. Conduct remediation and mobilization experiments (2-D) for representative DNAPL and soil mix

Two-dimensional remediation experiments were conducted to give initial information about the removal efficiency of DNAPL from the saturated subsurface and enable visualization of the remediation process for two different experimental setups (number and array of heaters, permeability of soil).

3.2. Remove and refill the two large-scale containers incl. installation of monitoring arrays

Two large-scale containers (6m x 6m x 4.5m and 3m x 6m x 4.5m) were manually excavated and refilled. Compaction and optimal water content throughout the refilled soil volume was confirmed by proctor tests. Moisture and dry density were controlled by the collection and analysis of numerous sample cylinders within different soil layers.

3.3. Determine experiment-specific adjustments of chemical analytical methods

During the design of the experiments, the expected experiment-specific range of concentration per sampling point was estimated and the needed accuracy was defined. Sampling costs, sampling method, sampling time and analysis were optimized.

3.4. Milestone 2 (month 12): DECISION: (a) Are further heat transport experiments in the specific setup needed? If not, proceed. (b) Is the planned experimental design adequate? If so, proceed. This marked the end of the experimental design phase and the start of the large-scale remediation experiments.

4. 3-D Experiments in Large Containers

4.1. Initiate Experiment 0 Large-Scale Container 1 (heat transfer)

Based on the results of 2-D and 3-D experiments and numerical simulations, it was decided that prior to beginning the remediation experiment (task 4.3), further heat transfer investigations were needed to gain a more comprehensive understanding of heat propagation as dependent on heater array, power input and groundwater discharge. A

complex heat transfer experiment was therefore conducted in large-scale container 1 with varying boundary conditions. Temperature distribution in the subsurface and the energy delivered were detected by automatic data logging and the results were compared to numerical simulations. The experiment provided data on heat transfer within the saturated zone and information about the needed boundary distances relevant to the large-scale remediation experiments.

4.2. Initiate Experiment 0 Large-Scale Container 2 (heat transfer)

With the experience of the above-mentioned heat transfer experiment in Container 1, this experiment was conducted in Container 2 utilizing a modified container set up (SVE installation, soil permeability). The experiment provided additional data on heat transfer within the saturated zone and information about the needed boundary distances relevant to the large-scale remediation experiments.

4.3. Initiate Experiment 1 Large-Scale Container 1 (high conc. / mobilization)

With the experience of the heat transfer experiments (Tasks 4.1 and 4.2), a complex large-scale remediation experiment was conducted by emplacing contaminant within a defined zone in the saturated subsurface. The mass of the emplaced NAPL was calculated from the first year's experiences of the project. The aim of the design of the experiment was to choose boundary and operating conditions to examine their effects and to quantify the success of in-situ thermal remediation by thermal wells even under difficult operational conditions.

4.4. Initiate Experiment 1 Large-Scale Container 2 (low conc. / mobilization)

With the experience of the first large-scale remediation experiment, the second was conducted with lower contaminant concentrations and by changing the thermal well setup and the mode of operation. The aim was to enable the demonstration of a successful in-situ thermal remediation.

4.5. Remove Material from Large-Scale Experimental Containers

The large-scale physical model containers will be emptied after the project ends. Soil with low residual contamination will be disposed separately, if needed.

5. Modeling and Generalization

5.1. Conduct Simulation Modeling of 1-D, 2-D and 3-D Experiments using STARS: Steam, Thermal, and Advanced Processes Reservoir Simulator

The purpose of the portion of this study conducted by MK Tech Solutions was to help quantify important mechanisms by simulating several of the experiments with STARS, a thermal simulator. Simulations of several 2-D flume and large-tank heating and remediation experiments were conducted. Both the temperature distribution in the containers and production rate of vaporized PCE were modeled.

5.2. Formulate TCH Applicability Generalizations: Field-scale design; Technology transfer; Guidance document input

The result from the foregoing investigations were taken together to generalize criteria or appropriate field applications of the thermal conduction heating (TCH) technology characterizing the necessary site-specific conditions for successful field remediations (e.g., depth to water table, stratigraphic and hydrogeological conditions, heater configuration, contaminant distribution, concentration, etc.)

4 Background

Estimates indicate that there are approximately 17,000 DoD sites potentially requiring cleanup and that the total DoD cleanup costs are valued at over \$35 Billion (the total estimate for DoD and DOE is over \$200 Billion) (SERDP/ESTCP, 2001). It is estimated that 3,000 of the 17,000 sites are contaminated with chlorinated volatile organic compounds (CVOCs) (EPA, 1997). Many if not most of the 3,000 CVOC sites are the result of the release and presence of dense non-aqueous phase liquid (DNAPL) in the subsurface. These CVOC sites could represent over \$6 Billion in cleanup costs for the DoD alone. Identifying effective CVOC DNAPL source zone treatment technologies and understanding their underlying mechanisms is crucial to the DoD and DOE in order to ensure appropriate selection, design, and implementation of treatment technologies for CVOC sites and to optimize expenditures.

As indicated in the SERDP/ESTCP Final Report on the expert panel workshop convened in 2001 on research and development needs for CVOC sites, assessment of in-situ thermal remediation technologies (ISTR) for CVOC DNAPL source treatment was ranked as a high-priority research need because of both the promise of ISTR technologies to effectively treat CVOC source zones (ultimately allowing site closure to be achieved) and the need to better understand the underlying mechanisms of ISTR (SERDP/ESTCP, 2001).

More recently, a Technical Report issued by SERDP/ESTCP entitled “Summary of SERDP and ESTCP Projects Focused on Characterization and Remediation of Dense Nonaqueous Phase Liquid (DNAPL) Source Zones” (SERDP/ESTCP, 2006A) included among its conclusions that “Thermal treatment is a very promising area for future investments of research funding. This conclusion reflects both the potential for in situ thermal treatment, and the current state of its development.”

A DNAPL Workshop convened by SERDP/ESTCP in 2006 (SERDP/ESTCP, 2006B) concluded among “overarching concerns” that “Guidance on the use of existing methods should first assess the level of precision required for varying site conditions and intended uses of the results.” The expert panel also identified development of treatment approaches for flow-limited portions of DNAPL source zones as a critical research need (SERDP/ESTCP, 2006B).

ISTR technologies are receiving receiving increasing attention and proving to be effective for remediation of DNAPL source zones in soil and groundwater, as documented by bench-scale studies (BAKER ET AL. 2001; DAVIS 2003; DEVOE AND UDELL 1998; HANSEN ET AL. 1998; HERON ET AL. 1998B; HIESTER ET AL. 2002; HIESTER ET AL. 2003A; HIESTER ET AL. 2006; HUNT ET AL. 1988B; SCHMIDT ET AL. 2002; TRÖTSCHLER ET AL. 2003; UDELL AND MCCARTER 1996; UGIRIS ET AL. 1995) and field-scale demonstrations (BAKER ET AL. 2004; BAKER ET AL. 2007; BERGSMAN ET AL. 1993; BIRSCHENK ET AL. 2008; BUETTNER ET AL. 1995; COLE ET AL. 2008; CONLEY AND JENKINS 1998; CONLEY AND LONIE 2000; CONLEY ET AL. 2000; EARTH TECH AND STEAMTECH 2003; GAUGLITZ ET AL. 1994; HERON ET AL. 1999; HERON ET AL. 2008; LACHANCE ET AL. 2004, 2006, 2008; MCGEE 2003; NEWMARK ET AL. 1994; NFESC, 1998; SHELDON ET AL. 1996; STEGEMEIER AND VINEGAR 1995; US DOE 1999; US DOE 2003; USEPA 2004; VINEGAR ET AL. 1997A; VINEGAR ET AL. 1999). The mechanisms governing contaminant behavior as energy is injected and the target zones heat up have been studied and discussed in fundamental theoretical and practical works (BAKER AND KUHLMAN 2002; DAVIS 1997; HERON ET AL. 1998A,C; HERON ET AL. 2006; HUNT ET AL. 1988A; IMHOFF ET AL. 1997; JOHNSON 2007; PENNELL 2007; NEWMARK AND AINES 1997; SCHMIDT ET AL. 1998,

2002; SHE AND SLEEP 1998; SLEEP AND MA 1997; STEGEMEIER ET AL. 1995; STEGEMEIER AND VINEGAR 2001; THEURER ET AL. 2003; UDELL 1996; UDELL AND FITCH 1985; USACE 2006; VINEGAR ET AL. 1997B). In particular, thermal conductive heating (TCH) takes advantage of the invariance of thermal conductivity across a wide range of soil types to effect treatment of DNAPL in both homogeneous and lower-permeability and heterogeneous formations alike. TCH thereby can complement steam-enhanced extraction (SEE), which is generally more applicable to higher permeability aquifers. The attributes and capabilities of TCH are sufficiently distinct from those of electrical resistance heating (ERH), and the associated benefits (greater predictability of treatment; lower cost) are sufficiently large, as to make a compelling case for the need to rigorously elucidate the mechanisms of DNAPL treatment by TCH. Large-scale experiments have proven indispensable for incorporating thermal interactions between soil layers of different permeability (HIESTER ET AL. 2002; HIESTER ET AL. 2003B), and have been implemented safely.

A significant limitation of in-situ remediation technologies that rely on the injection/extraction of fluids (e.g., soil vapor extraction and air sparging [SVE/AS], in-situ chemical oxidation [ISCO], surfactants, and enhanced reductive dechlorination [ERD]) is their inability to provide 100% sweep efficiency even in relatively uniform hydrogeologic settings. This is because even in uniform hydrogeologic settings, there are small but significant variations in soil properties (permeability, porosity, capillary pressure, etc.) that result in preferential flow and bypassing. At sites with heterogeneous hydrogeologic settings (e.g., interbedded sands and silts), the problem of preferential flow and bypassing is even more severe, resulting in large portions (e.g., >50%) of the source areas being untreated. Unfortunately, the benefits of treating less than 50% of a DNAPL source zone may not warrant the cost of doing so. The inability of fluid-based remediation technologies to effectively and reliably treat DNAPL source zones and the uncertainty associated with the benefits of partial treatment / mass removal both influence technology screening and selection decisions, as well as asset evaluation during base closure (e.g., when long-term pump-and-treat/ monitoring may be selected over source elimination.) A key research objective is therefore to determine whether 100% sweep of the TCH process is a reasonable expectation in heterogeneous source zones in aquifers. This study is designed to rigorously address this objective, using example layering typical of geological systems of interest. In addition, the research results will be used to determine the most appropriate scenarios for combining more than one thermal heating technique for optimal heating of complex sites such as multi-layered sedimentary deposits and fractured rock sites. The strength of such combined approaches was documented by the successful full-scale remediations at the Young-Rainey STAR Center in Florida (US DOE 2003; HERON ET AL. 2004) and at a site in Denmark (NIELSEN ET AL. 2008). In particular, the scenario where TCH is used to heat the low-permeable zones, and steam injection is used to heat the more permeable zones and reduce the amount of water flowing in from the sides, will be evaluated.

Recent field demonstrations have documented the complex nature of heat flow in geological materials, and the limits to current understanding of removal mechanisms at a scale in between 1-D and 2-D laboratory models (HERON ET AL. 1998B; HUNT ET AL. 1988B; JOHNSON 2007; PENNELL 2007; SCHMIDT ET AL. 2002; UDELL AND MCCARTER 1996) and field scale implementation (EARTH TECH AND STEAMTECH 2003; HERON ET AL. 1999; LACHANCE ET AL. 2008; KINGSTON 2008; MCGEE 2003; US DOE 2003). The knowledge gap is partly due to the small scale of past laboratory studies.

The justifications for having this research culminate in large-scale physical model experiments include the ability to control experimental conditions, thoroughly instrument the treatment zone, restrict thermal and other boundary effects to the outer edges of the experimental volume, and approach closing the mass balance to a greater extent than is otherwise possible. As a result, an understanding of the complex multiphase processes and mechanisms that occur during ISTR is more likely to emerge here than at smaller or larger scales.

5 Materials and Methods

5.1 Batch/1-D tests to select and characterize sandy / silty soils for large-scale physical model experiments (Task 1.1)

The objective of Task 1.1 was to create a soil mixture with certain predetermined characteristics (MARK, 2005; APPENDIX A).

The permeability tests were carried out using a compaction permeameter. Two different set-ups were used to measure the hydraulic conductivity: constant head and falling head. Due to the time efficiency of the falling head method, it became the method of choice throughout the study, although the constant head method was initially used to verify results from falling head measurements. From the final selected soil mixture, two samples were taken for grain size analysis. The grain size distribution was determined by Sedigraph analysis after dispersing in a solution containing 0.05M $\text{Na}_4\text{P}_2\text{O}_7$.

Based on the results of Task 1.1, the permeability distribution in the large-scale experiments was determined using the measured dry density.

5.2 Small-scale 2-D heat transfer experiments (Task 1.2)

A series of 2-D experiments have been conducted in a small-scale stainless steel flume set-up with the dimensions of 1100 x 740 x 85 mm (length x height x depth). The front panel consisted of a steel plate for homogeneous heating experiments (Task 1.2), and Pyrex® glass for the remediation experiment (Task 3.1) (Figure 1).



Figure 1: Front side of the 2-D flume.

The flume was equipped with 100 temperature sensors (PT100) (10 rows x 10 columns) to measure the progress of heating. Additionally, an infrared camera was used to visualize and document temperature distributions during the remediation experiments.

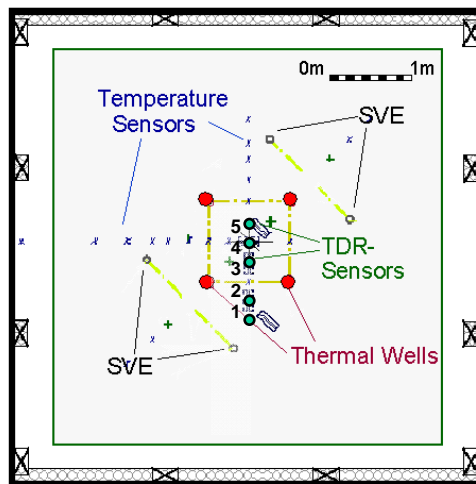
The material used in these experiments was called FSG (German for “fine grained mixture”) and is the same material that was used as the lower permeability layer in the large-scale heat transport experiments described in Section 5.3. The FSG material (60% GEBA (Dorfner, Germany) – a well-sorted fine sand, and 40% Dorsilit 2500 (Dorfner, Germany) – a quartz

flour of a permeability comparable to silt (MARK 2005) was mixed in a dry manner and then moistened with 10% (weight) of water using a concrete mixer. The mixture was layer-wise filled into the flume (around 3 cm each layer) and compressed with the help of a wooden compactor. The porosity after filling was 0.39. Since it is quite difficult to work in such a thin flume with many sensors distributed all around, it can be expected that the intended “homogenous” filling may not really have been that homogeneous.

5.3 Large-scale 3-D heat transfer experiments (Task 1.3)

The large-scale 3-D heat transfer experiments were conducted in a pre-existing large-scale container set-up from former thermally-enhanced soil vapor extraction (SVE) experiments (HIESTER ET AL. 2002; HIESTER ET AL. 2003A). The base of the container is 6 m x 6 m and its height is 4.5 m (Figure 2). A layer of a lower permeability material (saturated hydraulic conductivity, $K_s = 10^{-5}$ m/s) was embedded in coarse sand ($K_s = 10^{-3}$ m/s). More than 300 thermocouples and Pt-100 temperature sensors enabled monitoring of the temperature distribution in the subsurface. Additionally, 35 High Temperature- and Corrosion-resistant Time Domain Reflectometry (HTC-TDR) sensors were used to evaluate the water saturation in the subsurface. Furthermore, ground water level, discharges, pressures as well as temperatures in the SVE system were monitored. Non-isothermal numerical modeling performed in parallel with these experiments was used to simulate the physically dominant mechanisms and processes of the experiments. Several options concerning the boundary conditions of the heating experiments were intensively discussed at an early stage of the project.

Top View



Side View

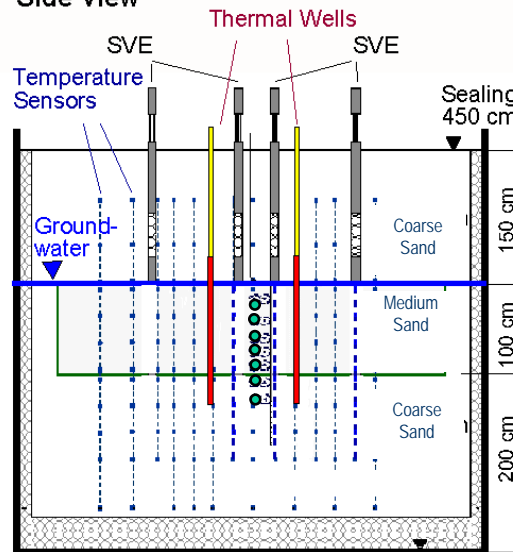


Figure 2 Plan view and side view of the existing large container (3-D heat transfer experiment for task 1.3). Red indicates heater elements.

5.4 Small-scale 2-D remediation experiments (Task 3.1)

To visualize the potential of PCE migration during heating, two visualization 2-D remediation experiments were designed and conducted. The experimental setup of the first experiment is sketched in Figure 3. The upper 50 cm consisted of a fine-textured layer ($K_s \sim 10^{-6}$ m/s) composed of “Mixture B” (defined below), while the lower 24 cm consisted of coarse sand ($K_s \sim 10^{-3}$ m/s). A 10 cm high x 20 cm wide coarse-textured sand lens was packed within the upper layer, with a thin transition zone of GEBA (Dorfner, Germany) – a

well-sorted fine sand, to prevent the eluviation of the fine-textured material into the sand lens. Mixture B is composed of GEBA, DORSILIT 2500 – very fine sandy and coarse silt, and DORSILIT 4900 (Dorfner, Hirschau, Germany) – a coarse silt, at a mass ratio of 30:50:20, respectively. The dyed PCE was infiltrated into the coarse sand lens in the middle. Two heating elements were located at both sides of the coarse lens and parallel to each other. Each heater was operated with a power input of 500 Watt. A blower was used to extract the vaporized PCE collected at the top of the flume. The off-gas was treated by an activated carbon filter.

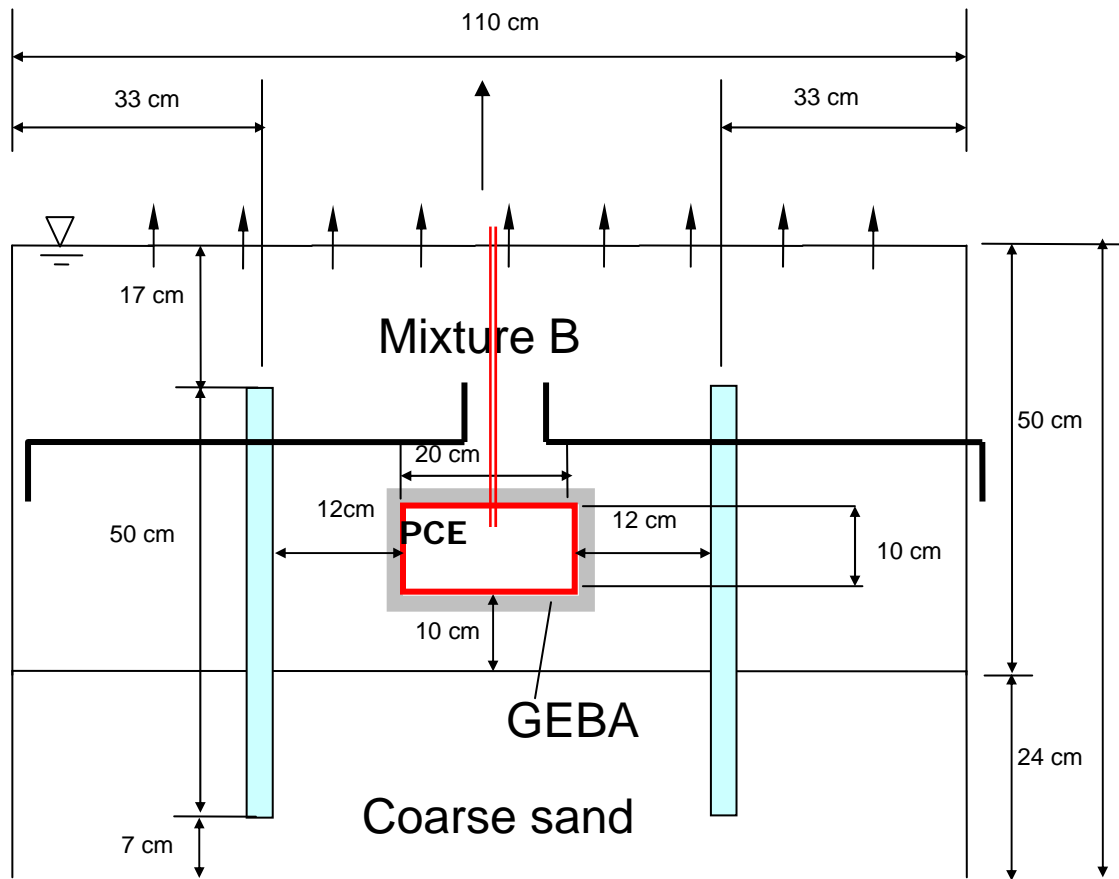


Figure 3: Experiment setup for the first 2-D remediation experiment. The blue-green rectangles indicate the locations of the two heaters. The red rectangle is the DNAPL release lens.

The PCE was dyed in red for visualization purpose. A total of 320g of PCE were infiltrated into the coarse sand DNAPL release lens with the help of a pre-embedded tube. After infiltration, the tube was sealed to prevent short-circuiting of vaporized PCE. The PCE was initially retained inside the coarse lens due to the capillary barrier below. A small amount of PCE moved into the fine layer due to the presence of air at the inner surface of the glass. A close-up of the emplaced PCE is shown in Figure 4.

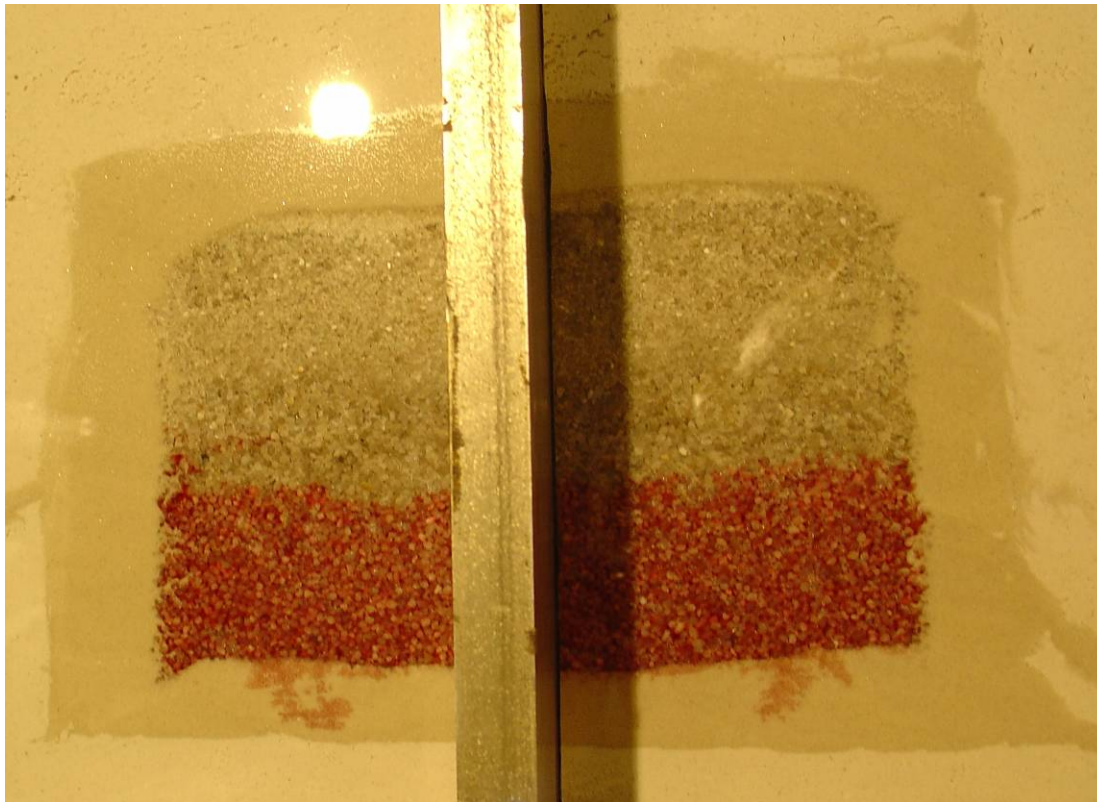


Figure 4: Close up of PCE emplaced in coarse sand lens.

A second visualization 2-D remediation experiment was designed and conducted to visualize the potential of PCE migration during heating with a tilted heater. The experimental setup is sketched in Figure 5. The upper 33 cm consisted of medium sand ($K_s \sim 1 \times 10^{-4}$ m/s), while the lower 41 cm consisted of a fine-textured layer using “Mixture B”. A 10 cm high x 20 cm wide coarse-textured sand lens ($K_s \sim 10^{-3}$ m/s), was packed within the lower layer, with a thin (2 cm thick) transition zone of GEBA (Dorfner, Germany) – a well-sorted fine sand, to prevent the eluviation of the fine-textured material into the sand lens during flooding of the flume or during the experiment. The Mixture B ($K_s \sim 10^{-6}$ m/s) is composed of GEBA, DORSILIT 2500 – very fine sandy and coarse silt, and DORSILIT 4900 (Dorfner, Hirschau, Germany) – a coarse silt, at a mass ratio of 30:50:20, respectively. The dyed PCE was infiltrated in the coarse sand lens. One heating element was located beneath the coarse lens and was tilted by 45° (Fig. 5). The heater was operated with a power input of 500 Watt. A blower was used to extract the vaporized PCE collected at the top of the flume. The off-gas was treated by an activated carbon filter. The PCE was dyed in red for visualization purposes. A total of 200g of PCE were infiltrated into the coarse sand DNAPL release lens with the help of a pre-embedded tube. After infiltration, the tube was sealed to prevent short-circuiting of vaporized PCE. The PCE was initially retained inside the coarse lens due to the capillary barrier below. A small amount of PCE moved into the fine layer due to the presence of air at the inner surface of the glass.

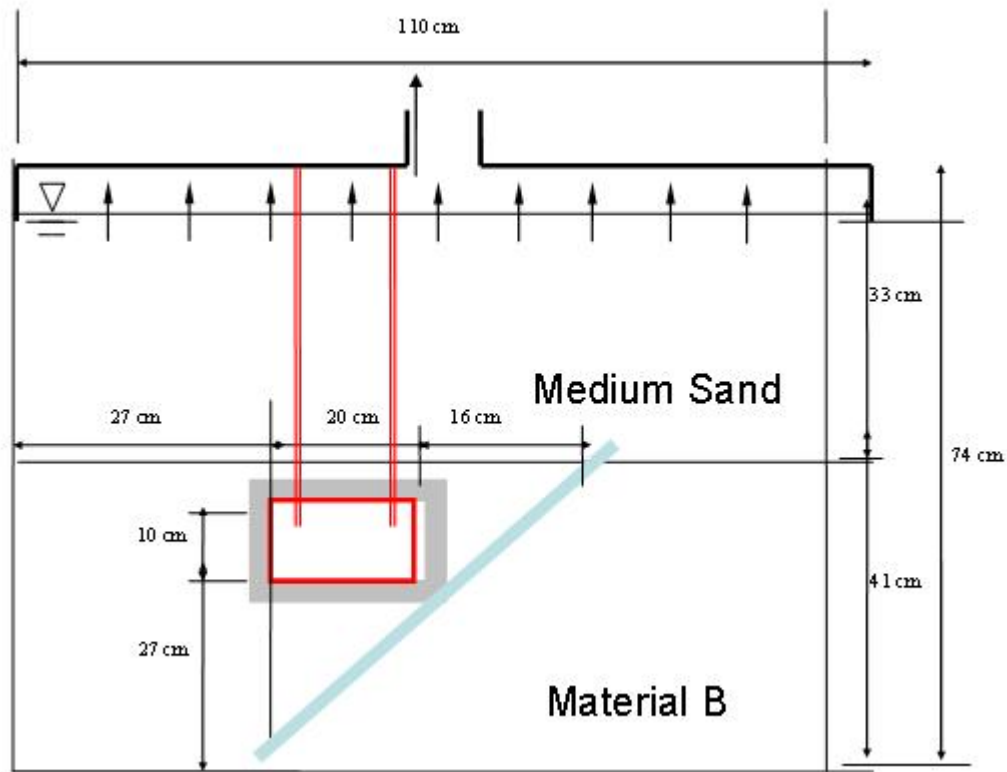


Figure 5: Experiment setup for the second 2-D remediation experiment. The blue rectangle indicates the location of the diagonal heater. The red rectangle is the DNAPL release lens.

5.5 Design and installation of new large-scale containers for heat transport and remediation experiments (Task 3.2)

Unlike the experiments described in 5.3 above, the next round of large-scale container experiments would include contaminants. Therefore, a new experimental design was needed, and was completed under Task 1.3. Before installing these new set-ups, two adjacent stainless steel tanks with a base of 3 m x 6 m and 6 m x 6 m had been emptied (Task 3.2, Figure 6), redesigned and filled with soil up to a height of 4.5 m (75 m³ and 150 m³).

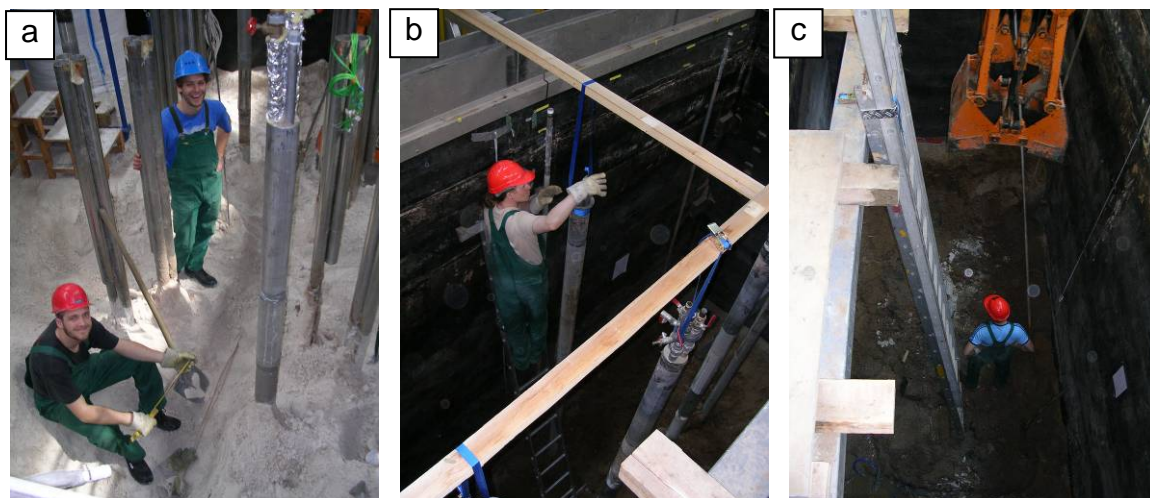


Figure 6: Impressions from excavation of old large container: removal of measurement devices (a), wells (b) and soil (c).

It was decided that the remediation experiments would be conducted using lower-permeability materials more relevant to this project ($K_s = 10^{-6} - 10^{-7}$ m/s). Based on the former container design (HIESTER ET AL. 2002), detailed bench-scale experiments and analyses were conducted at Göteborg University, Sweden (MARK, 2005), at VEGAS and in the USA to improve the understanding of the behavior of several fine sand and quartz flour mixtures being considered for this application. The layout and the realization of the 3-D experiment were designed with the aid of the numerical model. In addition to the monitoring of temperatures and water saturations, the new container set-ups were designed to allow sampling of the contaminated groundwater and soil vapor from the subsurface via porous sampling discs. Detailed plans for both sections of the newly designed container are shown in Figure 11 and Figure 13, respectively.

A layer of lower permeability (height 1.5 m) as a middle layer of each tank (i.e. representing an aquitard) was located between an overlying vadose zone layer and an underlying aquifer layer, both of higher permeability. The set-up of the smaller tank is illustrated in Figure 11. The tank specific data are summarized for both tanks in Table 1. In each tank, four (or if desired, eight) heater wells could be operated. They could be emplaced in a pattern of two squares, 1 m x 1 m and 1.25 m x 1.25 m. The groundwater level at the outflow was controlled to maintain a constant head boundary at 3 m above base (above base) at the top of the aquitard layer. The groundwater inflow varied depending on the experimental phase.

Each tank was equipped with Pt100-temperature sensors in 12 layers with 15 to 17 sensors per layer (approx. 200 sensors/tank), respectively. The temperature sensors were arranged in a V-shape between the inflow and the center of the container (Figure 11 Top: A-Z in blue color). Additionally, 36 (in the smaller tank) and 64 (in the larger tank) High-Temperature and Corrosion-resistant Time Domain Reflectometry (HTC-TDR) sensors were operated to measure the water saturation along the tank center line (Figure 11 top: profiles A-F in pink color (left-hand side)). In the large tank the HTC-TDR sensors were installed in a V-shape (Figure 13 top: profiles A-G and U-W in pink color).

To quantify the impact of the groundwater flow on the temperature distribution and steam front propagation, one heat transport experiment was conducted in each tank while varying the groundwater flux. The thermal wells operated at full power (6 kW) and the groundwater outflow was kept constant at a height of 3 m above base. The operational settings of both tanks are summarized in Table 1.

Figure 7 gives some impressions from the installation works done under Task 3.2: the soil material to be installed in the container had been stockpiled before installation on the floor of VEGAS's hydraulics lab (Figure 7a). Soil material was transported in big bags by crane into the container and emplaced and compacted manually in layers 10 cm thick (Figure 7b). Depending on the height, a variety of instruments and measurement devices were installed. Temporary wooden spacers like those shown in Figure 7c were removed before finishing the filling.

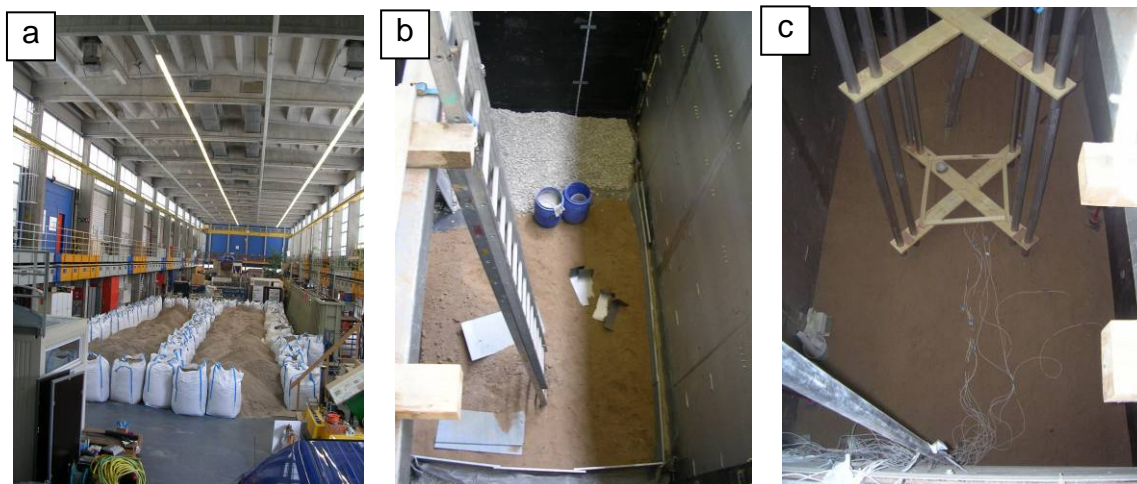


Figure 7: (a) Part of the soil material, (b) first layer within the smaller large-scale container, (c) installation of heater pipes and measurement devices (thermocouples) in the smaller large-scale container.

Templates were used to ensure a precise installation of measurement devices in each layer (Figure 8). The large amount of data sampling points were intended to allow generation of a detailed picture of the subsurface processes during heating and remediation.

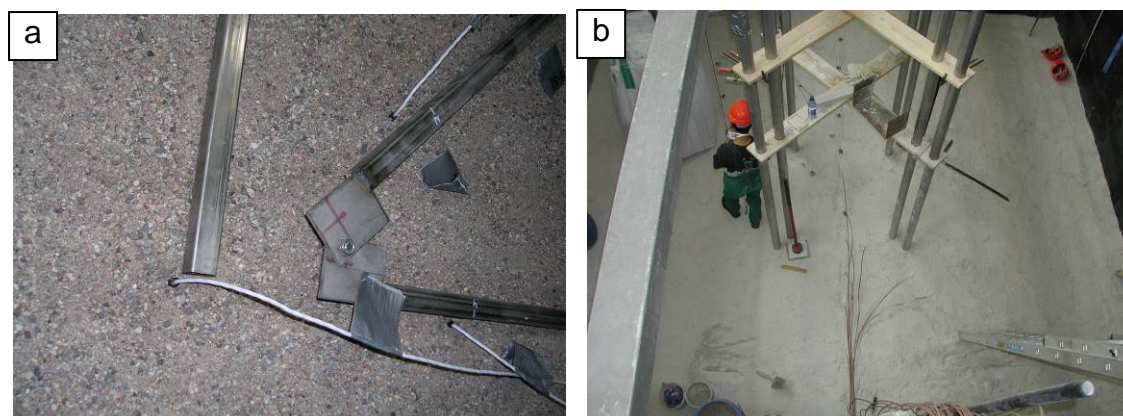


Figure 8: (a) Example of the installation of thermocouples, and (b) installation of HTC-TDR sensors between the heater pipes.

The emplacement of DNAPL pools with a defined mass in the large container was viewed as one of the most difficult tasks during the experiments. Due to the high number of measurement devices and several planned experiments, the DNAPL had to be delivered from outside (without excavation) after finishing the container filling. The infiltration of DNAPL in a water saturated soil material with a low permeability is difficult and could cause preferential flow paths due to the injection pressure that would be required. To overcome these limitations, “coarse sand DNAPL-release lenses”, like those that had been successfully tested in the 2-D remediation experiments (section 5; Figure 7 and Figure 8) were installed in the large containers as well (Figure 9). These lenses were installed inside the four wells of the heater array and were surrounded by lower permeability material at all sides (Figure 9, Figure 11 and Figure 13). This decision was justified because in all field-scale applications of the TCH technology to date, thermal wells have always been positioned so as to fully encompass the delineated source zone, i.e., the thermal wells are placed within and immediately outside the horizontal and vertical limits of the known DNAPL zone. To help ensure a uniform distribution of the DNAPL, it was infiltrated by using a DNAPL diffuser (infiltration pipe with eight outlets) pre-installed at the top of each release lens (Figure 9b). Two DNAPL

release lenses were installed in each container (Figure 11 and Figure 13). Both containers were sealed at the top by a high density polyethylene (HDPE) layer.

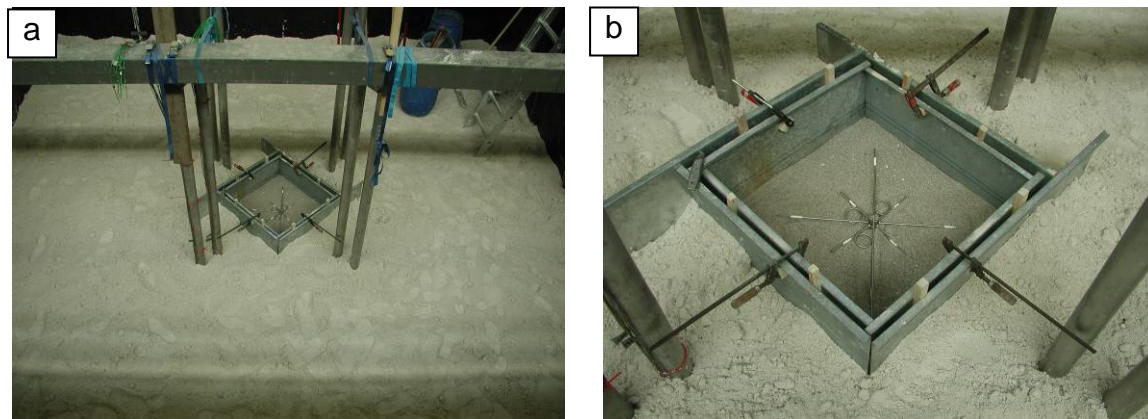


Figure 9: (a) Installation of the DNAPL release lens (coarse sand) in the LPL between the heater pipes, and (b) DNAPL Diffusor inside the DNAPL release lens. After being filled with coarse sand, the temporary forms were removed.

Table 1: Summarized Data from both tanks for the heat transport experiments (HTE)

	Smaller Container 1	Larger Container 2
Length	6 m	6 m
Width	3 m	6 m
Height	4.5 m	4.5 m
K_s of lower permeability soil layer	1 to 4 x 10 ⁻⁷ m/s	1 to 3 x 10 ⁻⁶ m/s
K_s of higher permeability soil layers	1 x 10 ⁻⁴ m/s	1 x 10 ⁻³ m/s
Power of heater array	2 kW and 6 kW (4 heaters)	6 kW (4 heaters)
Groundwater outflow (const. head)	3 m above base (m above base)	3 m above base (m above base)
Phase 0	333 l / (tank width x day); 2 kW	-
Phase 1a	333 l / (tank width x day); 6 kW	333 l / (tank width x day); 6 kW
Phase 1b	223 l / (tank width x day); 6 kW	167 l / (tank width x day); 6 kW
Phase 1c	167 l / (tank width x day); 6 kW	48 l / (tank width x day); 6 kW
Phase 1d	10 l / (tank width x day); 6 kW	1.7 l / (tank width x day); 6 kW
Phase 1e	667 l / (tank width x day); 6 kW	-
Phase 1f	1333 l / (tank width x day); 6 kW	-
Phase 2	1333 l / (tank width x day); 0 kW	0 l / (tank width x day); 0 kW
Phase 3	0 l / (tank width x day); 0 kW	-

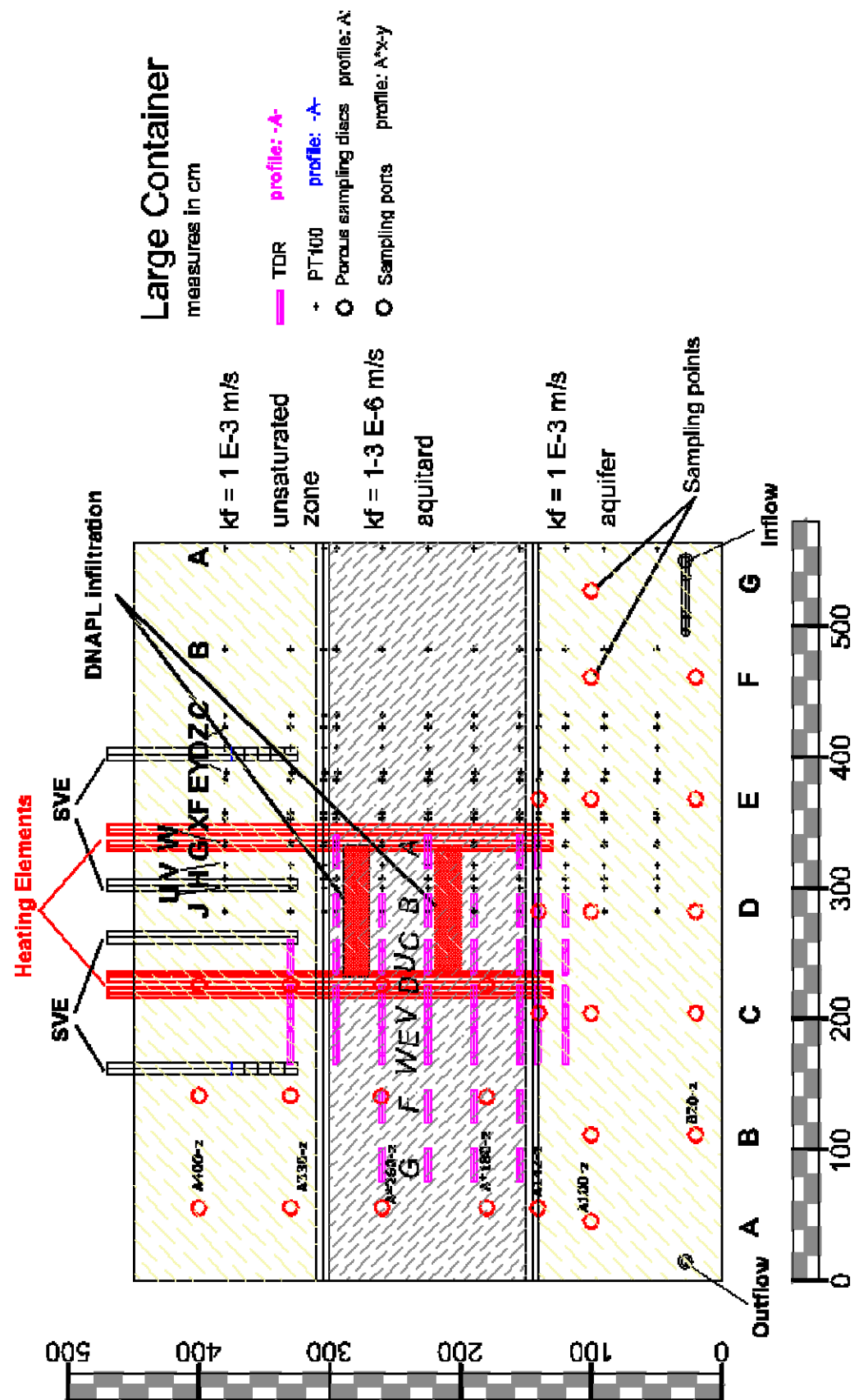


Figure 13: Side view of the larger 3-D tank 2.

For the remediation experiments, DNAPL pools were created by infiltrating a known substance into two NAPL-release lenses. These lenses were located in the aquitard at a height of 2.7 - 2.9 m (upper lens) and between 2.0 - 2.2 m (bottom lens) above base (above base). See Figure 11 and Figure 13. The lenses are shaded in red. To monitor a potential contaminant migration during the remediation experiments, sampling ports were emplaced in the set-up of both tanks on seven different levels with three to 25 ports on each level. A main focus of the research work was on a potential risk of downward migration of DNAPL into the underlying aquifer during heating. Most of the sampling ports were installed below the infiltration lenses. The operational settings of the remediation experiments are summarized in Table 2.

Table 2: Summarized Data from both Tanks for remediation experiments

	Smaller Container 1	Larger Container 2
Length	6 m	6 m
Width	3 m	6 m
Height	4.5 m	4.5 m
K_s of lower permeability soil layer	1 to 4 x 10 ⁻⁷ m/s	2 to 3 x 10 ⁻⁶ m/s
K_s of higher permeability soil layers	1 x 10 ⁻⁴ m/s	1 x 10 ⁻³ m/s
Power of heater array	6 kW (4 heaters) and 12 kW (8 heaters)	12 kW (8 heaters)
Groundwater outflow (const. head)	3 m above base	3 m above base
Phase 0	2330 l / (tank width x day); 6 kW	166.7 l / (tank width x day)
Phase 1	1000 l / (tank width x day); 6 kW	---
Phase 2	173.3 l / (tank width x day); 6 kW	---
Phase 3	173.3 l / (tank width x day); 6 kW	---
Phase 4	173.3 l / (tank width x day); 12 kW	---
Position of upper DNAPL lens	2.70 – 2.90 m above base	
Position of bottom DNAPL lens	2.00 – 2.20 m above base	
Infiltrated PCE per lens [kg]	10	3.5
Infiltrated Tracer (DCB)	2	0.7
Running time of the experiments	131 days	61 days
Numbers of operating phases	24	20
Contaminant recovery by SVE (SVE + GW plume)		
Upper lens [%]	83 (90)	97 (97)
Bottom lens [%]	7 (29)	88 (88)

5.6 Experiment-specific adjustments of chemical analytical methods (Task 3.3)

During the remediation experiments different samples had to be taken: liquid phase samples, dual phase samples (water and steam / gas) and soil samples. Specific analyses for each of these samples were needed.

Liquid phase samples:

All liquid samples were analyzed in VEGAS's laboratory. At first, analyses were performed with the GC-FID/ECD to enhance the accuracy of the measurements, but the calibration of the dichlorobenzene (DCB) tracers was not reliable. Thus, all liquid samples were analyzed by HPLC, with a detection limit of 0.005 mg/l (5 µg/l). This value was considered sufficiently low in view of the fact that the remediation target value for groundwater contamination sites in Germany is usually 10 µg/l and the threshold value is usually 40 µg/l.

Dual-Phase sampling:

In the unsaturated zone and in the steamed zone, the samples were collected with a special sampling system to obtain samples of both the liquid and gaseous phases at the same time. The system was attached to the sampling port via a flexible tube. A small pump extracted a steam / water / gas mixture from the large-scale container. After separating a certain volume of water / gas / steam, the sampling probe was cooled by a condenser (K2) and thus the steam was condensed to the liquid phase and collected. Liquid phase samples could now be taken from the collector and analyzed via HPLC in VEGAS's laboratory. The gaseous phase of the sample was accumulated in a so-called Tedlar Bag, a gas-proof and inert polyvinyl fluoride bag. This bag could be attached to the mobile GC-ECD and analyzed.

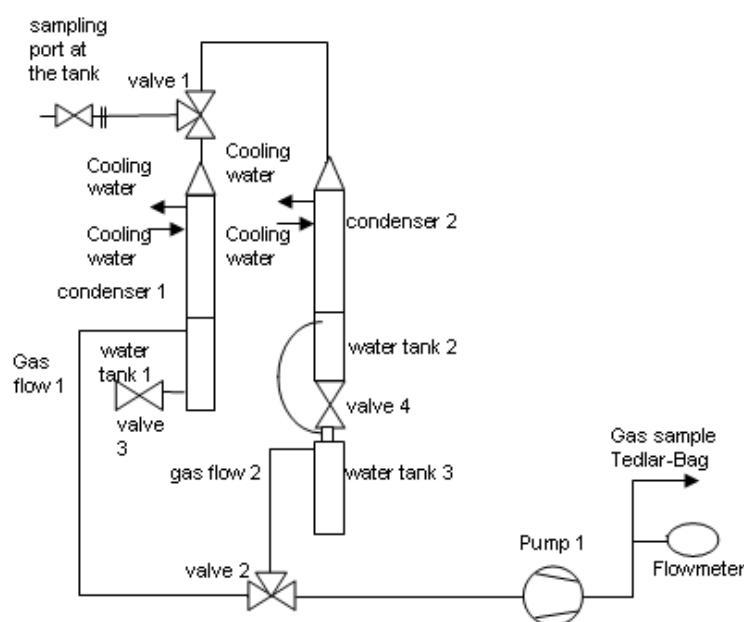


Figure 14: Dual-phase sampling system.

Soil samples:

In the small-scale remediation experiments (chapter 5.4), soil samples were taken and also analyzed in VEGAS's laboratory. The samples were extracted 15 minutes in an ultrasonic bath with Acetonitrile. Afterwards the samples were analyzed with the HPLC.

6 Results and Accomplishments

6.1 Task 1.1: Batch/1D tests to select and characterize sandy / silty soils for large-scale physical model experiments

The grain size distributions of the lower permeability mixtures B and M2 are shown in Figure 15. The fraction of sand is similar for both mixtures but the fraction of silt is higher for mixture M2 resulting in a difference in the permeability by one order of magnitude.

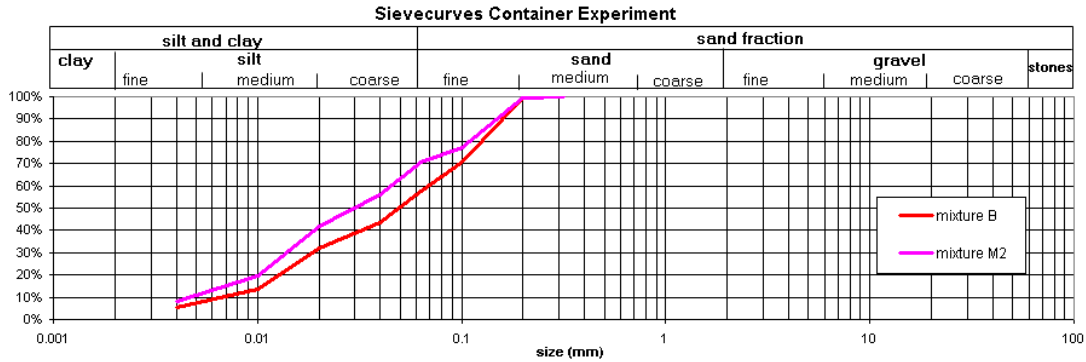


Figure 15: Grain size distribution of Mixtures B and M2.

Figure 16 shows the relationship between permeability and dry density for both of the lower permeability layer mixtures based on five different batch experiments. Permeability increases with decreasing dry density showing a high correlation coefficient of (almost) 1.

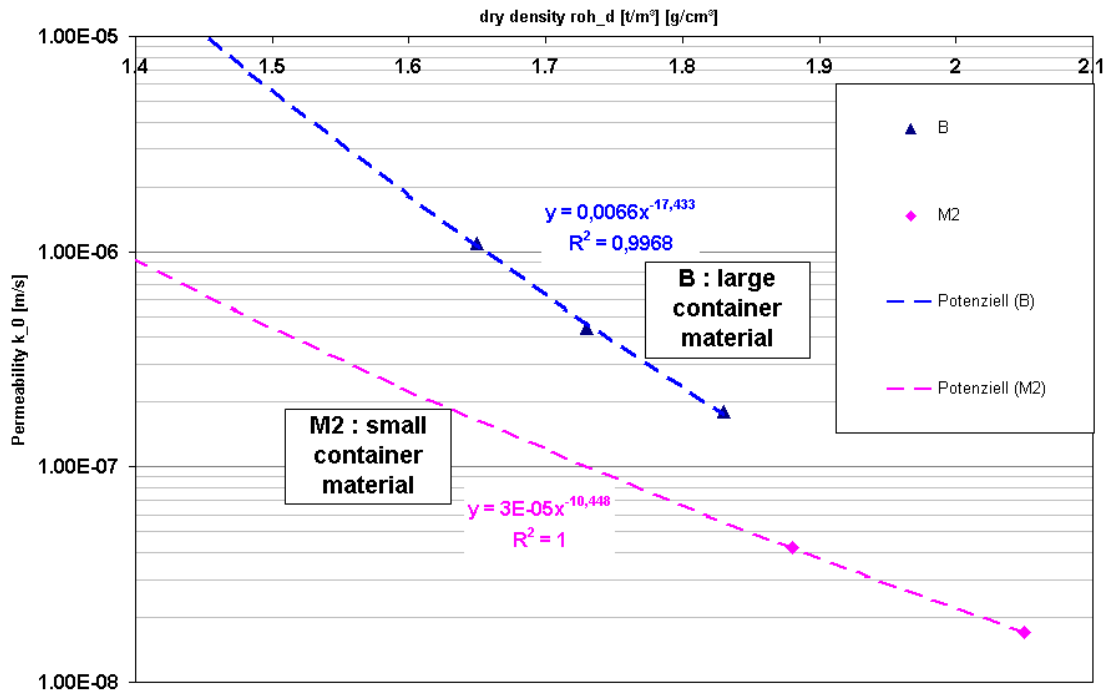


Figure 16: Permeability – dry density - relation of lower permeability soil from batch-scale experiments.

In Figure 17 the permeability in the large-scale containers was determined by the correlation between permeability and dry density using the correlation equation from the batch experiments of Task 1.1. The dispersion of the values is much higher for mixture B than for mixture M2.

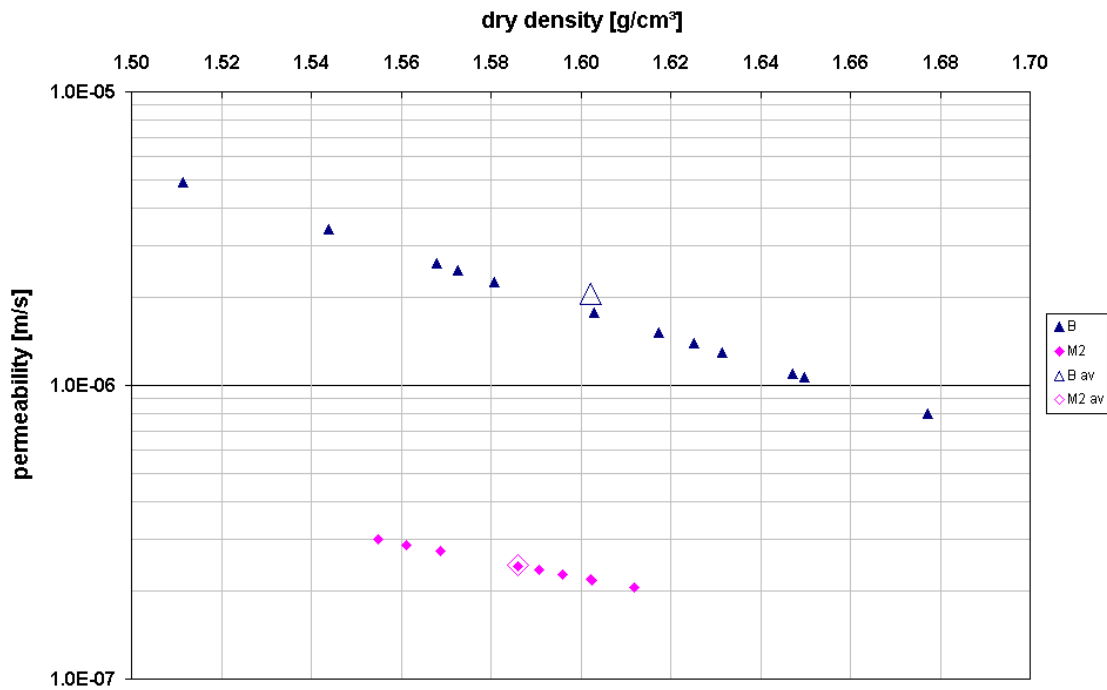


Figure 17: Permeability – dry density - correlation of low permeable soil in both large-scale containers.

The designated hydraulic conductivity for the lower permeability layers in the large-scale containers was 10^{-7} m/s for the small container (tank 1) and 10^{-6} m/s for the large container. Figure 18 shows the distribution of the permeability of both mixtures. Mixture B (large container) has an average permeability of 2.5×10^{-6} m/s, mainly ranging from $1 - 4 \times 10^{-6}$ m/s. Mixture M2 (small container) has an average permeability of 2.5×10^{-7} m/s mainly ranging from $2 - 3 \times 10^{-7}$ m/s.

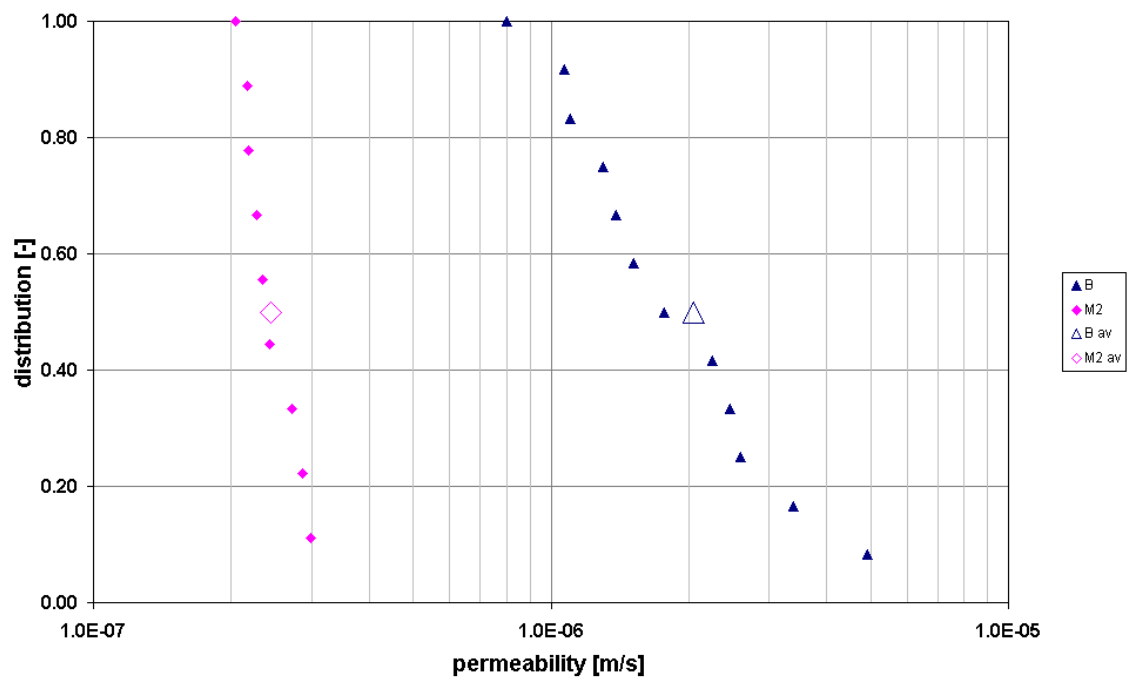


Figure 18: Permeability distribution of low permeability soil layers, implemented in large –scale containers.

6.2 Task 1.2: Small-scale 2-D heat transfer experiments

6.2.1 Introduction

The aim of the small-scale experiments (project tasks 1.2 and 3.1) was to investigate the principal processes that occur during the operation of thermal conduction heating (TCH) wells in the saturated zone. Data from the first experiments were given to MK Tech Solutions, Inc. for validation of the numerical model. Furthermore, data such as soil characteristics (e.g., grain size distribution, permeability, p_c - S_w -curve), groundwater conditions and temperature distribution were used for numerical back analyses and for the design of further 2-D experiments (Task 5.1). The following pages give an overview of the 2D experiments we conducted.

6.2.2 Homogeneous heating experiments

Two homogenous heating experiments with different levels of power input were carried out to investigate the heat propagation in the lower permeability material. The experimental setup is given in Figure 19. A vertically oriented heating element was located on the left side of the center of the flume. The right side of the flume – the groundwater outlet – was fully screened to provide a constant head boundary condition. The upper-left corner was screened to allow steam to exit (instead of it being trapped there during the experiments). The whole flume was fully water saturated before the experiments. During the experiments, the flume was insulated with glass wool and foam blocks with a thickness of about 6-8 cm.

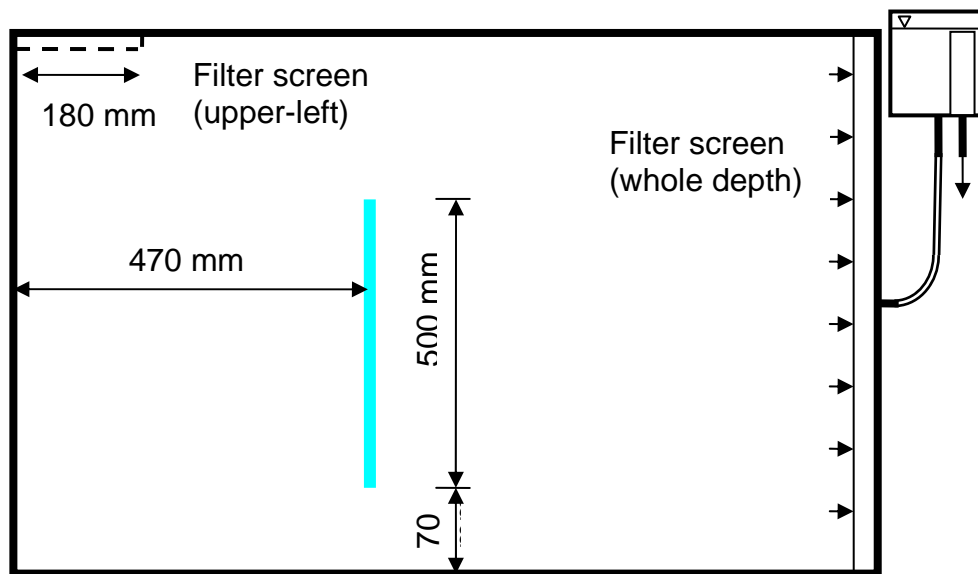


Figure 19: 2-D experimental setup – homogeneous heating. Colored vertical line indicates position of the heating element.

6.2.2.1 Homogeneous heating with high power input:

For this experiment, the flume was heated with 1200 W of power, meaning maximal power of the heating element. The results are shown in Figure 20. At the beginning of the heating period, a steam zone formed around the heating element (0 - 90 min, Figure 20). The steam zone increased laterally until breakthrough occurred at the right side (120 min). This wide horizontal steam propagation indicated that viscous forces were dominant relative to buoyancy forces (vertical heat expansion). The influence of the buoyancy forces appeared

only at the very late stage. This experiment was repeated once more. The results were quite similar. The attempt to measure the saturation with gamma radiation failed due to settlement of the fine material.

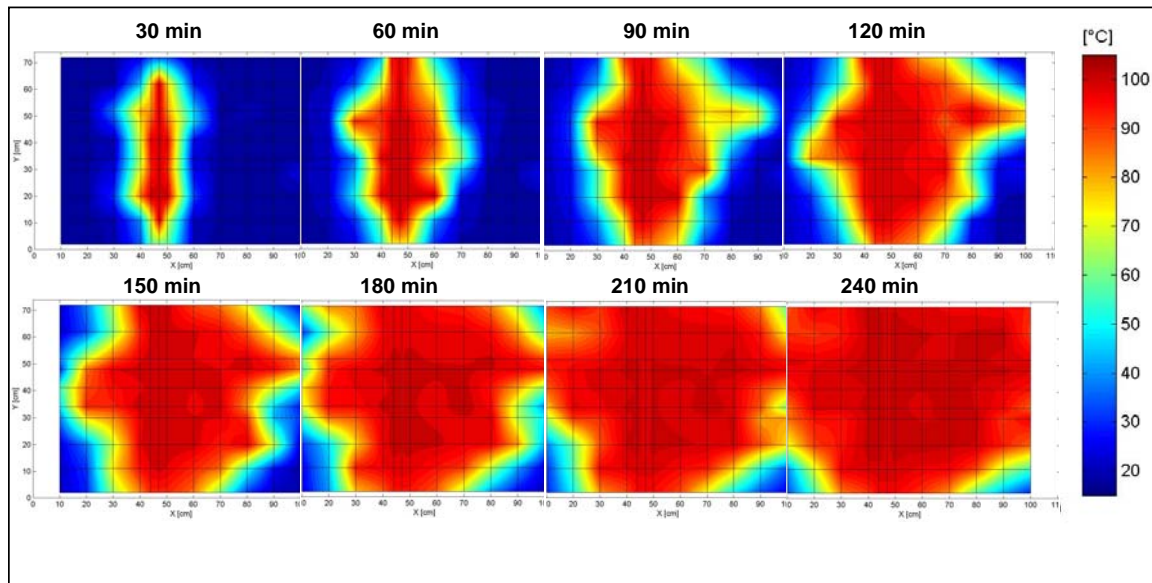


Figure 20: Measured temperature distribution, homogeneous heating in 2-D flume with high power input (1200 W).

6.2.2.2 Homogeneous heating with low power input

During this experiment, the flume was heated with 20 % power of the heater (240 W). The results are shown in Figure 21. Comparable to the previously described experiment, a steam zone formed around the heating element during the heating phase (0-9 h, Figure 21). Since the buoyancy forces became dominant halfway through the experiment, a V-shaped steam zone formed by the end of the experiment (18-27 h, Figure 21). An attempt to use even lower power input (120 W) failed due to heat losses, which could not be reduced by adding more insulation.

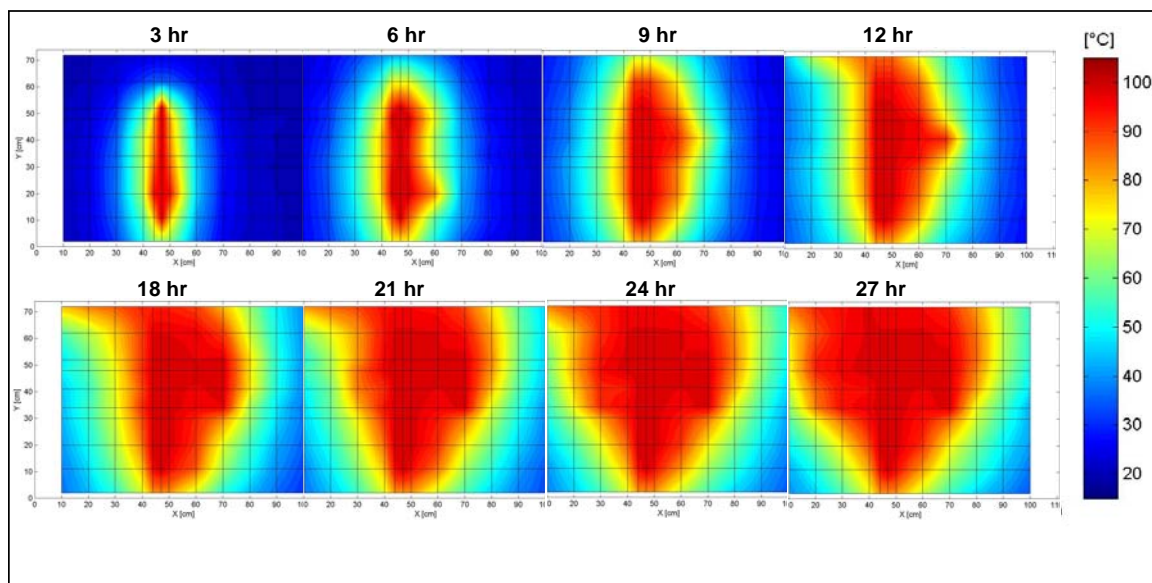


Figure 21: Measured temperature distribution, homogeneous heating in 2-D flume with low power input (240 W).

6.3 Task 1.3: Large-scale container heat transport experiments

The pre-existing large-scale container set-up from former experiments with Thermally-Enhanced SVE (TESVE) with thermal wells in the unsaturated zone (HIESTER ET AL. 2002) was modified so that it could be used for Thermal Conduction Heating (TCH) heat-transfer experiments in the saturated zone, Task 1.3 (Figure 2).

The research started with heat transport experiments without contaminants. During the first heating experiment the groundwater level was initially adjusted at 3 m above the bottom of the tank, which was at the top border of the lower permeability layer. The groundwater table was maintained at this position, creating a constant head boundary condition. In the overlying sand layer, each of the four SVE wells was operated with a constant flux of 5 m³ SATP/h. Heat propagation (temperatures), water saturation and SVE mass fluxes (water content and air) were measured throughout the experiments.

For the second large-scale heat transport experiment, the previous shorter heating elements inside each of the four thermal wells arrayed in a 1 m x 1 m square pattern were replaced by newly designed heating elements of 1.5-m length (Figure 2). Rather than maintaining a constant head boundary condition, the water table was allowed to drop off as water was evaporated (Phase 1), to determine the effect of heating on the fluctuation of the water table and pressure conditions.

Figure 23 shows the temperature distribution and the water saturation over time along the HTC-TDR transects at two measurement profiles: Profile No. 4 (located at the center position, midway between the four heaters) and Profile No. 2 (located just outside the square heater array). Examination of the various profiles indicates that the highest temperatures were achieved, as expected, in the midpoint between the heaters (Profile No. 4). Temperatures >100°C indicate that steam was produced in this region, which effected a desaturation of the initially saturated zone. With time, the extent of the heated zone increased (view Figure 23 from left to right), with an increasingly larger fraction of the soil starting at the top of the lower permeability layer (LPL) attaining the boiling point of water. Concomitantly, as water evaporated and was extracted by the soil vapor extraction (SVE), the soil at that level was observed by means of the HTC-TDR sensors to have become desaturated, until at about 25 d when it evidentially resaturated temporarily. This may have been a result of condensation of water vapor that was produced as heating extended into the underlying sand zone. After eight weeks (56 d), the entire volume of the LPL began to become desaturated. Similar effects could be observed just outside the central area (Profile No. 2), despite the fact that the temperatures there had been lower.

After 80 days of heating, the groundwater table, observed at the side of the container, had dropped below the LPL (dotted line at 200 cm above base [above base]) and was allowed to continue falling until reaching a height of 170 cm above base (108 d). As the groundwater table fell, the LPL as well as the sand below started to undergo drainage. This can be clearly seen after approx. 100 d. The drainage in the center of the heater array and outside the heater was approximately similar. As a result of the drainage, more injected heat energy could be stored in the subsurface, which could be seen at first by the rising temperatures in the upper half of the LPL. The temperatures at the bottom of the LPL reached about 90 °C by the end of Phase 1.

By contrast, just outside the square heater array (Profile No. 2), the temperatures at the top of the sand layer remained almost constant at about 60 °C, even after the underlying sand started to be drained.

In Phase 2 of this experiment, the influence of a rising groundwater table on the temperatures and the water saturations was of interest. The groundwater table was raised slowly and kept constant for the remaining experiment at 300 cm above base. After one week of heating with the high water level, the temperature distribution that was achieved was approx. similar to the distribution that had prevailed after one week of heating in Phase 1 of this experiment.

The water saturations increased immediately with the rising groundwater table. By continuing heating, the porous media again became partly desaturated by steam production within the LPL. The desaturated volume at the end of this experiment was about 10 to 15 % of the pore volume.

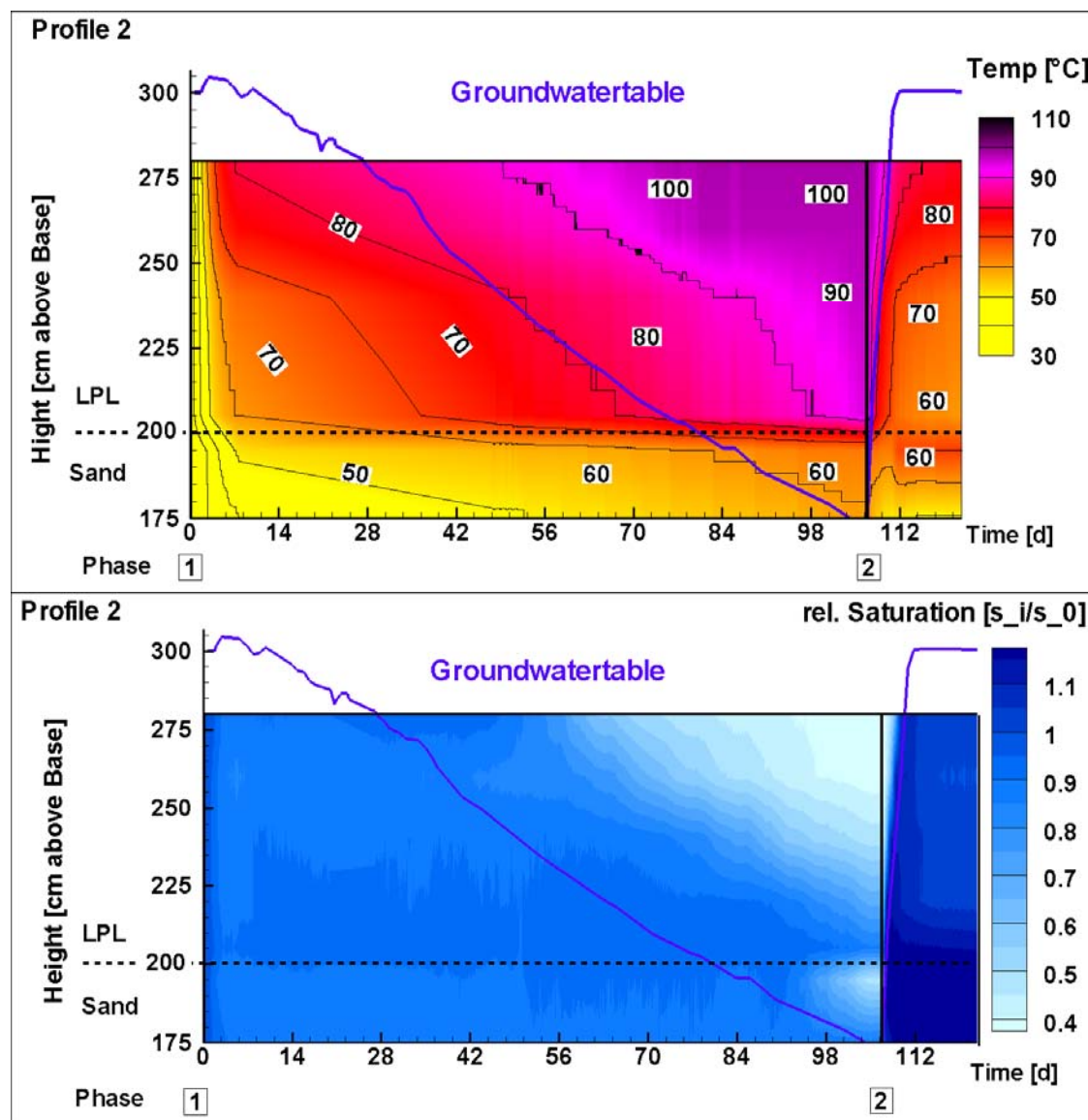


Figure 22 Progression of temperature and saturation measured in profile 2 (just outside the square heater pattern, at the position shown in Figure 2). The groundwater table was measured at the side of the large container in the coarse sand. LPL = lower permeability layer.

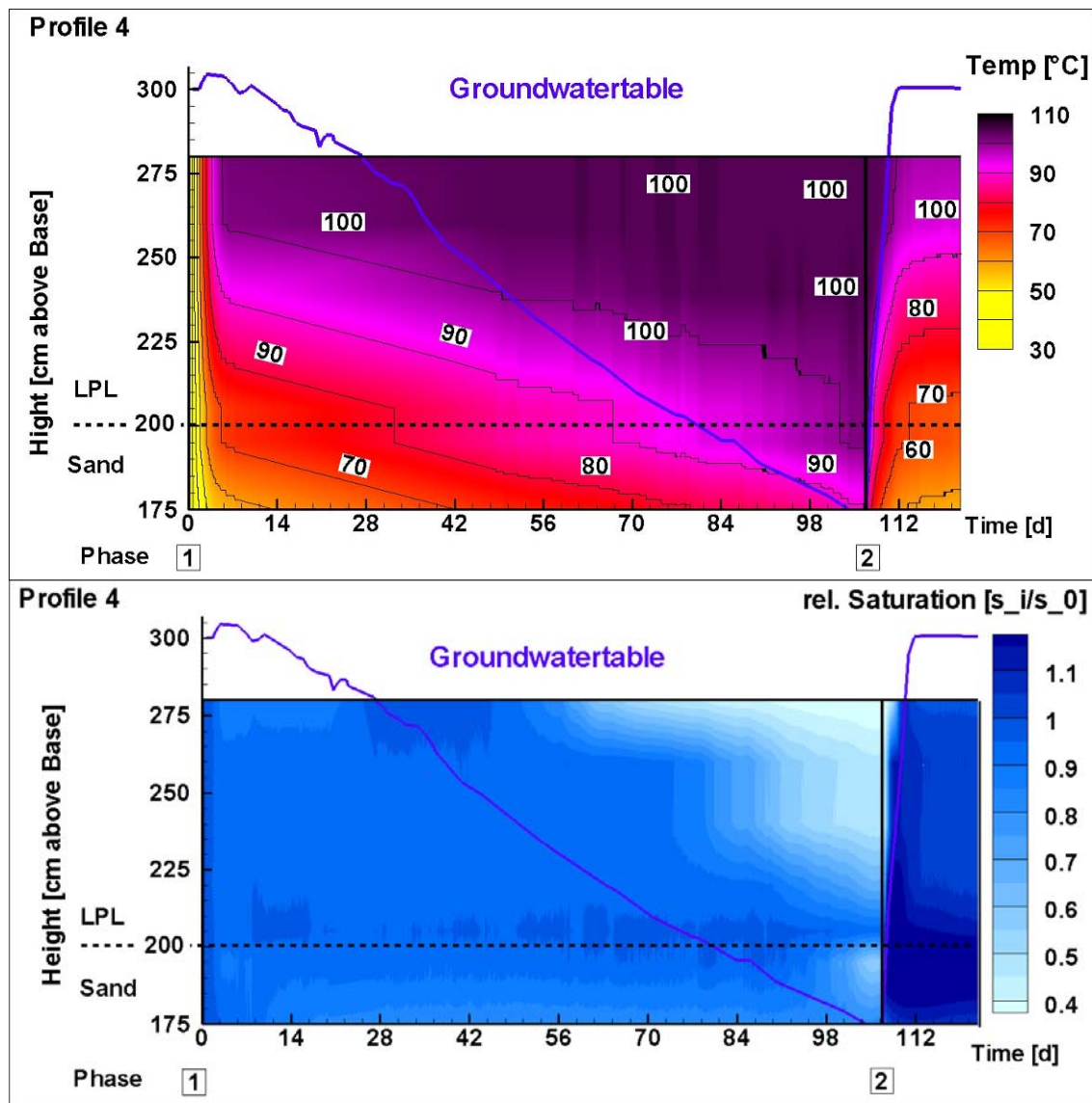


Figure 23 Progression of temperature and saturation measured in profile 4 (center profile midway between the four heaters, at the position shown in Figure 2). The groundwater table was measured at the side of the large container in the coarse sand. LPL = lower permeability layer.

6.4 Selection of representative DNAPL

In order to select the representative DNAPL for the large-scale remediation experiments, the properties (vapor pressure, Henry's Law coefficient, solubility, viscosity, surface tension, density and Octanol-Carbon Partitioning Coefficient) of different contaminants were investigated relative to their temperature dependence. Data shown in Figure 24 to 30 were calculated from compound-specific data, taken from REID ET AL. 1987, NIST 2005 and CRC 2008.

Vapor Pressure: [mbar]

Vapor Pressure increases with increase in temperature (Figure 24):

- Mercury (Merc) has a very low vapor pressure.
- Polycyclic Aromatic Hydrocarbons (PAHs), such as Naphthalene (Nap) and Anthracene (Ant) have relatively low vapor pressure values.
- Many chlorinated hydrocarbons (CHCs) have high vapor pressure values. PCE, Chlorobenzene (CBz) and Dichlorobenzene (DCBz) have vapor pressures less than water.
- Mercury is more affected by temperature than water.

The DNAPL constituents considered for use in the experiments behave similarly to each other. With an increase in temperature, their vapor pressures rise to a lesser degree than does the vapor pressure of water.

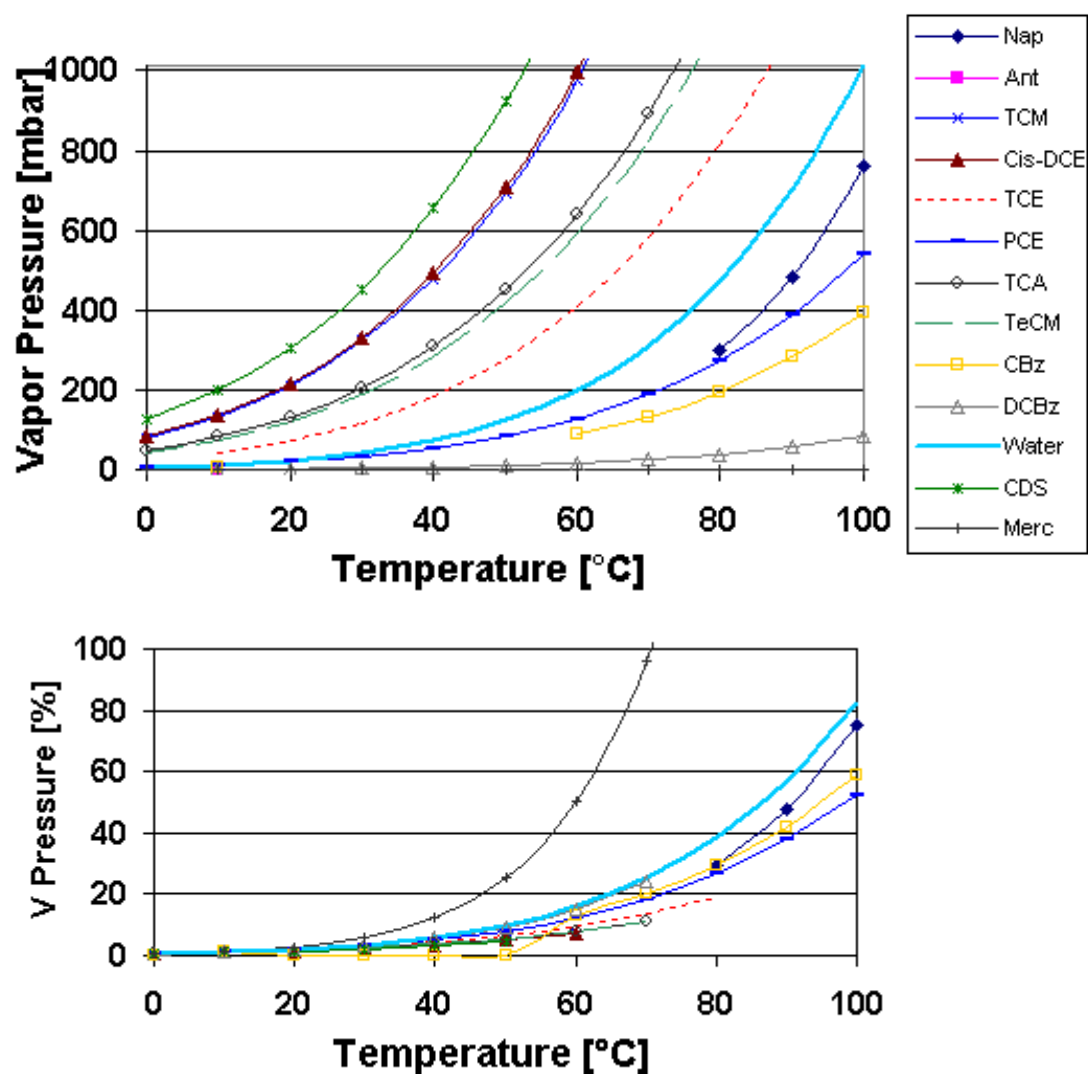


Figure 24: Temperature dependent vapor pressures (absolute and relative to 10°C) of different contaminants.

Henry's Law Constant: [atm·m³/mole]

Like vapor pressure, Henry's Law Constants increase with an increase in temperature. PAHs have low values compared to CHCs. The values for PAHs are in the range of 1×10^{-5} to 5×10^{-3} at 20 °C.

At this temperature, most CHC values are in the same range, i.e., 1×10^{-3} to 2×10^{-2} . With increasing temperature, the Henry's Law Constants for TCM, *cis*-DCE, CBz and DCBz increase almost linearly, while those of TCE, PCE, TCA and Tetrachloromethane (TeCM) increase exponentially.

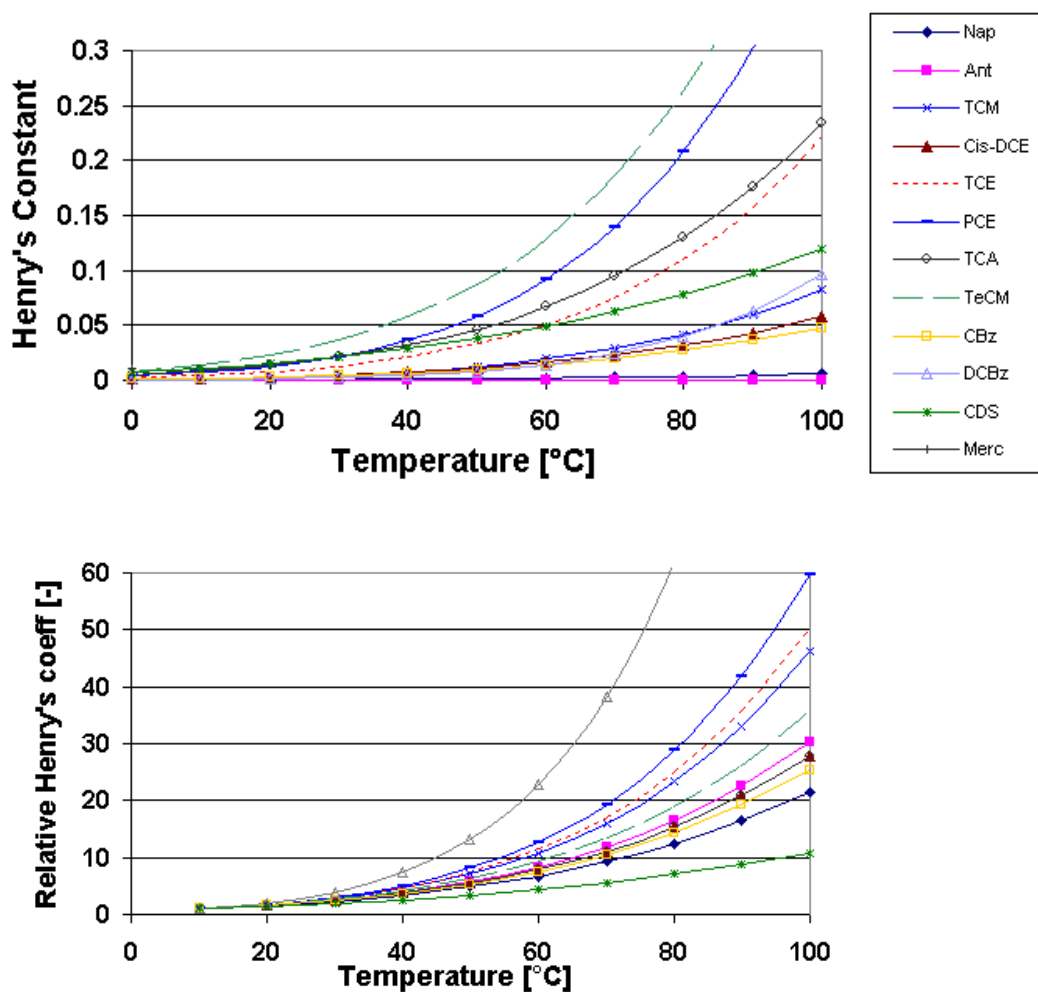


Figure 25: Temperature dependent Henry's Law coefficients (absolute and relative to 10°C) of different contaminants.

Solubility: [mg/L]

The solubility of some substances increases with an increase in temperature, while that of others decreases with an increase in temperature (CRC 2008):

- At 20°C, TCM, *cis*-DCE and TCA have high solubilities (about 9,000, 7,000 and 4500 respectively).
- CBz and DCBz are showing an increase of the solubility with increasing temperatures.
- The solubility of PCE and TCE shows a minimum for 20 / 25°C with higher temperatures for 0°C and 60°C and 80°C respectively.
- Anthracen and Naphthalene are showing a high increase of the solubility with increasing temperatures. Nevertheless, the solubility of both substances is low.

The influence of increasing temperatures on the solubility is inconsistent for different substances. HERON ET AL. 1998A showed the temperature dependence of the solubility of TCE.

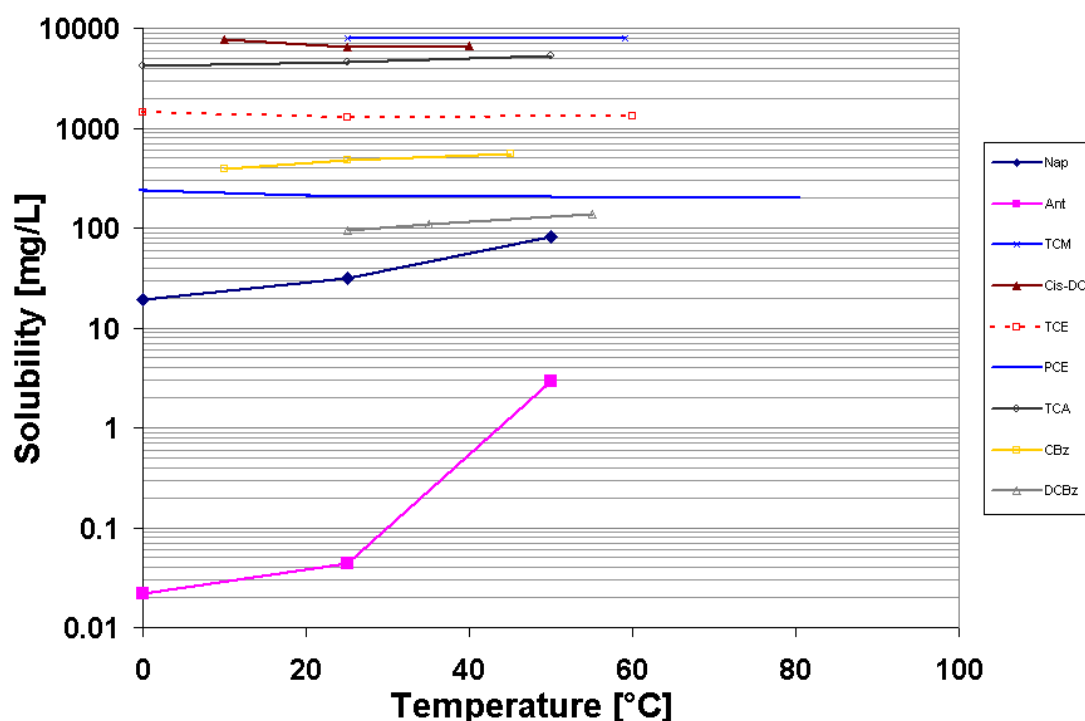


Figure 26: Temperature dependent solubility of different contaminants.

Viscosity: [centipoise, cP]

Viscosity decreases with the increase in temperature.

PAHs have high viscosity at low temperatures and with increasing temperature their viscosity decreases exponentially. They behave much like water. At 50°C, their viscosity becomes half of the value at 10°C. CHCs have low viscosity at low temperatures, and are affected comparatively less than PAHs as temperature rises. Between 70 and 90°C, their viscosity reduces to half of the value at 10°C.

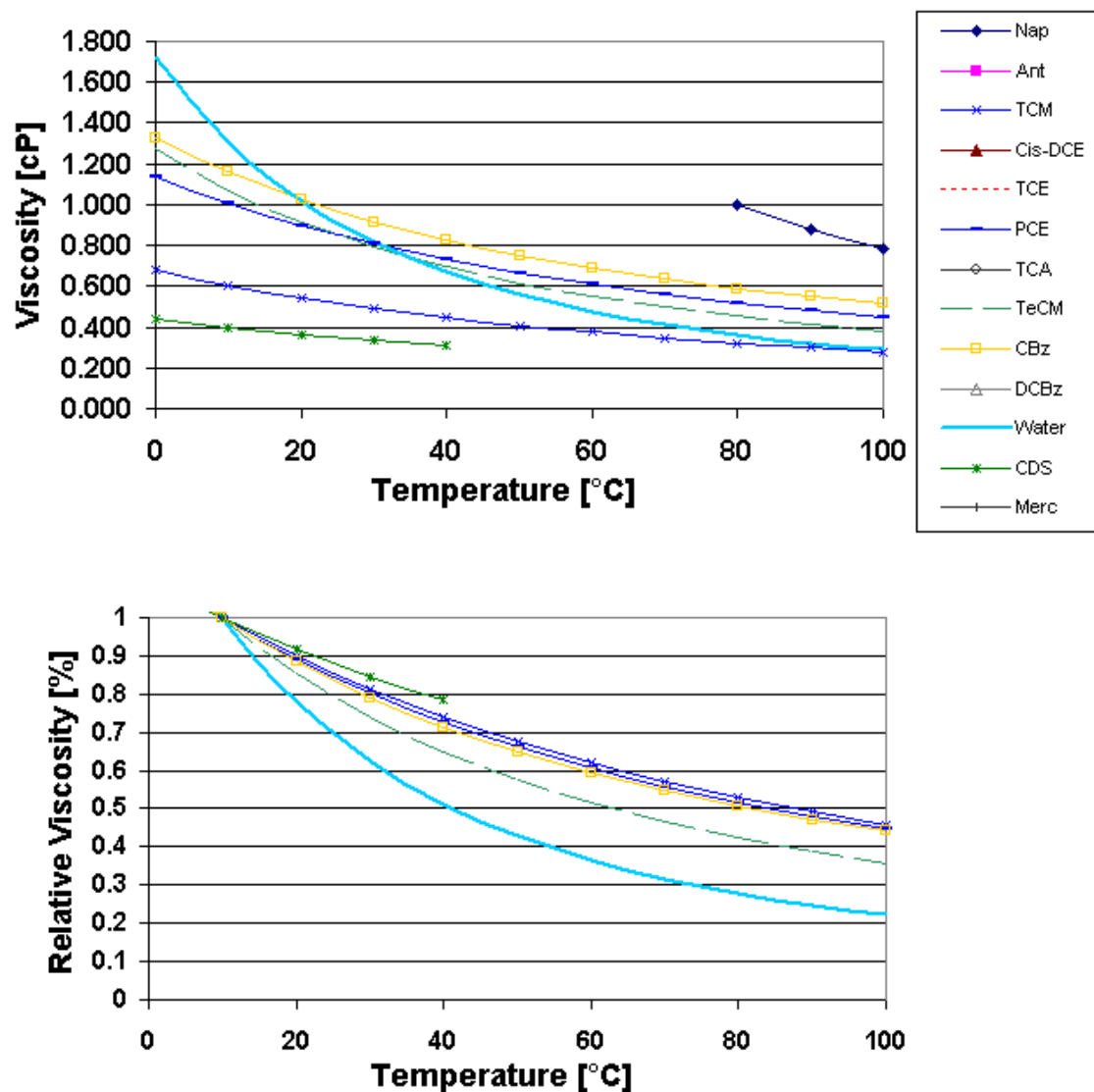


Figure 27: Temperature dependent viscosity (absolute and relative to 10°C) of different contaminants.

Surface Tension: [dyne/cm]

Surface Tension decreases with an increase in temperature.

Merc has the highest surface tension value, i.e. 486.50 dyne/cm at 20°C.

Water has a high surface tension of about 73 dyne/cm at 20°C.

Other DNAPLs have surface tensions within the range of 25 to 40 dyne/cm at 20°C.

Temperature has very little effect on the surface tension of mercury.

Other compounds are more affected than water. They show a linear decrease in surface tension with increasing temperature.

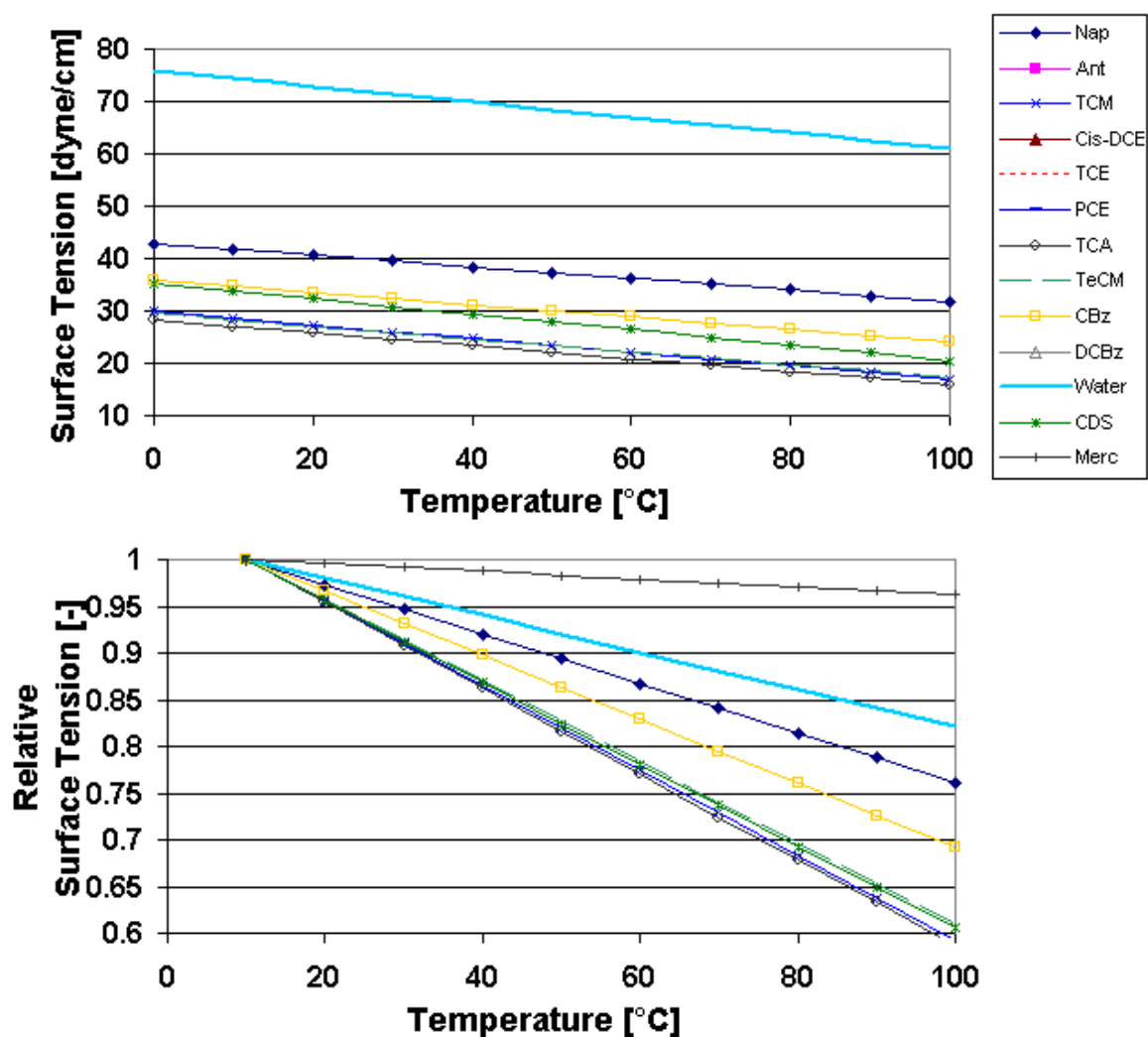


Figure 28: Temperature dependent surface tension (absolute and relative to 10°C) of different contaminants.

Density: [g/mL]

Merc has the highest density of 13.59 g/mL at 20°C.

PCE, TCE and TeCM have densities more than 1.45 g/mL at 20°C.

Nap and CBz have densities slightly more than water, while other substances have densities between 1.25 and 1.35 g/mL at 20°C.

Temperature has very little relative effect on the densities of these substances, which all show the same linear behavior.

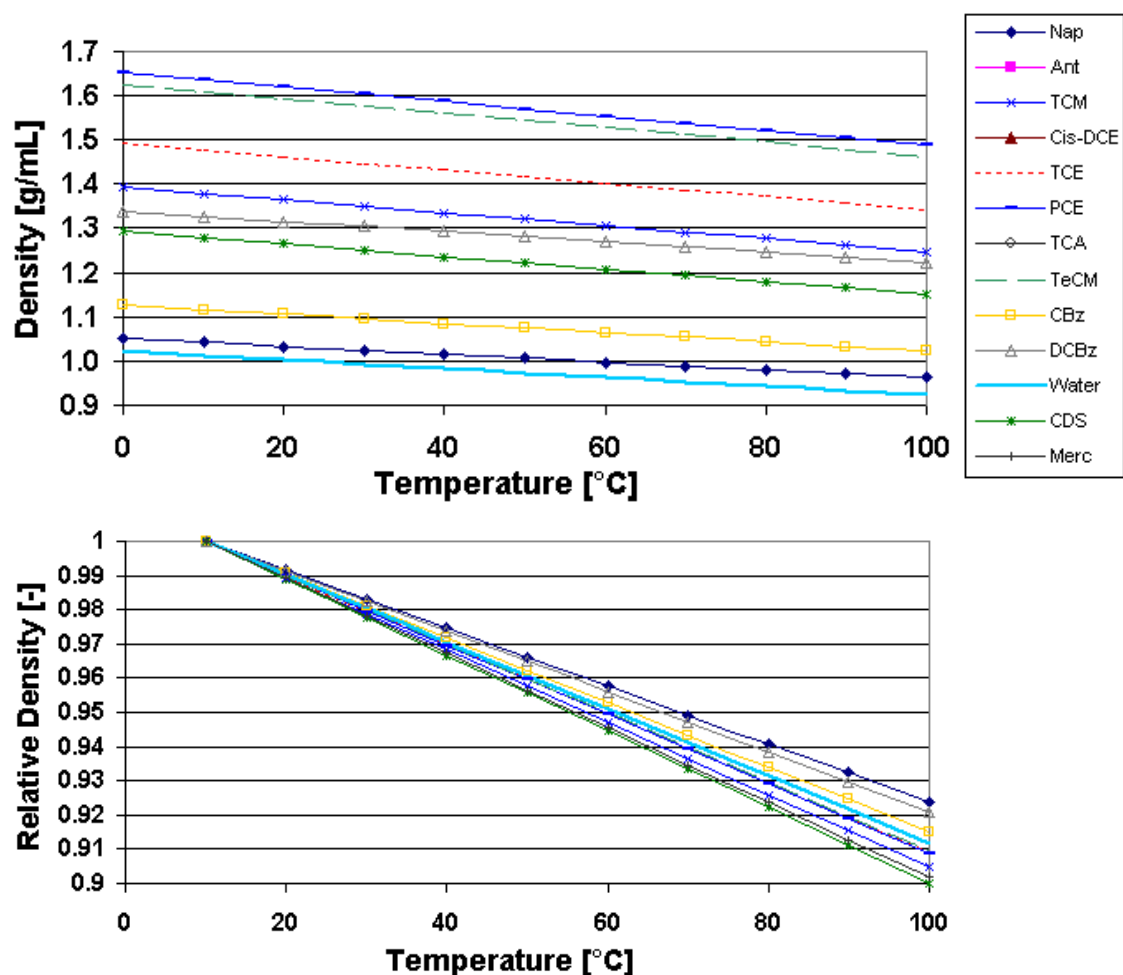


Figure 29: Temperature dependent density (absolute and relative to 10°C) of different contaminants.

Octanol-Carbon Partitioning Coefficient (K_{oc}):

The influence of increasing temperatures on sorption is unclear and only few data could be found. The influence of increasing temperatures to sorption processes is still object of research.

SLEEP AND MCCLURE 2001 showed that sorption coefficients of toluene, perchloroethylene, and naphthalene decreased by 35, 40 and 60 %, respectively when temperature was increased from 22-25 °C to 90 °C.

DELLE SITE 2000 found that the temperature effect on sorption isotherms is normally low for both hydrophobic and polar organic compounds.

Typically, in the absence of organic debris, adsorption is an order of magnitude smaller than other factors. Therefore, it was estimated to have minor to none relevance.

General overview of properties:

i) With respect to temperature, Vapor Pressure and Henry's Law Constant behave similarly. Figure 30 shows the ratio of the relative Henry's Law Constant (from Figure 25) to the relative Vapor Pressure (from Figure 24) as a function of temperature. The increase of the Henry's Law Constant is moderately higher than the increase of the Vapor Pressure (indicated by values >1, Figure 30). Nevertheless, the effect of temperature on increasing Vapor pressure and Henry's coefficient is within the same order of magnitude.

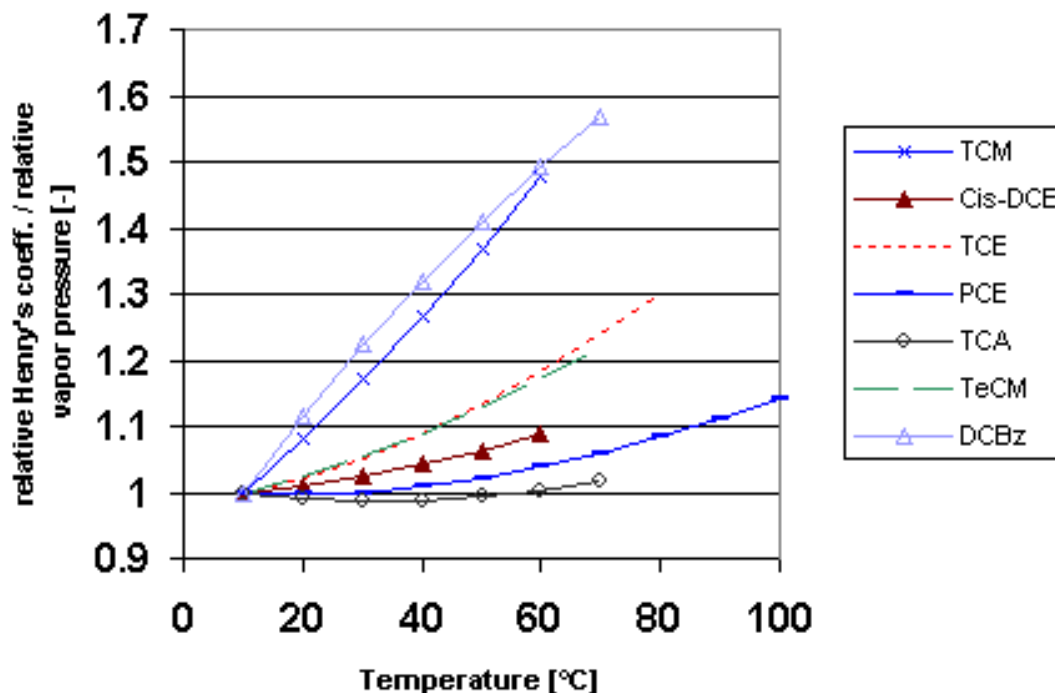


Figure 30: Temperature dependent Ratio of relative Henry's Law Constant to relative vapor pressure.

ii) Viscosity and Surface Tension decrease with increasing temperature, but exhibit dissimilar behavior, i.e., with change in temperature viscosity is relatively more affected at low temperatures and less so at higher temperatures. Surface tension, by contrast, exhibits

relatively little change with change in temperature at low temperatures, but the rate of change increases slightly at higher temperatures.

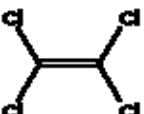

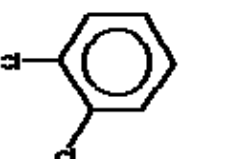
iii) Solubility and Sorption (K_{oc}) are affected inversely by changing temperatures: increasing solubility causes a decreasing sorption and *vice versa*.

After reviewing these property changes, we selected PCE for the large-scale remediation experiments (Task 4.3 and 4.4). TCE's properties are similar to those of PCE, but its density is lower than that of PCE. Thus, we regarded PCE as the more challenging contaminant and selected it for the experiments, while reserving TCE for future / optional remediation experiments.

It had previously been decided to install two NAPL-release lenses in each of the large-scale containers, one above the other (see Figure 11 and Figure 13). Therefore, we recognized that it would be desirable to select two tracers (one for each lens) to enable the recovered contaminant from the two lenses to be distinguishable. Seven substances were tested as possible tracers: 1,2-Dichlorobenzene, 1,4-Dichlorobenzene, 1,3-Dichlorobenzene, 2-Chlorotoluene (o-Chlorotoluene), 2-Chlorothiophene, 2-Bromothiophene and Monobromobenzene. Only the first two tracers could be detected accurately. The other five substances showed overlapping retention times. 1,2-Dichlorobenzene is a liquid that dissolves well in PCE, but the solubility in PCE of 1,4-Dichlorobenzene, (which is a crystalline substance) had to be assessed. We found that the 1,4-DCBz did dissolve fully in PCE, and was fully recoverable.

The methods of analysis of the selected contaminant and tracers are described in chapter 5.6.

Table 3: Overview of the selected contaminant and tracers.

	Tetrachloro-ethylene	1,4-dichloro-Benzene	1,2-dichloro-Benzene
Formula	C_2Cl_4	$C_6H_4Cl_2$	$C_6H_4Cl_2$
CAS Registry Number	127-18-4	106-46-7	95-50-1
Chemical structure			
Boiling point [°C]	121	174	180
Henry's Law constant (at 20°C) [atm m³/mol]	0.0131	0.00175	0.00130

6.5 Task 3.1 - Visualized 2-D remediation experiments:

6.5.1 Vertical twin-element heater

The results of the first remediation experiment in the 2-D flume are summarized in Figure 31. The infrared (Infrared) photos were taken by briefly removing the insulation and taking an Infrared photo through the Pyrex® glass front panel, after which the insulation was immediately replaced.

At the initial stage of the experiment, the steam zone mainly propagated within the underlying high permeability layer. When steam had flooded most of the high permeability layer, it started to expand into the overlying lower permeability zone. At about 60 min, the steam zone entered the coarse sand NAPL-release lens and started to vaporize the PCE. At 120 min, all the PCE had vaporized, but still no PCE was extracted and adsorbed on the activated carbon filter (the loading being determined by weight measurement, i.e., the carbon filter rested on a balance throughout the experiment). At this stage, all vaporized PCE remained within the steam zone, because the gas phase did not yet have a continuous pathway to the outlet of the flume. After about 180 min the steam zone broke through the top of the upper layer, and PCE started to be recovered (Fig. 9). The heating was suspended after 6 hours, although the soil vapor extraction system continued to operate until 14 hours. Overall, 92% of the PCE was recovered through soil vapor extraction. The mass difference of the activated carbon filter before and after the experiment was used to estimate the mass of the recovered PCE. As a loading of water in the activated carbon filter also results in a higher mass, this could lead to an overestimation of the PCE recovery.

Due to the low capillary pressure in the high permeability layer, the heat pipe (countercurrent outward transfer of heat by steam convection, and inward transfer of water by capillary wicking) (UDELL 1985; HIESTER ET AL. 2003) was destroyed after 60 min of heating. “Dry” zones were formed near the bottom of the heating elements, where all residual water was vaporized, and the heat was thereafter solely transferred by thermal conduction. The local temperature gradient around the heating elements became very high, with the temperature at the heating elements being at least 500°C.

After the experiment, the soil samples were analyzed. The PCE distribution as interpolated between sample locations is shown in Figure 33. The total PCE remaining in the soil amounted to less than 1 g. The mass balance deficit, i.e., the difference between the amount recovered through SVE and that remaining in the soil was 8% PCE (around 25 g). The missing PCE might have been desorbed from the activated carbon filter due to the high water content of the extracted soil vapor. On the other hand, the lack of recovery of contaminants in the soil samples may most likely be due to losses that occurred during the “open lid” sampling procedure.

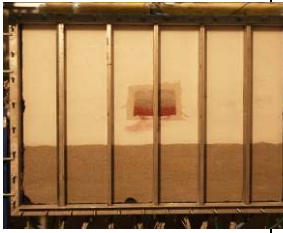


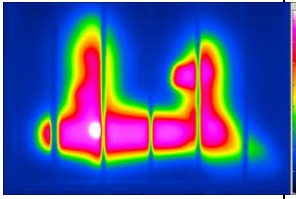
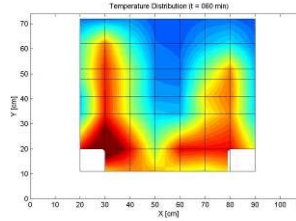

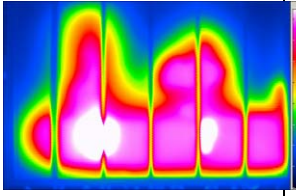
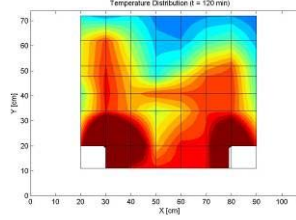

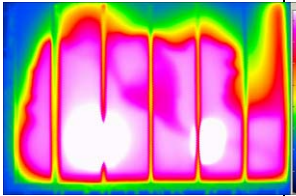
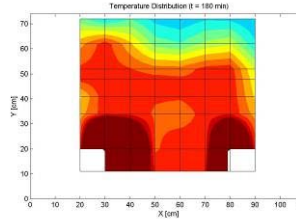


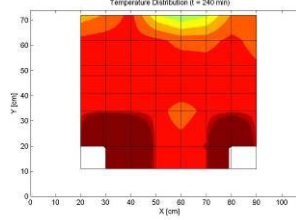

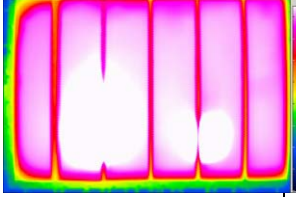
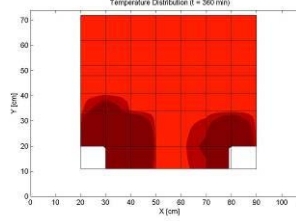
t	Digital Photos	Temp.-Distribution (Infrared)	Temp.-Distribution (Pt100)
0 min			
60 min			
120 min			
180 min			
240 min			
360 min			

Figure 31: Visualization, and temperature measurements during the first 2-D remediation experiment.

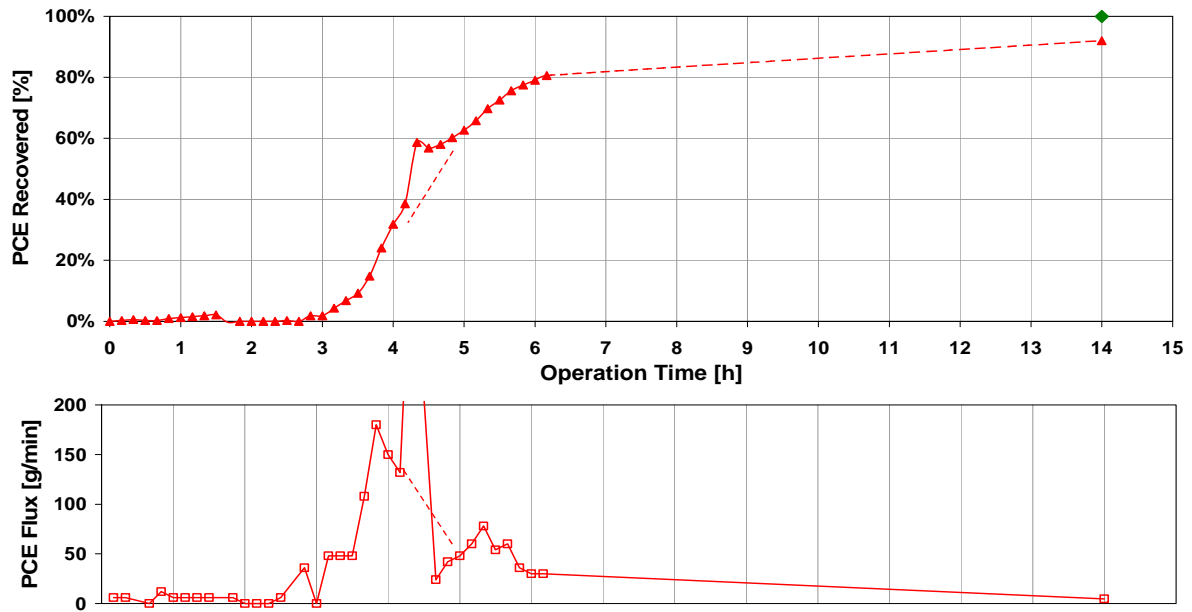


Figure 32: PCE recovery curve and PCE flux curve from the first 2-D remediation experiment.

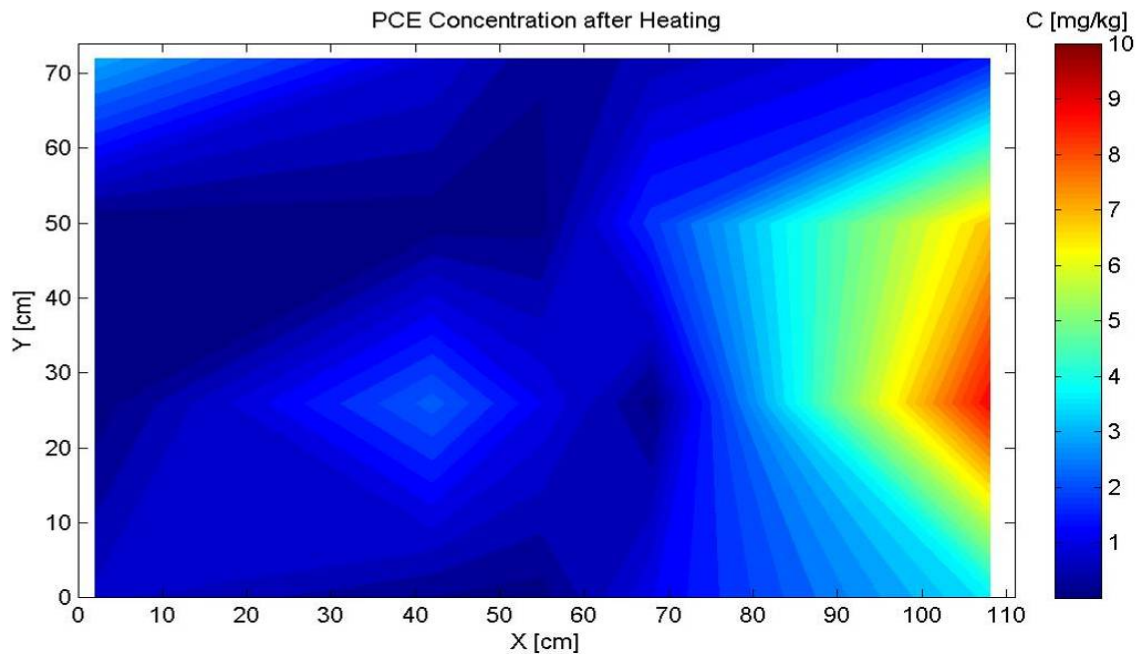


Figure 33: PCE distribution after the first 2-D remediation experiment. The PCE remaining in the soil totaled less than 1 g, relative to 320 g infiltrated initially.

6.5.2 Tilted single-element heater

The results of this second remediation experiment in the 2-D flume are summarized in Figure 34. The infrared (Infrared) photos were taken by briefly removing the insulation and taking an Infrared photo through the Pyrex® glass front panel, after which the insulation was immediately replaced.

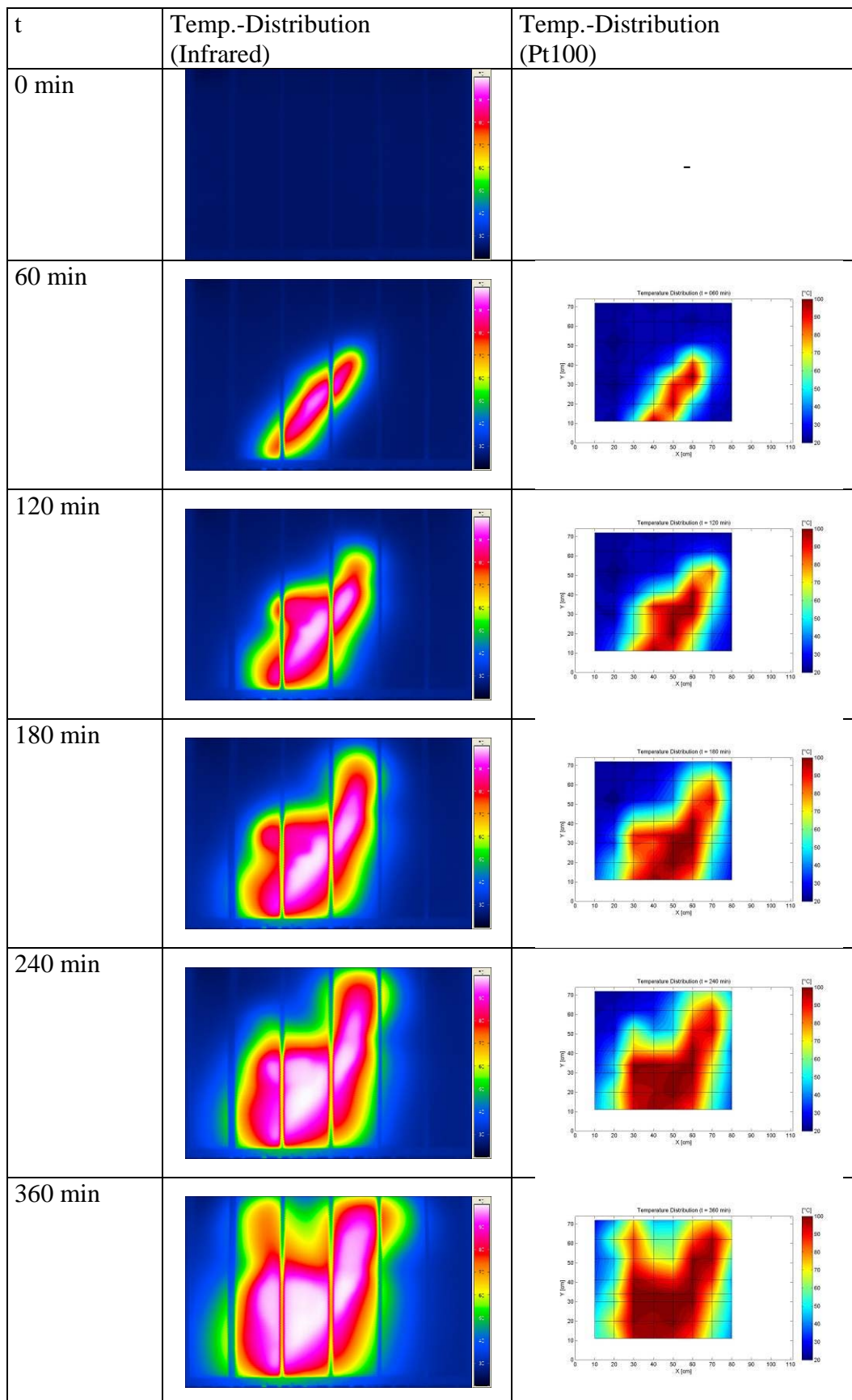


Figure 34: Results of the second 2-D remediation experiment.

At the initial stage of the experiment, the steam zone mainly propagated within the zone around the heater. At about 120 min, the steam zone entered the coarse sand NAPL-release lens and started to vaporize the PCE. The steam zone then started to extend to the higher permeability medium sand layer. After 240 min, all the PCE had vaporized, but still no PCE had been extracted and adsorbed on the activated carbon filter (loading controlled by weight measurement). At this stage, all the vaporized PCE was retained within the steam zone, because the gas phase did not yet have a continuous pathway to the outlet of the flume. After about 300 min the steam zone broke through the top of the upper layer, and PCE started to be recovered. The heating and the soil vapor extraction system was operated until 24 hours. The PCE recovery was similar to the recovery in the first 2-D remediation experiment. After the experiment, the soil samples were also analyzed. The PCE distribution is interpolated in Figure 35 showing a similar result as in the foregoing experiment irrespective of the very different heater array. The total PCE remaining in the soil amounted to less than 2 g.

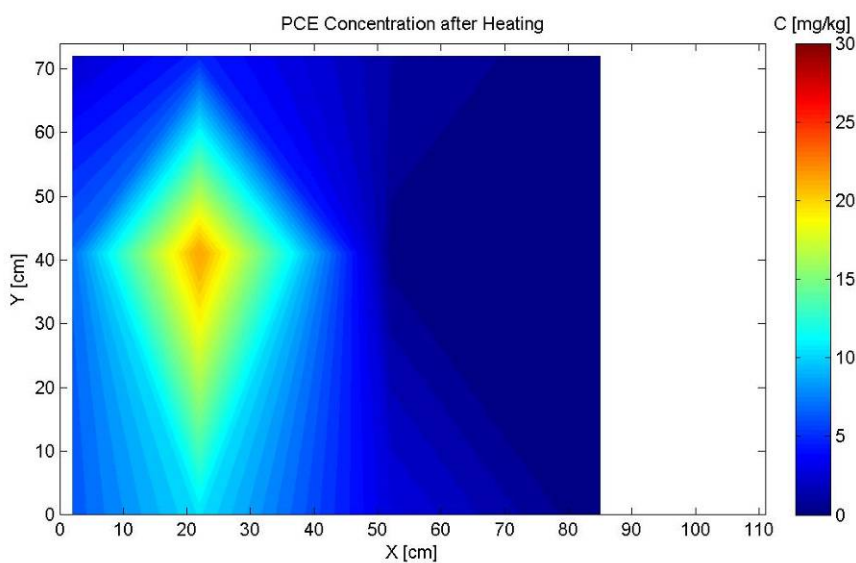


Figure 35: PCE distribution after the second 2D remediation experiment. The PCE remaining in the soil totaled less than 2 g, relative to 200 g infiltrated initially.

6.6 Conclusions from 2-D experiments and associated numerical simulations

The main conclusions from the 2-D experiments and associated numerical simulations / analyses were:

- Permeability of aquifer and aquitard influences the heat transport due to influence on the water migration and circulation (convection currents),
- The anisotropy of the permeability (vertical and horizontal) has also an influence on convective heat transport (observed from numerical models),
- The performance of the remediation is only good if the entire treatment target zone (TTZ) is steamed and if there is a connection established between the vapor recovery system, which in this case was the unsaturated zone soil vapor extraction, and the steam zone. This means that gas-phase pathways must connect the contaminated, steamed zone and the vapor recovery wells,
- The SVE system must enable a full recovery of the vaporized contaminants,
- Without these conditions, a highly efficient contaminant removal is not expected.

Further results of the 2-D experimental results can be seen in the numerical chapter.

The impacts on the design of large-scale experiments stemming from the 2-D experimental results and the numerical analyses and numerical simulations of 3-D conditions were:

- A soil vapor extraction in the lower permeability layer is not required due to the expected connection between steamed zone and unsaturated zone,
- Soil vapor extraction is only required in the unsaturated zone (higher permeability).

Furthermore, the large-scale experiments were designed to quantify the following impacts, observed in the 2-D experiments and the numerical simulations as important factors:

- Quantification of the impact of soil permeability on the steam front propagation in 3-D
- Quantification of the impact of groundwater flux on the steam front propagation in 3-D
- Quantification of the impact of NAPL source location on the remediation result
- Influence of water migration (due to permeability and groundwater flux) on steam front propagation
- Quantification of the impact of heater power, heater distance and location of the heating elements.

6.7 Task 4.1: 3-D Heat transport experiment in the large container 1 (smaller tank)

6.7.1 Phases of operation

Small-scale experiments in Oregon [JOHNSON, 2007] showed a marked reduction in liquid-phase permeability at low temperatures of approx. 50°C as a result of the appearance of gas bubbles by ebullition (degassing). It is important to note that in Johnson's experiments, he first supersaturated the water in his system with CO₂, which would be expected to have increased the formation of gas bubbles coming out of solution, as occurs when opening a bottle of carbonated beverage.

To monitor this effect, the first heat transport experiment in the small tank started in April 2007 with Phase 0. During phase 0 the total power of the heater array was set to 2 kW (one third of the total heater power) to investigate the appearance of gas bubbles in a large-scale experiment. The groundwater discharge was set to 1 m³/d (0.33 m³/(w*d)) as a result of the numerical simulations; the mass flux of the soil vapor extraction was between 9.3 and 10.5 kg/h during all phases. During Phase 0 it took 24 days until the temperatures were adjusted at approx. 50°C and until the saturations were constant in the TTZ.

During the following phases (Phase 1a to Phase 1f) the heaters were set to full power (6 kW). During Phase 1a the groundwater discharge remained at 1 m³/d to avoid a steam front migration from the aquitard into the lower aquifer. Downward steam front migration was expected from numerical simulation results to occur primarily at low groundwater fluxes. Steady state conditions (constant temperatures) were reached and kept constant for 43 days. In contrast to the numerical predictions, no steam front migration into the aquifer was observed for this GW flux.

To verify the predicted phenomena of steam front downward migration, the groundwater discharge was reduced during Phase 1b. Only in parts of the lower permeability layer did the temperatures reach values above 100°C (aquitard temperatures below 1.8 m above base were below 100°C). In general it was predicted by the numerical simulations that the steam front should break through into the underlying aquifer at small values of groundwater discharge.

The groundwater flow was therefore reduced in a stepwise fashion until the steam front reached the underlying aquifer.

The groundwater flow was first reduced for 13 days to 0.67 m³/day, then to 0.5 m³/day for another 8 days. As the steam front did not yet reach the underlying aquifer (temperatures < 100 °C at a height of 1.55 m above base), the groundwater flow was reduced again in order to determine the discharge at which a steam breakthrough occurred into the aquifer. The continuous groundwater inflow was turned off but a constant head condition at the outflow was maintained (replacement of evaporated water). Thus, the average flow during Phase 1d was 0.03 m³/day.

As the steam front did not reach the aquifer even for constant head conditions, the discharge was increased in order to detect the influence of high groundwater flow and in order to determine the groundwater inflow that is needed to permit steaming only the upper NAPL-release lens. During Phase 1e the groundwater inflow was doubled compared to the initial flow, to 2 m³/day. As a result, the temperatures at the lower surface of the lower NAPL-release lens fell below 100°C.

In Phase 1f the groundwater flow was increased again (4 m³/day), with the result that the temperatures in the entire lower NAPL-release lens fell below 100°C.

The heat transport experiment in the small tank was completed after 190 days with constant temperatures (Phase 1f). In the subsequent phases 2 and 3, the heating elements were switched off, removed and installed in the large tank. In order to drop the temperatures in the small container, the groundwater discharge was set to 4 m³/day for another two days. During Phase 3 (duration of 10 days) the groundwater flow was stopped. The soil vapor extraction was continued to constantly extract approx. 10 kg/h.

Table 4: Duration and mode of operation of the HTE in the small 3-D container.

Phase	Duration [days]	Power of heater array [kW]	GW discharge [m ³ /day]	SVE discharge [kg/h]
0	24	2	1	10.5
1a	43			9.3
1b	13		0.67	9.5
1c	8		0.5	10.4
1d	15		0.03	10.2
1e	25		2	10.1
1f	20		4	10.3
2	2	0	~ 4	~ 10
3	10		0	~ 10

6.7.2 Results

The central profile “j” is in the middle of the TTZ, equidistant and 0.75 m from the four heaters. Profile “g” lies halfway between two heaters, at a distance of 0.5 m and at the boundary of the TTZ. Profile “e” is along a line halfway between and perpendicular to two heaters but 0.5 m outside the TTZ, at a distance of 0.75 m to the heaters. The development of the temperatures in profiles “j” and “g” are given in Figure 36 and Figure 37. Figure 36 shows the development of the temperatures in profile “e”.

The development of the vapor saturation is shown in Figure 38 and Figure 39, reflecting the variation of the groundwater influx during the phases 1a – 1f (see Table 1). The central profile “A” is in the middle of the TTZ and the profile “B” is also located inside the TTZ at a distance of 0.325 m to the center point. Profile “C” is located outside the TTZ at a distance of 0.675 m from the center point. Further profiles outside the TTZ are not discussed in this report, because no vapor saturation was observed there.

During phase 0, the power of the heaters was regulated by a reference temperature to apply a power input of approx. 2 kW and to generate almost constant temperatures at 50 °C in the center between the heaters. During this phase, no changes in the saturation profiles were observed. Therefore no significant appearance of gas bubbles could be detected.

In Phase 1a, the groundwater flow remained the same as during Phase 0 and the heater power input was increased to 6 kW. As a result, after a few days the temperature in profile “j” and “g” increased over 100°C in the layers higher than 1.8 m above base. Outside the heater array (e.g., in profile “e”, 0.5 m from the edge of the TTZ), the temperature increase was remarkably slower. Here, only in layer 380 cm above base did the temperatures exceed 100°C at the end of Phase 1a.

In the unsaturated zone, the discontinuity of temperature increase that is evident on day 46 and day 52 in the layer 380 cm above base in profiles “g” and “j”, respectively is an effect of dewatering the layer, resulting in higher temperatures of the dried soil matrix under almost the same energy transfer but a lack of evaporation enthalpy consumption. This resulted in faster increasing temperatures (see Figure 36 and Figure 37 in the unsaturated zone above 300 cm above base).

In the aquitard, the steam front propagation extended into the lower NAPL-release lens during Phase 1a. Steam saturation in profile “A” and “B” increased up to values above 20 % (Figure 38), after temperatures exceeded 100°C. In profile “C”, the temperature increase was slower, so vapor saturation did not begin to increase until after 12 days of Phase 1a. In profiles “A”, “B” and “C”, the maximum steam saturation was observed to be above the lower NAPL-release lens. The steam saturation in the upper lens was nearly constant throughout the lens. In contrast to profiles “A” and “B”, the values in the upper NAPL-release lens in profile “C” are small except for an anomalous peak at day 44, which may be due to an error of the data interpolation.

In Phase 1b and 1c the groundwater flow was adjusted downward to 0.67 and 0.5 m³/d, respectively while the heater power input remained constant. Temperatures in profile “j” and “g” at elevations above 1.9 m above base were nearly constant, whereas the temperatures in profile “g” (layer 190 cm above base) responded by increasing moderately. Due to the modified groundwater flow the groundwater cooling effect that had been seen in Phase 1a lessened and the temperatures in the aquifer increased in all three profiles. In profile “e” the aquitard temperatures also increased.

Layer 155 is located at the bottom boundary of the aquitard and these data show as well some effects for the underlying aquifer. The spatial interpolation of temperature data in Figure 37 shows that the steam front remained nearly constant in the unsaturated zone (except for layer 380 near the top of the vadose zone) and in the aquitard. In profile “A”, increasing steam saturations were detected, whereas in profile “B” high steam saturations migrated as well downward from layer 190 to 155 six days after decreasing the groundwater inflow.

Although the temperatures increased in the aquifer, the temperatures remained far below the boiling point.

To generate the maximum steam front propagation, the groundwater flow was minimized during Phase 1d. While the temperatures in the aquitard at profiles “j” and “g” (except sensor g190) remained constant, the temperatures in the aquifer increased up to 90°C within layer 155. The values of steam saturation remained constant for profile “A” between both NAPL-release lenses, as well as within and above the upper NAPL lens and in profile “B” between 2.5 to 3.0 m above base. Above the lower NAPL-lens the steam saturation increased again moderately, while the steam saturation remained constant below that lens as well as in profile “C”. A steam front migration into the lower aquifer under no-flow groundwater conditions, as had been predicted by the numerical simulations could not be observed in the experiment.

The groundwater flow was next increased to 2 m³/d (phase 1e). The temperatures in profile “j” decreased significantly (almost 20°K) in the aquifer and at the bottom of the aquitard (layer 155) and decreased by approx. 5°K in layer 190. Temperatures in the upper aquitard remained almost constant and above 100 °C. The temperatures in profile “g” showed a similar development, although the temperatures in profile “e” decreased in all layers. The steam front collapsed below the bottom NAPL-release lens (profile “B”).

Whereas the decrease in temperature was very fast within the aquifer (the main decrease occurred in the first week after increasing the groundwater inflow) and the rate of decrease even higher, the decrease in temperature seen in the aquitard and in the unsaturated zone was slower and more moderate. Due to the increased groundwater cooling effect, the expansion of the steam front declined. At the end of phase 1e, the steam front was still inside the bottom NAPL-release lens at the edge of the TTZ (profile “g”) but above that lens it was only found in the center point (profile “j”). The steam saturation in the central profile (profile “A”) decreased. In the middle of the aquitard, spatially low steam saturations (e.g., from days 112 to 116) were detected. In addition, steam saturation inside both NAPL-release lenses decreased. The steam saturation decreased, but the steamed soil volume remained the same. The obvious abrupt steam front collapse in the steam saturation plot Figure 38 (profile “B”, day 115, layers 200 to 240) is physically impossible and was caused by an error in the measured data. The steam front collapsed in the lower aquitard in profile “C” and the steam saturation in the upper NAPL-release lens was moderate.

In Phase 1f the groundwater flow was doubled to 4 m³/day. In profile “j”, the temperatures in the aquifer as well as in the lower aquitard (layer 155 and 190) dropped immediately. Three days after starting this phase, the water supply was interrupted during a weekend. The missing cooling effect of the groundwater caused increasing temperatures up to 1.9 m above base (not only in the aquifer, also in the aquitard). As the groundwater flow was started again (4 m³/day), the temperatures decreased instantly. This interruption of the temperature decrease was observed in profiles “g” and “e” for almost all layers. The position of the bottom of the steam front (100°C) moved upwards, with the temperature in the lower NAPL-release lens falling below steam temperature in profile “j” by the end of the phase. In profile “g” the steam front had retreated to above the lower lens by the middle of Phase 1f, and approached the upper NAPL lens near the end of Phase 1f. The steam saturation in profile “A” decreased during Phase 1f. Near the end of the phase only the upper lens remained steamed. In profile “B” the interruption in groundwater flow produced an immediate downward expansion of the steam front.

Independent of groundwater flux, temperatures reached and remained above 100 °C in the upper NAPL-release lens during phase 1 of this experiment. The steam front encompassed the upper NAPL-release lens. Thus, no influence of groundwater flow on the temperatures in the upper part of the aquitard was observed.

In contrast to this for the given heater configuration, the groundwater flow dominated the achieved temperatures in the lower NAPL-release lens. For higher groundwater flows (phases 1e and 1f) the temperatures decreased and the steam front collapsed in the lower lens of the aquitard.

The experimental settings and the results during the final cool-down phases 2 and 3 were only of interest with respect to the timing of the next large-scale experiment in this tank. The details are thus not discussed in this report.

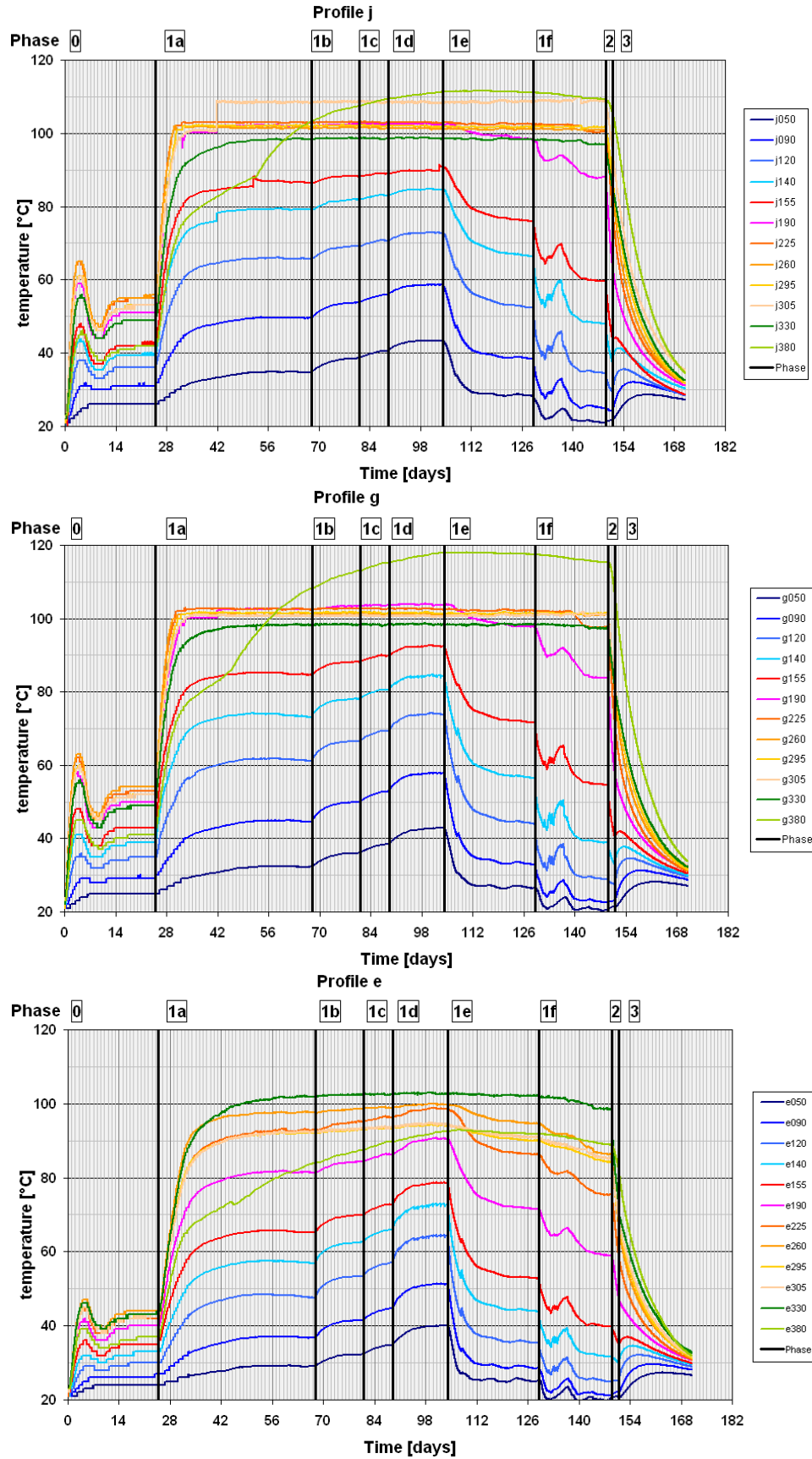


Figure 36: Temperature development of the HTE in the small container (time-variation curves).
Top: central profile j, located equidistant from the heaters (center point profile);
Center: Profile g, located between the heaters at the boundary of the TTZ;
Bottom: Profile e, located 0.5 m outside the TTZ.

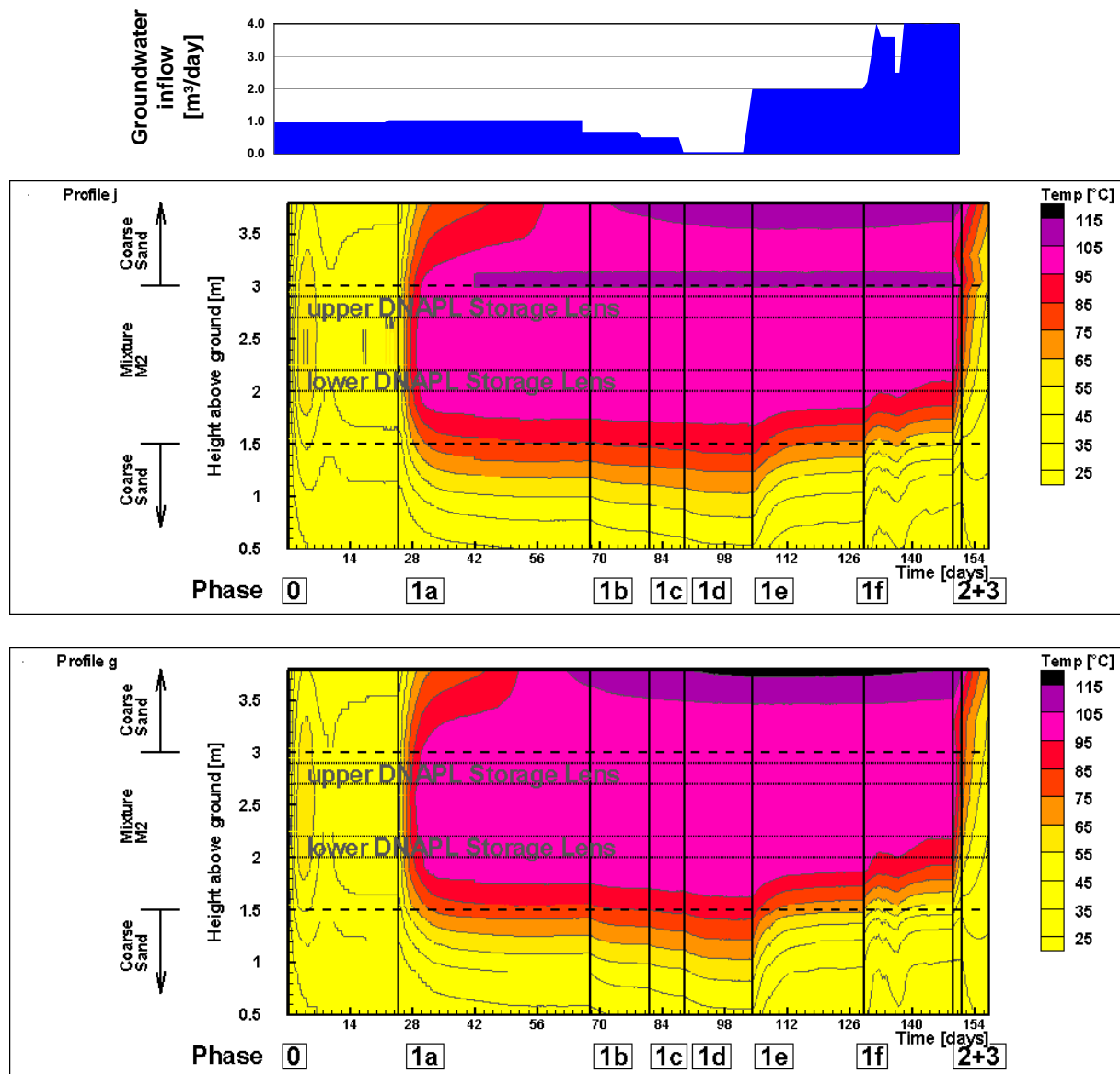


Figure 37: Temperature distribution of the the HTE in the small container (spatial interpolation of the measured data).

Top: Groundwater inflow during the HTE

Middle: Profile j, located equidistant from the heaters (center point profile);

bottom: Profile g, located between the heaters at the boundary of the TTZ.

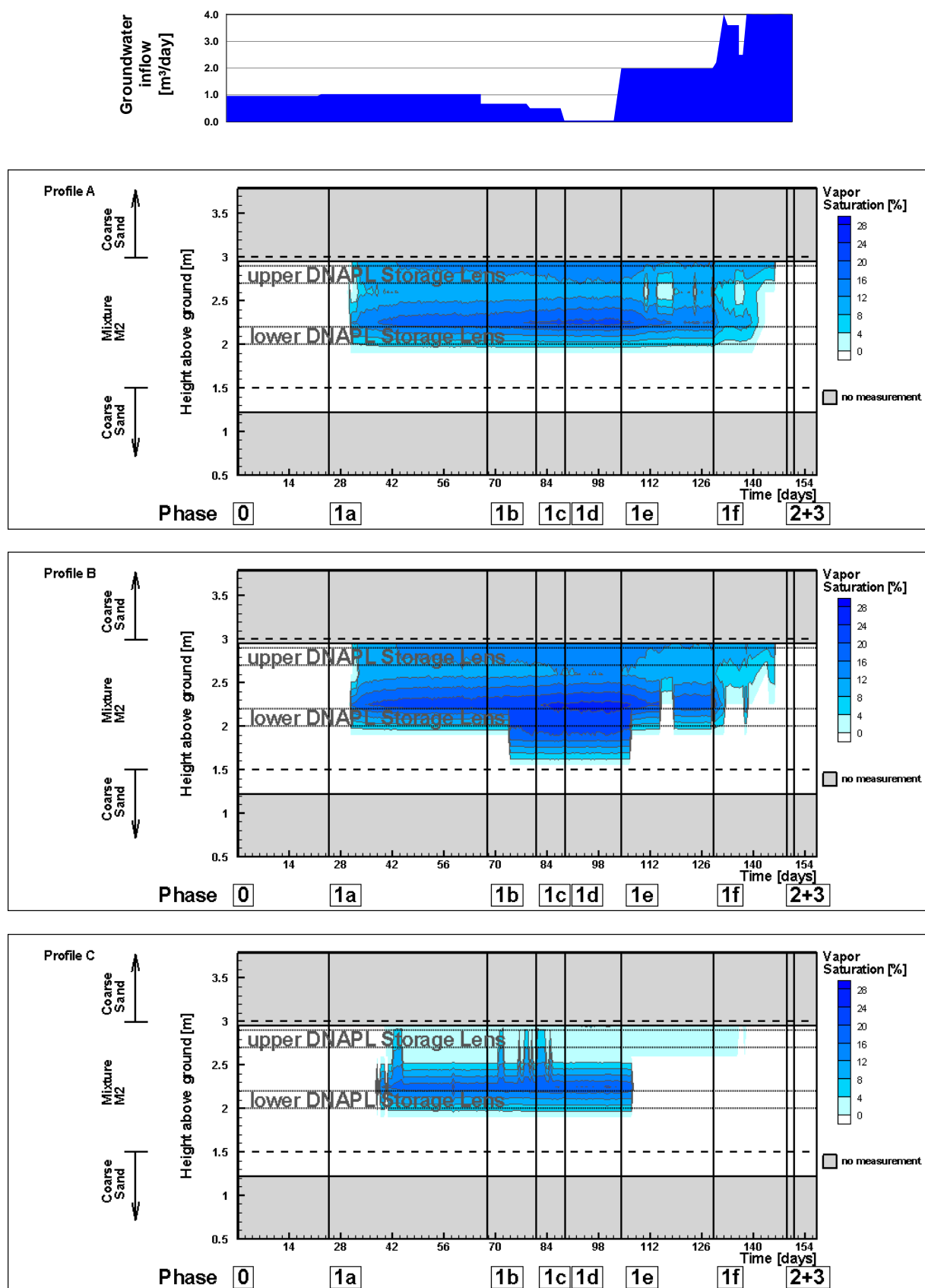


Figure 38: Steam Saturation of the HTE in the small container (spatial interpolation of the measured data).

Top: Profile A, located equidistant from the heaters (center point profile);

Center: Profile B, located between the heaters but inside the TTZ;

Bottom: Profile C, located between the heaters but outside the TTZ.

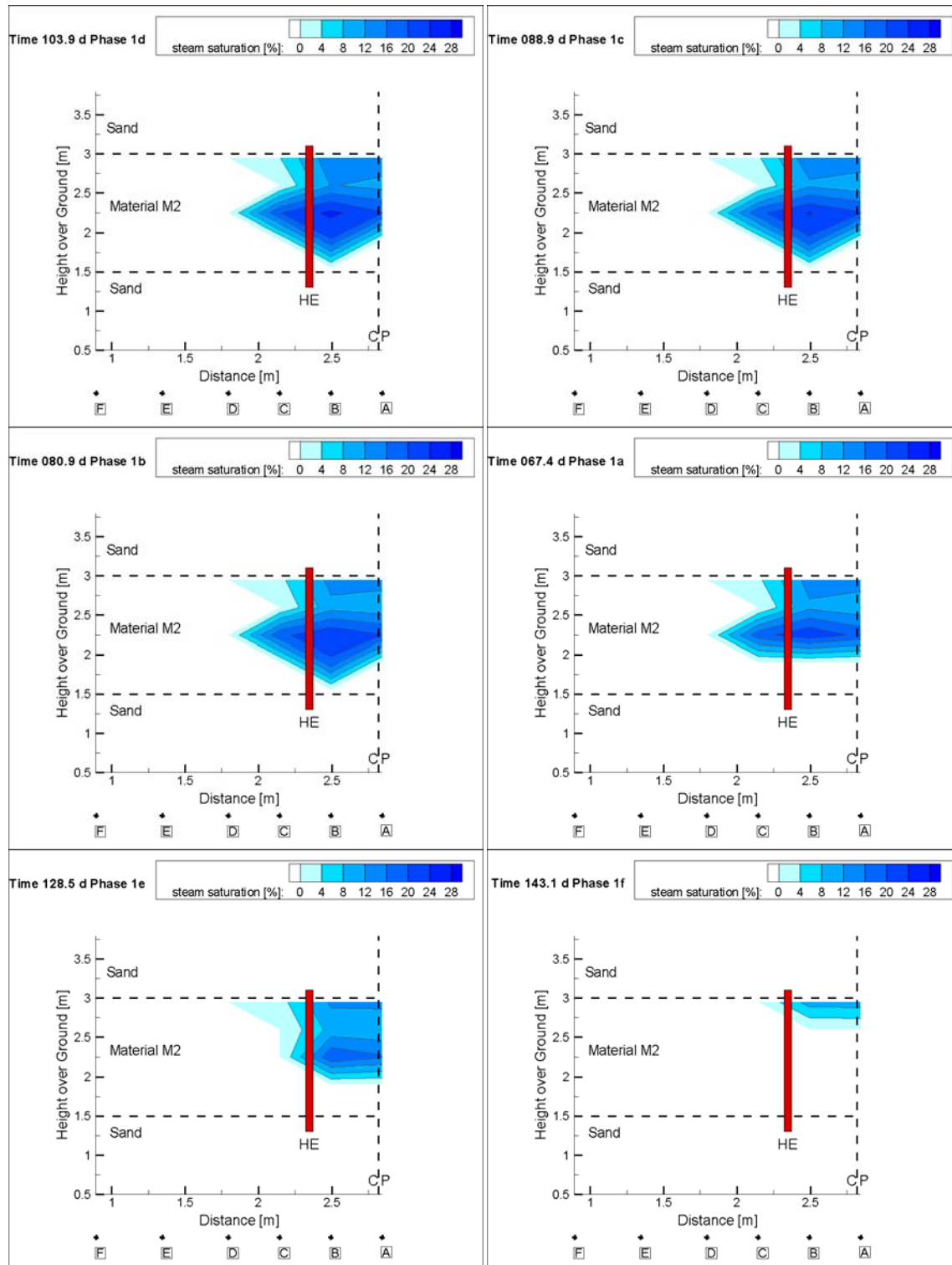


Figure 39: Steam saturation of the HTE in the small container (spatial interpolation of measured data of profiles A to F). Presented in order of increasing groundwater flux. HE = Heater Element; CP = Center Point.

**Top: Phase 1d (0.03 m³/day) and Phase 1c (0.5 m³/day);
Center: Phase 1b (0.67 m³/day) and Phase 1a (1 m³/day);
Bottom: Phase 1e (2 m³/day) and Phase 1f (4 m³/day).**

In Figure 39, spatial interpolations of steam saturation data collected during the heat transport experiment in the small 3-D container are shown for the end of each experimental phase (Phase 1a to Phase 1f) and sorted by the amount of the groundwater flow (from “no-flow” conditions to the highest groundwater discharge of 4 m³/day). High steam saturations are represented by a deep blue color, while locations without steam are shown in white color. The shape of the steam front during phase 1d, 1c and 1b looks very similar. The lateral and vertical steam propagation did not change significantly, but the amount of steam changed moderately, especially in profile “B” close to the heater. The downwards oriented steam front propagation was limited by an increasing groundwater flux (Phase 1a, 1e and 1f). The steamed zone collapsed for areas outside of the TTZ (outside of the heaters, Phase 1e). At an even higher flow, the steam front also collapsed between the heaters. The diagram of Phase 1f shows a snapshot of this phase. At the end of Phase 1f no vapor saturation could be detected.

Steam generation for a location 1.5 m below the groundwater table (1.5 m above base) requires a temperature of nearly 104°C due to the hydrostatic pressure of water (1150 mbar). During the heat transport experiment, the steady state temperatures at the bottom of the aquitard did not exceed 95°C indicating the lack of steam and the capability to steam water at this depth. Therefore, only a one-phase system (i.e., warm / hot water) existed at the bottom of the lower permeability layer and in the coarse sand aquifer. Moreover it indicated that power supply and heat transfer limited the vertical downward expansion of the steam front.

6.8 Task 4.2: Heat transport experiment in the large-scale container 2 (larger tank)

6.8.1 Phases of operation

To validate the results of the first experiments in a physical model with higher permeability, the second heat transport experiment was conducted in the large tank. Whereas the saturated hydraulic conductivity, K_s of the LPL in the small container was 10⁻⁷ m/s, it was ten times larger in the large tank, i.e., $K_s = 10^{-6}$ m/s. Likewise the K_s values for the higher permeability layer in the two tanks were 10⁻⁴ and 10⁻³ m/s, respectively (Table 1). Due to the long duration of the heat transport experiment in the small container, the experiment in the large container focused on fewer essential effects.

The heaters were operated with full power (6 kW). Since the volume of the large tank is twice the small one, four soil vapor extraction wells (instead of two) were installed. The SVE discharge was adjusted at approx. 20 kg/h. The heater power and the SVE discharge remained constant during all four heating phases.

To compare the results of both experiments, the first phase (Phase 1a) had a groundwater flow of 2 m³/d (= 1 m³/(d * m width)). Similar to the first phases in the HTE in the small tank, the groundwater flow was reduced stepwise during this second HTE, when temperatures became nearly constant at the end of each phase. In the central area, temperatures remained nearly constant. After 15 days the groundwater discharge was reduced to 1 m³/day. Since temperatures did not increase as expected, the discharge was further reduced to 0.29 m³/d after six days.

In Phase 1d the groundwater flow was switched off as it had been in Phase 1d in the small tank experiment to detect the maximum steamfront propagation. Constant head conditions lasted for six days with an effective groundwater inflow of 0.01 m³/d.

After six days of Phase 1d this HTE was completed, with Phase 2 commencing with a shut down of the heaters and the groundwater flow but with a continued SVE to accelerate cooling.

Table 5: Duration and mode of operation of the HTE in the large container

Phase	Duration [days]	Power of heater array [kW]	GW flow [m ³ /day]	SVE discharge [kg/h]
1a	15	6	2	19.9
1b	6		1	20.1
1c	8		0.29	20.2
1d	6		0.01	20.2
2	---	0	0	~ 20

6.8.2 Results

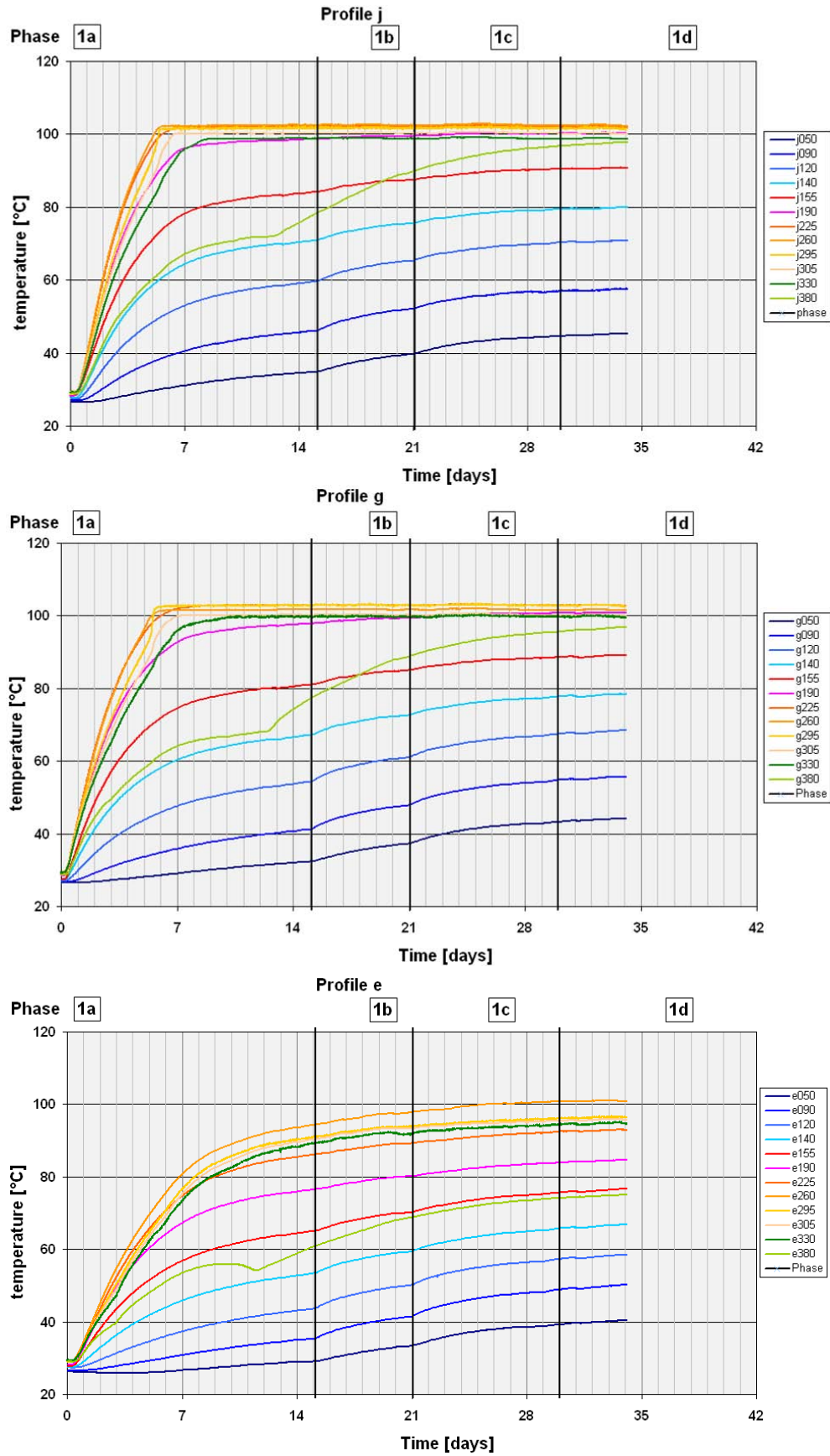
During the first week, the temperatures in profile “j” located in the aquitard in layers above the bottom NAPL-release lens exceeded 100°C and remained constant throughout the experiment. Temperatures in layers 190 and 330 reached nearly 100°C at the end of Phase 1a. The temperatures and the temperature gradients in the aquifer and within layer 155 were lower, compared to the HTE in the small container. Similar to that earlier experiment, the temperatures in the unsaturated zone (layer 380) show an inflection point after 12 to 13 days with subsequent higher rate of increase. Temperature curves in profiles “g” and “j” were similar even though the values varied slightly and the inflection point of curve “g 380” occurred earlier (Figure 40). Temperatures in profile “e” did not exceed 100°C but were still increasing at the end of Phase 1a. The curve of sensor “e 380” showed as well an inflection point after 11 days.

The spatial temperature interpolation of the profiles “j” and “g” were similar in Phase 1a (Figure 41). The temperature in the upper NAPL-release lens and above the lower lens exceeded 100°C in both profiles. Moreover, in both profiles the lower lens was almost “steamed” at the end of Phase 1a and 100°C was reached almost simultaneously. Heat propagation in the vertical direction was almost constant and indicated the attainment of 100°C temperatures in the region between both lenses after 6 days.

The groundwater flow was halved to 1 m³/day during Phase 1b. As a result, temperatures in the aquifer and in the lower part of the aquitard increased by a maximum of 5°K at profile “j”. The temperature increase was similar in profile “g”. Whereas the temperature gradient of layers above 190 cm above base were the same as at the end of Phase 1a, the increase in the subjacent layers was higher in Phase 1b. At the end of Phase 1b, temperatures in both lenses exceeded 100°C (profile “j” and “g”).

Temperatures in the upper aquitard and in the capillary fringe (layer 330) remained constant (profile “j”), even when the groundwater flow was reduced to 0.29 m³/day during Phase 1c. Temperatures in other layers increased, but gradients were not as high as at the beginning of phase 1b. At the end of phase 1c the temperatures in profile “j” were nearly constant. In profile “g” the temperature increase in the aquifer layers was nominally higher than in profile “j” and temperatures were still increasing at the end of the phase. Temperatures in the upper layer (aquitard and unsaturated zone except for layers 155 and 380) remained constant (profile “g”).

Temperatures were still increasing in all layers for profile “e”. Only in layer 305 were temperatures of 100°C exceeded at the end of the phase. The spatial interpolation of the temperatures showed a downward oriented expansion of the 100°C front in profile “j” and “g” but only a few portions below the bottom lens were steam filled (Figure 41).



**Figure 40: Temperature development of the second HTE in the large container (time-variation curves).
Top: central profile j, located equidistant from the heaters;
Center: Profile g, located between the heaters at the boundary of the TTZ;
Bottom: Profile e, located 0.5 m outside the TTZ.**

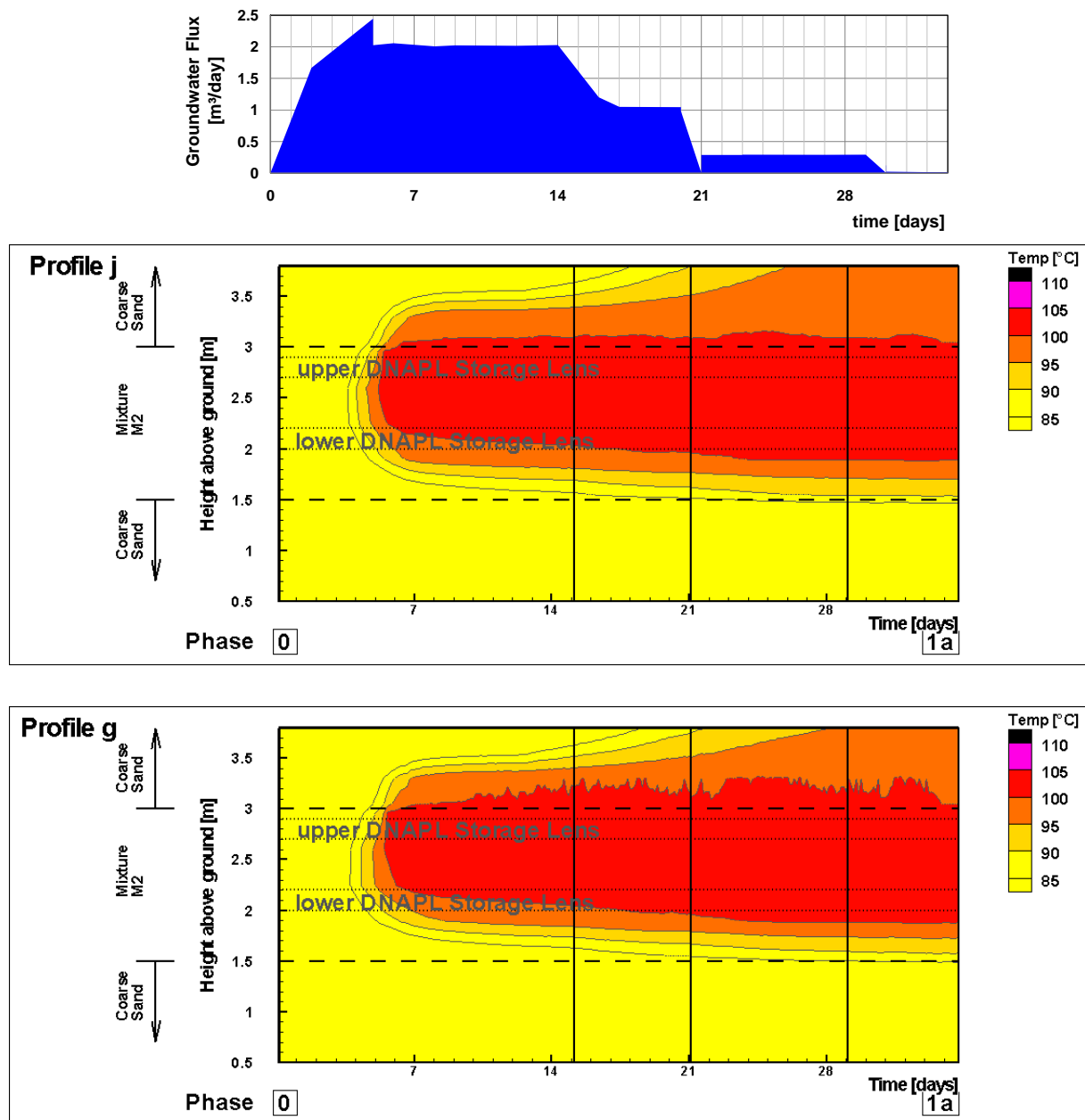


Figure 41: Temperatures of the second HTE in the large container (spatial interpolation of measured data).

Top: central profile j, located equidistant from the heaters;

bottom: Profile g, located between the heaters at the boundary of the TTZ.

Temperatures in all profiles only changed marginal by several degrees Kelvin and remained constant soon after the effective groundwater flow was reduced to steady state conditions ($0.01 \text{ m}^3/\text{d}$). Almost no change was observed in the spatial temperature interpolation (Figure 41).

6.9 Comparison and conclusions of the two heat transport experiments

Steady state temperatures at the top of the aquitard correlated well with the specific groundwater flow [$\text{m}^3 / (\text{tank width} \times \text{day})$] as shown in Figure 42. The data at the central profile “j” between the heaters of both heat transport experiments are illustrated.

Temperatures decreased with increasing groundwater flow due to the increased cooling effect (enhanced energy output). The polynomial correlations between temperature and groundwater flux (3rd order for the small tank, 2nd order for the large tank) show correlation coefficients $R^2 > 0.99$. For higher fluxes an asymptotic characteristic of the correlation is thermodynamically reasonable and was found. Due to the limited convective heat transfer coefficient across the boundary for a given energy input and a constant area of heat transfer between the lower and higher permeability zones, temperature decreases more slowly with higher groundwater flux. For a certain discharge, the energy loss by groundwater outflow achieves a maximum.

Although the soil permeability within the two tanks differed by one order of magnitude (Table 1), in the center profile “j” only minor temperature differences could be observed between the tanks in the lower part of the layer of lower permeability (Figure 42, 155 and 190 cm above base). Convective and conductive heat transfer is comparatively high between the heaters. Numerical simulations showed for the lower permeability soil that heat transfer by convection is as high as by conduction between the heaters during most of the experimental timeframe. In the permeable aquifer the temperature differences are higher than in the aquitard.

In both layers, aquitard as well as aquifer, higher temperatures were observed in the container with lower permeabilities. Here, the conductive heat transport was more important compared to advective heat transport early in the experiment. Following the heat transfer theory, for larger grain sizes the advective heat transfer will be higher. It seems reasonable that layers that are in contact with higher permeability soils will be colder than layers in contact with lower permeability zones. Similar correlations were observed for other profiles but the temperatures were not as high as in the central profile “j”.

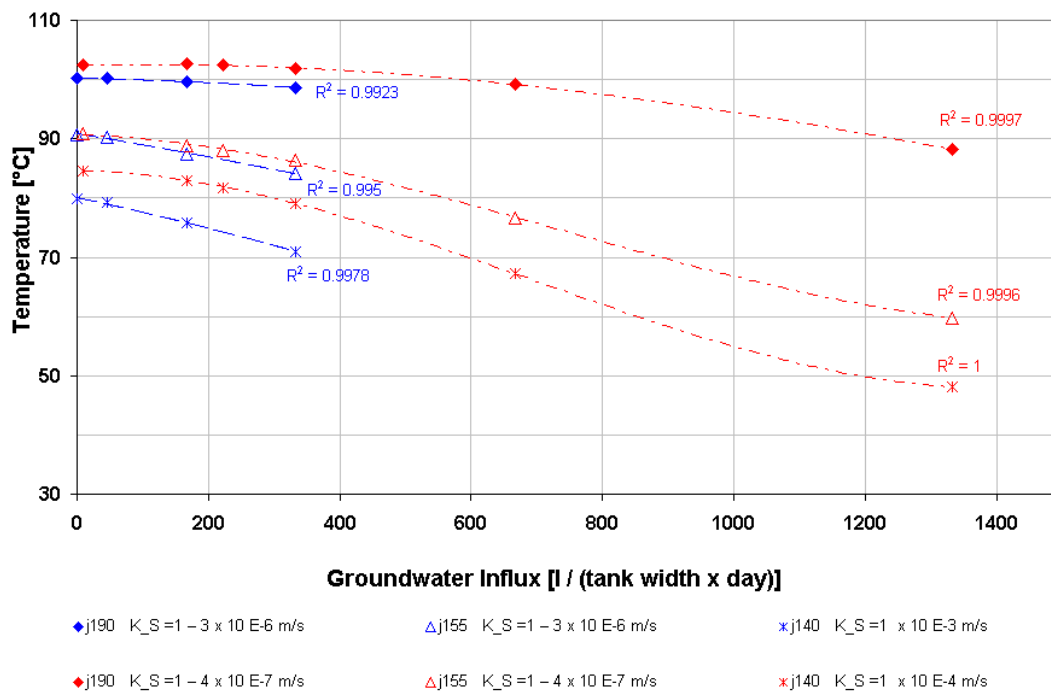
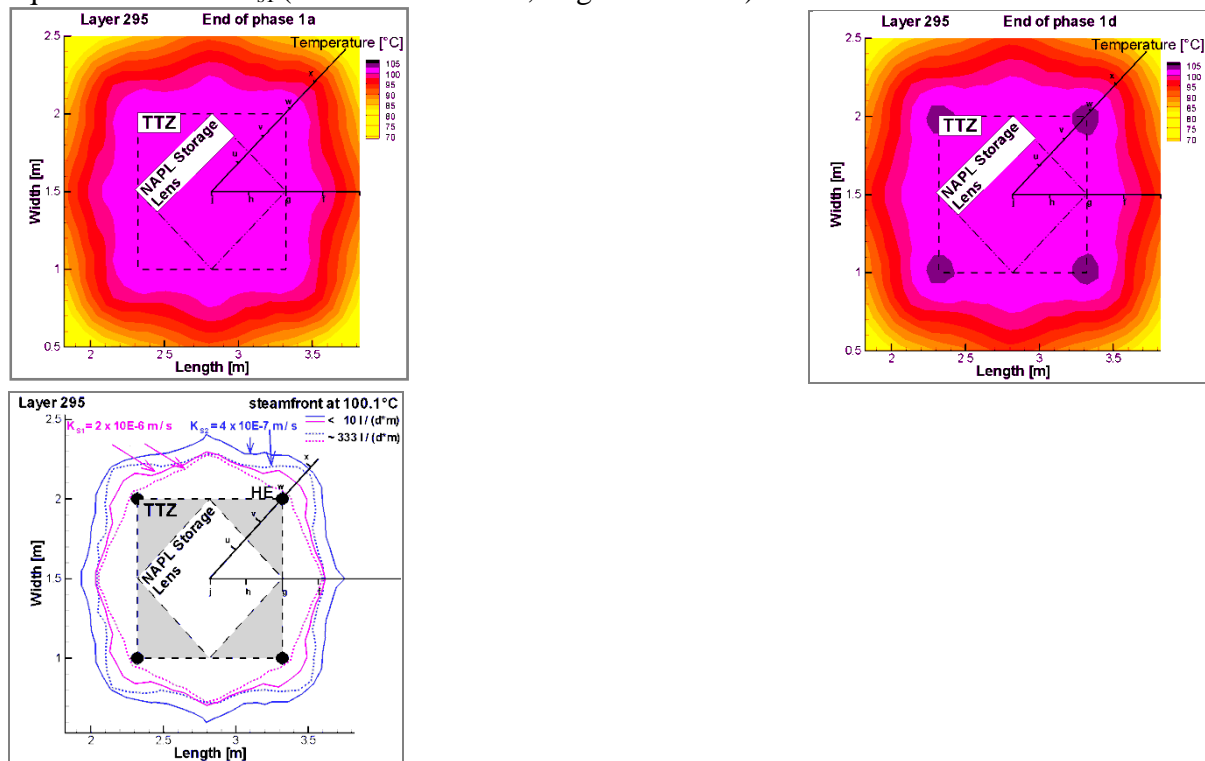
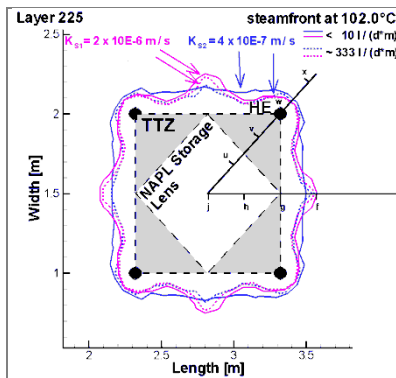
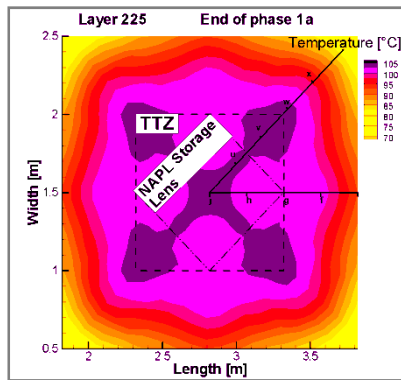
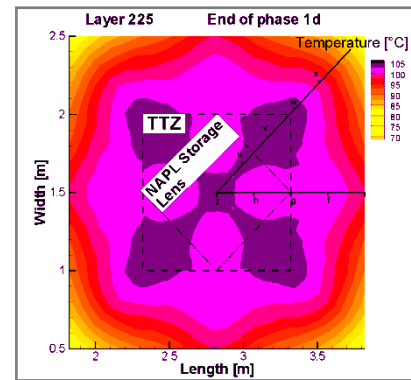
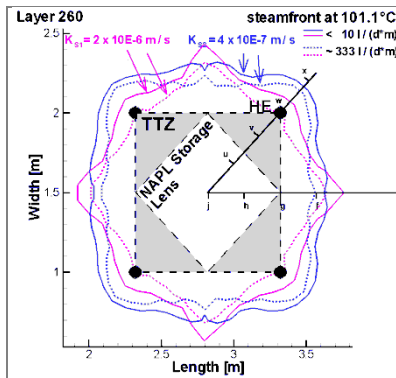
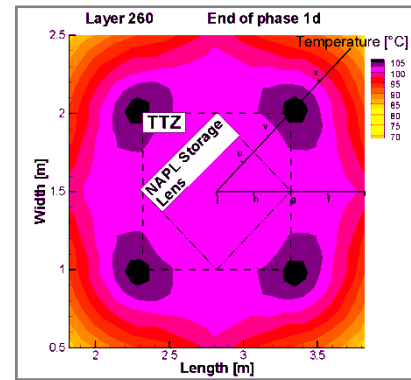
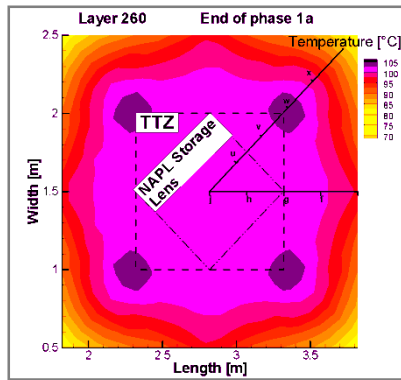


Figure 42: Correlation between groundwater flux and steady state temperatures during the experimental phases observed at the central profile “j” at 155 and 190 cm above base within the lower permeability layer, and 140 cm above base within the underlying aquifer.

In contrast to the bottom of the lower permeability layer, water was steamed in the middle and at the top of the lower permeability layer. The right-hand column of Figure 43 shows the interpolated steady state steam front extension in the larger tank (pink lines) and in the smaller tank (blue lines). Solid lines represent a constant head inflow boundary characterized by a low groundwater influx (below $10 \text{ l} / (\text{m}^2 \cdot \text{d})$), whereas dotted lines represent higher flow rates (about $333 \text{ l} / (\text{m}^2 \cdot \text{d})$). The boiling point (steam temperature) was calculated using the water vapor pressure curve and the existing pressure conditions (sum of atmospheric and hydrostatic pressure).

The cooling effect of increasing groundwater flux had almost no impact on the steam front in the middle of the lower permeability layer (225 cm above base) and only a moderate impact on the steam front extension at the top of the aquitard (260 and 295 cm above base). In contrast the steam front collapsed due to the increased groundwater flow and hot water remained in the center of the lower permeability layer about 40 cm above the aquifer ($K_{s2} (= 1 \text{ to } 4 \times 10^{-7} \text{ m/s}$, smaller container) at 190 cm above base). No significant steam front and steam zone were observed at 190 cm above base inside the relatively higher permeability aquitard material $K_{s1} (= 1 \text{ to } 3 \times 10^{-6} \text{ m/s}$, larger container).





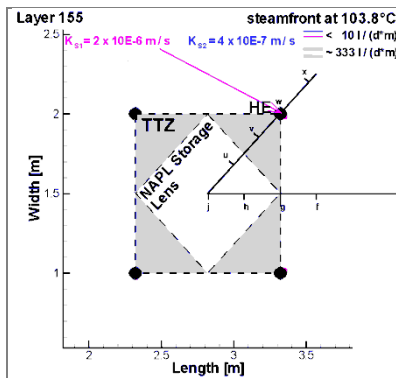
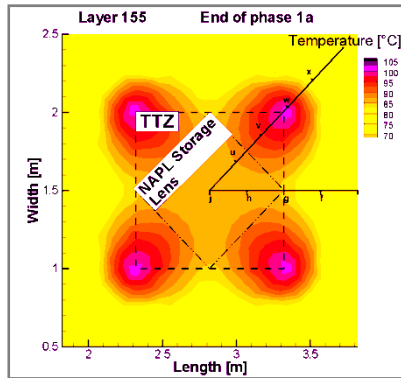
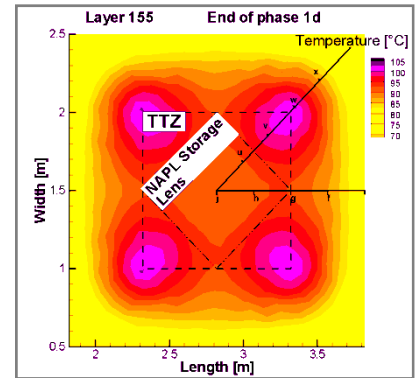
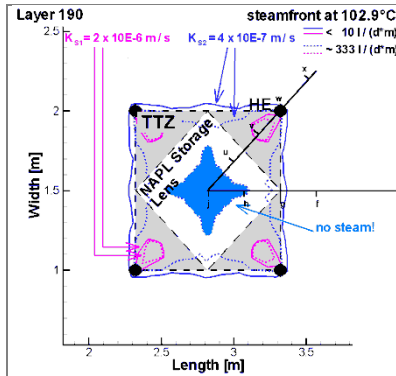
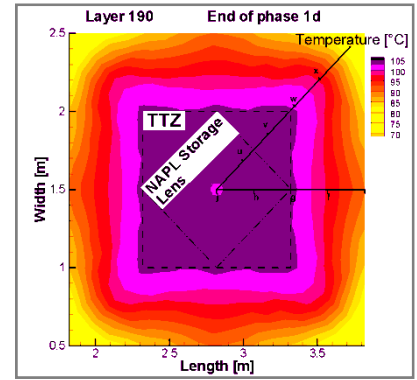
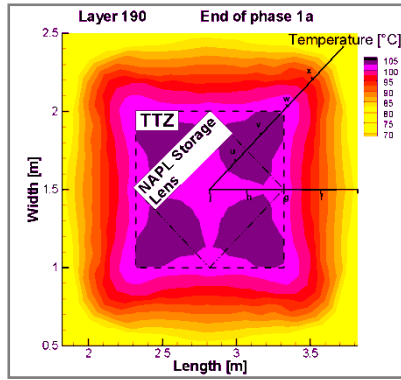


Figure 43: Temperature distribution (left-hand side and middle part) and steam front propagation for each layer in both tanks (right hand side, with different permeabilities). TTZ = Target Treatment Zone. Layer 295 was just above the upper DNAPL-release lens, while layer 190 was just beneath the lower DNAPL-release lens.

The result of the heat transport experiments in the new container setups can be summarized as follows:

- Steaming of water occurred in the middle and at the top of the lower permeability layer (independent of the power input of 6 or 12 kW).
- Cooling effect of increasing groundwater flux had almost no impact on the steam front in the center of the lower permeability layer, the aquitard (225 cm above base)
- Cooling effect of increasing groundwater flux had only moderate impact on the steam front extension at the top of the aquitard (260 and 295 cm above base)
- Steam front collapsed due to the increased groundwater flux, and hot water remained in the center of the lower permeability layer about 40 cm above the aquifer (K_{S2} at 190 cm above base)
- No steam production was observed at the bottom of the lower NAPL-release lens (referring to the measurements at 190 cm a.b = 40 cm above the bottom of the aquitard) with the exception of a groundwater flux of less than 10 l / (m x d) and the lower permeability aquitard. Only in this case was a coherent steam zone in cylindrical shape formed between the heating elements.
- No steam production occurred at the bottom of the aquitard (1.55 m above base). This is in contrast to numerical forecasts. Hence, a breakthrough of the steam front into the lower aquifer as predicted for very low groundwater flux was not seen.
- Steaming of the water in the aquitard is as important as the formation of a coherent steam zone (gas zone) in enabling a migration of gaseous NAPL into the unsaturated zone for an efficient NAPL recovery from the saturated aquitard.
- Steam generation is significantly impacted by:
 - Soil permeability
 - Hydrostatic pressure (dependent on the depth below the groundwater level)
 - Cooling (during the experiments) caused by the groundwater flux (mainly for zones in close contact with the permeable aquifer).
- An increase in the cooling effect was associated with the higher permeabilities in the large tank. Thus, the steady state average temperature was lower in the large tank than in the small tank experiment, which had a lower aquifer permeability.
- A high groundwater flux can limit the downward expansion of the steamed zone. The contaminant recovery of NAPL located in the lower aquifer via conductive heating and a SVE system would be impossible under these conditions.

6.10 Task 4.3: Remediation experiment in the small tank

6.10.1 Phases of operation

The remediation experiment in the small tank was divided into five phases represented by different boundary conditions. Furthermore, the effect of a short time interruption of the energy input (intermittent heater operation) was tested in sub-phases. The groundwater table was kept constant at the elevation of the groundwater outflow (constant head boundary condition) and the groundwater flow was adjusted at the inlet (constant flux condition). The intention of the different boundary conditions was to remediate sequentially the upper and bottom NAPL-release lenses. In a first step, the steam front would be adjusted between both lenses to steam only the upper lens. In a second step, the reduction of the groundwater flow would enable the downward propagation of a steam front to evaporate the contaminant emplaced in the lower NAPL-release lens. A suitable flow rate to accomplish this was selected from the results of the heating experiments (e.g. Figure 42).

The groundwater flow was set to 7 m³/day to position the steam front below the upper lens (Phase 0). Four heaters were operated in a square pattern (distance 1 m) and the SVE discharge was 9.1 kg/h.

Since the energy input from the heaters turned out not to be high enough to stabilize the steam zone as desired during the 21 days of Phase 0, the groundwater discharge was set to 3 m³/d for another 15 days (Phase 1) and finally adjusted to be 0.52 m³/day for 33 days (Phases 2, 3 and 4). To enlarge the lateral extension of the steam zone, the heaters were replaced and installed in the outer square pattern of jacket tubes (distance 1.25 m), with a continued groundwater inflow and a SVE discharge (Phase 3).

Since the energy input of four heaters proved to be too low to enable a downward propagation of the heat front under the tested conditions, another four heaters were installed in the inner square of the jacket tubes and all eight heaters were then operated simultaneously. Additionally the SVE discharge was reduced to be 6.25 m³/d (Phase 4), aiming at a reduction of heat losses.

Table 6: Duration and mode of operation of the remediation experiment in the small tank.

Phase	Duration [days]	Power of heater array [kW]		GW discharge [m³/day]	SVE discharge [kg/h]
0	21	6	4 inner	7	9.11
1	14.7			3	
2	33			0.52	
3	14.2		4 outer		
4	48.8	12	8		6.25

As mentioned before, the operation of the heaters was stopped temporarily during Phase 4 to trigger a collapsing of the steam zone. A collapsing steam zone produces a relative vacuum and a localized release of heat of enthalpy. It was posited that this should lead to an evaporation of liquid entrapped organic phase in the soil matrix at the boundaries of the former steam front, analogous to the effect of pressure cycling, as practiced in Steam Enhanced Extraction (e.g., HERON ET AL. 2004). The intermittent operation of the heaters was thus intended to enhance contaminant recovery.

Table 7: Time and duration of heater interruptions during the first remediation experiment in the smaller tank.

Phase	Time [days]	Duration [days]	Phase	Time [days]	Duration [days]
2	42.60	0.52	4	118.90	0.15
2	47.99	0.65	4	119.99	0.07
End of 2	68.04	0.67	4	120.75	0.21
End of 3	82.85	0.02	4	123.92	0.11
4	111.71	0.04	4	124.65	0.16
4	113.85	0.08	End of 4	131.65	---

6.10.2 Results

6.10.2.1 DNAPL release and initial conditions

Small-scale experiments and feasibility tests had been conducted to optimize the infiltration procedure by testing different options. Furthermore, the maximum capillary retention capacity had been checked by literature research and performing additional feasibility tests. As a result, it was decided to infiltrate a high amount of DNAPL phase within the large 3D remediation experiment.

Tetrachloroethene (PCE) had been chosen as a characteristic DNAPL contaminant with a relatively high boiling point relative to other CVOCs. The upper and lower DNAPL release lenses were each filled with 10 kg of PCE. To enable differentiation between the recovery of contaminant originating from the upper versus the lower DNAPL release lenses, we mixed Dichlorobenzene (DCB) into the PCE as a tracer substance. The tracer mass was 20% of the PCE mass. A mixture of 1,4-Dichlorobenzene (1,4-DCBz) and PCE had been infiltrated into the upper lens, while 1,2-Dichlorobenzene (1,2-DCBz) and PCE had been infiltrated in the lower lens. We had earlier established that 1,4-DCBz, 1,2-DCBz and PCE could each be readily and separately detected with the installed gas chromatography (GC) to enable quantification of the soil vapor recovery.

The two DNAPL mixtures were infiltrated into each DNAPL release lens by using a separate diffuser with eight outlet pipes (Figure 9b) and a peristaltic pump. The infiltration was carried out in two steps over a 24-hour period, with an interruption overnight. The average infiltration flux per lens was 0.83 kg NAPL per hour.

6.10.2.2 Temperature development

Since the initial temperatures in the tank's aquifer zone (approx. 20°C due to heat left over from the preliminary HTE) were higher than the temperature of the inflowing groundwater (approx. 10°C), they decreased during the high groundwater inflow of 7 m³/d (Figure 44, Phase 0, profiles "j", "g" and "e").

The eutectic temperature or heterogeneous azeotrope (boiling point of a binary mixture [ATKINS, 1988]) of water and liquid PCE at atmospheric pressure is 88°C. By the end of Phase 0, the temperatures of profiles "j" and "g" exceeded 90°C in the upper lens (i.e., NAPL could thermodynamically no longer be present), while they remained below 90°C in the bottom lens. In profile "e" the temperatures were below 70°C in all layers. At those temperatures, PCE and water still existed in the liquid phase.

When the groundwater flow was reduced from 7 to 3 m³/d (Phase 1), the temperatures increased in all profiles. In profile "j" the temperatures exceeded 100°C in the aquitard top layers and reached almost 90°C below the bottom NAPL-release lens (layer 190). The temperature of the same layer in profile "g" was below 90°C. The lateral heat propagation was moderate. Thus temperatures in profile "e" were below 80°C (except in the vertical center of the heaters (layer 260)). The increase of the temperature almost stopped after one week.

In the beginning of Phase 2 (reduced GW flow from 3 to 0.52 m³/d), larger temperature gradients compared to the beginning of Phase 1 were observed. In profile "j" (and as well profile "g") temperatures achieved or exceeded 100°C below the lower NAPL-release lens (layer 190) and at the bottom of the aquitard (layer 155), and increased by more than 20°K in

the aquifer. The temperature increase between day 35 to 48 in profile “e” between layer 225 and layer 380 was steep and reached about 80°C in the aquitard as well as in the unsaturated zone (except 260 cm above base with temperatures up to 90°C). After one week of continuous operation, the heaters were switched off for a few hours (day 42) in order to increase the contaminant output. Temperatures decreased in all profiles in all layers due to the energy output of the groundwater and the missing energy input from the heating elements. On day 48 the heaters were switched off again followed by decreasing temperatures. The temperatures increased again after restarting the heaters and one week later, a steady state temperature distribution was observed for all profiles and layers.

Phase 3 began with the heaters re-installed in the outer square of jacket tubes at a spacing of 1.25 m. Due to the larger distance, the temperatures decreased significantly in all three profiles, in some layers by 20°K. Changing the heater array had only a small effect in the layers of the aquifer; the effect was the highest in the lower and middle part of the aquitard.

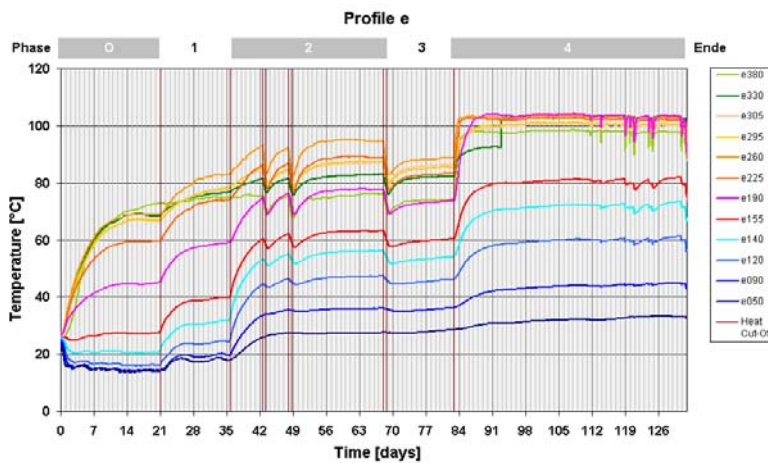
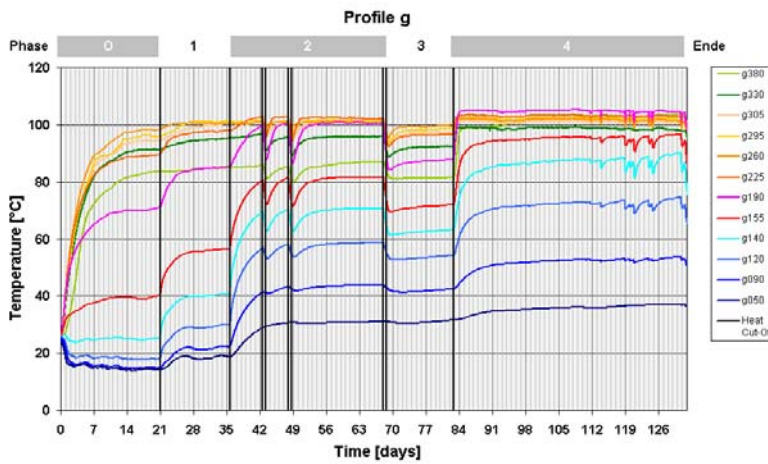
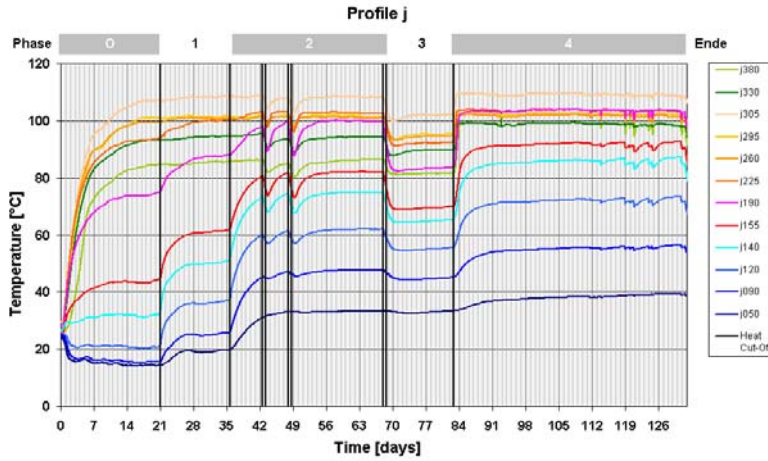
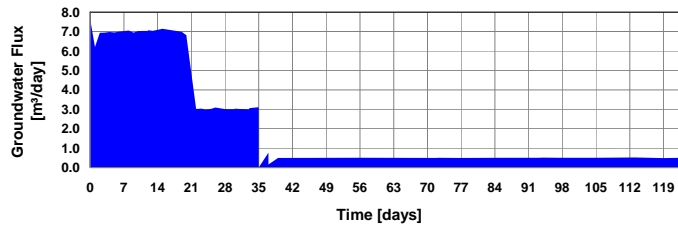


Figure 44: Temperatures during the first remediation experiment. Top: central profile j, equidistant from the heaters; Center: Profile g, located between the heaters at the boundary of the TTZ; Bottom: Profile e, located 0.5 m outside the TTZ.

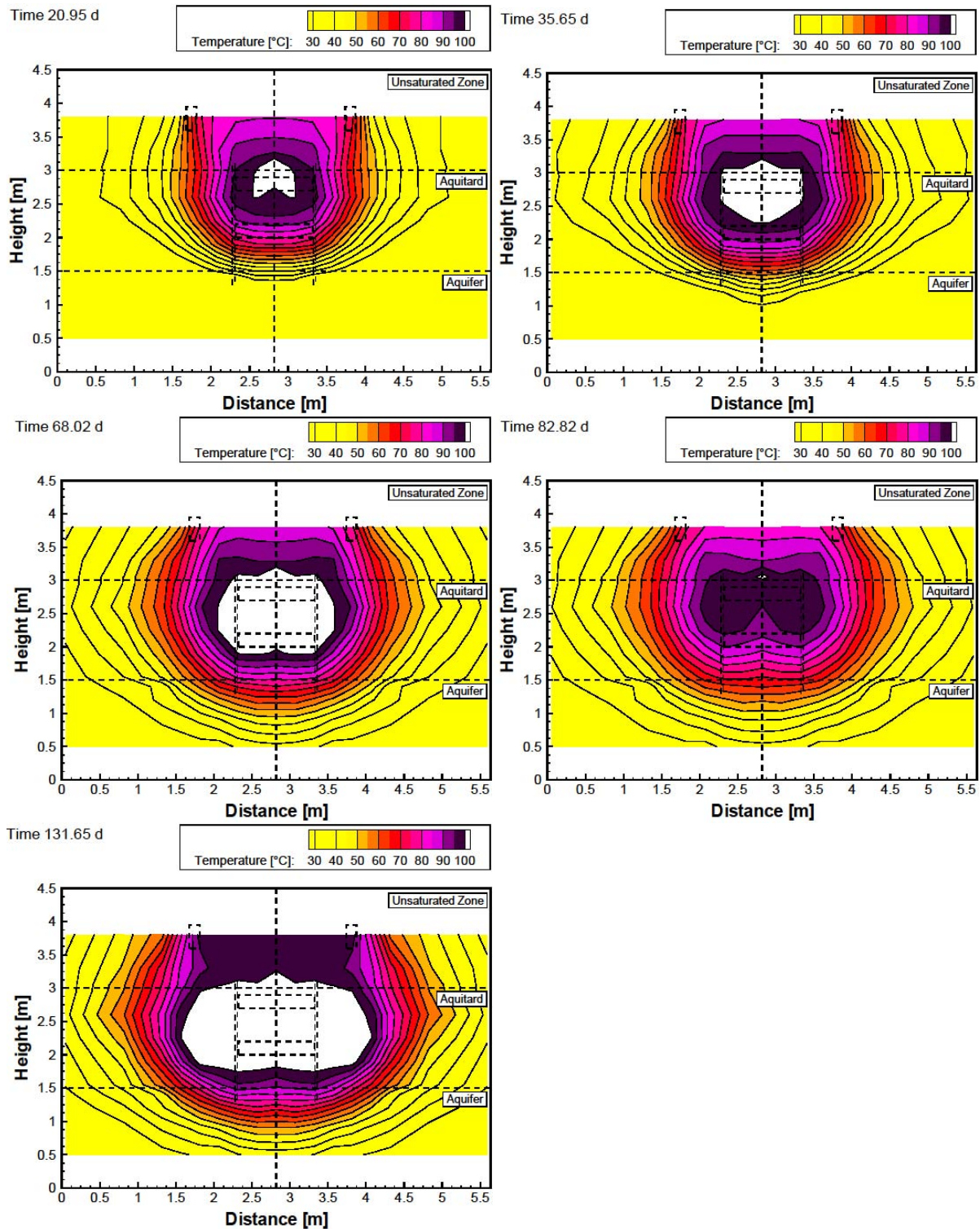


Figure 45: Temperatures during the first remediation experiment (spatial data interpolation along a cross-section through the centerline of the tank from profile “j” to “a”, which are indicated in Figure 10 as “J” and “A”). The positions of the heaters are shown by projection.

Top: end of Phase 0 and end of Phase 1;

Center: end of Phase 2 and end of Phase 3;

Bottom: end of Phase 4.

In profile “j” the Phase 3 temperatures in all aquitard layers decreased below 100°C, which impressively demonstrates the significance of heater distance on the achievable temperatures.

An extension of the distance of two heaters by 25 cm leads to a temperature reduction of up to 20°K. The steam zone collapsed and remained only in the near-field of the heater wells.

At the beginning of the last experimental phase (Phase 4), power input was doubled by the installation of four additional heating elements. During this phase the heaters were switched off and on seven times (not marked in Figure 44). In profiles “j” and “g” the temperatures in the upper aquitard and in the unsaturated zone increased to values similar to Phase 2, whereas the temperatures in the lower aquitard and in the aquifer were significantly higher. The maximum temperature increase of 20°K could be observed at the bottom of the aquitard (layer 155 and 190). The temperatures in the aquifer increased less. The changes at the boundary (profile “e”) were the largest. The steam front propagation led to a large increase of temperature in the aquitard. Temperatures in layer 190 were rising to above 100°C (increase by nearly 30°K) and at the boundary between aquifer and aquitard (layer 155), temperatures increased by 20°K). After 29 days of Phase 4 (8 heaters), intermittent heater operation was restarted, with the heaters being switched off seven times. Thus, the temperatures fluctuated by several degrees Kelvin in the three profiles “j”, “g” and “e”. The fluctuation was very moderate in the lower aquifer and increased with elevation.

The spatial temperature distributions at the end of each phase are shown in Figure 45. The temperature data were mirrored to show a complete cross section through the container. Profile “a” is located at the tank boundary and profile “j” in the center of the x-axis (compare with Figure 10, where they are indicated as “J” and “A”). Dashed lines mark the position of both NAPL-lenses (2-2.2 m and 2.7-2.9 m above base) and that of both SVE wells (3.25-3.75 m above base)

At the end of Phase 0, temperatures in the entire upper part of the TTZ (including the upper NAPL-release lens) were above 95°C with a lateral propagation up to the boundary of the upper lens. Temperatures in the lower lens were below 90°C. Only in the center of the upper lens was a two-phase steam zone created on the pore-scale, with NAPL and water being heated past the eutectic temperature. Temperatures in the aquifer did not show a significant increase. Due to its higher permeability and the higher groundwater flow in the aquifer, energy was dissipated.

During Phase 1, under diminished GW flow, the temperatures in the aquifer increased, especially in the central profiles. The groundwater outflow temperature increased from 23°C to 28°C. This was attributable to an addition of 0.73 kW for a groundwater influx of 3 m³/day. The steam zone extended in all directions and completely steamed the upper lens. Above the lower lens, temperatures exceeded 95°C.

At the beginning of Phase 2, the further reduction of the GW flow resulted in temperatures of 100°C and a steam front expansion just above the lower lens. The aquifer was also heated to temperatures above 60°C.

During Phase 3 (changed heater set-up), the temperatures inside the TTZ decreased below 100°C and the steam zone collapsed. Outside of the TTZ, the temperature changed only to a minor degree. Although the energy input remained constant the distance between heaters and the central point was too wide and steam was only produced in the direct vicinity of the heaters.

In Phase 4, a doubling of the power input by a simultaneous operation of 8 heaters resulted in steaming of the entire TTZ. Downward steam front propagation changed only moderately

compared to Phase 2, but in the lateral direction the steam front propagated in the range of 0.5 m (Figure 45, bottom). So the volume of the steamed zone increased significantly.

6.10.2.3 Contaminant extraction

The extracted soil vapor was continuously analyzed by a gas chromatography using PID detection. The concentration of the groundwater outflow was measured by HPLC from manually-collected samples. PCE and tracer concentrations are plotted in a logarithmic scale over time (linear scale) in Figure 46. The different phases of operation are indicated at the top of the diagram; the vertical brown lines show the interruption of the energy input. Fat lines show concentrations in the soil vapor, whereas thin lines show concentrations in the groundwater outflow. PCE, the contaminant is depicted in pink, the tracer substances 1,4-DCBz in green and 1,2-DCBz in blue.

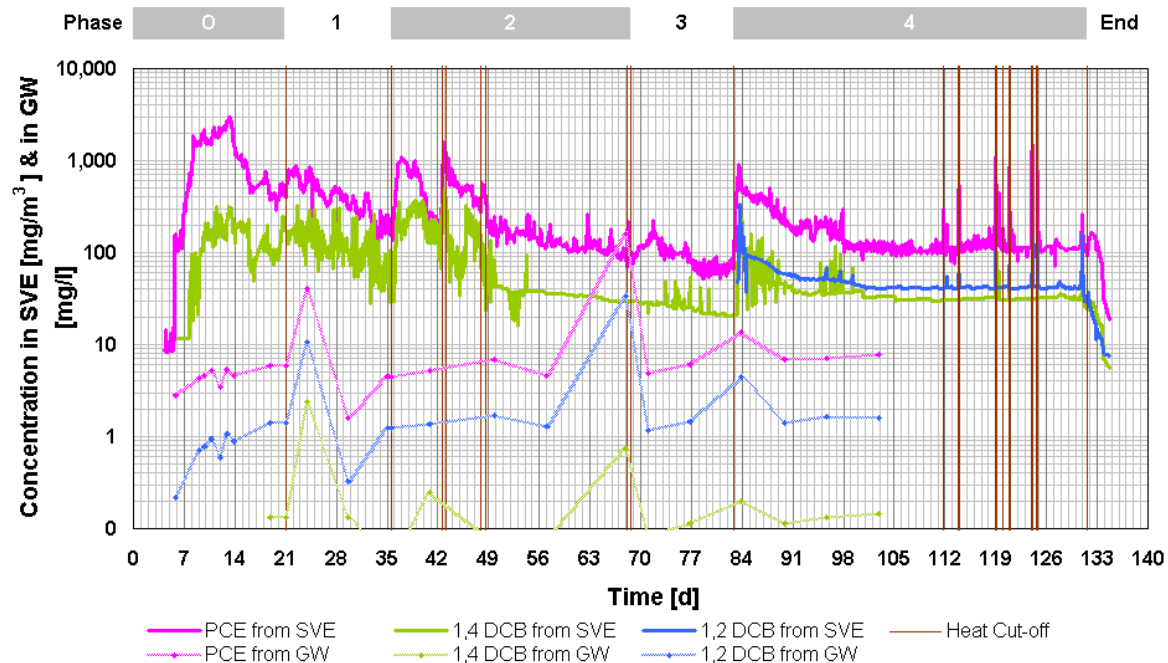


Figure 46: Concentrations of PCE and tracer compounds recovered via SVE [mg/m³] and GW outflow [mg/l]. 1,4-DCBz tracer added to top NAPL-release lens; 1,2-DCBz tracer added to bottom NAPL-release lens.

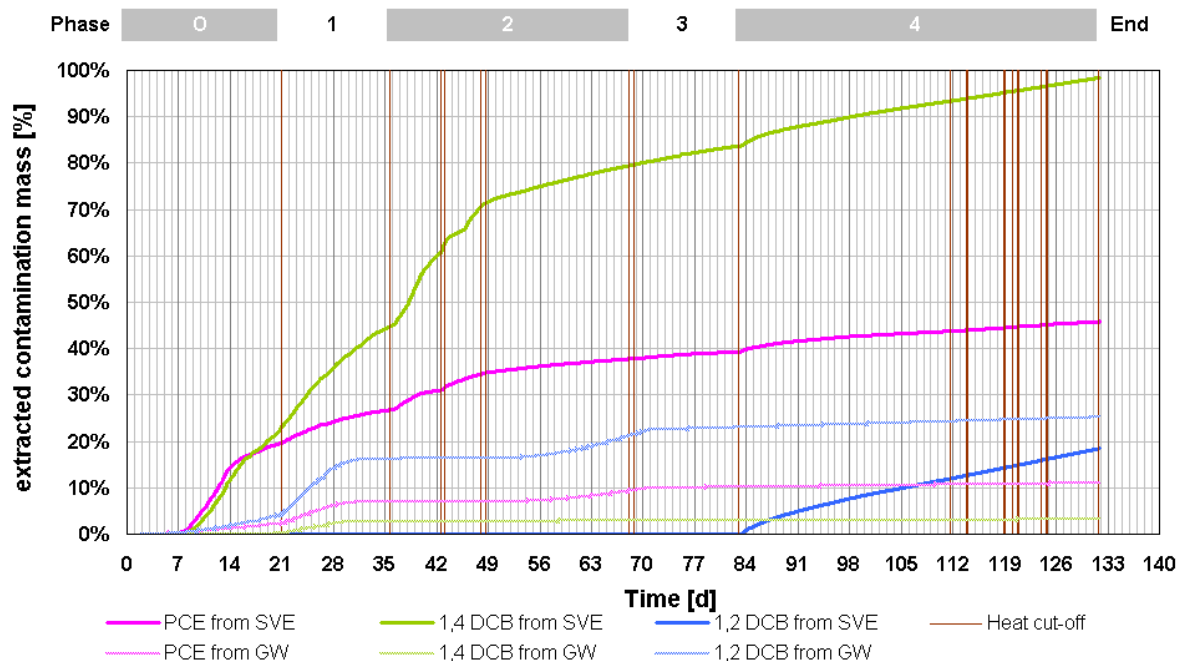


Figure 47: Total PCE and Tracer Recovery via SVE and GW outflow (cumulative curve)
 1,4-DCB tracer added to top NAPL-release lens; 1,2-DCB tracer added to bottom NAPL-release lens.

The concentration of PCE in the soil vapor increased strongly at day 5 (Phase 0) due to the breakthrough of the steam front to the extraction wells in the unsaturated zone. During the following two weeks, the vapor concentrations remained at a high level of between 1,500 and 3,000 mg PCE/m³. Afterwards they decreased and settled down to approx. 600 mg/m³. The concentrations increased moderately at the beginning of Phase 1 but decreased after several days again and remained at 200 mg/m³ at the end of this phase.

The further reduction of the GW-inflow during Phase 2 led to an increase of PCE concentrations in the SVE again of up to 1,000 mg/m³, but they also decreased after one day to 200 mg/m³. Each interruption of the energy input led to the same effect: a strong increase followed immediately by a decrease of the concentration, but the increase was faster the second time. At day 49 the energy input was interrupted again, but the associated peak-like contaminant removal was smaller than before and the PCE concentrations had decreased to 100 mg/m³ by the end of Phase 2.

During Phase 3 (with heaters re-installed within the outer square), PCE concentrations decreased continuously to 60 mg/m³. Doubling the heater power in Phase 4 led to an increase of the concentration again up to 900 mg/m³, but the concentrations decreased again in the following days. The intermittent heater operation led to several peaks of the vapor concentration with values up to 1,000 mg/m³.

The concentrations of the 1,4-DCBz (the tracer added to the upper lens) show similar effects as the PCE concentrations, although a retardation of one day can be seen. The values are smaller by approx. one order of magnitude due to the lower mass of infiltrated tracer. The second tracer 1,2-DCBz (infiltrated into the bottom lens) was only detected during Phase 4 due to the much later steaming of the bottom lens. The breakthrough of the tracer caused concentrations of up to 350 mg/m³, but the extraction and the concentration reduced

rapidly on a level of 40 mg/m³. The intermittent heater operation led to several concentration peaks, but they were not as high as the PCE peaks.

An increase in the contaminant recovery via SVE resulted from reducing the GW inflow or increasing the energy input (Phase 4). The increase of the distance between the heaters had no positive effect on the contaminant output (due to the collapse of the steam zone), but the intermittent operation showed temporarily higher contaminant concentrations caused by the vacuum evaporation of condensed contaminants at the steam front.

The PCE and tracer concentrations in the groundwater outflow were also measured. However, the temporal resolution was less accurate compared to the automated SVE sampling because groundwater samples were taken manually and less frequently.

The breakthrough of concentrations from the SVE could not be seen in the groundwater outflow. The concentrations of all three contaminants show a parallel trend for the complete experiment. During the first two weeks, the concentrations of PCE and 1,2-DCBz (the tracer added to the bottom lens) increased continuously. At the beginning of Phase 1, the concentration of the three contaminants showed a peak, but this was based on only one measurement. A constant increase of the concentrations cannot be assumed. Afterwards, concentrations were rather constant. At the beginning of Phase 3 (heaters relocated to the outer square), PCE concentrations increased and almost exceeded the solubility limit. The tracer concentrations also showed a significant increase. The concentrations of all contaminants remained during the subsequent measurements at the level of Phase 2.

The cumulative mass recovery via SVE and groundwater is plotted against operation time in Figure 47. Only 45 % of the infiltrated mass of PCE was extracted via SVE during the first remediation experiment. The major portion was extracted during the first two weeks; 20 % of the total PCE was recovered during Phase 0. An additional 10 % of the total mass was recovered during the following three weeks. Although during Phase 4 the highest energy input was used to generate elevated temperatures and a larger steam zone, only 5 % of the infiltrated PCE could be extracted via SVE during that phase.

The mass extraction results for the two tracers were in sharp contrast, indicating the differing degrees of remediation that occurred within and around the upper versus the lower NAPL-release lenses. Almost 100 % of the 1,4-DCBz (representing the upper lens) was removed via SVE. At the end of Phase 0, approx. 20 % of 1,4-DCBz had been removed, which suggests that all of the recovered PCE during Phase 0 came from the upper lens. More than 20 % of 1,4 DCBz was removed during Phase 1 and 35 % was removed during Phase 2 with a long-lasting increase after the first heater was switched off. During Phase 3 (enlarged heater distance), the extraction of 1,4-DCBz decreased and during Phase 4 a steady recovery of the remaining 15 % was observed. The 1,2-DCBz tracer from the bottom lens was first detected in the soil vapor during Phase 4. The contaminant recovery rate was rather constant and by the end of the experiment only 20 % of the infiltrated mass had been recovered via SVE.

The “recovery” via groundwater was dominated by the contaminant from the bottom lens. From the end of Phase 1 until the middle of Phase 2, the extraction of all substances remained constant at values of 8 % for PCE and 17 % for 1,2-DCBz. During the end of Phase 2, up until the beginning of Phase 3, the rate of extracted mass recovery accelerated. After that, the increase of mass recovery was moderate for 1,2-DCBz and for PCE. Finally, 25 % of the initially infiltrated 1,2-DCBz and 11 % of the PCE (almost completely from the bottom lens)

were recovered with the groundwater outflow. Mass recovery for 1,4-DCBz (top lens tracer) was dominated by one measurement value in the third week (Figure 46). All other samples showed no or minor concentrations, so only 3 % of the 1,4-DCBz from the top lens had been recovered in the groundwater outflow by the end of the experiment (Figure 47).

Due to the ability to distinguish between the two tracers, it is possible to attribute the extracted mass of PCE to relevant lenses. Almost 87 % of the infiltrated PCE could be recovered from the upper lens and only 27 % of the PCE was recovered from the lower lens. In total, 56.4 % of PCE (45.5 % by SVE and 10.9 % by GW), 101.5 % of 1,4-DCBz (98.3 % by SVE and 3.1 % by GW, with small errors in the analyses leading to a sum over 100 %) and 43.6 % of 1,2-DCBz (18.4 % by SVE and 25.2 % by GW) were removed.

To monitor a potential migration of the contaminant into the aquifer, sampling ports had been installed in both tanks, especially in the lower part of the tanks. Most of the sampling ports were installed in the aquifer to monitor dilution processes and signal NAPL displacement due to elevated contaminant concentrations in aquifer. Figure 48 provides a condensed view of the aforementioned Figure 10, which shows the sampling ports in plan view and Figure 11, which shows them in side view. The sampling port locations are designated by capital letters (e.g., “A”, “B” and “C”) located beneath the drawings (black font).

In the aquitard (layers 180 and 260), only three sampling ports (porous sampling discs) were installed per layer (profile “A” and “C” along the tank’s center line and profile “B” offset 0.75 m from the center line (halfway between the center line and the wall of the tank)). Samples were taken regularly according the experimental procedure. The following diagrams illustrate time steps when concentrations changed significantly (Figure 49).

The diagrams on the left hand side of Figure 48 show PCE concentrations in the tank for each layer. The origin (point 0,0,0) of the coordinate grid represents one of the lower corners of the tank; thus, the heater elements are located at 2.5 and 3.5 on the x-axis. The concentrations are laterally interpolated within each of the layers (not vertically between the layers). On the right hand side of Figure 48 the concentrations of both tracers are shown as mass fractions for 1,4-DCBz and 1,2-DCBz in relation to the total DCB concentration (for example: $x_{1,4} = m_{1,4} / (m_{1,4} + m_{1,2})$). The first letter represents the tracer. T (top) stands for the tracer in the upper lens (1,4-DCBz) and B (bottom) stands for the tracer in the bottom lens (1,2-DCBz). The values that follow represent the mass fraction in percent of the respective tracer. Sampling ports where no tracer was detected are given the value “0”.

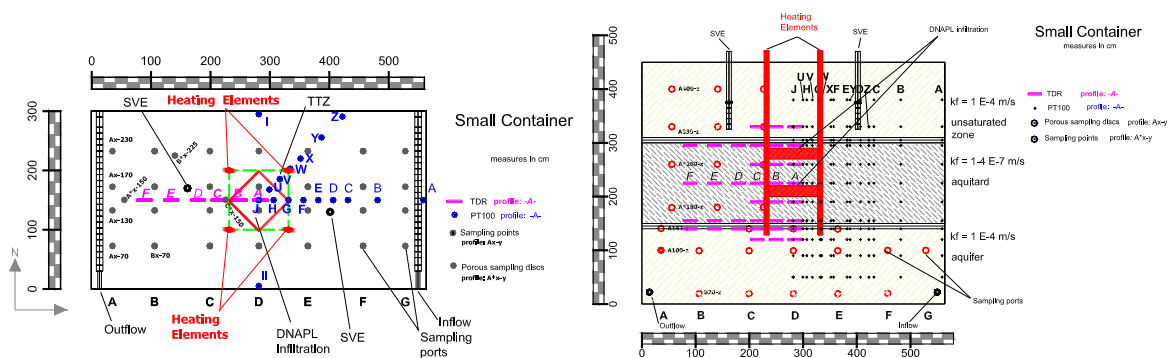
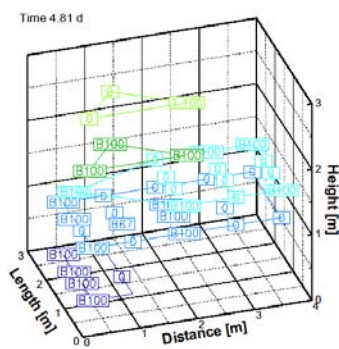
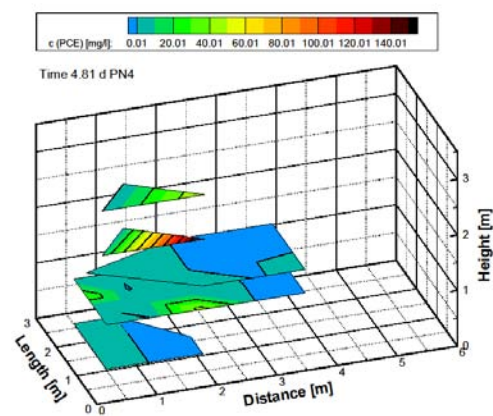
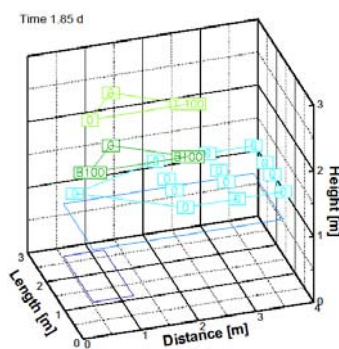
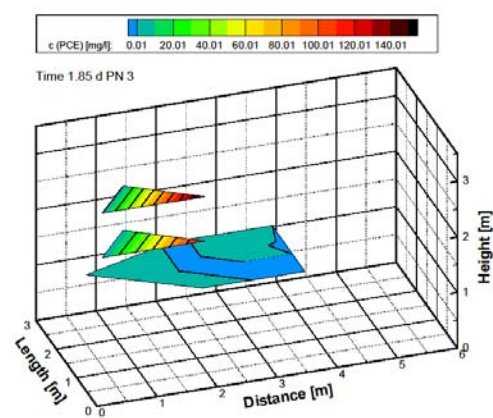
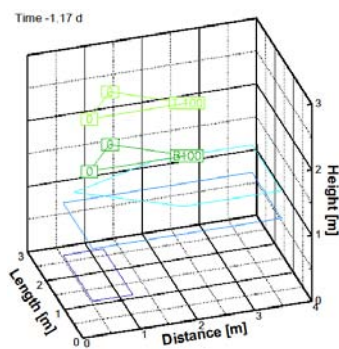
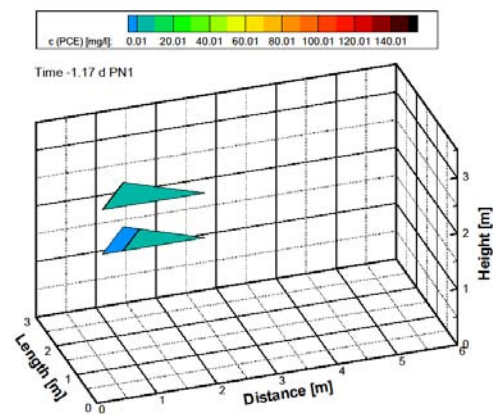
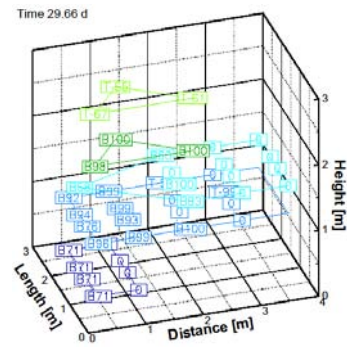
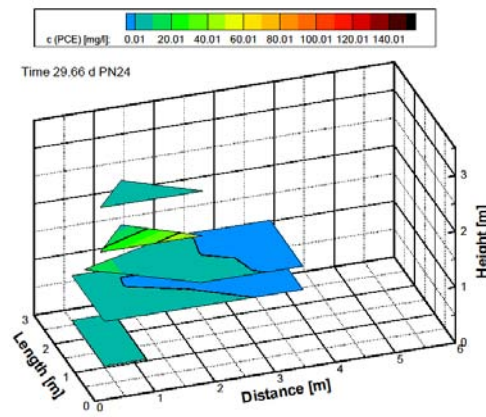
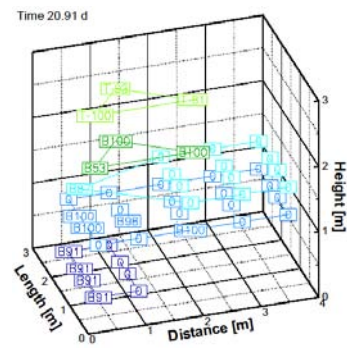
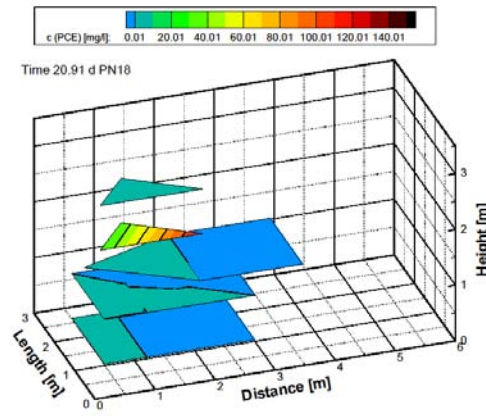
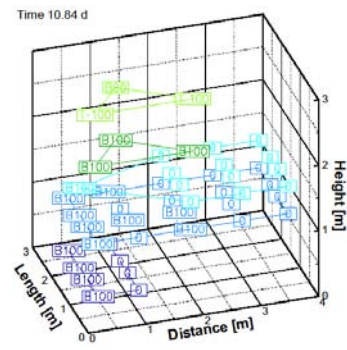
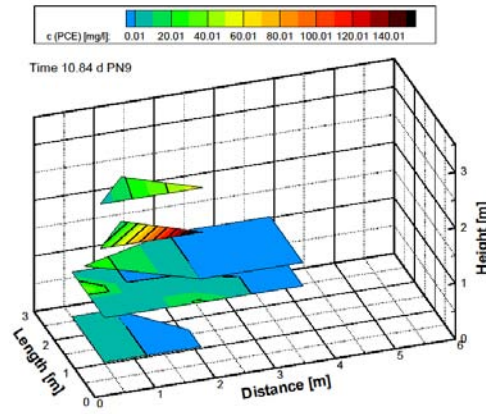


Figure 48: Set-up of the smaller tank 1. Left: Plan view; right: side view. Refer to Figures 10 and 11 for greater detail.





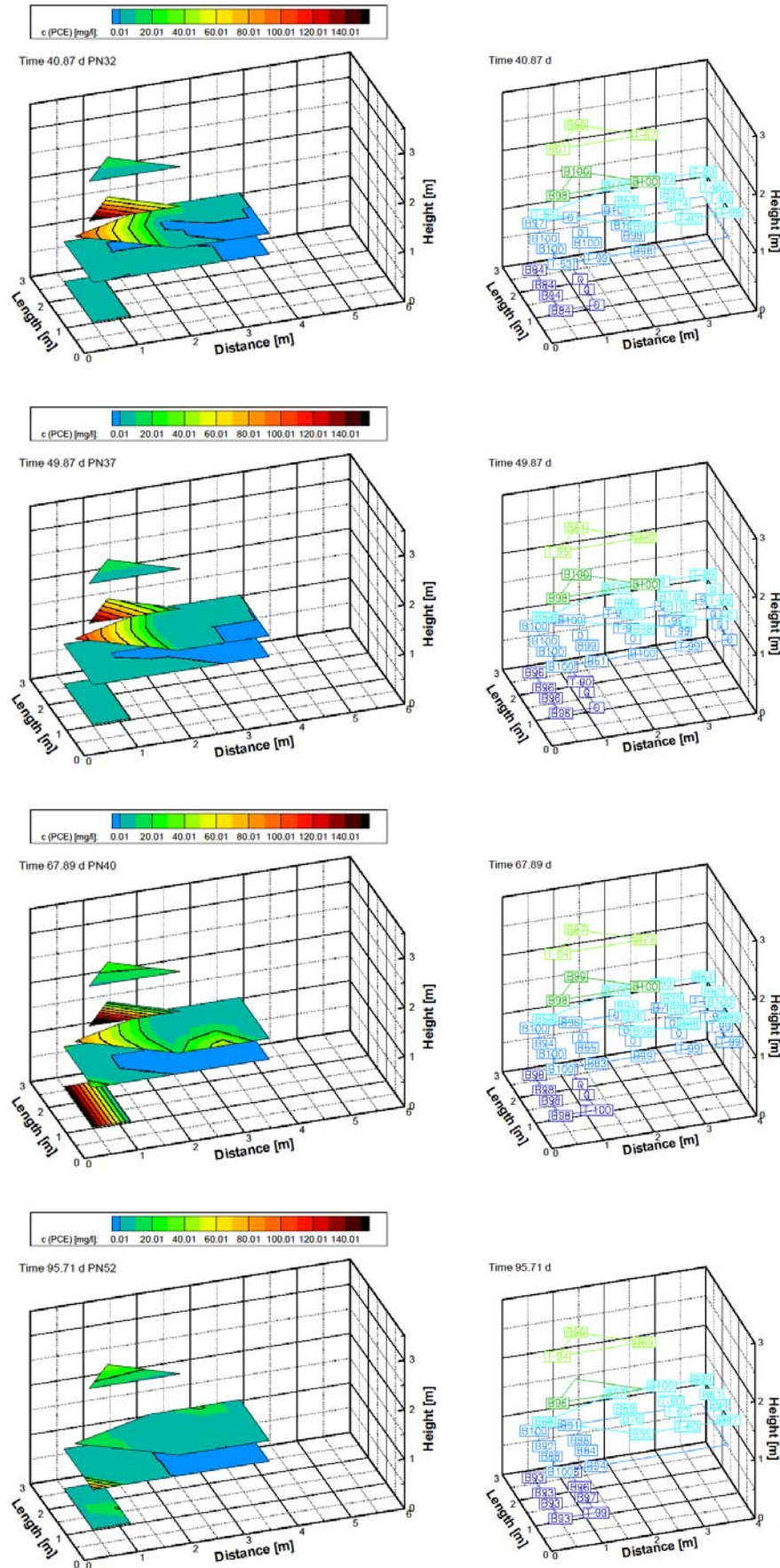


Figure 49: Interpolated PCE concentrations per layer at different time steps. See text for explanation.

PCE concentrations of up to 10 mg/l were measured in profile “C” (layer 180 and 260, located 10-cm laterally from the corner of the NAPL-release lenses, and 10 cm below the bottom of each of the lenses, respectively) immediately after contaminant infiltration (day - 1.17, with day 0 indicating the onset of heating). Thus DNAPL migration began prior to heating. The concentrations increased over the next two days and values in the range of the solubility limit (160 mg/l for PCE) were detected in profile “C”. Tracers associated with the top and bottom lenses could clearly be attributed to each lens. 1,2-DCBz, which was infiltrated into the lower lens was detected in the bottom sampling port (layer 180) and 1,4-DCBz infiltrated into the top lens was measured in the upper sampling port (layer 260), both within the aquitard.

Five days after energizing the heaters, PCE was detected in two profiles of layer 260 and tracer was found according the initial infiltration in the lenses. In the aquifer PCE was measured in remarkable concentrations. In the sampling ports “A100-170” (Profile “A” at a height of 100 cm above base and 170 cm distant from the tank boundary) and “C100-70” (Profile “C” at a height of 100 cm above base and 70 cm distant from the tank boundary), PCE concentrations climbed up to 50 mg /l. Contaminants were also detected in sampling port “A 142” (profile “A” on the center line, height 142 cm above base, 150 cm distant from the tank boundary) and in the groundwater outflow. Concentrations in layer 260 decreased to 40 mg /l. At sampling port B260 contaminants were also detected. 1,2-DCBz was detected only in the bottom layers below the bottom NAPL release lens, whereas 1,4-DCBz was measured only in layer 260.

Six days later, the PCE concentration in sampling point “B260” increased to 20 mg /l and up to 80 % of the detected tracer was from the bottom lens. The concentrations of the contaminants in the aquifer stayed constant except for point “A142”, which showed an increase in the concentrations.

On day 21, the aquifer sampling ports with previously high concentrations were sampled again. To obtain a more representative sample the sampling volume and time was extended to monitor the concentrations in an integrative way. Analyzing the samples for different sampling times representing increasing distances from the single sampling point produced inconsistent results. For all of these sampling points the concentrations did not increase until the next sampling campaign, which was after a 6 day pause. The PCE concentrations in layer 260 decreased in all three profiles and were below 10 mg /l (one order of magnitude lower than 10 days before). The mass fraction of 1,2-DCBz decreased in Profile “A” and “B” in layer 260, but in profile “C” 25 % of the tracer was still from the bottom lens. At day 25.91 (not shown in the diagrams) at sampling port A180-150 (profile “A” at a height of 180 cm above base along the center line), PCE was detected as a NAPL. NAPL was extracted until no separate phase could be detected visually. In total 34.4 g PCE as free product were extracted.

The next sampling campaign was on day 30. The concentration at sampling port “C180” decreased by 50 % to 54 mg /l. Again, PCE as free product was extracted from sampling port “A180-150” (70.1 g). In total, 270 g of NAPL were extracted through the sampling ports during the whole experiment indicating the presence of a preferential flow path extending laterally from the lower infiltration lens. The PCE concentration in Profile “A142” increased to 15 mg /l including an increase of the mass fraction of 1,4-DCBz. The mass fraction of 1,2-DCBz in layer 260 also decreased, which indicated a vertical movement of both tracers (upwards and downwards, respectively).

During Phase 2, contaminant concentrations in the groundwater continued to increase. The mass fraction of 1,2-DCBz in layer 260 increased as well. Concentrations at the sampling ports “A142” and “A180” almost exceeded the solubility of PCE with equal tracer concentrations (~1:1-ratio), which indicates a strong mixing of the contaminant from both NAPL-release lenses. The mass fraction of 1,4-DCBz increased in the bottom aquifer (layer 100) even with locally higher values of tracer from the upper lens (1,4-DCBz). PCE concentrations in profiles “C142-230” and “D142-230” increased by two orders of magnitude. According to the observed tracer concentration and composition, the increased PCE concentration originated from the bottom lens (1,2-DCBz). Although PCE concentrations were small, in layer 100 a higher mass fraction of the upper tracer (1,4-DCBz) was detected. This indicated a vertical downward movement of the PCE that had been infiltrated into the upper lens.

By the end of Phase 2 (day 68), contaminant concentrations in the aquifer were still increasing. In the outer sampling port “A100” and at ports “C142” and “D142” concentrations increased to 35 mg /l. At port “D142”, the concentrations were up to 50 mg /l. The concentration in sampling port “A142” remained at a high level but it slightly decreased. In layers 142 and 180 the contaminant approached from the bottom lens (tracer:1,2-DCBz). The PCE concentration in the outflow was high with values above the aqueous solubility of 160 mg /l.

During Phase 4, the concentrations in layer 142 decreased, except for the outer sampling port of “D142” where concentrations increased to above 23 mg /l. In layer 100 the concentrations increased again, especially the outer sampling port of “A100” (100 mg /l). The PCE concentration in the groundwater outflow decreased to 7 mg /l. The mixing of both tracers was less apparent than before. Only in layer 260 and at the groundwater outflow did the tracer from the upper lens dominate.

6.11 Task 4.4: Remediation experiment in the large tank

6.11.1 Phases of operation

In the large tank the remediation experiment lasted for 61 days with only one phase subject to an intermittent operation. Eight heaters were operated with a total power input of 12 kW during continuous operation. The heaters were periodically turned off (intermittent operation) as indicated in Table 9. The groundwater discharge was 1 m³/day and the SVE discharge was varied between 10 to 20 kg/h.

Table 8: Duration and mode of operation of the remediation experiment in the large container

Phase	Duration [days]	Power of heater array [kW]	Heater set-up	GW discharge [m ³ /day]	SVE discharge [kg/h]
0	61	12	8 heaters	1	10.0 - 20

Table 9: Time and duration of heater interruptions during the second remediation experiment in the large container

Time [days]	Duration [days]
20.91	0.25
26.00	0.21
26.99	0.30

Time [days]	Duration [days]
28.00	0.21
30.50	1.61
34.06	0.16

Time [days]	Duration [days]
46.02	0.20
48.01	0.19
52.94	0.19

6.11.2 Results

6.11.2.1 DNAPL release and initial conditions

As successfully applied in the previous 3D remediation experiment, again a mixture of PCE as the main contaminant and DCB as a tracer contaminant was infiltrated into each of the two DNAPL storage lenses. In the case of the upper lens, 1,4- Dichlorobenzene (1,4-DCBz) had been mixed with PCE, whereas a mixture of 1,2-Dichlorobenzene (1,2-DCBz) and PCE was chosen for the bottom lens. The tracer mass in each case was 20% of the PCE mass. In total, per lens 3.5 kg PCE and 0.7 kg DCB were infiltrated.

The contaminant mixtures were infiltrated per lens over a 24 hour period in two steps by means of separate diffusers, each with eight outlet pipes (Figure 9 b) and a peristaltic pump. The average infiltration flux per lens was reduced to 0.35 kg NAPL per hour. No significant contaminant migration could be observed within the following days. In contrast to the previous experiment, the contaminant mixtures remained in the DNAPL lenses until the heaters were switched on eight days after finishing the DNAPL infiltration.

6.11.2.2 Temperature development

During the first three weeks, the power input of the eight heaters produced a rapid increase in temperature. In profile “j” all layers located above 1.55 m above base quickly reached or exceeded a temperature of 100°C. In layer 155, temperatures rose above 90°C and after three weeks became almost constant. In the unsaturated zone (layer 380), a inflection point indicating dewatering could be seen at day 14 (Figure 50).

In profile “g” this inflection point was already evident between day 9 and day 10. In profile “e” no inflection point could be seen. The temperatures in profile “g” were similar to profile “j”, but in layer 155 the temperatures were higher than in profile “j”. Profile “e” temperatures were lower than in the TTZ, but after three weeks 100°C was exceeded for layer 190. Due to the subsequent intermittent heater operation, the temperatures decreased by a maximum of 10°K. The influence of the intermittent heater operation was minor in the aquifer relative to the aquitard. In profiles “j” and “g” the most notable decreases in temperature after shut-off were in the top aquifer and the lower aquitard (layers 140, 155 and 190), whereas the most prominent decrease in profile “e” was in the central layers of the aquitard (layers 190, 225 and 260). Depending on the time step between two shut-offs, the temperatures were allowed to reach the same levels as before. Especially during longer periods of power interruption, temperature decrease was significant.

The spatial temperature distributions during the second remediation experiment are shown in Figure 51, specifically the distributions after four days (heat-up period) and at the end of the experiment. Since the boundary conditions (specific GW influx [$0.17 \text{ m}^3 / (\text{tank width} \times \text{day})$], 8 heaters) was similar to phase 4 in the first remediation experiment in the small tank, differences in the temperature distribution are mainly a function of the different permeabilities of the materials in the two tanks (compare the top right and bottom figures in Figure 51).

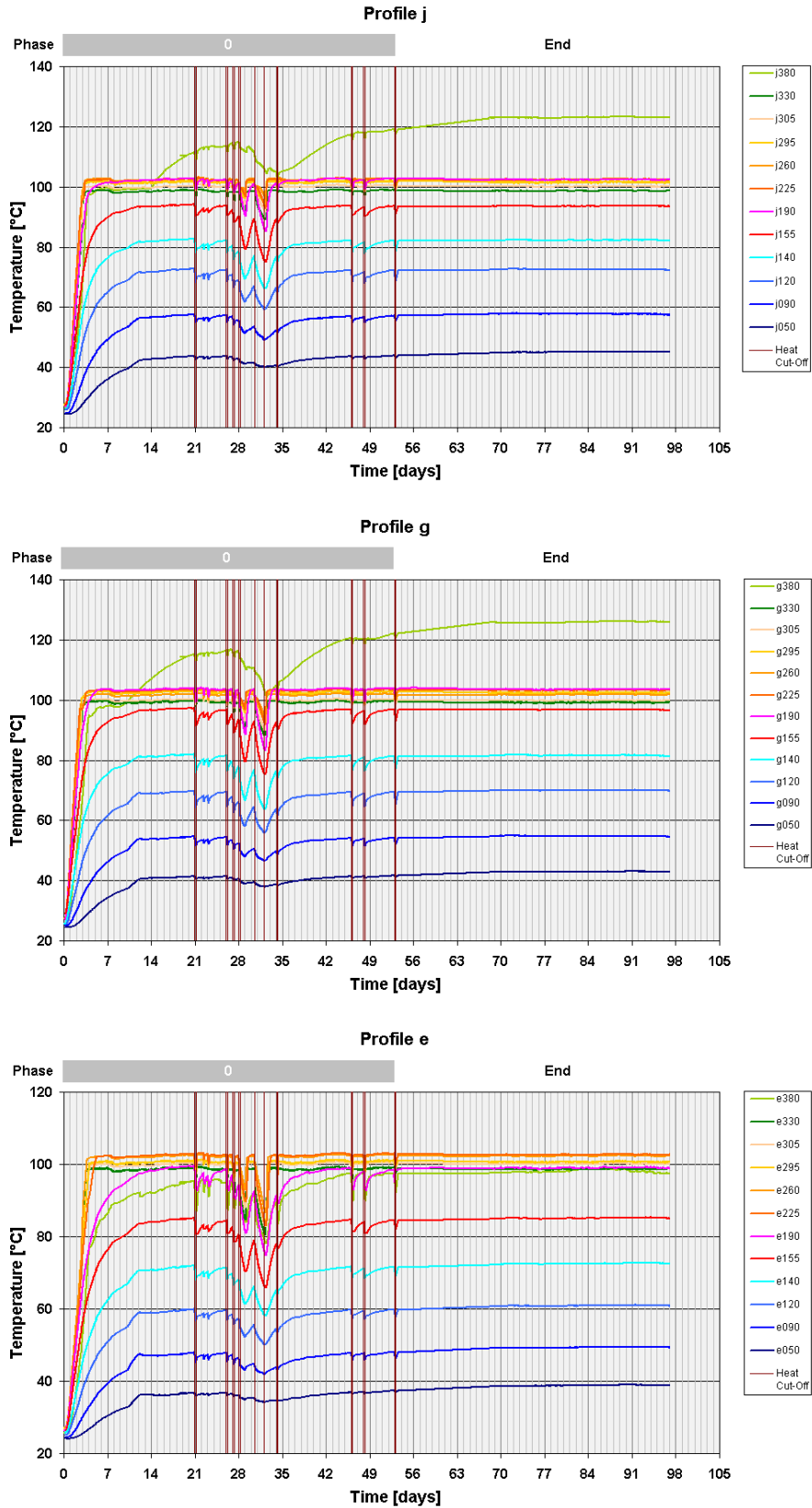


Figure 50: Temperatures during the 2nd remediation experiment (Temperature development vs. time). The groundwater flux was constant. Vertical bars indicate intermittent heater shut-down events.
Top: central profile j, located equidistant from the heaters;
Center: Profile g, located between the heaters at the boundary of the TTZ;
Bottom: Profile e, located 0.5 m outside the TTZ.

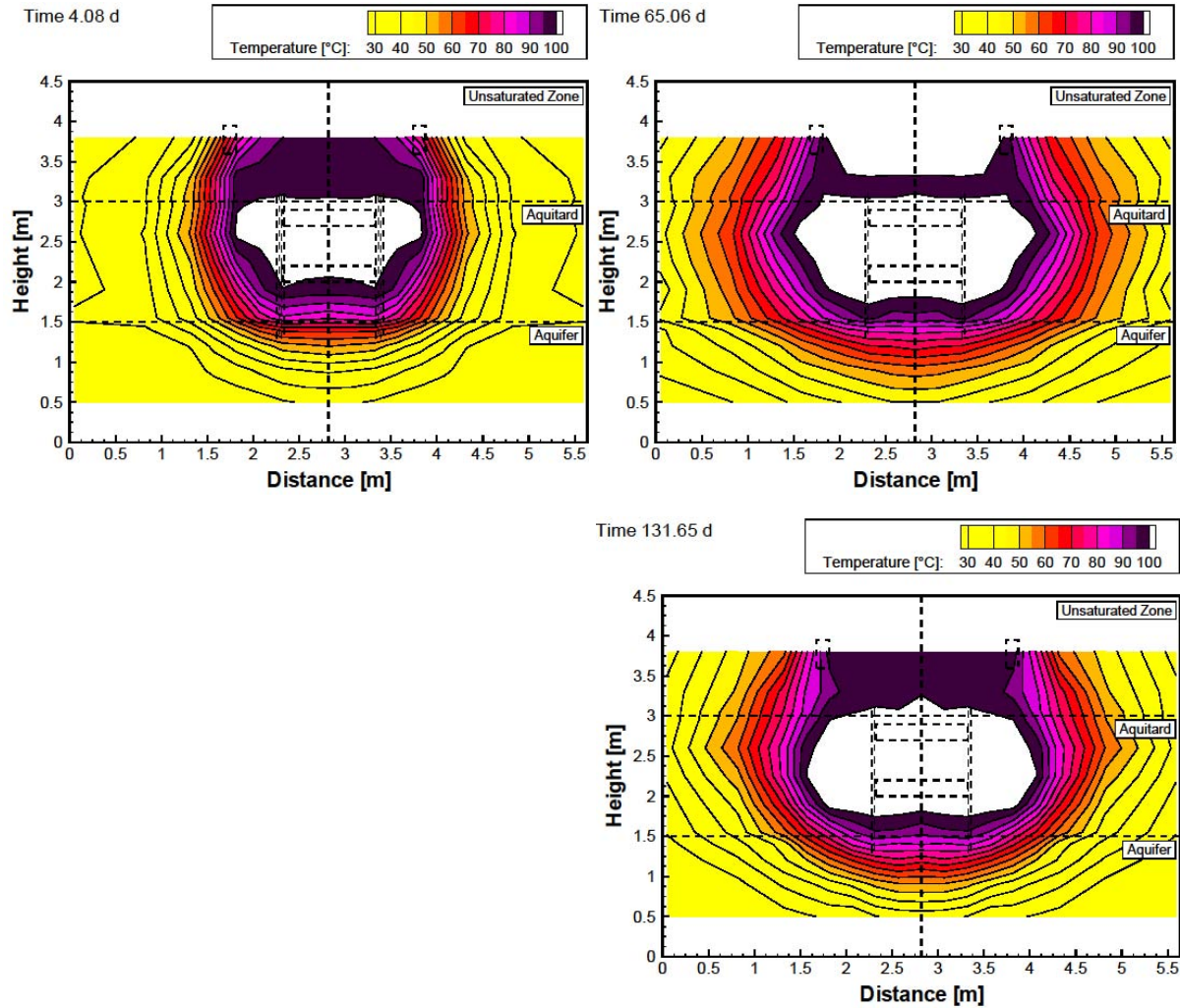


Figure 51: Temperature distribution (spatial interpolation of the measured data across a vertical cross-section through the center line from profile “j” to profile “a”, which are indicated in Figure 12 as “J” and “A”). The positions of the heaters are shown by projection.

Top left hand side: beginning of the experiment (heat-up period);

Top right hand side: end of the experiment;

Bottom: The end of phase 4 of first remediation experiment, shown for comparison.

The temperature development and increase in the aquitard was virtually identical in the two tanks. In principle the lateral steam front propagation was comparable for both experiments. Due to the higher permeability of the aquitard, aquifer and unsaturated zone in the large tank, convective processes were more dominant in the second remediation experiment. The heat propagation in the aquifer was faster and in a wider range in the large tank. Therefore the steam propagation in a vertical, downward direction was wider, less enthalpy was released to the environment (heat losses) and less steam condensed. Thus, the steam zone was larger than in the first experiment. Especially in the aquifer the higher permeability led to an increased propagation of heat due to convection processes.

Figure 52 and Figure 53 visualize the steam front propagation from isotherms of the interpolated steam front shape in tank 2 based on the temperature data. Isotherms are given in steps of 1 hour (steam front reached upper / bottom lens, left column, Figure 52 and Figure

53, respectively) and 5 hours (steaming of upper / bottom lens is completed, right column, Figure 52 and Figure 53, respectively). The steam front reached the upper lens after 2.75 days. After 3.32 days the complete upper lens was steamed. The steam front reached the bottom lens after 3.35 days inclined from above. The velocity of the front was approx. 30 cm/day in average and on a planar view. It was almost the same for the upper lens (20 – 30 cm/d). After 5.51 days the entire lower lens was steamed and the front was leaving the bottom lens parallel to the bottom.

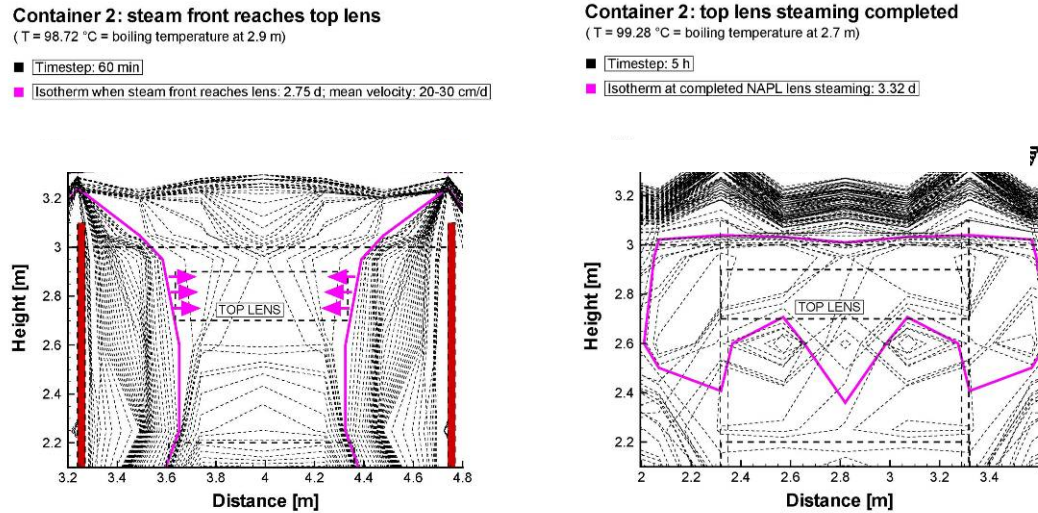


Figure 52: Interpolated steam front shape isotherms of the large tank experiment (container 2) reaching upper lens (left side) and completing steaming of upper lens (right side).

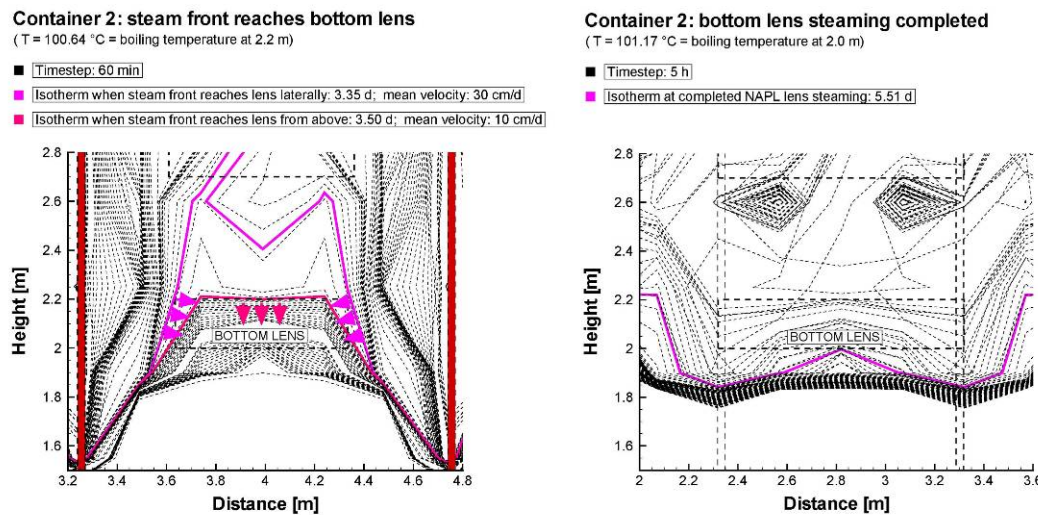


Figure 53: Interpolated steam front shape isotherms of the large tank experiment (container 2) reaching bottom lens (left side) and completing steaming of bottom lens (right side).

The steam front propagation in the aquitard was similar for both tanks in a qualitative sense. The upper NAPL-release lens was steamed from the sides whereas due to gravity forces the lower NAPL-release lens was steamed from above with an inclined front shape. However, the duration for steaming was longer due to the lower heater power input in the small tank experiment. For the small tank experiment it took almost 12 days for the steam front to

approach to the top lens with a steam front velocity of approx. 5 cm/day and after 25 days the lens was completely steamed.

The steam front velocity is only a reference value, which may be examined in further numerical simulations. This can be seen with the compression of the isotherms. After 36 days the steam front reached the bottom lens with a steam front velocity of 2.5 m/day and the steaming was completed after a total of 84 days. The steam front also stayed within the bottom lens and left the lens after a change of the operation phase.

6.11.2.3 Contaminant recovery

The breakthrough of all three substances could be seen at day 3, when the upper lens was completely steamed. The contaminant concentrations for the peak-wise extraction were for PCE 40,000 mg/m³, for 1,4-DCBz 1,000 mg/m³ and for 1,2-DCBz 500 mg/m³. Within one day 75 % of the total amount of infiltrated PCE was extracted following these high concentrations. During the following 18 days the contaminant concentrations decreased to 30 mg/m³. The intermittent heater operation (vertical lines in Figure 54) during the next two weeks caused several peaks with higher concentrations but the trend shows decreasing concentrations up to day 35 (1 mg PCE/m³). During the following continuous operation of the heaters a coherent steam zone was created and the concentrations increased again. Until the end of the experiment PCE concentrations were rather constant with peaks associated with intermittent operation. The concentrations in the groundwater outflow were low or below the detection limit of 5 mg/m³ (for PCE and both tracers).

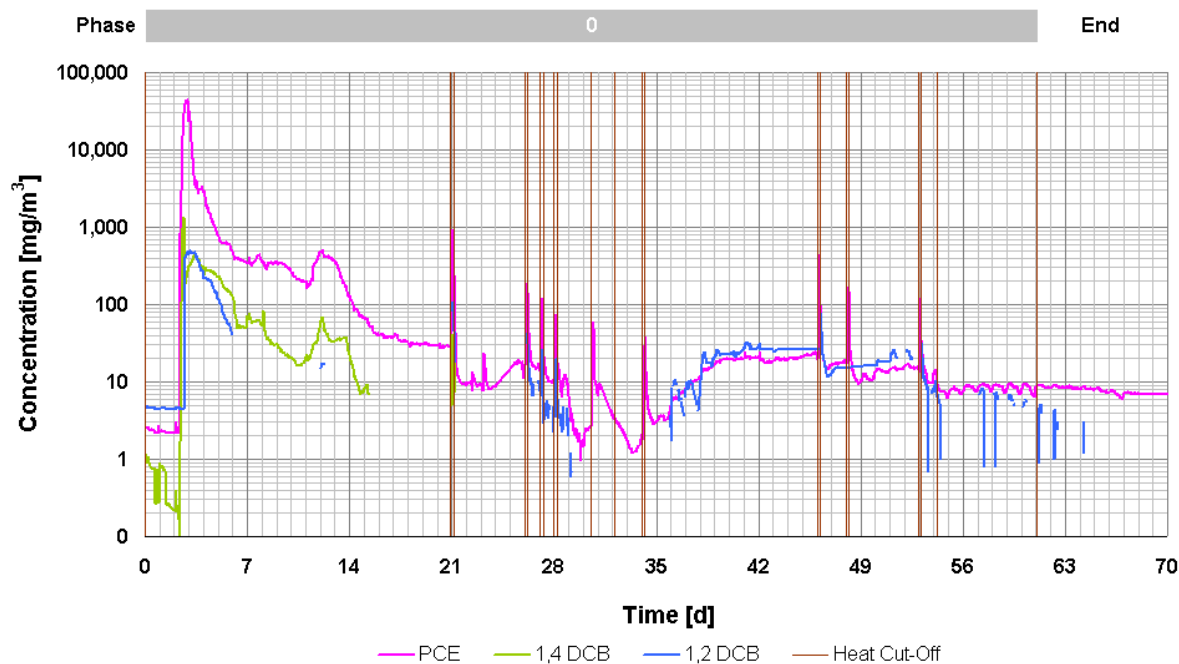


Figure 54: PCE and Tracer Extraction with SVE [mg/m³] in the second remediation experiment. 1,4-DCB tracer added to top NAPL-release lens; 1,2-DCB tracer added to bottom NAPL-release lens. Vertical bars indicate intermittent heater shut-down events.

1,4-DCBz concentrations showed a similar behavior as the PCE concentrations. Only during the first two weeks were 1,4-DCBz concentrations detected. After two weeks, 1,4-DCBz concentrations were below the detection limit.

1,2-DCBz concentrations were difficult to detect. Due to the high concentrations of DCB the peaks were not clearly separated by the GC-PID but a two peak-shape was observed on the chromatograms.

Most of the contaminant mass was recovered during the first week. After seven days, 80 % of the infiltrated PCE was removed with an extraction of 75 % mass PCE within one day. During the next week, an additional 10 % of the PCE was recovered. The mass recovery by SVE summed up to 93% by the end of the remediation experiment.

Both tracer substances had a breakthrough at the same time. After two weeks no further recovery of the tracer from the upper lens (1,4-DCBz) could be detected. The extracted mass of 1,4-DCBz reached its final value of 46 %. The extraction of the bottom lens tracer (1,2-DCBz) remained constant after one week until day 37 at 26 %. After changing the settings of the GC-PID, 1,2-DCBz could be detected again and the recovered mass increased within two weeks to 38 %. The detected mass of both tracers was significantly less than the recovered mass of PCE.

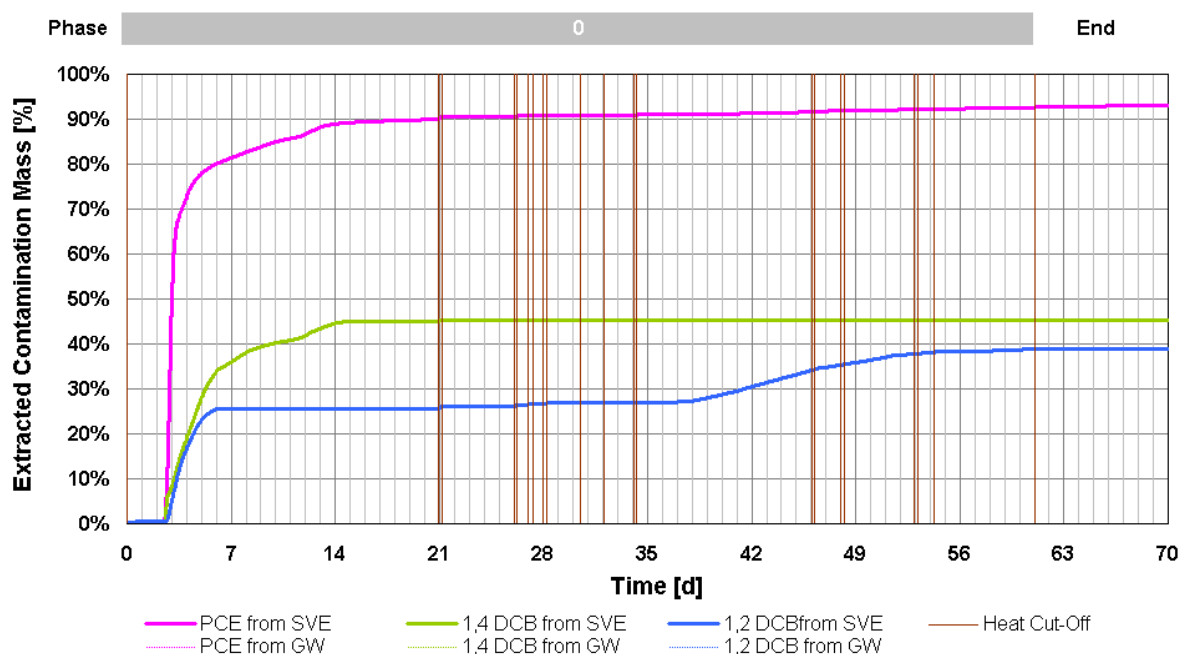


Figure 55: Total PCE and Tracer Extraction with SVE and groundwater (summation curve). 1,4-DCB tracer added to top NAPL-release lens; 1,2-DCB tracer added to bottom NAPL-release lens. Vertical bars indicate intermittent heater shut-down events.

During this remediation experiment high amounts of the infiltrated mass could be removed: 97 % PCE from the upper and 88 % from the lower lens. The contaminants were extracted mainly by SVE. Concentrations in the groundwater outflow were small and only 0.04 % of the infiltrated masses of all three substances were recovered via the groundwater.

The aqueous dissolved PCE distribution for different time steps in the aquitard is shown in Figure 57 and Figure 58. The tracer substances were not interpolated since 1,4-DCBz was not detected. The first measurement was after the NAPL infiltration but before the heaters were energized. NAPL was found in profile “C”. Five days after the infiltration (corresponding to

day -1.94) the PCE concentration in layer 180 was 5 mg/l. The concentrations increased to 15 mg/l for both layers (180 and 260) within 4 days after starting the heater operation. At this time, the temperatures in profile “C” (at the boundary of the NAPL-release lenses) were above 100 °C indicating the steaming of this profile. 75 % of the infiltrated NAPL was extracted via SVE at this time.

After a few days, concentrations in profile “C” decreased (1 mg/l in both layers). Within the next two weeks, concentrations in profile “B” (layer 260) increased to almost 15 mg/l. The concentration in profile “A 180” increased to 5 mg/l through day 53.

During the experiment no significant concentrations were detected in the groundwater outflow. The concentrations were between 0 and 40 µg/l.

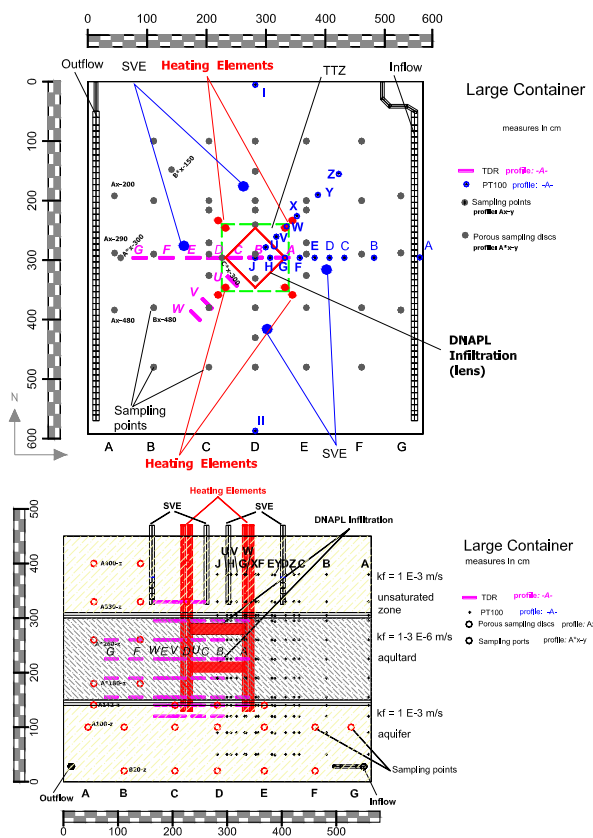


Figure 56: Set-up of the larger tank 2. Left: Plan view; right: side view. Refer to Figures 12 and 13 for detailed views.

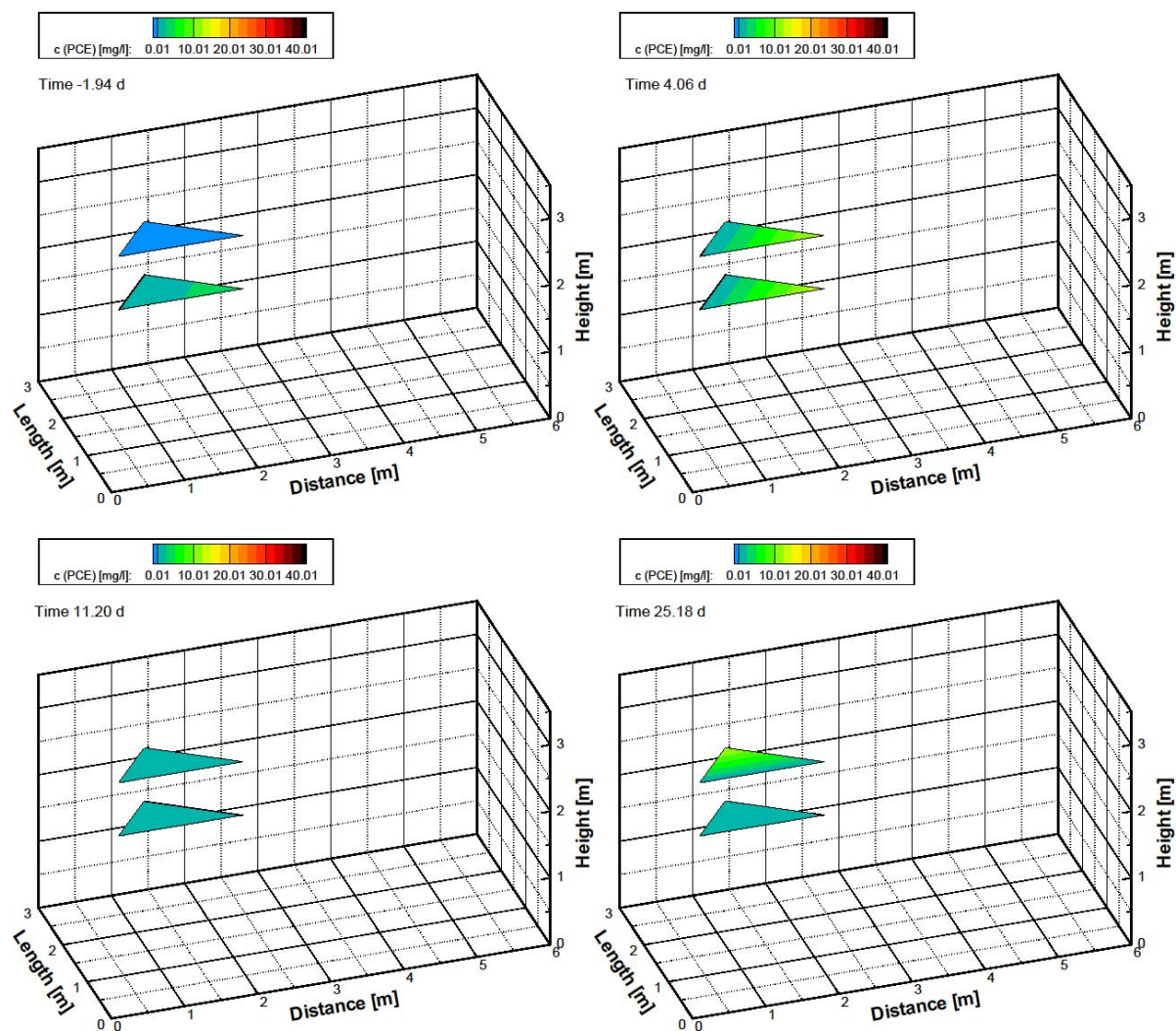


Figure 57: PCE concentrations in the large container experiment, interpolated in layers at different time steps; top: day -1.94 and day 4.06, bottom: day 11.2 and day 25.18. See text accompanying Figure 49 for explanation of how to interpret figures.

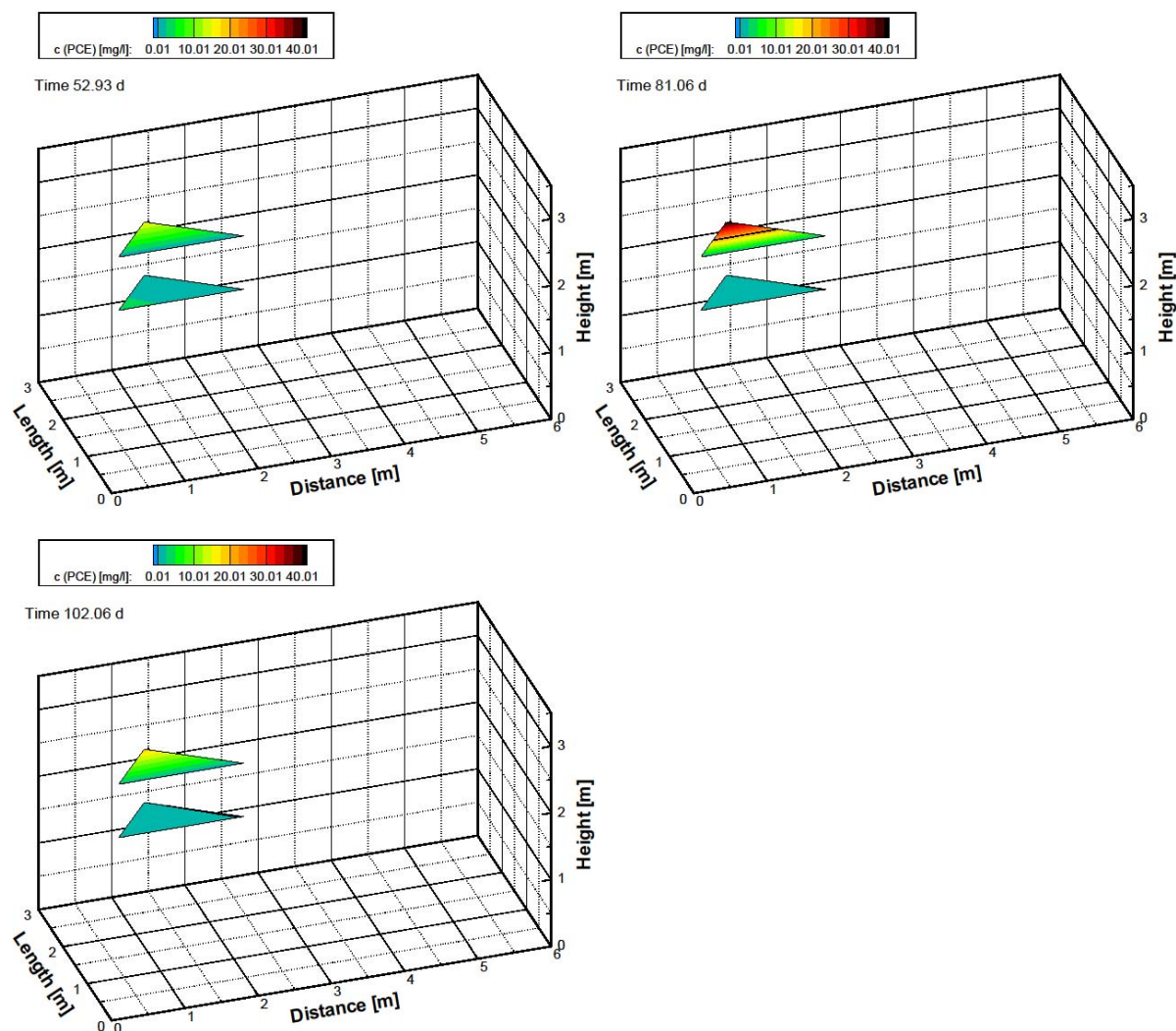


Figure 58: PCE concentrations in the large container experiment, interpolated within layers at different times; top: day 52.93 and day 81.06, bottom: day 102.06. See text accompanying Figure 49 for explanation of how to interpret figures.

The groundwater concentrations showed a maximum in Profile “B” due to the condensation of contaminant at the boundary of the steamed zone. As Profile “C” was within the steamed zone and Profile “A” was outside the steamed zone, no contaminant condensed in these profiles and the groundwater concentration was less than in Profile “B”.

6.12 Comparison and conclusion of the two remediation experiments

In order to compare the two experiments, the moment when the generated steam zone approached the single lens and the moment when the contaminant source lens was entirely steamed were determined. These moments are the starting and the ending points of the x-axis in Figure 59 (i.e., the duration to complete the steaming of the NAPL lens). On the y-axis the contaminant recovery rate for the single contaminant source lenses by SVE is shown for the moments when the single lenses were completely steamed (lower curve) and at the end of the experiments (upper curve).

The wide difference in the duration is caused by the different power supply (and the different permeabilities of container 1 and 2). The area below the lower curve describes the portion of

the contaminant mass that was immediately captured by the SVE until the time that steam had completely filled the NAPL-release lens. The area between the two curves is the portion of the NAPL mass that was recovered during the maintenance of a steamed zone in the lenses. Above the upper curve is the part of the contaminant that was not recovered through the end of the experiments because this contaminant fraction has either migrated, been displaced or evaporated and condensed at the steam front. A portion of this contaminant mass was removed by the groundwater flow.

These experiment results are specific to these experimental set-ups. A transfer to other experiments is difficult due to impact of the set-up specific boundary conditions of the experimental results to other heater set-ups or initial NAPL distributions.

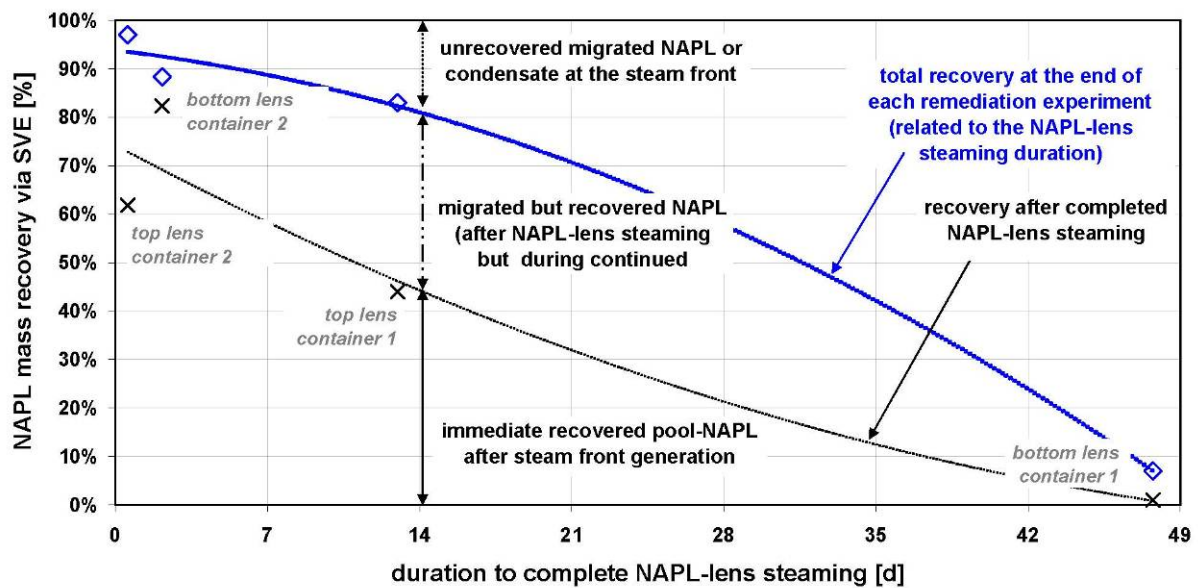


Figure 59: Correlation between time generating a steam space in a lens and the generated contaminant output.

7 Simulation Modeling

7.1 Need for more reliable numerical simulations

The purpose of the modeling portion of project ER-1423 was to help understand the mechanisms that control DNAPL remediation below the water table in lower-permeability porous media. Thermal conduction heating (TCH), as embodied within the In Situ Thermal Desorption (ISTD) technology, is an ideal method of treating DNAPL in lower-permeability media not only due to its ability to achieve a specified target temperature throughout the delineated treatment zone, but also because the technology has the ability to increase permeability as water or other materials are liberated, mobilized or vaporized. TCH is gaining acceptance for remediating DNAPLs in clays and other very tight soils and is reported to be the leading method for recovering oil from shale in the United States Naval Petroleum Reserves. The techniques used for these widely diverse applications are similar, and much that is learned from one application could be used in the other.

The challenges faced in these applications are similar. Any heating method is limited by infiltration of water from the edges of a heater array or an underlying aquifer. It is fairly common, for instance, to have a contaminated glacial till or clay aquitard with a hydraulic conductivity on the order of 10⁻⁶ cm/sec capping a sandy or gravely aquifer with a conductivity of 1 to 10 cm/sec. Moreover, the DNAPL that is vaporized by heating may be recovered most efficiently if it is diluted (stripped) by a mobile liquid or gas. So, understanding how the fluids flow and are heated both by conduction and convection is very important.

For DNAPLs, such as chlorinated hydrocarbons, the situation is complicated because the contaminant of concern (COC) can exist in four phases, as a liquid, dissolved in water, diluted in a vapor such as steam or air, and adsorbed on the soil. Thus, a simulator that can accurately model transfer of the COC among these phases is needed.

The multiphase movement of fluids within porous media is largely controlled by physical properties of the fluids, as well as constitutive properties of the medium including the permeability, hydraulic gradient, capillary pressure-saturation relationship and interconnectivity of the pore network. As an example, gradients in capillary pressure during TCH can drive imbibition of liquids into lower-permeability media. This can enhance movement of gases out of the lower-permeability media, resulting in displacement of fluids in an underlying higher-permeability layer, unless water is continuously added, as would occur in an aquifer. While the potential for downward movement of DNAPL as a liquid is often a concern, DNAPL saturations are generally low enough that movement in either the aqueous or gas phase often dominates over a short time period. In the practice of ISTR, it is desirable to employ a simulator that can model these types of movement and predict how these and related phenomena can be controlled to aid or at least not hinder the remediation process.

The boundary conditions of any process being modeled are key considerations. In a simulator like STARS, it is possible, for example to model TCH heaters as enclosed within pipes, use separate permeability and capillary pressure relations for every cell, and model heat losses to adjacent experimental tank units and the atmosphere. This allows the modeler to vary, record and visualize flow conditions inside models to help understand how the process behaves.

The ultimate need for simulation in the context of ISTR is to guide optimization of the design and operation of field projects (where new situations are frequently encountered) and to help understand retrospectively why projects performed as they did. For example, if PCE needed to be remediated from 10 m of lower permeability glacial till situated between a 10-1 cm/sec aquifer and the foundations of a building, it would be advisable to study the problem first with simulations to select the most efficient method. The purpose of this aspect of the research is to improve the understanding of the physical processes during TCH so that projects similar to that just described can be more confidently modeled, designed and implemented.

7.2 General description of STARS

STARS is the simulator that was used for this research. It is a product of the Computer Modeling Group of Calgary, Alberta and has been under development and use for almost 30 years. STARS is the thermal member of a family of simulators that also is widely used to model immiscible fluid, compositional, and chemical problems in the petroleum and environmental fields. As the Advanced Process Simulation member of this family, STARS is widely used for thermal problems and has been described as a simulator that is “capable of modeling processes that do not yet exist.” It is supported by both a pre- and post-processor. The pre-processor is capable of converting geological data into geostatistically realistic models of projects. The post-processor converts several gigabytes of information that is stored by the simulation into summaries of performance and visual or graphical distributions of saturations, temperatures, pressures, compositions and flow fields.

STARS builds on the usual geological package that includes multiple models of dual-porosity and dual-permeability characteristics of a reservoir or a subsurface zone of interest by including composition, pressure and temperature controlled phase behavior in K-value tables, adsorption, relative permeability and capillary pressure-saturation (P_c - S_w) relations as well as equilibrium and non-equilibrium chemical reactions. Its phase behavior package is sophisticated enough to model ice formation if a freeze wall were used to control aquifer influx. Its electrical-resistance-heating option is used to model both Joule heating in the oil patch and in numerous environmental projects. Since multiple solid components can form or be decomposed, STARS is even used to model in-situ bioremediation or microbial-enhanced oil recovery. A geomechanical model is also included that can model compaction or fracture formation in porous media.

Up to thirty components and an unlimited number of chemical reactions can be included if the information is available and deemed significant. If enough computing power is available several million cells could be used. This SERDP project was conducted on dual-processor, 64-bit, Dell work stations with eight gigabytes of RAM. The simulations only had three to five components, no chemical reactions, and approximately 25,000 cells. They were typically completed in six to twelve hours, with multiple simulations often being completed and summarized in a day.

7.2.1 Application of STARS to simulation of processes during TCH remediation in the saturated zone

STARS is a simulator of choice for both ISTR modeling and oil shale retorting and reclamation. The same modeling techniques are used in both applications although the conditions tested in ISTR reclamations are much less severe. Separate from this SERDP project, TerraTherm has commissioned MK Tech Solutions (MKTS) to model approximately 15 remediation projects, primarily during the design stage. These simulations have included treatment of high-boiling compounds such as PCBs and PAHs, mixtures of chemicals in landfills, and solvents at industrial plants and fuel depots. The subsurface settings within which TCH has been applied have generally been of low to moderate permeability but have included both unsaturated and saturated zones, fractured porous media (clay, saprolite and bedrock), and underlying aquifers.

This SERDP research project was primarily a study of how heat and contaminant transport in a meter-scale remediation project targeting DNAPL in lower-permeability saturated soil (i.e., an aquitard) may be affected by water flux through an underlying high-permeability aquifer. Since a large amount of temperature, pressure and saturation data can be collected during such experiments, this was an opportunity to understand how a high-permeability aquifer interacts with a lower-permeability contaminated aquitard in a thermal remediation project, and was expected to have wide applications to ISTR in general.

7.2.2 Open questions to improve the reliability of the simulated results

Since STARS began being used in 2000 for modeling ISTR and oil-shale projects, many basic questions have been addressed, and there have even been follow-up simulations (history matches) of some completed field projects. Over the years, MKTS has learned to model water bound in clays and organic media, several dozen concurrent chemical reactions, heat transfer near very hot wells, the effect of capillary pressure on countercurrent (heat pipe) flow of water to the heaters, and how to manage the energy input at heater-vacuum wells to enhance extraction or destruction of chemicals. However, almost all of these simulation projects are limited in scope and duration, as is the corresponding field data collection in comparison with this SERDP research project. Moreover, water influx, as from heavy rainfall or high flux subsurface conduits if unrecognized or improperly managed can add to the heating demand, result in unwanted contaminant condensation and increase remediation cost. It was intended that the modeling conducted during this project would elucidate the physical mechanisms of ISTR that occur during remediation of DNAPL below the water table, aid in technology selection, improve management of water influx into flow-limited source zones from an adjacent aquifer, and optimize the cost-effective recovery of the DNAPL.

The research focused on heating and treating DNAPL in lower-permeability zones with saturated hydraulic conductivity (K_s) ranging from 10^{-4} to 10^{-5} cm/s, rather than zones of even lower permeability. This is because field experience has shown that utilizing TCH to remove DNAPL from saturated, low permeability (e.g., $K_s=10^{-6}$ to 10^{-8} cm/s) silty-clays and clays is rather straightforward and very effective (LaChance et al. 2004, 2006; Baker et al. 2006), largely because groundwater influx into the heated zone is so limited, while gas-phase permeability increases during TCH. It is more challenging to optimize the application of ISTR in moderate-permeability DNAPL source zones or aquitards. Because such layers

are relatively low in permeability compared to the underlying or adjacent high permeability aquifer layer, we refer to them here as “lower-permeability” layers.

Water influx in previous ISTR simulation projects using STARS has primarily been from the surface or boundaries of the model. Few projects have had an active aquifer immediately underneath the lower-permeability layer, and none of the contaminated layers have been as thin as the 1.5-m thick lower-permeability layers that were the subject of the 3D experiments in this study. Thus influx from an aquifer or underlying vadose zone has been limited in previous ISTR models. The relatively small size of the 3D physical models in this project, relative to the field-scale, offered an opportunity to use relatively small grid cells and to begin to understand the details of the interaction between the heated, lower-permeability layer and the cooler underlying aquifer zone.

Capillary pressure and relative permeability of water in the heated desaturated zone that forms in the initially saturated, lower-permeability soil were important elements of this study. Since the vapor pressure of any contaminant being tested was known over a range of temperatures and the contaminants’ solubilities in water were also known, less information was needed about their properties. Adsorption of the COC, although a rather weak function of temperature, was also of some interest.

7.3 Modeling methodology and results

Appendix B contains a full report on the simulation modeling done for this project. This Section 7 is intended to be a more succinct presentation of what was learned and to reiterate the research needs that we presented to SERDP at their request in a White Paper on the subject dated August 2007.

7.4 Lessons learned from the current research

7.4.1 Validation of the numerical model with 2D-experimental data

The results of 2D and 3D heating experiments carried out during the project were matched. The first STARS modeling used within this SERDP project was to model the 2D experimental data presented in Sections 5.2 and 6.2. The temperatures predicted for one of the 2D experiments were compared with the corresponding physical data in Figure 1. In this simulation of an 8.5-cm wide by 1-m long by 0.74-m high physical model (“2D flume”), the capillary pressure adjacent to the 240-W heater was the most important parameter because the resulting wicking of water toward the heater prevented drying of the soil around the heater. Anisotropy in saturated hydraulic conductivity (K_h/K_v) was also important. Note that the cells in these flume simulations are very small (approximately 20 cm³ pore volume) compared to the larger cells (940 cm³ pore volume) in the 3D tank model. Thus, numerical dispersion was smaller in the 2D simulation, and it proved necessary to use a higher capillary pressure to maintain realistic temperatures at the heaters since capillary pressure drives the heat pipe effect (Udell and Fitch 1985) that cools the heaters. The geometry of the 2D experiment was also very important because the looser packed and possibly coarser soil at the top of the model apparently allowed preferential movement of fluids (and heat) towards the left side of the box. Overall, the match obtained between simulated and observed data for the various 2D experiments was considered good.

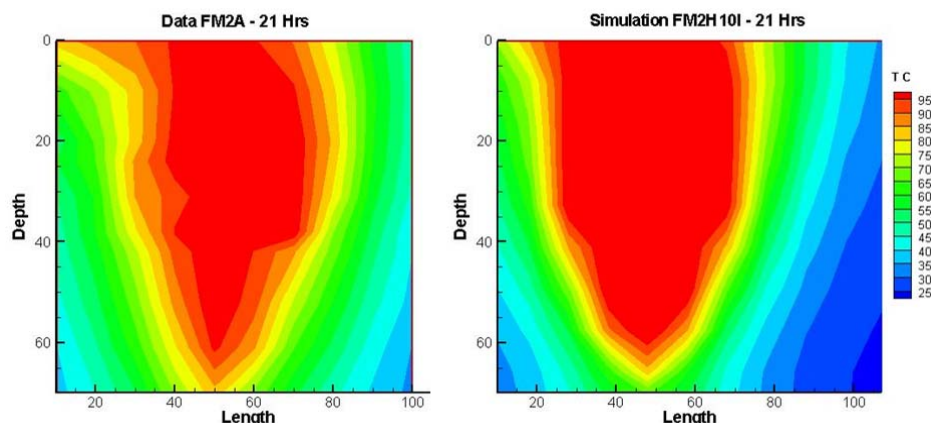


Figure 60: Temperature in the 2D, Fine Sand (3×10^{-2} cm/s) Heat Transfer Experiment at 21 Hours, 240 W, $K_h/K_v=4.0$. Physical Model is at left; Simulation at right.

7.4.2 Application of the numerical model to analyze the 3D heat transport processes

As reported in Appendix B, we also extensively modeled the earlier 3D heat-transfer experiments in the original setup described in Sections 5.3 and 6.3 (6 m x 6 m x 4.5 m high; 1-m thick intermediate fine sand layer, $K_s=10^{-3}$ cm/s between upper and lower coarse sand layers each 1.5-m thick, $K_s=10^{-1}$ cm/s; four 1.2 kW heaters). A prediction of the temperature and gas velocity distribution from one of the first simulations conducted in 2006 is shown in Figure 2. This figure shows that the maximum temperature in the model is 216°C, and that the gas-velocity vectors shown as arrows in the figure extend throughout the model. The temperature of 216°C means that portions of the model in the heated zone are dry since the temperature will not exceed that defined by the vapor pressure of water if liquid water is present. The gas vectors at the bottom of the tank indicate that free gas (mostly air with some water vapor) is present in this cool zone.

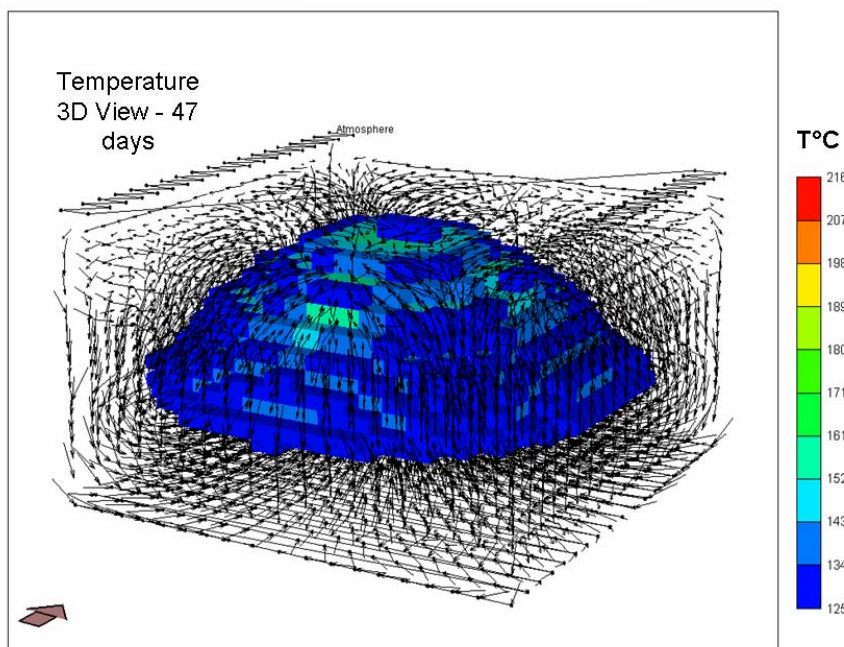


Figure 61: Early Temperature Prediction for 4.5-m 3D Heat Transfer Experiment in the Original Setup.

The temperatures and implied saturations shown in Figure 2 can be compared with the temperature and saturations reported in Figure 3 by *VEGAS* for the physical experiment. The results in that figure show that the temperatures are much lower, that the water table was allowed to drop slowly as water was evaporated from the tank, and is 1.75 m from the bottom of the tank after 100 days before the water table was raised again.

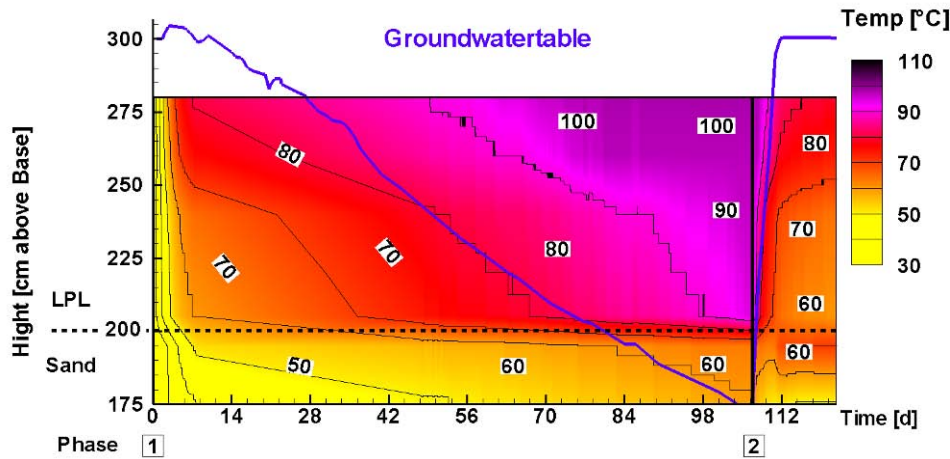


Figure 62: Progression of Temperature Data Recorded in 4.5-m 3D Heat Transfer Experiment in the Original Setup (at Profile 2, just outside the square heater pattern). LPL = Lower Permeability Layer, here a fine sand.

After over 100 simulations of this 3D experiment we began to understand why differences occurred between the initial prediction of results and the actual experimental data:

1. Lower power input caused by the controllers on the heaters. The actual power input was approximately one-half of the maximum power that the heaters could have delivered.
2. In 3D simulations with coarser grid cells, the end point of the drainage capillary pressure curve cannot be set as high as in the 2D simulation, because numerical dispersion also has the effect of moving water towards the heaters. Thus, the lesson learned from the earlier 2D flume simulations in a sense had to be unlearned for the 3D model with larger grid cells.
3. Another new technique was developed in these simulations. In earlier models of TerraTherm projects, cells were larger and often the permeability was lower. The heaters could be treated as a heat source in the continuous porous media. Now, primarily due to the higher permeability of the lower-permeability soil layer that is the subject of these experiments, cross flow of water prevents high temperatures at the heater and the heaters tend to operate at full power. This was corrected in the model by enclosing each heater in an impermeable metal canister (as they actually are in reality). Now, energy input into the model can be more accurate, and the flow of fluids and modification by capillary pressure and relative permeability can be studied.
4. The K_h/K_v of the soil in the 3D tank could be lower than that determined by history matching the 2D flume experiments.

After making these modifications, the water levels and temperatures recorded in the experiment were more closely modeled. Again, as noted above, the capillary pressures of both the high- and lower-permeability soils were the factors that controlled movement of water into the heated zone and therefore the temperatures in that region.

The heat lost at the boundaries and surface of the tank, although artifacts of the experimental apparatus, also proved important to model. In our initial proposal, we postulated that the meter-scale of the 3D experiments would enable heat losses at the boundaries to be minimal compared to experiments in a smaller-scale apparatus. While we found them to indeed be small, they cannot be ignored. Most simulations that also matched the temperature and saturation profiles lost over 20 percent of the power input to the tank through convection to the atmosphere and conduction into surrounding tanks. All of this heat is lost by conduction through the sides and sealed top of the box and then by convection into the atmosphere or into an adjacent tank. The temperature increases at the metal walls of the tank exposed to the laboratory space were approximately 1.6 to 1.7°C; the increase was 15°C at the sealed top of the tank and 5°C at the wall of a neighboring (filled) tank.

Figure 4 illustrates the complexity of the flow field and temperature distribution in the original setup of the 3D container experiments. Figure 4 shows that the heated zone ($> 30^{\circ}\text{C}$) reaches to the top of the tank but does not reach the sides or bottom of the tank. However, mass and energy are predicted to be circulating through the vadose zone (and also the remainder of the saturated zone) in the mobile gas and water phases. Since the temperature in one-half of the tank is being displayed, only half of the soil vapor extraction (SVE) wells but all of the air-inlet pipes are visible. Air is drawn into the tank by the SVE wells, but gas circulates wherever a gas phase has been created by heating or imbibition. Thus, convection dominates heat transfer as it eventually does in all but low-temperature ISTR projects, and capillary pressure prevents drainage of water from the lower-permeability soil.

After history matches of the temperature distributions of the 2D flume experiments were achieved, the temperature in a 3D heat transfer experiment was predicted. Input data such as heater power and capillary pressure data were assumed, because no measured data were available at that stage of the project. As illustrated in Figure 2, those temperatures were too high. Figure 5 compares an early temperature prediction with the prediction of temperature from a later simulation whose water saturation distribution is shown in Figure 6. In the early simulation the temperature rose quickly and the region near thermocouple T4240 (2.4 meters from the bottom between heaters) quickly exceeded 100°C . Due to the discrepancy between predicted and measured temperatures, the numerical model was validated sequentially. In the subsequent improved model, the temperature did not rise quite as quickly, and water took almost two months to boil. For this example, the two largest differences between the two simulations are that the heater power declined steadily in the later simulations (about 50 percent of the maximum heater power was actually used because we learned that it had been reduced by the heater controllers in the experiment), and the capillary pressure of both the lower- and high- permeability soil were less than half of that used in the earlier simulation. In addition, the capillary pressure-saturation data for most of the experimental materials, which became available after the initial simulations, facilitated the determination of the effect of capillary pressure in the experiment.

Typical vertical water-saturation distributions at the start of a simulation and after 70 days of heating are shown in Figure 6. The nominal bottom of the vadose zone is initially at 3.0 meters, but the water saturated zone extends some distance above that due to capillary rise. After heating for 70 days, water had imbibed from the underlying, high-permeability soil region (aquifer) into the higher-capillary-pressure, lower-permeability soil layer.

The nominal, final water level in the experiment is approximately 1.5 meters from the base in the center of the tank. This is below the level reported for the experiment at that time (2.1 meters at the edge), but the water level measured near the wall of the tank is slightly higher because the internal pressure in the center of the tank is slightly raised by the energy added by the heaters. This pushes water towards the walls and raises the pressure at the bottom of the tank. The higher pressure is reflected in higher measured water levels in external gauges.

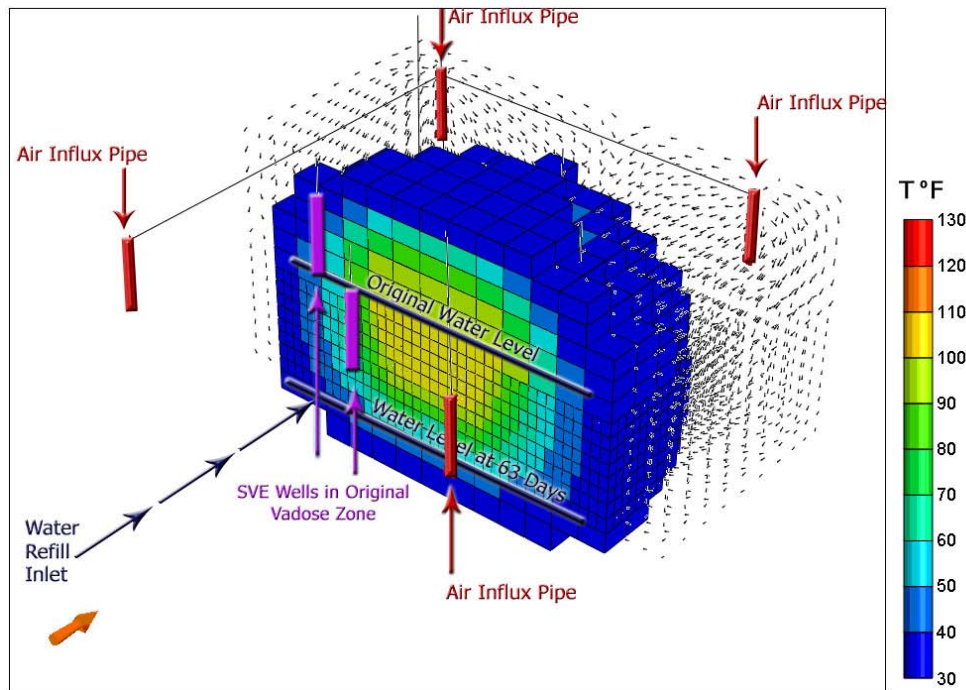


Figure 63: 3D Cross-Sectional View of the Temperature Distribution at 63 Days in the 3D Heat Transfer Experiment in the Original Setup, with Gas-Velocity Vectors. “SVE Wells in Original Vadose Zone” Refers to the Conditions Studied by Hiester et al. 2002.

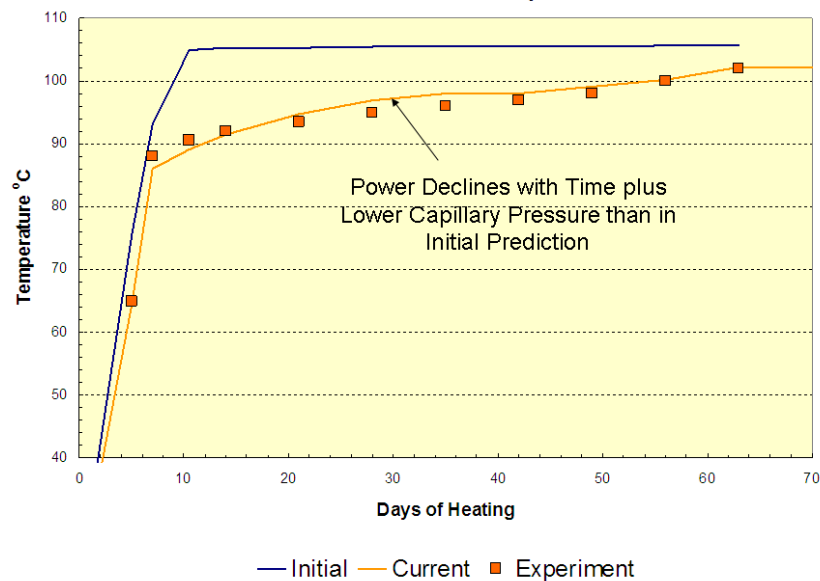


Figure 64: Comparison of the Measured Temperature at Thermocouple T4240 with an Early Simulation (“Initial” Prediction) and the Result from the Validated Model (“Current” Prediction) for the 3D Heat Transfer Experiment in the Original Setup.

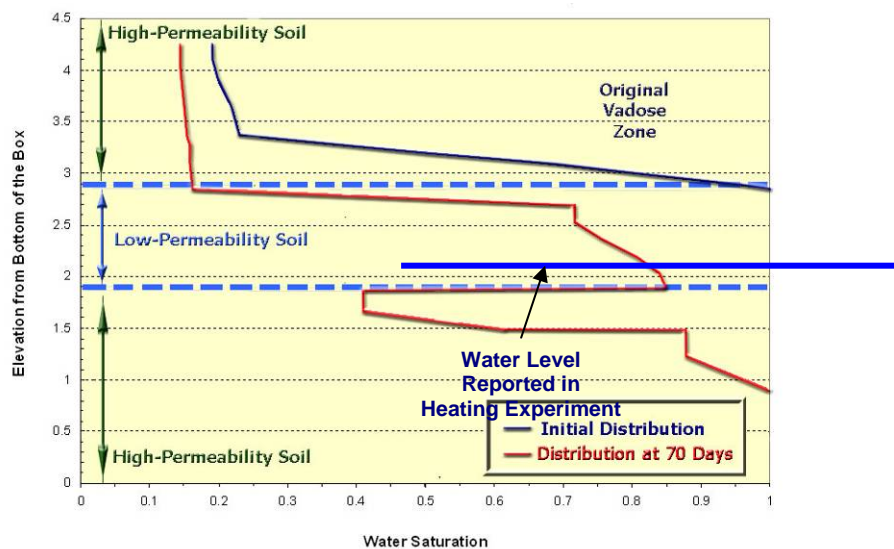


Figure 65: Water Saturation Distribution, Initially and after 10 Weeks of Heating in the 3D Heat Transfer Experiment in the Original Setup.

7.5 Summary of the numerical model validation

While differences still exist between experimental observations and predictions over a range of parameters, the following controlling phenomena have been identified:

- a) capillary pressure causes imbibition into higher capillary pressure regions such as the lower-permeability soil and near the heaters;
- b) the water saturations are nearly level; and
- c) gas moves freely throughout the enlarged but cooler unsaturated zone. Removal of the COC from a cooler zone will occur much more slowly and therefore condensation within such zones should be avoided.

Table 1 evaluates the relative importance of the variables that affect temperature and water distribution in the heating experiments and their possible effect on remediation.

Table 10: Effect of Several Variables on Heating and Remediation during TCH

Provisional Ranking of the Different Factors:

++, + (very high, high) importance; o moderate; - of minor importance; x no effect;

?? uncertain, subject to future research;

NA ranking unavailable due to small scale

Factor of Importance		Variable and Main Effect	Comments / Explanations
2D small scale	3D large scale		
++	++	Heater Power – declines as the tank heats up when controller maintains constant (e.g., 500°C) heater temperature	Most important – controls rate of water evaporation
+	+	Length and Position of Heaters relative to the Target Treatment Zone (TTZ); Distance between the Heaters	Energy density and heater geometry control where heat is delivered to each layer.
+	+	Isothermal Capillary pressure for water and air in lower-permeability soil – draws water from aquifer	Important – controls dispersion of fluids. A general difficulty and challenge for this research is that the P_c-S_w function decreases with increasing temperature. This effect must be factored into the numerical models, even if no measurement data will be available.
NA	o	Capillary pressure in higher permeability soil – resists imbibition from aquifer, but may enable upward unsaturated flow of water to vadose zone to replace water lost by evaporation	Low high-end capillary pressure for the higher perm. soil slows drop of water level by reducing upward unsaturated flow to the vadose zone. Perhaps of higher relevance to specific field applications with stratified layers of permeable soil (low to moderate thickness) within a low permeable matrix.
??		Non-isothermal and three-phase NAPL impacts on the capillary pressure-saturation description	Measurement of these parameters was beyond the scope of this research. The fundamental research and process understanding is incomplete, because it is not of widespread interest. A general difficulty and challenge for this research was that the parameters needed to characterize the effects of these processes had to be predicted / estimated, because no measurement data were available.
o	o	Air flux at SVE wells – Air can potentially circulate through the entire model if gas-filled pathways become interconnected	Might not want excessively high gas flux, since supply of water to generate steam in-situ can aid remediation of DNAPLs – must be recorded since gas flux increases with time.
+	+	K_h/K_v of the soils - controls drainage rate of water	2D: Important for the prediction of the temperature distribution 3D: Low K_h/K_v promotes dispersion of COC and delays or accelerates remediation under aquifer influxes. A general difficulty and challenge for this research was that it had to be predicted / estimated, because typically no measurement data were available.

Factor of Importance		Variable and Main Effect	Comments / Explanations
2D small scale	3D large scale		
++ to +	o to -	Heat Loss at boundaries – Highest at the top of the tank; smaller with high-gas flux because more energy is consumed by evaporation. Also smaller on sides with adjacent tanks than on sides exposed to the atmosphere. Very small with increased aquifer influx.	Least important in 3D – although losses at the walls of a tank increase with low gas or water flux.
NA	+	Impact of the groundwater flux in the underlying aquifer on the heat front distribution in the layer of lower permeability	3D: Expected to be an important factor for numerical simulations
-	??	Impact of gas migration from the lower perm. layer into the aquifer on the remediation success / NAPL migration	2D: Unimportant due to scale 3D: Occurs when water level is low; expected that it may be an important factor for numerical simulations
-	??	Incomplete remediation / remaining NAPL in the subsurface (unsaturated zone, aquitard, aquifer) / “polishing” concepts	2D: Unimportant due to scale 3D: Under specific conditions, might be a factor to be discussed.
-	??	Impact of kind of NAPL and/or mass of NAPL on the remediation success	Impact on remediation time and downward migration behavior under specific conditions expected
-	??	Impact of initial NAPL location on the remediation process and success	Affects the time needed to move the vaporized NAPL to the SVE wells
NA	??	Impact of adsorption (K_d) on the processes	Typically, in the absence of organic debris, adsorption is an order of magnitude smaller than other factors.
NA	??	Impact of potential gas bubble formation on water saturations during moderate heating	Question from interaction with R.L. Johnson’s SERDP Project
-	??	Change of contaminant distribution in the subsurface during remediation	Affects the volume in the subsurface within which contaminants migrate (undesirable if beyond the boundaries of the TTZ).
-	??	Impact of mass recovery on the ongoing heat front propagation	
Factor of Importance		Variable and Main Effect	Comments / Explanations

2D small scale	3D large scale		
	??	Change of saturation in the former saturated and unsaturated zones	Controlled by aquifer flow. Important factor to characterize the changes in flow behavior in the liquid and gaseous phases. Impact on the prediction of the remediation processes and remediation success was studied.
+ to ++	+ to ++	Impact of the conceptual model design on the reliability of the simulation results with respect to prediction of heat front propagation, remediation progress and remediation success	Impact of 2D- or 3D-model, size of grid cells, reproduction of heater, etc.
??	??	Impact of numerical dispersion on the reliability of the simulation results with respect to prediction of heat front propagation, remediation progress and remediation success	
x	x	Resistivity of porous media	Not applicable to TCH, since electric current flows only through heating element, not through soil.

7.6 Application of the numerical model to predict the remediation behavior in the large container remediation experiments

By March 2007, the 3D containers had been emptied of their previous contents and refilled with new contents (see Section 5.5), which can be described as follows: Smaller Container: 6 m x 3 m x 4.5 m high; 1.5-m thick intermediate silty layer, $K_s=10^{-5}$ cm/s between upper and lower fine sand layers each 1.5-m thick, $K_s=10^{-3}$ cm/s; four 1.5 kW heaters; and Larger Container: 6 m x 6 m x 4.5 m high; 1.5-m thick intermediate very fine sand layer, $K_s=10^{-4}$ cm/s between upper and lower coarse sand layers each 1.5-m thick, $K_s=10^{-1}$ cm/s; four 1.5 kW heaters. Originally we proposed to proceed with remediation experiments in the newly refilled containers; however, as we explained at the 2007 IPR, we did not have enough confidence in the ability of the simulations to predict the 3D remediation experiments, and thus we proposed to proceed with additional 3D heat-transfer experiments in the newly set up containers first. The number and wattage of the heaters just listed pertain to those additional heat-transfer experiments.

The observations reported in the previous section suggested that a successful (rapid removal of 99.99 percent of the contaminant) remediation experiment in any 3D container with these relatively small dimensions will occur only when the water flux conditions in the underlying aquifer are such that undesired migration of the steam front into the aquifer is prevented. It appeared that a water flux through the tank of 2 m³/day would be needed for an array of four heaters with average individual heater power of 1.8 kW. If less power were used, less water flux would be needed. This is somewhat an artifact of the experimental conditions, because if this set of conditions were encountered in the field, TerraTherm would elect to combine TCH for heating the lower permeability zone, with Steam-Enhanced Extraction (SEE) for heating the underlying aquifer zone, and the latter would have to be designed to incorporate a sufficient multiphase extraction rate to ensure that COC vapors could not condense in clean zones. However, the 3D experimental setup used in this project (i.e., the refilling described above) was designed to test TCH alone, with the possibility that future experimentation could be done in combination with SEE (although beyond the scope of ER-1423). Given this experimental constraint, it was predicted that remediation success in the context of this

project would not depend primarily on permeability, or heat loss to the aquifer, important as they may be, but rather on preventing the water level in the tank from falling below the position of the DNAPL infiltration/storage lens. A vaporizable contaminant can move freely in the gas phase and will condense at the edge of the heated regions, given the chance. This is what the simulations suggested, although as mentioned the reliability of the predictions remained uncertain.

Simulations of TCE removal from a high permeability ($K_s=10^{-2}$ cm/s) DNAPL infiltration/storage lens placed within lower permeability ($K_s=10^{-4}$ cm/s) soil were then conducted. The 1-m thick, lower-permeability soil layer was positioned between two $K_s=10^{-2}$ cm/s sand layers, similar to the original 3D setup (Hiester et al. 2002). As noted previously, the initial water level was 3 m from the base of the tank and the lower-permeability layer started 2 m from the base. Figure 7 illustrates the distribution of TCE remaining in a simulation of the 4.5-m-deep tank after 20 days of heating. It was predicted that 42 g (0.2 %) of the original 20 kg of TCE would remain in the tank.

The residue shown was invariably predicted to be located at the edge of the heated zone. In this simulation with 2 m³/day of aquifer flow, the condensation boundary was 1 m from the edge and approximately 2.5 m from the bottom of the tank. The residual TCE condensed at the edge of the saturated zone (no gas velocity vectors mean there was no gas) where the temperature was less than 70°C. Thus, in the absence of groundwater controls in the aquifer zone inside the tank, maintaining a water level within the lower-permeability soil layer was predicted to be very useful in relatively small-scale 3D experiments like these, because it prevents the unsaturated zone from expanding into the cooler underlying aquifer, and therefore limits how far the relatively volatile TCE can propagate in the gas phase. Before these simulations, this was not intuitively obvious. This high water level is typically provided by nature in field-scale projects where water flows in from the side of the heated zone, i.e., there is water flow at the lateral boundaries of the field-scale projects, but not in a tank experiment unless intentionally induced.

It should be clear that the success of remediation experiments like those in this project is very much dependent on prior simulation and planning of the operational procedures for the experiment. Thus, key parameters such as capillary pressure of the actual soils used and the actual values of the power applied at the heaters should be known very well. Actual values of gas extracted at the SVE wells and the best estimates of K_h/K_v are also necessary to minimize the number of simulations needed to understand the remediation process. A simulator like STARS can predict what happens in a flow field when a specific amount of energy or gas is used, but might not predict the amount of energy or gas flow as accurately as they can be measured. Fortunately, at the water influx levels under which the experiment appeared likely to be most successful, the heaters would be at full power, making the heat input within short experiments relatively easy to quantify.

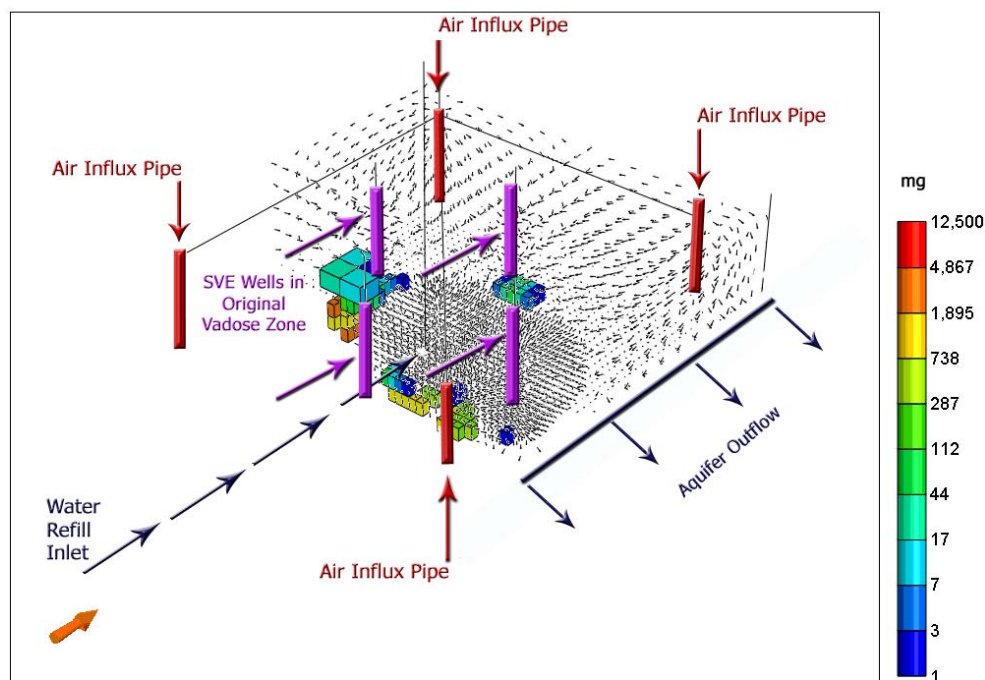


Figure 66: Milligrams of TCE Remaining after 20 Days in 3D Aquifer Influx Simulation in the Original Setup. “SVE Wells in Original Vadose Zone” refers to the conditions studied by Hiester et al. 2002, not to the water level conditions examined during the simulation.

7.7 Context of the additional large-scale container heat transfer experiments

Simulations performed in 2007 predicted that for the conditions modeled, successful remediation experiments would occur only when the gas front did not move down into the top of the aquifer below the lower-permeability layer, i.e., when water influx remained above a specific level determined by the permeability and capillary pressure in the model. Thus, it was seen as essential that those parameters and both the heat input and losses from the tanks be known accurately in order to be certain what aquifer flow would be needed. To help model this, an additional heat transfer experiment was performed within the each of the new 3D setups, wherein the aquifer influx was adjusted in steps while the temperatures and saturations were measured during each step. It was felt that once those simulations had been successfully completed and modeled, the optimum operating conditions of the subsequent experiments could be predicted with more certainty.

7.8 Proposed additional simulations and data

In the 2007 White Paper, we stated that significantly more effort would be needed to understand what occurred in the earlier heat-transfer experiment in the original setup since distributions of fluids and the temperature had not been exactly matched. In addition, the additional heat-transfer experiments in the new setup with step-wise adjustments in the aquifer influx would need to be modeled. After that, we indicated that the 2D remediation experiments conducted by VEGAS would need to be revisited. Finally, the several proposed 3D remediation experiments would need to be modeled before being conducted and also history matched after they had been performed. We indicated that additional data collection should include measurements of capillary pressure-saturation curves for the high-permeability soils in the experiments, which were not measured in the earlier round of

analytical work. SERDP did not, however, elect to fund this additional proposed level of simulation or analytical effort.

7.9 Need for additional experimental data to improve the process understanding and validation of the numerical model

As outlined above, the inputs that are required for a 3D simulation include accurate water-air capillary pressure-saturation data, accurate power input data as well as flow rates of all outlet streams. The simulator then predicts the saturation, temperature and compositional distribution, which are compared to actual measurements. Enough temperature and saturation data were taken from the tank during the heat transfer experimentation, but it was pointed out in the 2007 White Paper that additional pressure data would be desirable, especially at the bottom of the tanks since this is a check on the water level that is measured externally. The internal pressure in the heated zone of a tank is generally slightly higher than atmospheric. This higher pressure can raise the apparent water level in a sight gauge or external overflow and can even drive more fluid through the outlet of the tank than expected from simple gravimetric overflow. In addition, temperature monitoring in the adjacent tanks that may or may not also be undergoing heating is important (the large 3D tanks were not isolated). In that way, heat losses from one heated tank could be better quantified.

During the 3D remediation experiments, the same temperature data were taken, but it would also have been desirable if it were possible to measure the composition of the effluents at SVE wells and the aquifer exit at least daily. These data would have facilitated monitoring of the progress of the experiment and also closing of the mass balance on the tank. The composition of the outlet streams could then be matched; however, it should be recognized that the concentration of the COC in these streams would be expected to become very low after the bulk of the contaminant has been removed. This means that the composition and the volumetric flow rate of the outlet streams would need to be measured very accurately, more accurately than was within the project's scope. Moreover, it was apparent that the water level in the tank at the end of the experiment should be maintained as the experiment cooled down, since migration in the gas phase can disperse the COC wherever the gas can go, as emphasized above.

7.10 Additional large-scale container experiments and outcome of the simulation work

As explained above, without validated numerical models, an interpretation of the simulated prediction of the remediation processes and the remediation success is difficult due to the uncertainty of reliability in the assumptions and estimated input data. To bridge this gap, additional 3D heat transport experiments were conducted to investigate in more detail the coupled heat and mass transport processes as a function of soil permeability, groundwater flux, SVE flux and, last but not least, energy input.

The heat front propagation seemed to be more important for TCH remediation success in the saturated zone than it was for the previous 3D experiments (Hiester et al. 2002) that focused on a related TCH technology, thermally-enhanced SVE (TESVE) in the unsaturated zone. The major reason seemed to be that water boiling and steam production has to be generated within the lower permeability, initially saturated layer to enable COCs to be volatilized and extracted. This is a difference as compared to application of TESVE in the unsaturated zone, where even a semi-heated unsaturated soil would enable an increase of COC mass extraction.

Furthermore for the application of TCH in a saturated aquitard layer, the increase of mobility of the DNAPL phase due to the reduction of surface tension and viscosity will not in most cases be a sufficient enhancement of a pump-and-treat system to justify liquid phase DNAPL removal alone. For any significant degree of remediation, vaporization of the DNAPL is essential. In lower permeability layers that injected steam cannot readily heat, in-situ steam production is required, as with TCH.

At the time that the 2007 White Paper was issued, it was expected that propagation of the steam front within the former saturated zone, as governed by the rate of groundwater flux through the container, in turn would determine the remediation outcome. In contrast to the original proposal, in which we had proposed to move directly into the remediation experiments in the new setups, we justified performing additional 3D heat transport experiments in each of the new setups (i.e., the larger and the smaller container) as essential to quantify this dynamic relationship between steam propagation and groundwater flux, and to enable a validation of the numerical models. We felt that with these validated models for each of the two containers, the outcome of the remediation experiments could be predicted with more confidence. Unlike the remediation experiments themselves, we imposed a series of differing boundary conditions in a step-wise sequence during each of the additional heat-transfer experiments, varying the heater power, groundwater flux and potentially the heater spacing in stages. This extended the overall duration of the heat transfer experiment and the effort commensurately, but produced much more information as a result than would have been produced from conducting a single remediation experiment. This work led us to conclude that contrary to earlier predictions, steam did not in fact significantly propagate into the former saturated zone during low aquifer flow conditions (see Sections 6.7 and 6.8).

As explained within the 2007 White Paper, the scope of work within ER-1423 did not include enough of a level of effort for simulation modeling to set up, validate and run models for all the scenarios tested in the experimental program, let alone many others of interest for the technology transfer document. Nevertheless, SERDP did not elect to provide additional funds to expand the simulation modeling program, so it remains incomplete and a subject for further research efforts. Appendix B presents in full detail the simulation modeling that was accomplished during this project.

7.11 Conclusions of the simulation modeling

Several heating and remediation experiments were modeled as part of SERDP project ER-1423. The results (see [Appendix B](#)) show the following:

1. Capillary pressure is the most important variable affecting both heating and remediation experiments because it controls imbibition of water into the aquitard and vadose zone, and migration of the DNAPL into cooler or hotter regions of the tanks.
2. The capillary pressures used in these models are lower than the capillary pressures measured for the aquitard material because numerical dispersion in the simulations has the same affect on movement of water as does capillary pressure.
3. Dilation of freshly packed, unconsolidated sand appeared to be very important in the flume experiment because the evaporation rates were relatively high compared to the volume of the box, but are not as likely to be important in the tank experiments because the relative heating rate is lower and expanding fluids can move into quite a large volume.

4. While PCE is vaporizing at a high rate at approximately 90°C, the models suggest it may not be due to boiling of an azeotrope, and may instead be due to steam distillation of PCE by vaporizing water. This conclusion, however, may in part be due to the absence of azeotropic behavior within the STARS code.
5. Migration of PCE was the variable that affected the remediation experiments most. Migration can be the result of
 - a. The SVE wells drawing vaporized DNAPL into cooler regions of the model where it condenses
 - b. Expansion of the steam chamber into the aquifer where the DNAPL will be flushed away by water or condensed and immobilized.
 - c. Downward movement of PCE when the upward flux of water is low. In the 2D-flume experiment the PCE migrated into a hot zone where it could be produced by steam distillation. In the small-tank 3D remediation experiment the PCE migrated laterally, due not to heating alone, but also preferential flow and a slow propagation of the steam front, after which some of the DNAPL migrated into the aquifer and was flushed away in the water.
 - d. Horizontal migration caused by high, aquifer-flushing rates into cooler regions where the only recovery mechanism can be extraction as a dissolved component in water.
 - e. Upward flushing with water into the vadose zone where the DNAPL could be stripped and produced by air drawn into the SVE wells.
6. In the tank experiments an aquifer flux of approximately 0.55 m/day (2 m³/d in a 6 m x 6 m tank) controlled most of these migration mechanisms and resulted in remediation of 90% of the PCE within two weeks.
7. The migration mechanisms listed above are mostly artifacts of the experiments conducted in this project because in field ISTD/TCH projects the SVE wells are inside the heater array and not outside it. Moreover, migration of DNAPL has invariably occurred in a time frame of years and seldom at the beginning of a remediation project lasting a few months.
8. The heat transfer in the tank experiments appeared to be strongly affected by convection of heat inside the heater cans, and 20% of the energy from the heated zone appeared to have migrated upward by this mechanism.
9. STARS proved to be a relatively robust simulator for this project. The problems encountered in this project were generally those related to history matching of poorly known variables, such as the amount of heat that conducts upward inside of the heater cans in the tank experiments or the balance between capillary forces and numerical dispersion.
10. It is clear that the grids used in these experiments were not fine enough, nor were the permeability differences between refined blocks large enough to model either the fingering of dissolved DNAPL constituents or the countercurrent fingering of DNAPL and dissolved DNAPL constituents that transferred some of the PCE into the aquifer in the small-tank-remediation experiment.

If future modeling of these experiments is conducted, it should be done with models that include geostatistically-generated permeability distributions and all that is known about DNAPL migration using more powerful computers than were available when this modeling study started.

8 Technology Transfer and Applicability Generalizations

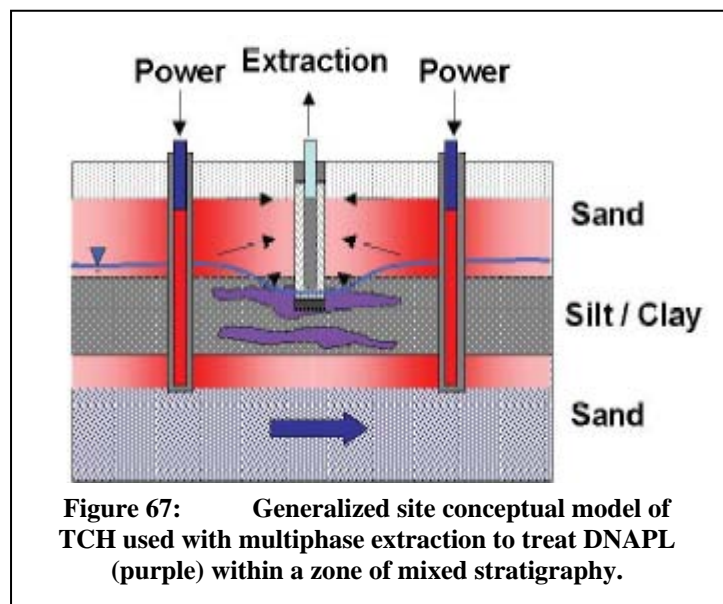
8.1 Background and Historical Context of the Study

Thermal conduction heating (TCH), which when combined with vapor extraction is termed In Situ Thermal Desorption (ISTD) came into remediation practice in the mid-1990s primarily focused on the treatment of high-boiling organic contaminants such as PCBs in soil (VINEGAR ET AL. 1997B). This type of in situ thermal treatment required attainment of target temperatures in the soil in the neighborhood of 325°C. At such temperatures, the vapor pressures of the PCBs increase by several orders of magnitude relative to ambient temperature, enabling PCBs to behave as if they were VOCs, and be readily extractable from the soil as a vapor. Five field-scale demonstrations and field-scale projects, including two at Superfund sites (SHELDON ET AL. 1996; VINEGAR ET AL. 1997) and three performed for the DoD (CONLEY AND JENKINS 1998; CONLEY AND LONEY 2000) showed this process to be very effective, consistently reducing even high concentrations of PCBs indicative of the presence of DNAPL to non-detect (STEGEMEIER AND VINEGAR 2001). The technology was considered by some to be fairly expensive, however, which imparted to TCH a reputation as being relatively costly albeit very robust.

In 1997 a Shell subsidiary, TerraTherm Environmental Services Inc. turned their attention for the first time at a manufacturing site in Portland, IN to the possibility of utilizing TCH for treatment of chlorinated solvents. They adopted a similar design approach as had been used for PCB projects, specifically to elevate the temperature in the target treatment zone (TTZ) above the boiling point of water for thorough removal of the CVOCs (VINEGAR ET AL. 1999; USEPA 2005). About two-thirds of the TTZ did in fact achieve such elevated temperatures. In the course of heating the site, however, it was found that within one sizeable portion of the thermal well field, where stone ballast beneath a former railroad line allowed the influx of perched water into the TTZ, temperatures during heating did not exceed the boiling point of water. Even so, confirmatory sampling later indicated that the CVOCs had been effectively steam-stripped from the soils, including that higher-permeability portion of the site. This result was the first indication that TCH could be used to treat CVOC-contaminated sites, including those below the water table, in much the same way that had at that time recently emerged for treatment of CVOCs using Steam-Enhanced Extraction (SEE) and Electrical Resistance Heating (ERH) (NEWMARK ET AL. 1994; GAUGLITZ ET AL. 1994).

On the basis of these developments, TerraTherm, Inc. began in 2003 to expand upon prior TCH practice to utilize TCH for remediation of CVOC sites by steam distillation at the boiling point of water. By the time that the current research project was first proposed to SERDP in 2004, TerraTherm had proven this approach at field-scale at a Confidential DNAPL site in Ohio (LACHANCE ET AL. 2004). Although each of the three treatment areas at that site consisted entirely of clayey soils, lateral recharge of perched groundwater through fractures in the clay during heating cooled the treatment zone during each of several large rain events. Subsequently, adaptive installation of supplemental heater borings enabled the remedial goals to be achieved at all three TTZs. It was recognized, however, that an influx of high-velocity groundwater could hinder, and perhaps even prevent the effectiveness of TCH as applied to treatment of CVOC sites. More recently, TCH / ISTD has been used successfully to treat numerous CVOC / DNAPL sites, including several in aquitards below the water table (LACHANCE ET AL. 2006, 2008; BAKER ET AL. 2008; BIRSCHENK ET AL. 2008; COLE ET AL. 2008; HERON ET AL. 2008; NIELSEN ET AL. 2008). This approach is gaining

acceptance as at least as effective, and cost-effective, as SEE and ERH. Notwithstanding some applications of ERH in high groundwater flux zones (USACE ET AL. 2008), guidance indicates that TCH and ERH are primarily applicable to low and moderate-permeability sites, while SEE is best suited for higher permeability aquifers (USEPA 2004; USACE 2006). Many chlorinated solvent sites, however, have TTZs that encompass low, moderate and/or higher permeability layers, a type of heterogeneity that we term “zones of mixed stratigraphy.”



Although the present study focuses on the use of TCH / ISTD by itself (Figure 67), zones of mixed stratigraphy containing CVOC DNAPLs represent a challenge to such an approach, and may better be addressed by combining In Situ Thermal Remediation (ISTR) technologies. At the Young Rainy STAR Center Area A site in Largo, FL, the presence of DNAPL in both a sandy aquifer and lower permeability clays was effectively addressed through the combined, simultaneous use of ERH and SEE (HERON ET AL. 2005). More recently, the combined use of TCH

and SEE has been successfully used at a mixed stratigraphy dry cleaning site in Denmark (NIELSEN ET AL. 2008). Today TCH / SEE combinations are in the process of being implemented at larger DNAPL sites in Santa Fe Springs, CA and Arnold AFB, TN. The empirical understanding by practitioners of when best to combine ISTR technologies versus utilize them singly is just beginning to emerge.

Commercial TCH projects tend to be designed and implemented rather conservatively to ensure success. The commercial realm of guaranteed fixed price contracting is not the place to push the margins of what is known empirically to work. Nor do commercial projects typically invite the installation of high-density monitoring networks necessary to gain an intimate knowledge of the heating process, e.g., at the scale of individual thermal wells. Nevertheless, efficiencies might well be garnered from attention to better understanding the practical limits of a given technology, as well as by being able to view its processes in greater detail.

This research project was motivated by a desire to examine, at the meter-scale, the physical mechanisms of TCH under more highly controlled conditions than exist in the field. We chose to push the limits of the applicability of TCH in aquitards, and therefore to hopefully reveal, for example, when too high a groundwater flux through an aquifer beneath a lower permeability source zone may limit the ability of TCH used alone to remediate CVOCs in aquitards. A trade-off implicit in this decision to push the limits was the possibility that the planned remediation experiments may not be “successful” from the standpoint of remediation efficiency. This was deemed an acceptable risk, as completely successful experiments might not have revealed any useful technological limits. We believed that the study could still be

deemed worthwhile if it produced knowledge not readily obtainable through either small laboratory experiments or at the field scale.

8.2 How were the study conditions selected, and how do they relate to the field-scale?

The meter-scale tanks available at *VEGAS* inspired the design of the physical experiments performed in this study. They had already been used to conduct thermally-enhanced SVE (TESVE) experiments (HIESTER ET AL. 2002; HIESTER ET AL. 2003B, HIESTER 2009). Thus the physical scale of the tanks was to a large degree predetermined. Nevertheless, during the experimental design process our research team considered and selected a number of experimental conditions and methods:

- Soil layering – For the 3D experiments, a three-layer system was decided upon early on, consisting of a coarse sand vadose zone overlying a lower permeability aquitard, in turn overlying a coarse sand aquifer. This mixed stratigraphy setting was viewed as representing a type of site potentially amenable to TCH, either alone or in combination with SEE.
- Type of soil in the lower permeability layer (LPL) – It was decided at the onset to avoid clay materials, which would be difficult to pack into the tanks uniformly. Based on experience from former experimental research (HIESTER ET AL. 2002; HIESTER ET AL. 2003B), we were able to inspire a cooperative thesis project in Sweden (MARK 2005), which examined various mixtures of available manufactured quartz flours in the fine to coarse silt size class, from the standpoint of what could practicably be mixed and handled, and what would yield repeatable results at a relatively low saturated hydraulic conductivity. Mark's work [Appendix A] led us to select the precise composition of the aquitard layers in the tank experiments.
- Elevation of the water table and velocity of groundwater flux – The water table would be near or at the top of the aquitard, representing a common case encountered at many DNAPL source areas and in plumes. The velocity of groundwater flux in the underlying aquifer would be a major experimental variable, to help elucidate the critical sensitivities of TCH to groundwater cooling.
- Method of DNAPL release – Several approaches were considered, including release into one or more pre-positioned lenses, and release via a conduit such as buried tubing. Based on experience gained during the remediation experiments conducted in the 2D flume, we selected a composite approach of two DNAPL release lenses, each with its own delivery conduit.
- Position of the DNAPL release lens or lenses (TTZ) – We decided to position two DNAPL release lenses one above the other, within the LPL (aquitard). We selected two lenses to enable discrimination of heating and removal behavior at two distinctly different types of locations: the easier-to-remediate upper portion of the aquitard, and a more challenging location near its bottom, i.e., closer to the underlying aquifer. We defined the TTZ as being the area of the aquitard encompassed by the two lenses.
- Placement of transitional GEBA (fine sand) layer around the DNAPL release lenses – This decision was made based on experience. Without such a transition layer, fines from the surrounding LPL would likely eluviate into the coarse sand DNAPL release lenses during the process of flooding the tank.
- Conditioning of the DNAPL release lenses – To avoid entrapment of gas bubbles within the DNAPL release lenses during initial water flooding of the tanks, they were

filled with CO₂ prior to very slowly raising the water table. This practice had been used in the 2D flume experiments with good success.

- Amount of DNAPL release – We made this decision based on calculations and simulations of how much DNAPL would need to be released to help ensure detection and facilitate chemical analysis over the life of an experiment of reasonable (1-3 months) duration.
- Number, position (horizontal and vertical) and power of the thermal wells relative to the TTZ – In large part we based this decision on the earlier TESVE experiments, which had utilized a square array of four heaters (i.e., to honor the symmetry in the rectangular tanks). We considered this to represent a reasonable although not very robust base case. Simulations and the results of the first HTE confirmed that the selected spacing and power would be feasible, i.e., it would heat the selected TTZ to boiling within several weeks.
- Position of SVE wells and extraction rate – These were a carry-over from the earlier TESVE experiments at VEGAS, with a focus on measurement and understanding of subsurface processes during operation of TCH in the saturated zone in the absence of vapor recovery means in the saturated zone. Of course, placement of the vadose zone SVE wells outside the heater array, while consistent with the earlier TESVE experiments, is not standard ISTD field practice.
- Number, type and position of monitoring and sampling devices – These were to some degree also a carry-over from what had worked and had been proven practical during the earlier TESVE experiments. An exception was the addition of porous cup samplers for liquid or gas samples, which afforded the ability to better track contaminant transport within the aquitard and aquifer zones during heating.

Our experimental design team recognized that few of the selected conditions mentioned above could be accurate representations of field conditions. It was apparent to us that the experimental set-ups were physical models, not reality. SERDP Scientific Advisory Board members asked whether or not the selected method of controlled DNAPL release would resemble the aging seen in field contamination settings. We replied that an implementation of these effects in the model design was simply not possible within the constraints of time available.

In several crucial respects, the physical model selected for the large tank experiments differed significantly from “usual” field site conditions as follows:

- Field TCH sites are never heated with only a single square array of four thermal wells. In the field, pilot tests usually require a minimum of 7 to 12 heater borings. In addition, in field practice triangular heater arrays are the norm, and when operated at typical levels of heater power are approximately 10% more efficient than rectangular arrays (STEGEMEIER 2000). Nevertheless, we felt that a square array would better fit and mirror the rectangular geometry of the VEGAS tanks, enabling symmetry to be honored in monitoring, visualization, and simulation work. Our choice of a single square array was a balance between resorting to an overly bullet-proof design, with for example an octagonal array, and the risk of possibly under-heating the TTZ with too few thermal wells.
- In field practice, thermal wells are always placed so as to fully surround the known, delineated limits of the target treatment zone. This ensures that all portions of the TTZ achieve the treatment temperature, and prevents unwanted contaminant mobilization. Here, we knowingly put the system at risk of possibly facilitating

DNAPL mobilization, in exchange for testing the limits of the technology under the tested groundwater flow rates and DNAPL release conditions.

- In the field, we design thermal wells to extend 1 to 1.5 m beneath the bottom of the delineated limits of the TTZ. This ensures that the bottom of the TTZ between heater borings is adequately heated, and prevents condensation of vapors in cool locations or unwanted mobilization. Once again, we pushed the limits in the tanks by extending the heating elements only 0.7 m below the bottom of the lower DNAPL release lens.
- Vapor extraction wells in field sites typically pull gases from within the heated zone, either by means of co-located heater and vapor recovery wells, or by means of multiphase extraction wells, which remove liquids and gas. Reliance on these approaches helps ensure the full recovery of mobilized contaminant vapors and steam, and prevents unwanted condensation of contaminants in cool locations. Here, however, we adopted an SVE design in the overlying vadose zone that had been used in VEGAS's earlier TESVE experiments, largely to facilitate comparison with the earlier experimental results. Furthermore, the experimental set-up enabled measurement of process data impacted only by TCH and GW flow in the saturated zone. The absence of SVE impacts within the saturated aquitard layer enabled us as well to utilize simpler numerical models.
- Finally, and perhaps most importantly, whereas in the field a robust approach for a mixed stratigraphy zone such as the one being represented would compel us to select a combination of TCH across the aquitard and SEE focused on the underlying aquifer, here the funded experimental approach was limited to TCH, with acknowledgement by the Scientific Advisory Board and Thermal Technical Advisory Committee (TAC) that combining TCH and SEE would be considered as a subject of possible future research. Thus, in the 3D remediation experiments we chose to purposely expose the limitations of TCH as a single technology to a degree that we assiduously avoid in field remediation practice.

8.3 What have we learned, and with what limitations?

8.3.1 General Observations and Caveats

- ❖ Both opportunities for successfully applying TCH within the saturated zone and the limitations inherent in doing so were shown through this work.
- ❖ It would be a mistake to conclude from the results of the remediation experiments that TCH applied at the field-scale to aquitard layers in source zones or plumes results in incomplete remediation of DNAPL, or promotes its uncontrolled mobilization. As explained in the preceding bulleted list, experienced ISTR practitioners employ a degree of design conservatism that intentionally avoids exposing the limitations of the thermal technology being used. For the same reason, however, a better understanding of the boundaries between safe and risky practices is not often deliberately obtained through field projects. In this R&D project, however, we purposefully adopted sets of conditions bracketing the safe and risky application of TCH, to systematically attempt to discover critical design parameters.
- ❖ Large tank experiments have inherent advantages and disadvantages.
 - + *Advantages* include the ability to examine mesoscale (i.e., well-scale) processes in a layered, quasi-realistic setting. For example, they allow us to study how heat moves out three-dimensionally from thermal wells, and more specifically the shape that a steam front takes as it progresses within layers of

different permeability during heating including breakthrough to extraction points. They allow us to quantify various effects such as the effect of different levels of groundwater flux on heating. They allow calculations of mass and energy balances.

- *Disadvantages* include the artificial nature of the physical model setting. It is not possible to replicate field conditions during a tank-filling operation. The soil mixtures differ in a number of ways from field soils. Indeed, the huge effort required to install soil and instruments in a 53 or 106 m³ laboratory tank means that repeated experiments are costly and time-consuming, constraining the number of experiments that can be performed. The hundreds of instruments and monitoring points that we install to enable the collection of data on a close grid also may have a tendency to interfere with or affect the very phenomena being studied (analogous to how the Heisenberg Uncertainty Principle operates at the quantum level). Thus one must exercise caution in extrapolation of tank data to field practice.
- ❖ Simulation modeling, like experiments with physical models, has inherent pluses and minuses. Here we focus on the use of 3D, multiphase, multicomponent, non-isothermal models as employed in this study.
 - + *Advantages* include the ability to run many simulations in the time required to do a few large tank experiments or one field trial. The cost to run many such simulations is far less. The effects of individual parameters can be isolated, permitting sensitivity analyses to be carried out that provide insights into the nature of physical phenomena. Models can be calibrated to measured conditions, lending them some degree of credibility as predictive tools, especially with regard to heat transfer.
 - *Disadvantages* include the great complexity of the type of simulation models utilized. The number of grid blocks, although large, is inevitably limited by the computing time and power available. Numerous values have to be selected to parameterize the models, and in some cases the values have to be taken from the literature (e.g., capillary pressure-saturation relationships) instead of being derived from measured properties of the media being studied. In other cases the values have to be inferred, because they have seldom been measured anywhere (e.g., three-phase flow parameters as functions of temperature, especially near boiling). In addition, the models adopt a random distribution of soil properties within each layer to represent realistic heterogeneities of packing, whereas in reality the physical conditions are different. Numerical dispersion, which is a mathematical phenomenon, at times has a greater effect on results than advective dispersion. These and other limitations are inherent in numerical models.

8.4 TCH Applicability Generalizations and Design Guidance

The following summarizes the main lessons learned, and guidance for future field applications of thermal technologies for DNAPL sites.

8.4.1 Delineation of the DNAPL Source and Target Treatment Zone

As the tank experiments have shown, it is important to understand the conceptual site model and the DNAPL distribution before completing a thermal design. The site conditions that governed the migration and final DNAPL architecture prior to remediation will also affect the migration of other fluids such as water, air and steam, and thereby impact the thermal design.

For a proper TCH application, the following must be known with relative certainty:

- The top of each DNAPL zone.
- The bottom of each DNAPL zone.
- The perimeter of each contaminated zone that exceeds the clean-up criteria.

Often the cleanup criteria are in the range of 1 mg/kg, which for TCE and PCE corresponds to soil concentrations two orders of magnitude lower than the concentrations where residual DNAPL is present (100-300 mg/kg). This provides some degree of safety for the designer – if the target treatment volume is larger than the DNAPL area, the risk of leaving DNAPL outside of the treatment zone is small.

The proper delineation of the DNAPL distribution requires a substantial amount of data. Screening-level methods such as Membrane Interface Probe (MIP) are well suited for generating a site-wide picture of the contaminant distribution. Typically, MIP or similar methods can be used to narrow in on the target treatment volume, and soil and groundwater sampling can be used to verify the overall pattern and levels of contamination indicated by the screening-level data.

8.4.2 Selection of the Most Appropriate Heating Technology for a Site

The most critical factors controlling the ability to heat a site to the target temperatures are:

- Groundwater flow, which can lead to cooling where water enters the treatment volume. Each design must address the potential for groundwater influx and cooling. In certain clay formations, permeable fractures can lead to rapid groundwater flow and cooling, as observed at a site in the Midwest U.S. (LACHANCE ET AL. 2004). Other sites with groundwater zones with significant flow rates may be addressed either by limiting the flow using pumping or barriers, or by combining TCH with the injection of steam to heat the more permeable zones (BAKER AND HERON 2004).
- Air inflow due to the applied vacuum, leading to cooling. This is typically very minor due to the low heat capacity of atmospheric air, and the modest flow rates.
- Target zone geometry (very shallow sites and irregularly shaped sites take longer due to large surface areas and heat losses, whereas deep sites and equi-dimensional sites heat faster due to lower heat losses).

Each thermal design involves a careful review of the geometry, and specifically the hydrogeology and potential impacts of water flow on the heating regime. Where needed, a detailed 3D numerical simulation is used to evaluate impacts and worst-case scenarios.

For TCH, heating depends primarily on thermal conduction – therefore the “sweep” is highly uniform. Clay layers, sand zones, and gravel zones heat up at very similar rates due to small variations in thermal conductivity (varying by a factor of only approximately three from sand to clay) and heat capacity of various minerals, sediments, soils, and rocks. This is the primary advantage of TCH – that the heating pattern and therefore treatment duration is highly

predictable. This allows the treatment performance (as determined by reduction in contaminant concentrations) to be highly predictable as well, provided the design is adequate.

A potential disadvantage is the inability to heat a zone from which groundwater flow can carry heat away or that can be cooled through entry of cold water. As discussed above, such cooling has to be either limited by means of a barrier (hydraulic or physical), overcome by injecting steam into the highly conductive zones, or overcome by adding more TCH heaters to increase the power density in such zones. A good and detailed analysis of the site hydrogeology is key to managing this potential disadvantage. Figure 68 illustrates a TCH-SEE combination used for a site in Denmark for thermal treatment at a PCE DNAPL site (HERON ET AL. 2009). There, TCH was the only heating method deemed appropriate for the tight clays under the building, and SEE was used to treat the top of the aquifer below it, and to provide a heated bottom of the clay layer. This was used to prevent condensation of PCE near the bottom of the clay. The project was completed successfully in 2008, without any signs of PCE spreading. It should be noted that the contamination indicated in the sand/gravel aquifer outside of the target treatment zone is being addressed by pump-and-treat.

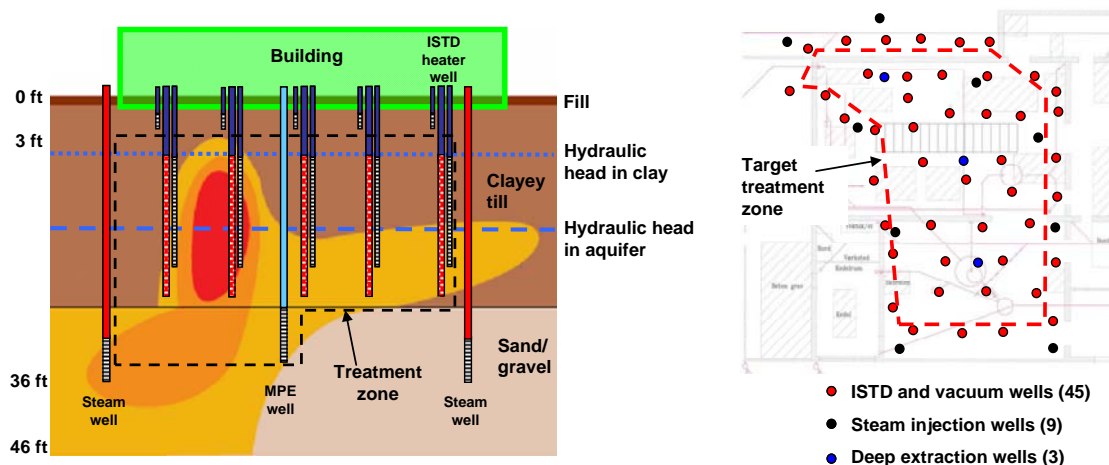


Figure 68: Example TCH-SEE Combination used at the Knullen Site in Denmark.

Each site is analyzed in detail, and the heating, vapor and water recovery approach is determined based on site-specific conditions.

8.4.3 Prevention of DNAPL Condensation in Unwanted Places

As the physical experiments in this project have shown, high concentrations of CVOCs in the steam formed and migrating during TCH can, under certain circumstances, lead to condensation of DNAPL at the steam front. Such condensation could potentially deposit DNAPL in places that were not contaminated before the treatment started, if the field design did not properly account for the risk.

This points to the following guidance for field design and implementation:

- Properly investigate the maximum depth of DNAPL impact before determining the treatment depth and heating method.
- Apply energy to the layers that are suspect for DNAPL condensation, such that they are heated to a temperature higher than the eutectic point for the DNAPL-water mixture. This will effectively prevent condensation in those layers. In practical terms,

this means heating the zone below the DNAPL (between 1 to 2 m thick) such that vapors cannot condense at depth, heating the clean perimeter around the DNAPL source such that vapors cannot condense around the target zone, and preventing condensation in the zone above the DNAPL treatment zone by addition of energy into the layer above it.

- Ensure that the generated steam can migrate freely to recovery points, and apply sufficient vacuum to extract the steam at the rate it is generated (i.e., don't allow the steam to "push" outward). In practical terms, this may include installation of vertical or horizontal vapor recovery wells, application of a permeable vapor plenum under the insulated cover, and/or installation of sand packs around heaters to facilitate upward flow of hot vapors during heating. In addition, vapor extraction systems must be designed with extra capacity, such that a proper vacuum and flow is maintained at all times. Typically, the vacuum system has a backup power supply as well, preventing substantial down-time in case of line power outages.
- At permeable sites with high DNAPL saturations, co-injection of air with steam, and injection of air to create flushing of the heated zone may be considered. The air will flow through the heated zone, and carry CVOCs towards extraction points. The theory behind air injection during thermal projects is described by GERDES and coworkers (1998) and KASLUSKY AND UDELL (2002). The capture of the injected air is essential for effective capture of the CVOCs; therefore such injection should be used when the pneumatic properties of the formation are well understood.

Figure 69 shows an example of a CVOC DNAPL source zone in a silt and clay formation, with TCH heaters extending both above and below the DNAPL source zone. At this site, eight separate DNAPL source zones were treated to near non-detect concentration, without any signs of DNAPL condensation or spreading.

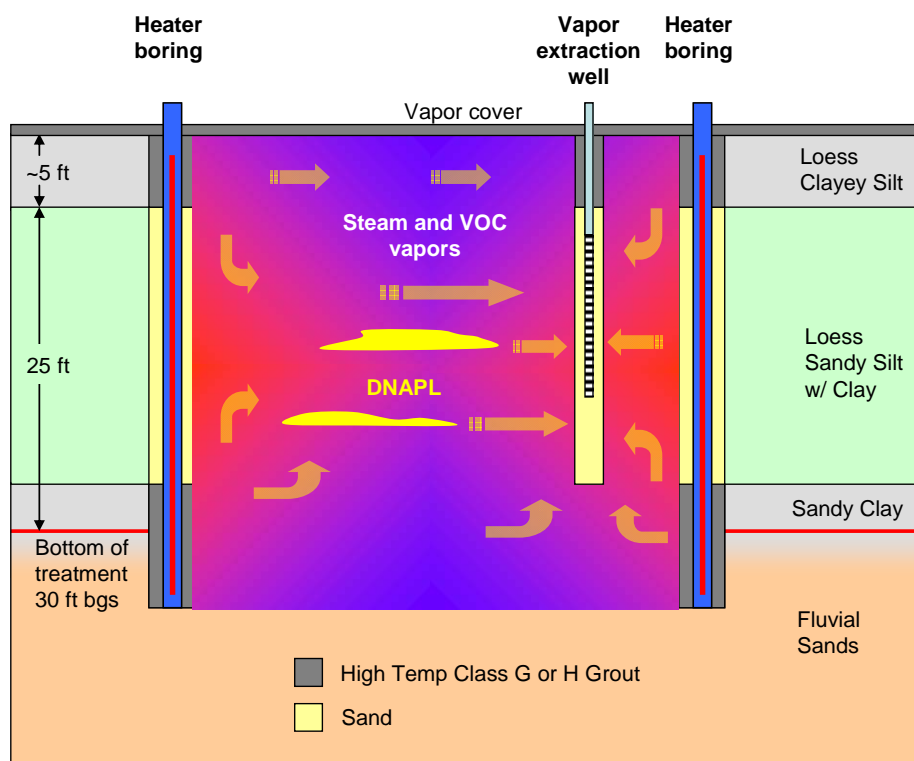


Figure 69: Example TCH Design with Heating Below the Zone of DNAPL Impact (HERON ET AL. 2009).

For shallow DNAPL sites, heating all the way to the surface may be necessary to prevent DNAPL from condensing at shallow depths. A vapor cover is typically used for such sites. The cover serves three purposes:

1. It provides thermal insulation and prevents contaminants from condensing near the land surface, which will occur if the soil is cool.
2. It prevents rainwater infiltration, which could lead to unwanted cooling of the treatment zone.
3. It provides a vapor seal and increases the radius of influence of the vapor extraction screens.

These elements should be included in the design of thermal treatment systems. A vapor cover was included in the project referenced above (Figure 69).

Sites that pose more than an average challenge are the following:

- DNAPL sites where there is not a clear capillary barrier that arrested the vertical migration. At such sites, the permeability of the layers below the DNAPL may be sufficient to allow convective steam flow at a significant rate. If DNAPL depletion, rather than capillary forces, arrested the downward migration of DNAPL, the concentration would be expected to be relatively modest. This may reduce the risk of further spreading of the DNAPL downward, since the steam generated will be dominated by water vapor, and the CVOC concentration may be modest.
- Sites with highly unpredictable hydrogeology, such as fractured clay or bedrock. Such sites pose challenges even in terms of characterization and determination of the treatment area and depth. As guidance, a thermal design should include heating and treatment of a buffer zone around the known DNAPL source in order to minimize the risk of condensation on the perimeter, top and bottom.

TerraTherm is implementing several field projects currently, with great attention to these lessons, and to the potential implications of insufficient data and improper design. Among them are an ESTCP-funded demonstration of TCH for treatment of DNAPL in fractured rock at the former Naval Air Warfare Center (NAWC) site, W. Trenton, NJ, project ER-0715.

8.4.4 Utility and Economic Feasibility

While it is beyond the scope of this project to provide a comprehensive evaluation of economic aspects, it is germane that over the five years since the initial proposal for ER-1423, ISTD / TCH has been applied at over a dozen field-scale CVOC sites, most of which addressed TTZs that included moderate to low permeability media below the water table. All met or exceeded their goals. Typical turnkey unit costs (including design, permitting, fabrication, mobilization, drilling, construction, provision of all equipment and labor, installation, startup, operations, demobilization, reporting and power) of these more recent projects have ranged from \$75 to \$150/cubic yard for sites with TTZs of >15,000 cy, and from \$100 to \$250/cubic yard for sites with TTZs of 1,000 to 15,000 cy. Most were performed under guaranteed fixed-price contracts, and in many cases were awarded after competitive bidding with bids also received from other ISTR vendors.

A recent completed project of particular relevance to the DoD is the application of ISTD / TCH at Defense Depot Memphis, a former Defense Logistics Agency site under the Base

Realignment and Closure Program (BRAC). The project was funded by the U.S. Air Force Center for Engineering and the Environment (AFCEE). At Memphis Depot, Memphis, Tennessee, TerraTherm, under contract to e²M treated eight separate treatment zones totaling 49,800 cy simultaneously in less than 175 days of heating. Pretreatment concentrations indicative of DNAPL were reduced to post-treatment concentrations below 0.1 mg/kg for CVOCs, meeting the stringent target criteria. The overall turnkey cost, including oversight and sampling, was \$79/cy (HERON ET AL. 2009).

Defense Depot Memphis, TN received the 2009 Secretary of Defense Environmental Award – the only one awarded in the Environmental Restoration category. The use of thermally-enhanced SVE was cited as “a key component of the program’s success”. “In addition to meeting the established goals ahead of schedule, the process saved taxpayers more than \$2.5 million.” (DEFENSE LOGISTICS AGENCY 2009).

Renewable forms of electric power can be utilized in ISTD projects if desired. Reliable and rapid achievement of remedial goals, facilitating reuse of underutilized property and/or restoration of valued groundwater resources is inherently sustainable.

In closing, ISTD / TCH is now a commercially available, proven and cost-effective ISTR technology worthy of the DoD and DOE’s consideration for treatment of CVOC sites in a wide variety of geologic settings, including aquitards. Use of TCH and SEE in combination, as is being currently being designed for use at Arnold Air Force Base, Tullahoma, Tennessee, may be a desirable option at CVOC sites with mixed stratigraphy, e.g., with lower permeability aquitard layers well-suited to treatment with TCH, and highly transmissive aquifer zones amenable to treatment with SEE.

9 Conclusions

- ❖ During this research, dominating processes, those of more minor importance, and even small-scale effects could be identified. The process understanding of the application of TCH in the saturated zone was significantly improved.
- ❖ As occurs with application of TCH for remediation of VOCs in the unsaturated zone, steam distillation is the major dominating process (OBJECTIVE 1). It is helpful that the process of steam distillation (co-boiling of water and NAPL) first occurs at temperatures below 100°C, e.g., below the boiling point of either pure water or pure PCE. Consequently, contaminants present as a separate phase have already vaporized by the time that steam production due to boiling of water in the initially water-saturated aquitard layer begins.
- ❖ Nevertheless, an efficient NAPL recovery from the saturated zone by an overlying SVE system requires not only vaporization of the NAPL but also development of one or more contiguous flow paths via which the gaseous phase can travel towards and reach the unsaturated zone and the SVE recovery wells. It follows that steaming of the water within the aquitard in the given large 3D physical models, which occurs at about 100°C (depending on pressure), is important in enabling the desired migration of gaseous NAPL constituents into and through the unsaturated zone for recovery.
- ❖ The generation of steam at a given location during the experiments was significantly affected by the energy intensity (a function of heater power and spacing), soil permeability, depth below the GW level and the cooling effect caused by the GW flux, as especially exemplified by 3D remediation experiment 1 (OBJECTIVE 2).

- ❖ Furthermore, the extent of lateral versus vertical steam zone propagation is mainly affected by: (a) site-specific conditions such as anisotropy, presence of preferential flow paths and capillary pressure - saturation relations; (b) heater system design factors such as aspect ratio (i.e., the ratio of heater length to heater spacing), the number of heaters and their lateral and vertical positioning relative to the TTZ, and (c) vapor recovery system design factors such as the position of SVE wells and specifically their filter screens, negative pressure exerted and recovery rate (especially for filter screens in the former saturated zone).
- ❖ The recovery of contaminant vapors emanating from a previously saturated aquitard layer through placement of SVE wells only in the unsaturated zone is possible. For field applications, extension of the SVE recovery system into the LPL (aquitard) is often recommended to accelerate the remediation process, even though energy losses from the LPL will be higher.
- ❖ Condensation of vaporized contaminants at the steam front results in longer remediation times. To minimize formation of this condensate, the heater array must fully encompass and surround the TTZ. This requires adequate site characterization prior to design. A certain amount of condensate is transported by the so-called Heat-Pipe effect (UDELL AND FITCH 1985) as liquid phase back into the steamed zone.
- ❖ For a given level of heater power, the higher the soil permeability the greater will be the cooling effect of GW flux, and thus achieved temperatures will be lower at steady state conditions (OBJECTIVE 2).
- ❖ For the given power and spacing of the heater wells relative to the position of the NAPL, a high GW flux limits the lower expansion of the steamed zone indicating that NAPL located close to the boundary between water saturated aquitard and aquifer may not be recovered (OBJECTIVE 3) without implementation of combined remedies (e.g., TCH and SEE).
- ❖ The experimental results indicate that advanced numerical simulations would be very helpful to predict steam front propagation, temperature distribution and DNAPL recovery. The accuracy of input data such as geological / hydrogeological information, soil parameters, and contaminant distribution, however, affect simulation results. In some respects, predictions gleaned from numerical simulations proved of value to process understanding; in other respects they differed from the experimental results.
- ❖ Advanced simulations are needed to answer very specific questions in detail. Lack of basic knowledge, however, such as the impact of temperature on three-phase parameters prevents numerical results from being of sufficient reliability. Further research is needed to improve the results by a better application of some (small-scale) effects of interest.
- ❖ Nevertheless, we learned that the model design itself can affect the overall results of the simulations. As an example, recognition of heat transfer within the heater cans and the degree of anisotropy were discovered to have a significant impact on the results, e.g., of the temperature distribution and therefore on all interrelated processes.
- ❖ Both the temperature distribution in the large-scale containers and production rate of vaporized PCE were modeled well.
- ❖ Capillary pressure and DNAPL relative permeability were the most important variables controlling heating of the containers and migration of the DNAPL.
- ❖ Migration of PCE from the DNAPL-release lenses was not predicted well.
- ❖ The capillary pressures used in the simulations were significantly lower than measured capillary pressures because numerical dispersion in simulations affects movement of fluids in the same way as capillary pressure does.

- ❖ To facilitate future simulations, it is useful to bear in mind that many flow, transport and remediation effects can be anticipated with no more than an accurate prediction of the temperature distribution. Therefore, researchers who follow us may do well to focus on the quantification of those factors that affect heat transport. By doing so, reliability of numerical simulations may be improved.

10 References

- ATKINS, P.W. 1988. *Physikalische Chemie*. VCH Verlagsgesellschaft, Weinheim, 1. edition. ISBN 3-527-25913-9
- BAEHR, H.D. AND K. STEFAN. *Heat and Mass Transfer*. Springer Verlag, Berlin Heidelberg, 1998. ISBN 3-540-63695-1.
- BAKER, R.S., GALLIGAN, J.P., MCLAUGHLIN, H., SEMENAK, R., POLOGRUTO, M.P., AND K.R. WEEKS. 2001. *In-Situ Thermal Destruction Treatability Study of Explosives-Contaminated Soil from Massachusetts Military Reservation*. In: Proceedings of the Fourth Tri-Service Environmental Technology Symposium, 18-20 June 2001, San Diego, CA.
- BAKER, R.S. AND G. HERON. 2004. “*In-Situ Delivery of Heat by Thermal Conduction and Steam Injection for Improved DNAPL Remediation*.” Paper 2B-18, in: A.R. Gavaskar and A.S.C. Chen (Eds.), *Remediation of Chlorinated and Recalcitrant Compounds—2004*. Proceedings of the Fourth International Conference on Remediation of Chlorinated and Recalcitrant Compounds (Monterey, CA; May 2004). ISBN 1-57477-145-0, Battelle Press, Columbus, OH.
- BAKER, R.S. AND M. KUHLMAN. 2002. “*A Description of the Mechanisms of In-Situ Thermal Destruction (ISTD) Reactions*.” In: H. Al-Ekabi (Ed.), *Current Practices in Oxidation and Reduction Technologies for Soil and Groundwater*, ORTs-2, Toronto, Ontario, Canada, Nov. 17-21, 2002.
- BAKER, R.S., J.C. LACHANCE, M.W. KRESGE, R.J. BUKOWSKI, AND J.P. GALLIGAN. 2004. “*In-Situ Thermal Destruction (ISTD) of MGP Waste in a Former Gasholder: Design and Installation*.” Proceedings of Gas Technology Institute’s Natural Gas Technologies II Conference, Phoenix, AZ, Feb. 8, 2004.
- BAKER, R.S., J.C. LACHANCE, G. HERON, U. HIESTER, H.-P. KOSCHITZKY, O. TRÖTSCHLER, A. FÄRBER, AND M. KUHLMAN. 2006. “*DNAPL Removal from the Saturated Zone using Thermal Wells*.” *Remediation of Chlorinated and Recalcitrant Compounds: Proceedings of the Fifth International Conference* (May 22-25, 2006). Battelle, Columbus, OH.
- BAKER, R.S., D. TARMASIEWICZ, J.M. BIERSCHEK, J. KING, T. LANDLER AND D. SHEPPARD. 2007. “*Completion of In-Situ Thermal Remediation of PAHs, PCP and Dioxins at a Former Wood Treatment Facility*.” 2007 International Conference on Incineration and Thermal Treatment Technologies (IT3), May 14-18, 2007, Phoenix, AZ. Air & Waste Management Association, Pittsburgh, PA.
- BAKER, R.S., J.M. BIERSCHEK, J. LACHANCE, J.P. GALLIGAN, D. TARMASIEWICZ, G. HERON AND W.R. LEACH. 2008. “*Why In Situ Thermal Desorption Can Be the Most Cost-Effective Remediation Method for Many Sites*.” Paper N-003, in: Bruce M. Sass (Conference Chair), *Remediation of Chlorinated and Recalcitrant Compounds—2008*. Proceedings of the Sixth International Conference on Remediation of Chlorinated and Recalcitrant Compounds (Monterey, CA; May 2008). Battelle Press, Columbus, OH.

BAUER, B., TAUBNER, H., AND R. TIPPKÖTTER. 2001. *Messung der mechanischen und hydraulischen Verdichtungsfähigkeit von bindigen Substrate mit einem verbesserten Proctorversuch*. Wasser & Boden, 53/6, pp. 27-29.

BERGSMAN, T., J.S. ROBERTS, D.L. LESSOR, AND W.O. HEATH. 1993. "Field test of six-phase soil heating and evaluation of engineering design code." In R.G. Post (ed.). Working Towards a Cleaner Environment. Symposium on Waste Management at Tucson, AZ. WM Symposia, Inc., Tuscon, AZ, February 28-March 4: 861-865.

BEZIAT, A., DARDAINE, M. AND V. GABIS. 1998. "Effect of Compaction Pressure and Water Content on the Thermal Conductivity of some Natural Clays." Clay and Clay Minerals , Vol.36 No.5, pp. 462-466.

BIERSCHENK, J.M., J. LACHANCE, J. GALLIGAN, G. HERON, D. TULLY, A.-M. KOZLOWSKA AND S. LANGFORD. 2008. "Thermally Enhanced Soil Vapor Extraction Closing DNAPL Sites - Case Studies." Paper P-012, in: Bruce M. Sass (Conference Chair), Remediation of Chlorinated and Recalcitrant Compounds—2008. Proceedings of the Sixth International Conference on Remediation of Chlorinated and Recalcitrant Compounds (Monterey, CA; May 2008). Battelle Press, Columbus, OH.

BLUME, H.-P.: *Handbuch des Bodenschutzes*. Landsberg/Lech, ecomed Verlagsgesellschaft, 1990.

BUETTNER, H.M., AND W.D. DAILY. 1995. "Cleaning contaminated soil using electrical heating and air stripping." Journal of Environmental Engineering, August: 580-589.

BUSCH, K.-F., LUCKNER, L., AND K. TIEMER. 1993. *Geohydraulik*. Gebrüder Borntraeger Berlin Stuttgart 3. neubearbeitete Auflage.

CHIOU, C.T., KILE D.E., AND MALCOM, R.L. 1998. "Sorption of vapors of some organic liquids on soil humic acid and its relations to partitioning of organic compounds in soil organic matter." Environ. Sci. Technol., 22 (3), pp. 298-303, Washington, DC.

CHOWN, J.C., KUEPER, B.H., AND D.B. MCWHORTER , 1997. "The use of upward hydraulic gradients to arrest downward DNAPL migration in rock fractures." Journal of Ground Water, Vol. 35, No. 3, pp. 483-491.

COLE, J., W.J. MCELROY, J. GLASGOW, G. HERON, J. GALLIGAN, K. PARKER AND E.F. DAVIS. 2008. "In Situ Thermal Treatment of Trichloroethene at Marshall Space Flight Center." Abstract P-032, in: Bruce M. Sass (Conference Chair), Remediation of Chlorinated and Recalcitrant Compounds—2008. Proceedings of the Sixth International Conference on Remediation of Chlorinated and Recalcitrant Compounds (Monterey, CA; May 2008). Battelle Press, Columbus, OH.

CONLEY, D.M., AND K. JENKINS. 1998. "Application of ISTD to Remediate PCBs from Soil at the Former Mare Island Naval Shipyard, Vallejo, CA". Presented at the 3rd Annual Tri-Service Conference, San Diego, CA, August 15-17, 1998.

CONLEY, D.M., AND C.M. LONIE. 2000. "Field Scale Implementation of In Situ Thermal Desorption Thermal Well Technology." pp. 175-182. In: G.D. Wickramanayake and A.R.

Gavaskar (eds.) Physical and Thermal Technologies: Remediation of Chlorinated and Recalcitrant Compounds. Battelle Press, Columbus, OH.

CONLEY, D.M., K.S. HANSEN, G.L. STEGEMEIER, H.J. VINEGAR, F.R. FOSSATI, F.G. CARL, AND H.F. CLOUGH. 2000. "In Situ Thermal Desorption of Refined Petroleum Hydrocarbons from Saturated Soil" pp. 197-206. In: G.D. Wickramanayake and A.R. Gavaskar (eds.) Physical and Thermal Technologies: Remediation of Chlorinated and Recalcitrant Compounds. Battelle Press, Columbus, OH.

CRC 2008. *Handbook of Chemistry and Physics*. CRC Press, Taylor & Francis Group, 89th edition, 2008

DAVIS, E.L. 1997. *How Heat Can Enhance In-Situ Soil and Aquifer Remediation: Important Chemical Properties and Guidance on Choosing the Appropriate Technique* USEPA/540/S-97/502, U.S. Environmental Protection Agency, Washington, USA, April 1997.

DAVIS, E.L. 1998. *Steam Injection for Soil and Aquifer Remediation*. US EPA Issue paper EPA/540/S-97/505.

DAVIS, E.L. 2003. *Steam injection treatability studies for wood treater contaminants*. USEPA National Risk Management Laboratory, Ada, OK. Draft Environmental Research Brief. September.

DAVIS, E.L., G. HERON AND J. LACHANCE. 2006. *Does Field Data Show Downward Mobilization of DNAPL during Thermal Treatment?* Poster paper presented at Remediation of Chlorinated and Recalcitrant Compounds—2006. Fifth International Conference on Remediation of Chlorinated and Recalcitrant Compounds (Monterey, CA; May 2006).

DEFENSE LOGISTICS AGENCY, 2009. DLA Press Release dated 4/27/2009, available at http://news.yahoo.com/s/usnw/20090421/pl_usnw/former_memphis_depot_wins_a_secretary_of_defense_environmental_award.

DELLE SITE A. 2001. *Factors Affecting Sorption of Organic Compounds in Natural Sorbent-Water Systems and Sorption Coefficients for Selected Pollutants. A Review*. J. Phys. Chem. Ref. Data, Vol. 30, No. 1, 2001

DEVOE, C. AND UDELL, K.S. 1998. "Thermodynamic and Hydrodynamic Behavior of Water and DNAPLs during Heating," Proceedings from the First Conference on Remediation of Chlorinated and Recalcitrant Compounds, pp 61-66, Monterey CA.

DIAMOND, S. 1971. "Microstructures and Pore Structures of Impact Compacted Clays." Clays and Clay Minerals, Vol. 19, pp. 239-249.

DIN 18125. 1986. *Bestimmung der Dichte des Bodens*, Beuth Verlag.

DIN 18127. 1993. *Proctorversuch*, Beuth Verlag.

DVWK. 1994. *Grundwassermessgeräte*. DVWK-Schriften 107, Bonn, Kommissionvertrieb Wirtschafts- und Verlagsgesellschaft Gas und Wasser.

EARTH TECH AND STEAMTECH. 2003. *Site 61 Treatability Study Report, Steam Injection. Northwest Main Base, Operable Unit 8*. Draft report submitted to US Air Force Flight Test Center, Environmental Restoration Division, Edwards AFB, California.

FETTER, C.W. *Contaminant Hydrology*. Prentice Hall, Simon & Schuster, New Jersey, USA, 1993. ISBN 0-02-337135-8.

GABENER, H.-G. 1983. *Untersuchungen über die Anfangsgradienten und Filtergesetze bei bindigen Böden*. Grundbau und Bodenmechanik, Heft 6, Universität-Gesamthochschule Essen.

GABERELL, M., A. GAVASKAR, E. DRESCHER, J. SMINCHAK, L. CUMMING, W.-S. YOON, AND S. DE SILVA. 2002. "Soil Core Characterization Strategy at DNAPL Sites Subjected to Strong Thermal or Chemical Remediation." in: A.R. Gavaskar and A.S.C. Chen (Eds.), *Remediation of Chlorinated and Recalcitrant Compounds—2002*. ISBN 1-57477-132-9. Battelle Press, Columbus, OH.

GAUGLITZ, P., J. ROBERTS, T. BERGMAN, R. SCHALLA, S. CALEY, M. SCHLENDER, W. HEATH, T. JAROSCH, M. MILLER, C. EDDY-DILEK, R. MOSS, AND B. LOONEY. 1994. *Six-Phase Soil Heating for Enhanced Removal of Contaminants: Volatile Organic Compounds in Non-Arid Soils*. Integrated demonstration, Savannah River Site. Report No. PNL-10184, UC-406. Pacific Northwest Laboratory, California, USA.

GERDES, K. S., S. KASLUSKY AND K.S. UDELL. 1998. "Containment of Downward Migration of DNAPLs During Steam Enhanced Extraction." *Nonaqueous Phase Liquids Remediation of Chlorinated and Recalcitrant Compounds*. Battelle Press, Columbus, OH.

HANSEN, K.S., D.M. CONLEY, H.J. VINEGAR, J.M. COLES, J.L. MENOTTI, AND G.L. STEGEMEIER. 1998. "In Situ Thermal Desorption of Coal Tar." *Proceedings of the Institute of Gas Technology/Gas Research Institute International Symposium on Environmental Biotechnologies and Site Remediation Technologies*. Orlando, FL, December 7-9, 1998.

HEIBROCK, G. 1996. *Zur Rissbildung durch Austrocknung in mineralischen Abdichtungsschichten an der Basis von Deponien*. Ruhr-Universität Bochum, Institut für Grundbau, Heft 26.

HELMIG, R.. *Multiphase Flow and Transport Processes in the Subsurface*. Springer-Verlag, Heidelberg, 1997. ISBN 3-540-62703-0.

HELMIG, R., H. CLASS, A. FAERBER, AND M. EMMERT. 1998. "Heat transport in the unsaturated zone - comparison of experimental results and numerical simulations." *Journal of Hydraulic Research*, Vol.36, 1998, No.6.

HERON, G., R.S. BAKER, J.M. BIRSCHENK AND J.C. LACHANCE. 2006. "Heat it All the Way - Mechanisms and Results Achieved using In-Situ Thermal Remediation." Paper F-13, in: Bruce M. Sass (Conference Chair), *Remediation of Chlorinated and Recalcitrant Compounds—2006*. Proceedings of the Fifth International Conference on Remediation of Chlorinated and Recalcitrant Compounds (Monterey, CA; May 2006). ISBN 1-57477-157-4, published by Battelle Press, Columbus, OH.

HERON, G., R.S. BAKER, J.M. BIERSCHEK AND J. LACHANCE. 2008. "*Use of Thermal Conduction Heating for the Remediation of DNAPL in Fractured Bedrock.*" Paper P-003, in: Bruce M. Sass (Conference Chair), Remediation of Chlorinated and Recalcitrant Compounds—2008. Proceedings of the Sixth International Conference on Remediation of Chlorinated and Recalcitrant Compounds (Monterey, CA; May 2008). Battelle Press, Columbus, OH.

HERON, G., CARROLL, S AND S.G. NIELSEN. 2005. "*Full-Scale Removal of DNAPL Constituents using Steam Enhanced Extraction and Electrical Resistance Heating.*" Ground Water Monitoring and Remediation, 25(4): 92-107.

HERON, G., CHRISTENSEN, T.H. AND C.G. ENFIELD. 1998A. "*Henry's Law Constant for trichloroethylene between 10 and 95 C.*" Environmental Science and Technology , 32 (10), 1433-1437.

HERON, G., CHRISTENSEN, T.H., HERON, T. AND T.H. LARSEN. 1998C. "*Thermally enhanced remediation at DNAPL sites: The competition between downward mobilization and upward volatilization.*" In Proceedings of the First International Conference on Remediation of Chlorinated and Recalcitrant Compounds, May 18-21, Monterey, CA. Battelle Press, 1(2), pp. 193-198.

HERON, G., LABRECQUE, D. AND H. SOWERS. 2000. "*Steam Stripping/Hydrous Pyrolysis Oxidation for in-situ remediation of a TCE DNAPL Spill.*" In Proceedings of the 2000 Battelle Conference on Chlorinated and Recalcitrant Compounds, Monterey, CA, Volume C2-5 pp. 149-156. Battelle Press, Columbus, OH.

HERON, G., K. PARKER, J. GALLIGAN, AND T.C. HOLMES. 2009. "*Thermal Treatment of Eight CVOC Source Zones to Near Non-Detect Concentrations*". Submitted to Ground Water Monitoring and Remediation, February 2009.

HERON, G., H. STEFFENSEN, S.G. NIELSEN AND H. SKOU. 2009. "*Combined Steam and Conductive Heating for a PCE DNAPL Site.*" Poster presented at the Nineteenth Annual AEHS Meeting and West Coast Conference Soils, Sediments and Water, San Diego, Ca, March 9-12, 2009.

HERON, G., VAN ZUTPHEN, M., CHRISTENSEN, T.H. AND C.G. ENFIELD. 1998B. "*Soil heating for enhanced remediation of chlorinated solvents: A laboratory study on resistive heating and vapor extraction in a silty, low-permeable soil contaminated with trichloroethylene.*" Environmental Science and Technology , 32 (10), 1474-1481.

HIESTER, U. 2009. *Technologieentwicklung zur In-situ-Sanierung der ungesättigten Bodenzone mit festen Wärmequellen*, Mitteilungen Heft 178, Institut für Wasserbau, Universität Stuttgart, Diss. 2008, ISBN 3-933761-82-8.

HIESTER, U., H.-P. KOSCHITZKY, O. TRÖTSCHLER, A. FÄRBER, R.S. BAKER, J.C. LACHANCE, G. HERON, AND M. KUHLMAN. 2006. "*Thermal Well Operation in the Saturated Zone – New Options for DNAPL Remediation.*" Proceedings of the International Symposium and Exhibition on the Redevelopment of Manufactured Gas Plant Sites (MGP2006), Reading, England, April 4-6, 2006. Journal of Land Contamination and Reclamation, 14(2):615-619.

HIESTER, U. AND G. SCHMID. 2004. *Entwicklung von temperatur- und schadstoffbeständigen TDR-Sonden zur Sättigungsmessung bei der Thermischen In-situ Sanierung THERIS*, Sonderheft Wassertechnologien.

HIESTER U., V. SCHRENK, AND T. WEISS. 2003. "Environmental Balancing of 'Cold' SVE and Thermally Enhanced Soil Vapor Extraction – Practical Support for Decision Makers." pp. 2253-2262. In O.Uhlmann (Ed.), *Conference Proceedings: 8th International FZK//TNO Conference on Contaminated Soil (ConSoil 2003)*. 12-16 May 2003, Ghent, Belgium. <http://www.consoil.de>

HIESTER U., T. THEURER, A. WINKLER, AND H.-P. KOSCHITZKY. 2002. "Large-Scale Experiments to Develop a Thermally Enhanced Remediation Technology." Paper 2E-12. In A.R. Gavaskar and A.S.C. Chen (Eds.), *Remediation of Chlorinated and Recalcitrant Compounds—2002*. ISBN 1-57477-132-9. Battelle Press, Columbus, OH.

HIESTER, U., THEURER, T., WINKLER, A. AND H.-P KOSCHITZKY. 2003A. *THERIS: Sanierung der ungesättigten Bodenzone mittels fester Wärmequellen*, Symposium Ressource Fläche und VEGAS - Statuskolloquium 2003, Schrenk, V., Batera, K. Barczewski, B., Weber, K. & H.-P. Koschitzky, Institut für Wasserbau, Universität Stuttgart, 9/2003. - Nr.: 124 – pp 173-183.

HIESTER U., T. THEURER, A. WINKLER, H.-P. KOSCHITZKY AND A. FÄRBER. 2003B. "Technical Scale Investigations for the In Situ Remediation of Low Volatile Contaminants by Thermal Wells." pp. 3539 -3549. In O.Uhlmann (Ed.), *Conference Proceedings: 8th International FZK//TNO Conference on Contaminated Soil (ConSoil 2003)*. 12-16 May 2003, Ghent, Belgium. <http://www.consoil.de>.

HÖTZL, C. 1998. *Optimierung einer TDR-Apparatur zur Untersuchung der dielektrischen Relaxation von H₂O, D₂O und wässrigen Tetraalkylammonium-bromidlösungen*. Regensburg, Universität, naturwissenschaftliche Fakultät IV Chemie und Pharmazie, Diss.

HUNT, J.R., N. SITAR, AND K.S. UDELL. 1988A. "Nonaqueous phase liquid transport and cleanup 1. Analysis of mechanisms." *Water Resources Research* 24, no. 8: 1247-1258.

HUNT, J.R., N. SITAR, AND K.S. UDELL. 1988B. "Nonaqueous phase liquid transport and cleanup 2. Experimental Studies." *Water Resources Research* 24, no. 8: 1259-1269.

IMHOFF, P.T., FRIZZELL, A. AND MILLER, C.T. 1997. "Evaluation of Thermal Effects on the Dissolution of a Nonaqueous Phase Liquid in Porous Media." *Environ. Sci. Technol.*, 31, 1615-1622.

JASMUND, K. AND LAGALY, G. (Hrsg.). 1993. *Tonminerale und Tone*. Darmstadt. Seinkopfverlag.

JOHNSON, R. L. 2007. *In Situ Thermal Remediation of DNAPL Source Zones*. Oregon Health & Science University, SERDP In-Progress Review Meeting, Washington, D.C.

JURY, W., W. GARDNER AND W. GARDNER. *Soil Physics*. John Wiley Sons, Inc., USA, 1991. ISBN 0-471-83108-5.

KASLUSKY, S.F., AND K.S. UDELL. 2002. "A Theoretical Model of Air and Steam Co-Injection to Prevent the Downward Migration of DNAPLs during Steam-Enhanced Extraction." *J. Contaminant Hydrol.*, 55, 213-232.

KEUPER, B.H. REDMAN, D., STARR, R.C., REITSMA, S. AND M. MAH. 1993. "A Field experiment to study the behaviour of tetrachloroethylene below the water table. Spatial distribution of residual and pooled DNAPL." *Ground Water*, Vol. 31, No. 5, pp 756-766.

KINGSTON, J.L.T. 2008. "A Critical Evaluation of In-Situ Thermal Technologies." *Ph.D. Dissertation, Arizona State Univ., Tempe, AZ.*

LACHANCE, J.C., R.S. BAKER, J.P. GALLIGAN, AND J.M. BIERSCHEK. 2004. "Application of 'Thermal Conductive Heating/In-Situ Thermal Desorption (ISTD)' to the Remediation of Chlorinated Volatile Organic Compounds in Saturated and Unsaturated Settings." Paper 2B-21, in: A.R. Gavaskar and A.S.C. Chen (Eds.), *Remediation of Chlorinated and Recalcitrant Compounds—2004. Proceedings of the Fourth International Conference on Remediation of Chlorinated and Recalcitrant Compounds* (Monterey, CA; May 2004). ISBN 1-57477-145-0, published by Battelle Press, Columbus, OH.

LACHANCE, J., R. BAKER AND G. HERON. 2008. "Use of Thermal Conduction Heating for the Removal and Controlled Mobilization of a Mixed-Waste DNAPL Source Zone." Abstract P-003, in: Bruce M. Sass (Conference Chair), *Remediation of Chlorinated and Recalcitrant Compounds—2008. Proceedings of the Sixth International Conference on Remediation of Chlorinated and Recalcitrant Compounds* (Monterey, CA; May 2008). Battelle Press, Columbus, OH.

LACHANCE, J., G. HERON AND R. BAKER. 2006. "Verification of an Improved Approach for Implementing In-Situ Thermal Desorption for the Remediation of Chlorinated Solvents." Paper F-32, in: Bruce M. Sass (Conference Chair), *Remediation of Chlorinated and Recalcitrant Compounds—2006. Proceedings of the Fifth International Conference on Remediation of Chlorinated and Recalcitrant Compounds* (Monterey, CA; May 2006). ISBN 1-57477-157-4, published by Battelle Press, Columbus, OH.

LIDE, D. R., HRSG. *CRC Handbook of Chemistry and Physics*. CRC Press, Inc., Boca Raton, Florida, USA, 79. edition, 1998-1999.

MARK, J. 2005. *Permeability and Grain Size Relationships: Designing Specific Soil Properties for Thermal Remediation Experiments*, M.S. Thesis, Earth Science Department, Göteborg University, Sweden.

MCGEE, B.C.W. 2003. "Electro-Thermal Dynamic Stripping Process for in situ remediation under an occupied apartment building." *Remediation*, Summer: 67-79.

NAVAL FACILITIES ENGINEERING SERVICE CENTER. 1998. *Tech Data Sheet: A Demonstration of In-Situ Thermal Desorption*. TDS-2051-ENV, March 1998. Port Hueneme, CA.

NEWMARK, R.L. ET AL. 1994. *Demonstration of Dynamic Underground Stripping at the LLNL Gasoline Spill Site*, Final Report UCRL-ID-116964, Vol. 1-4. Lawrence Livermore National Laboratory, Livermore, California.

NEWMARK, R.L. AND R.D. AINES. 1997. *Dumping pump and treat: rapid cleanups using thermal technology*. Lawrence Livermore National Laboratory report UCRL-JC-126637, Livermore, California.

NEWMARK, R.L. AND R.D. AINES. 1998. "They all like it hot: Faster cleanup of contaminated soil and groundwater." *Science and Technology Review*, May.

NIELSEN, S.G., H.E. STEFFENSEN, T. HERON, G. HERON, M. KUHLMAN, H. SKOU, N. JUST AND L. DISSING. 2008. "First Thermal Remediation Using a Combination of Steam and ISTD." Paper P-015, in: Bruce M. Sass (Conference Chair), *Remediation of Chlorinated and Recalcitrant Compounds—2008*. Proceedings of the Sixth International Conference on Remediation of Chlorinated and Recalcitrant Compounds (Monterey, CA; May 2008). Battelle Press, Columbus, OH.

NIST. 2005. *Chemistry WebBook* National Institute of Standards and Technology. <http://webbook.nist.gov/chemistry>, 15.09.2005, 12:00

O'CONNER, K. AND C.H. DOWDING. 1999. *Geo Measurements by Pulsing TDR cables and Probes*. Boca Raton; London; New York; Washington D.C, CRC Press.

O'HARA, S. K., JORGENSEN, P. R. AND J.A. CHERRY. 2000. "Trichlorethene DNAPL flow and mass distribution in naturally fractured clay: Evidence of aperture variability." *Water Resour. Res.*, 36(1):135-147.

OOCHS, S.O., HODGES, R.A., FALTA, R.W., KMETZ, T.F., SUPAR, J.J., BROWN, N.N. AND D.L. PARKINSON. 2003. "Predicted heating patterns during steam flooding of coastal plain sediments at the Savannah River Site." *Environmental & Geological Geoscience*, Vol IX, No. 1, Feb 2003, pp. 51-60.

PENNELL, K.D. 2007. *In Situ Thermal Remediation of DNAPL Source Zones*. Georgia Institute of Technology, SERDP In-Progress Review Meeting, Washington, D.C.

PERSSON, M. AND R. BERNDTSSON. 2002. "Measuring nonaqueous liquid saturation in soil using time domain reflectometry." *Water Resources Research*, vol.38 No. 5.

REID, R.C., PRAUSNITZ, J.M. AND B.E. POLING. *The Properties of Liquids and Gases*. McGraw Hill, New York, USA, 4th edition, 1987.

SERDP/ESTCP. 2001. *Final Report, SERDP/ESTCP Expert Panel Workshop on Research and Development Needs for Cleanup of Chlorinated Solvent Sites*. August 6-7, 2001. Available in electronic form from: <http://www.estcp.org/documents/techdocs/chlorsolvcleanup.pdf>

SERDP/ESTCP. 2006a. *Technical Report, Summary of SERDP and ESTCP Projects Focused on Characterization and Remediation of Dense Nonaqueous Phase Liquid (DNAPL) Source Zones*. February, 2006. Available In Electronic Form From: <http://www.estcp.org/documents/techdocs/chlorsolvcleanup.pdf>

SERDP/ESTCP. 2006b. *Final Report, SERDP and ESTCP Expert Panel Workshop on Reducing the Uncertainty of DNAPL Source Zone Remediation*. March 7-9, 2006. Available in electronic form from:

<http://www.estcp.org/documents/techdocs/chlorsolvcleanup.pdf>

SCHMIDT, R., C. BETZ AND A. FÄRBER, 1998. "LNAPL and DNAPL behaviour during steam injection into the unsaturated zone," Proc. GQ'98 Conference Tübingen, Sept. 1998, IAHS Publ. No. 250 (111-117).

SCHMIDT, R., J. GUDBJERG, T.O. SONNENBORG, AND K.H. JENSEN. 2002. "Removal of NAPLs from the Unsaturated Zone using Steam: Prevention of Downward Migration by Injecting Mixtures of Steam and Air." J. Contaminant Hydrol., 55, 233-260.

SHE, H.Y. AND B. SLEEP. 1998. "The Effect of Temperature on Capillary Pressure-Saturation Relationships for Air-Water and Perchloroethylene-Water Systems." Water Resour. Res., 34, 2587-2597.

SHELDON, R.B., I.E.T. IBEN, W.A. EDELSTEIN, H.J. VINEGAR, E.P. DEROUFFIGNAC, F.G. CARL, J.L. MENOTTI, J. COLES, J.M. HIRSCH, W.B. SILVERSTEIN, S.R. BLAHA, C.R. SCATENA, AND G.W. SIEGEL. 1996. "Field Demonstration of a Full-Scale In-Situ Thermal Desorption System for the Remediation of Soil Containing PCBs and Other Hydrocarbons." Proceedings of the HAZWaste World-Superfund XVII Conference, Washington, D.C., Oct. 15-17, 1996.

SLEEP, B.E. AND Y. MA. 1997. "Thermal variation of organic fluid properties and impact on thermal remediation feasibility." Journal of Soil Contamination, 6(3), 281-306.

SLEEP B. E AND P. D. MCCLURE 2001. *The effect of temperature on adsorption of organic compounds to soils*. Can. Geotech. J. 38: 46-52 (2001)

STEGEMEIER, G.L. AND H.J. VINEGAR. 1995. "Soil Remediation by Surface Heating and Vacuum Extraction," paper SPE 29771, Proceedings of 1995 SPE/EPA Exploration and Production Environmental Conference, Houston, TX, March 27-29.

STEGEMEIER, G.L. 2000. *Personal communication*.

STEGEMEIER, G.L. AND H.J. VINEGAR. 1995. "Soil Remediation by Surface Heating and Vacuum Extraction," paper SPE 29771, Proceedings of 1995 SPE/EPA Exploration and Production Environmental Conference, Houston, TX, March 27-29.

STEGEMEIER, G.L. AND H.J. VINEGAR. 2001. "Thermal Conduction Heating for In-Situ Thermal Desorption of Soils." Ch. 4.6, pp. 1-37. In: Chang H. Oh (ed.), Hazardous and Radioactive Waste Treatment Technologies Handbook, CRC Press, Boca Raton, FL.

THEURER, T., A. WINKLER, U. HIESTER AND H.-P. KOSCHITZKY. 2003. "Mathematical and Numerical Modeling of Thermally Enhanced In-Situ Remediation with Thermal Wells." pp. 1981-1992. In O.Uhlmann (Ed.), Conference Proceedings: 8th International FZK//TNO Conference on Contaminated Soil (ConSoil 2003). 12-16 May 2003, Ghent, Belgium. <http://www.consoil.de>

THIENEMANN, J. 1999. *Zur Bedeutung von Wassergehalt und Struktur für die mechanische Stabilität und hydraulische Dichtigkeit von mineralischen Deponieabdichtungen aus Geschiebemergel*. Institut für Pflanzenernährung und Bodenkunde, Christian-Albrechts-Universität, Kiel.

TRÖTSCHLER, O., A. FÄRBER, K. WEBER, T. HASLWIMMER AND H.-P. KOSCHITZKY. 2003. "Development and technical implementation of the thermally enhanced soil vapour extraction using steam injection for the saturated and unsaturated zone," 8th International FZK / TNO Conference on Contaminated Soil, Proc. of ConSoil 2003, ICC, Gent, May 12 - 16, 2003.

UDELL, K.S. 1996. "Heat and mass transfer in clean-up of underground toxic wastes." In Annual Reviews of Heat Transfer, Vol. 7, Chang-Lin Tien, Ed.; Begell House, Inc.: New York, Wallingford, UK, pp. 333-405.

UDELL, K.S. AND J.S. FITCH. 1985. "Heat and Mass Transfer in Capillary Porous Media Considering Vaporisation, Condensation and Non-Condensable Gas Effects." Paper presented at 23rd ASME/AIChE National Heat Transfer Conference, Denver, CO.

UDELL, K.S. AND R. MCCARTER. 1996. *Treatability test of steam enhanced extraction for the removal of wood treatment chemicals from Visalia Pole Yard soils*, Final report, submitted to Southern California Edison, Rosemead, CA 91770.

UMWELTRECHT. 2001. Beck-Texte. München, deutscher Taschenbuchverlag 13.Auflage.

U.S. ARMY CORPS OF ENGINEERS. 2006. *Engineer Manual: In Situ Thermal Remediation*. EM 1110-1-40XX.

U.S. ARMY CORPS OF ENGINEERS, EPA KERR ENVIRONMENTAL RESEARCH LABORATORY, PACIFIC NORTHWEST NATIONAL LABORATORY AND THE UNIVERSITY OF FLORIDA. 2008. *East Gate Disposal Yard Thermal Remediation Performance Assessment After Action Report, Fort Lewis Logistics Center, Fort Lewis, Washington*. Prepared for Fort Lewis Public Works – Environmental Division, Fort Lewis, Washington 98433 and Army Environmental Command, Washington DC. April 15, 2008.

US DOE. 1999. *Steam Stripping and Hydrous Pyrolysis Pilot Project for the Portsmouth Gaseous Diffusion Plant, Portsmouth, Ohio*. Final report for DOE # DOE/OR/11-3032&D1.

US DOE. 2003. *Pinellas Environmental Restoration Project, Northeast Site Area A NAPL Remediation Final Report*, Young-Rainey STAR Center. US Department of Energy, Grand Junction, CO. September 2003.

USEPA. 1997. *Cleanup of the nation's waste sites: Markets and technology trends*. EPA 542-R-96-005. Washington, DC.

USEPA. 2004. *In Situ Thermal Treatment of Chlorinated Solvents: Fundamentals and Field Applications*. Office of Solid Waste and Emergency Response. EPA 542-R-04-010. Washington, DC.

UZGIRIS, E.E., EDELSTEIN, W.A., PHILIPP, H.R., AND I.E.T. IBEN. 1995. "Complex Thermal Desorption of PCBs from Soil." *Chemosphere*, 30(2):377–387.

VINEGAR, H.J., E.P. DEROUFFIGNAC, J.L. MENOTTI, J.M. COLES, G.L. STEGEMEIER, R.B. SHELDON, AND W.A. EDELSTEIN. 1997A. "Remediation of Deep Soil Contaminants Using Thermal Vacuum Wells." paper SPE 39291, Proceedings of the 1997 SPE Annual Technical Conference, San Antonio, Texas, October 5–8.

VINEGAR, H.J., E.P. DEROUFFIGNAC, R.L. ROSEN, G.L. STEGEMEIER, M.M. BONN, D.M. CONLEY, S.H. P. HILLIPS, J.M. HIRSCH, F.G. CARL, J.R. STEED, D.H. ARRINGTON, P.T. BRUNETTE, W.M. MUELLER, AND T.E. SIEDHOFF. 1997B. "In Situ Thermal Desorption (ISTD) of PCBs." Proceedings of the HazWaste/World Superfund XVIII Conference, Washington, DC, December 2, 1997.

VINEGAR, H.J., G.L. STEGEMEIER, F.G. CARL, J.D. STEVENSON, AND R.J. DUDLEY. 1999. "In Situ Thermal Desorption of Soils Impacted with Chlorinated Solvents." Proceedings of the Annual Meetings of the Air and Waste Management Association, Paper No. 99-450.

WINKLER, A., THEURER, T., HIESTER, U. AND H.-P. KOSCHITZKY. 2001. *Experimentelle und numerische Untersuchungen zur thermischen In-situ Sanierung mit festen Wärmequellen*, VEGAS-Statuskolloquium 2001, 12. Oktober 2001, pp 31-37.

Appendix A: Supporting Data: Mark, 2005 Thesis

Permeability and Grain Size Relationships

Designing Specific Soil Properties for Thermal
Remediation Experiments

J. Mark

*Earth Science Centre
Dept. of Geology
Göteborg University*

Abstract

This Master's Thesis presents research conducted to help select the soil mixture to be used in room-size in-situ thermal remediation experiments, to be performed under SERDP Project CU-1423, "Large-Scale Physical Models of Thermal Remediation of DNAPL Source Zones in Aquifers." The soil mixture is subject to certain requirements, specifically that its saturated hydraulic conductivity (K_s), at a preset value of dry bulk density (ρ_d) be relatively low. There is also a need to recycle material on-hand at the VEGAS facility, Institute of Hydraulic Engineering, Stuttgart Universität, Germany where the large-scale experiments will be conducted, in an effort to design the new mixture most cost effectively, since many cubic meters are required in the experiments. In addition to this, it was felt that the materials selected should have a sufficiently wide grain size distribution to prevent eluviation of fines. Thus, the objective of this study is to design a soil mixture with regard to hydraulic conductivity, cost efficiency and possibly preventing eluviation. Furthermore, the objective also aims to estimate hydraulic conductivity as a function of grain size.

Permeameter tests were carried out on mixtures with varying content ratios of industrially manufactured quartz-derived silts and sand to achieve a preferred saturated hydraulic conductivity of $K_s = 1.0\text{E-}7$ m/s. It was found that the initially provided materials could not generate the preferred hydraulic conductivity at the suggested dry bulk density.

A new, finer material was suggested as a possible candidate to further lower the hydraulic conductivity. To facilitate the design of the soil mixture, a model was developed to estimate component ratios for a given value of hydraulic conductivity as a function of void ratio (e) and effective grain size (d_{10}).

The opportunity arose to validate the estimated results through experiments using a sample of the new component. Measured results indicated that to reach the targeted hydraulic conductivity a slightly lower effective grain size was needed than that indicated by the model. The empirical results also revealed that boundary conditions regarding cost efficiency and eluviation had to be compromised to meet the more significant requirements of hydraulic conductivity and dry bulk density; even so, the closest result measured $K_s = 1.4\text{E-}7$ m/s. Grain size analysis of the final soil mixture after permeameter testing did not indicate evidence of eluviation, although the initially suggested preventive measures to add a specific distribution had not been taken. To address the issue of cost efficiency, it is felt that proctor density of the final soil mixture should be studied further to assess the possibility of applying a higher dry bulk density, thus allowing for a larger amount of recycled material in the final soil mixture.

Sammanfattning

Detta examensarbete, för Magisterexamen, är en undersökning av hydraulisk konduktivitet i en jordartsblandning tänkt för användning i ett storskaligt laborationsförsök gällande termisk sanering in-situ: SERDP Project CU-1423, "Large-Scale Physical Models of Thermal Remediation of DNAPL Source Zones in Aquifers." Jordartsblandningen är föremål för ett antal villkor av vilka mättad hydraulisk konduktivitet (K_s), vid en förutbestämd torrdensitet (ρ_d) ska vara relativt låg. Det finns också en önskan om att återanvända redan befintligt material i största möjliga utsträckning som ett led i en kostnadseffektiv lösning. Detta material återfinns vid VEGAS, Institute of Hydraulic Engineering, Stuttgart Universitt, Tyskland, dr de storskaliga laborationsförsöken kommer att ga rum. Ytterligare ett kriterium r att jordartsblandningen ska uppvisa en tillrckligt osorterad kornstorleksfördelning fr att undvika partikelförflyttning i materialet som en flj av genomströmmande vtska, s kallad eluviation. Sledes r mlet i denna studie att skapa en kostnadseffektiv jordartsblandning med fokus p hydraulisk konduktivitet, samt att om mjligt frhindra eluviation i den samma. Vidare har studien ocks fr avsikt att modellera hydraulisk konduktivitet som en funktion av kornstorlek.

Permeameterförsök utfördes p jordartsblandningar med varierande produktinnehll av industriellt framstlld silt och sand av kvarts fr att n en skt konduktivitet av $K_s = 1.0E-7$ m/s. Det uppdragades att de material vilka stllts till frfogande var inkapabla att skapa frutstningar fr det skta konduktivitetsvrdet vid den frutbestmda torrdensiteten. Ett nytt, finkornigare, material freslogs fr att ytterligare snka konduktivitetsvrdet. D materialet inte fanns till hands utvecklades en modell fr att uppskatta ndvndiga produktmngder fr ett bestmt vrde p hydraulisk konduktivitet. Modellen uppskattar K_s som en funktion av portal (e) och effektiv kornstorlek (d_{10}).

Tillflle gavs att vrdera de uppskattade resultaten med hjlp av ett prov av det freslagna, finkornigare, materialet. Uppmtta resultat gjorde gllande att fr att n den skta konduktiviteten behövdes en ngot mindre effektiv kornstorlek n det modellerade vrdet. Försöken uppdragade ocks ndvndigheten av att kompromissa önskemlen gllande kostnadseffektivitet samt tgrder mot partikelförflyttning fr att kunna uppn kriterierna angende konduktivitet och torrdensitet. Under dessa omstndigheter uppmttes en lgsta hydraulisk konduktivitet av $1.4E-7$ m/s.

Kornstorleksanalys av den slutgiltiga jordartsblandningen uppvisade inga tecken p partikelförflyttning, ven d de freslagna tgrderna att tillstta en specifik kornfördelning negligerats. Fr att underltta frgan angende kostnadseffektivitet fresls en detaljstudie av den slutgiltiga jordartsblandningens packningsegenskaper, s kallade *proctor test*, fr utvrdering av mjlighet till ökad torrdensitet med pfljande mjlighet till ökad teranvndning av befintligt material.

Acknowledgements

I would like to thank my supervisor, Dr. Rodney Stevens at the Earth Science Centre, Göteborg University, for constructive comments during the course of this work and for guidance during the writing process.

I would also like thank Dr. Ralph Baker, CEO of TerraTherm, Inc. for providing me with the opportunity to carry out this study as a part of TerraTherm's SERDP funded project. Dr Baker also deserves thanks for sharing his experience concerning both practical as well as theoretical aspects relevant for this study.

Great thanks also go out to doctoral candidate Mr. Uwe Hiester who, on behalf of VEGAS, University of Stuttgart, provided the sample material used in the tests and spent much time and effort providing detailed key information, without which this project would not have been possible. My wife, Megina is thanked for helpful comments and corrections of this work. Chalmers Technical University is acknowledged for kindly lending permeameter equipment. Hans Alter is thanked for manufacturing some special equipment for this study.

Finally, I would like to thank all my friends at the Earth Science Centre, Göteborg University, for a great time during the four years of geology studies, culminating in this Master's Thesis. Thank you.

Table of Contents

<u>ABSTRACT</u>	<u>I</u>
<u>SAMMANFATTNING</u>	<u>II</u>
<u>ACKNOWLEDGEMENTS</u>	<u>III</u>
<u>TABLE OF CONTENTS</u>	<u>IV</u>
<u>1 INTRODUCTION</u>	<u>1</u>
1.1 OBJECTIVE	3
1.2 LITERATURE SURVEY	3
1.2.1 PERMEABILITY	3
1.2.2 PORE GEOMETRY	4
1.2.3 GRAIN SIZE PROPERTIES	4
1.3 MATERIALS USED	5
1.4 BOUNDARY CONDITIONS	7
<u>2 METHODS</u>	<u>7</u>
2.1 EQUIPMENT	8
2.2 CONTENT COMPOSITION	9
2.3 COMPACTION	9
2.4 SATURATION	9
2.5 MEASURING PERMEABILITY	10
2.5.1 CONSTANT HEAD	10
2.5.2 FALLING HEAD	10
2.5.3 VACATING THE PERMEAMETER CELL	11
2.6 GRAIN SIZE ANALYSIS	11
<u>3 MODELING PERMEABILITY</u>	<u>11</u>
3.1 MODEL OUTLINE	11
3.1.1 LEVEL 1	11
3.1.2 LEVEL 2	12

4	<u>RESULTS</u>	<u>12</u>
4.1	MEASURED HYDRAULIC CONDUCTIVITY	12
4.2	ESTIMATING PERMEABILITY	13
4.2.1	EXTENDED EQUATION OF CHAPUIS	13
4.2.2	NEW PREDICTIVE EQUATION	14
4.2.3	PREDICTING SUITABLE SOIL MIXTURE	15
4.3	DESIGNING THE FINAL MIXTURE	17
4.4	GRAIN SIZE ANALYSIS	17
4.4.1	VERIFICATION OF PRODUCT DATA	18
4.4.2	ELUVIATION	19
5	<u>DISCUSSION</u>	<u>19</u>
5.1	INACCURACIES IN MANUFACTURER’S DATA	19
5.2	METHOD AND MEASURED RESULTS	21
5.2.1	SATURATION	21
5.2.2	COMPACTION	21
5.3	MODELED RESULTS	22
5.3.1	PREDICTIVE EQUATION	22
5.3.2	GRAIN SIZE DISTRIBUTION MODEL	23
5.3.3	INTRODUCING A NEW DISTRIBUTION	23
5.4	ELUVIATION	23
6	<u>CONCLUSION</u>	<u>24</u>
7	<u>REFERENCES</u>	<u>25</u>
	<u>APPENDIX I</u>	<u>I</u>
	<u>APPENDIX II</u>	<u>III</u>
	<u>APPENDIX III</u>	<u>XIII</u>

1 Introduction

An investigation, focused on remediation of dense non-aqueous phase liquid (DNAPL) source zones in aquifers through large-scale physical model tests, has been funded by the U.S. Department of Defense's Strategic Environmental Research and Development Program (SERDP). (Baker et al., 2004). The results presented herein address the issue of selecting the soil materials to be utilized for the low-permeability layer within the large-scale experiments that will be conducted during the SERDP project.

Source zones are volumes of the subsurface within which high concentrations of organic pollutants have accumulated. They vary in size, mostly depending on geology in the area and the quantity of released pollution. Permeability of the soil is a key factor in the migration of contaminants. To understand their movement within the subsurface, it is imperative to gain information about the soil permeability. This can be achieved, in part, by direct measurements either on undisturbed or remolded samples. However, from an economic standpoint it is sometimes desirable to estimate hydraulic conductivity rather than using actual measurements.

There are many factors that affect permeability. One of the foremost is grain size distribution; if the predominant fraction consists of fine-grained material, the resulting permeability is low. If on the other hand the soil holds a large proportion of coarse particles, the resulting permeability will be orders of magnitude higher.

Compaction is another significant factor that greatly affects the soil permeability. A loosely compacted soil yields a higher permeability than a well compacted soil. However, source zones are most often well compacted as they are situated in the ground where the soil has been subject to natural compactive forces.

Particle shape is also significant for the resulting permeability. Elongated particles

may result in a matrix with relatively large pores hence allowing for a higher permeability. The opposite situation where the soil consists of different sized spheres, results in a lower permeability as the matrix has a higher maximum compaction than in the previous situation. Increased particle angularity may lower the hydraulic conductivity due to increased frictional effects (Hillel, 1998).

Another influencing factor is that of saturation. An unsaturated soil shows a lower relative permeability than would the same soil during saturated conditions. In the field, this refers to soil above or below the ground water surface.

To exemplify how these factors influence contaminant dispersion, consider the following example. A discrete release of an organic pollutant in a low permeability soil where the ground water surface is deep may not pose as serious a risk as such a release in a higher-permeability soil. This is due to the fact that a continuous release in a highly permeable soil with a shallow ground water surface spreads more quickly and to a greater extent. However, the polluting effect on biological life can be significant even in low concentrations. Therefore a minor release has the potential of creating the same harmful situation for the ecological system as could a much larger release of the same pollutant.

The source zone used in the large-scale experiments is intended to replicate the general conditions often encountered in nature. Due to the complex systems present in natural soil, certain priorities are made when designing the soil mixture to be used in this study. Factors significant to the test outcome are considered, while at the same time striving to keep the mixture as uncomplicated as possible. The soil mixture is designed to mirror silty conditions. As a consequence of this, clay minerals have been excluded due to their swelling characteristics. To achieve a certain permeability, the included materials range from clay size fractions to very fine sand where the

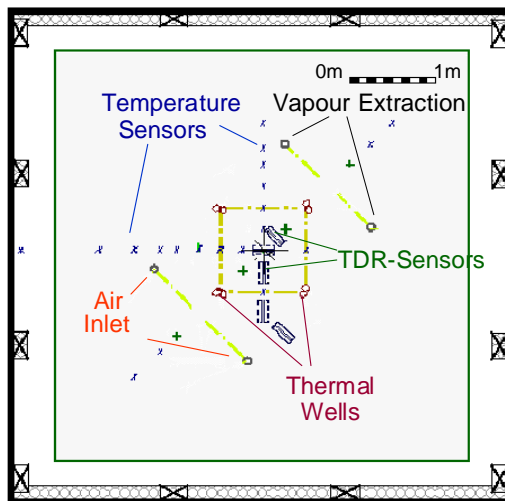
predominant amount consists of coarse silt. The materials considered suitable for the SERDP-funded research are industrially produced quartz products. As it has been argued that clastic sediments are the results of only a few populations of grain sizes (Spencer, 1963), one may claim that these products do not properly replicate grain size distributions found in nature and therefore question their suitability. Despite this argument, industrially produced quartz products are deemed to be acceptable for use in the SERDP project, as they exhibit many of the key physical properties of natural soils.

The remediation process that is in the focus of the SERDP project is carried out using in-situ thermal conductive heating. The method, known as in-situ thermal desorption (ISTD), has been in commercial use since 1996 (Stegemeier and Vinegar, 2001) for treatment of volatile organic

compounds (VOCs). Thermal wells operating at temperatures of up to 700°C heat the soil to a target temperature of 100°C. The vaporized contaminants migrate towards vacuum wells where they are evacuated from the soil and conducted to an off-gas treatment unit. There the gases are stripped of their hazardous constituents.

The large scale test equipment to be utilized during the SERDP project is located at the VEGAS¹ facility, Institute of Hydraulic Engineering, Stuttgart Universität, Germany. Prior to large-scale tests, the test material will be placed in two containers, measuring 6.0 m x 6.0 m x 4.5 m and 3.0 m x 6.0 m x 4.5 m (Fig. 1). These are equipped with thermal and vacuum wells as well as measuring devices to carefully monitor the tests. Material from previous experiments is readily available at VEGAS. This material is referred to as the *FSG*² mixture.

Plan View



Vertical Section

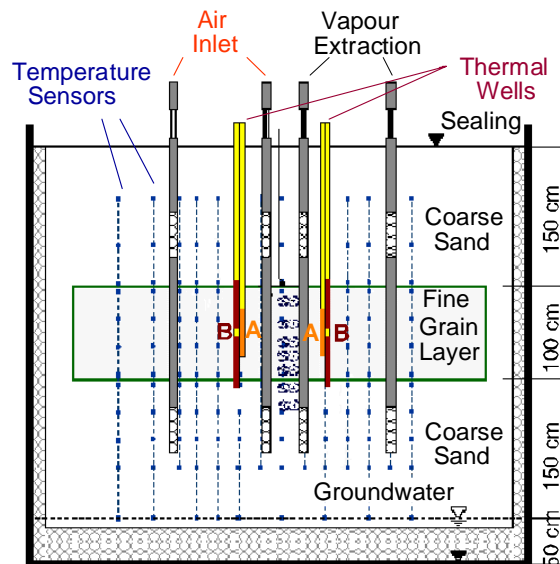


Fig. 1. Container layout of previous, similar large scale experiments (Baker et al., 2004).

¹ Versuchseinrichtung zur Grundwasser- und Altlastensanierung

² Feinsandgemisches

1.1 Objective

The objective of this study is to create a soil mixture with certain predetermined characteristics to serve as the DNAPL source zone in the large scale experiments of the SERDP project. The test material is subject to a number of boundary conditions applied to control certain properties both during placement of the test material into the test containers, as well as throughout the subsequent tests. Hydraulic conductivity (K_s) is set to $1.0\text{E-}7$ m/s to reflect general natural conditions of greatest interest and applicability to the use of ISTD below the water table (Baker et al., 2004). The dry bulk density (ρ_d) is estimated at 1.65 t/m^3 based on information from the SERDP project group. The soil mixture is to contain Dorosilit 4900 and Dorosilit 2500, the latter in addition to that already present in the FSG mixture, to prevent possible eluviation³. Recycling of available FSG mixture is desired to the highest extent possible to reduce cost.

An additional objective is to find a suitable method to estimate the hydraulic conductivity for the suggested types of materials.

1.2 Literature Survey

The following chapter describes several specific fundamental relationships upon which underlying assumptions are based during the course of this study. Permeability, pore geometry, and grain size properties will be explored.

1.2.1 Permeability

Darcy's law (Eq. 1) describes discharge during saturated conditions and laminar flow (Fetter, 2001).

$$\text{Eq. 1} \quad Q = -K_s A \left(\frac{dh}{dl} \right)$$

Q , Discharge (L^3/T)

K_s , Hydraulic conductivity (L/T)

A , Cross sectional area (L^2)

$\frac{dh}{dl}$, Hydraulic gradient (L/L)

Eq. 2 introduces specific discharge, q , as a function of discharge and area through which fluid flow takes place.

$$\text{Eq. 2} \quad q = \frac{Q}{A}$$

Combining Eq. 1 & 2

$$\text{Eq. 3} \quad q = -K_s \frac{dh}{dl}$$

Rearranged

$$\text{Eq. 4} \quad K_s = -q \div \left(\frac{dh}{dl} \right)$$

K being the function of specific discharge and hydraulic gradient is also explained in Fig. 2.

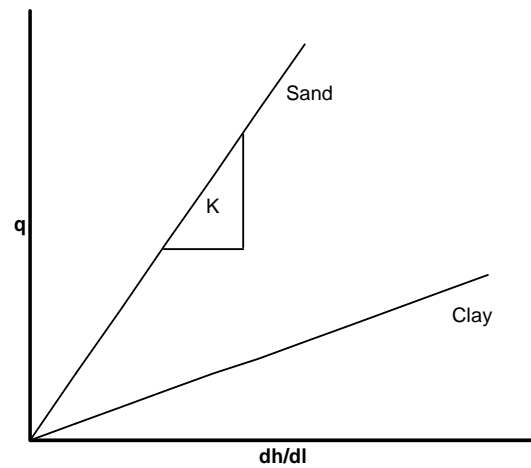


Fig. 2. Relation between specific discharge and hydraulic gradient.

³ Removal of soil materials in suspension or in solution from surface horizons, and with partial deposition in the lower horizons of soil profiles (Allaby and Allaby, 1999).

1.2.2 Pore Geometry

Intergranular pore space is a prerequisite for fluid flow to be conducted through porous media (Hillel, 1998). As it is not feasible to measure the actual size and shape of the multitude of pores in a soil, fluid flow is predicted based on material properties related to pore geometry (e.g. Marshall, 1958).

A widely used function for predicting permeability (a unit which depends only on the porous medium not the fluid, and hence not to be confused with hydraulic conductivity) is the Kozeny - Carman equation (Eq. 5) (Chapuis and Aubertin, 2003). This equation is based on porosity and specific surface, the latter being analogous to the wetted area.

$$\text{Eq. 5} \quad k = \frac{\Phi^3}{(1-\Phi)^2 c S^2}$$

k , Permeability (L^2)

Φ , Porosity (L^3/L^3)

S , Specific surface (L^2)

1.2.3 Grain Size Properties

Masch and Denny (1966) present a method to predict hydraulic conductivity from grain size properties. They found that average grain size (d_{50}) and dispersion (σ) are key parameters influencing hydraulic conductivity.

Another investigation focusing on grain size to predict hydraulic conductivity is that of Hazen (1911). He authored the formula known as Hazen's Equation (Eq. 6), relating hydraulic conductivity to the square of the effective grain size, d_{10} . This refers to the grain size at which ten mass percent of the sample is finer.

$$\text{Eq. 6} \quad K = C d_{10}^2$$

C , Coefficient \propto Particle properties governing fluid flow

d_{10} , Effective grain size

Hazen's method requires a coefficient of uniformity (C_U) < 5 . C_U is the relation between d_{60} and d_{10} , hence it describes sorting of a distribution. A material where C_U is less than 4 is considered well sorted, whereas a material where C_U is more than 6 is poorly sorted (Fetter, 2001). Other requirements are maximum porosity and $0.1 < d_{10} < 3.0$ mm. These conditions practically limit the use of this method to clean, loose, sands.

Folk and Ward (1957) suggest refined methods of characterizing sediments in order to better understand their origin. An extended use of these characteristics is to gain understanding of the sediment properties, e.g. regarding permeability. These characteristics include:

- Mean size (M_z)
- Standard deviation (σ_I)
- Inclusive Graphic Skewness (Sk_I)
- Graphic Kurtosis (K_G)
- Mode

Mean size (M_z)

The predominant grain size is characterized using the descriptive terms in Table 1. Permeability is directly proportional to grain size.

Standard deviation (σ_I)

Sorting is described by the standard deviation of the grain size distribution. A poorly sorted material is described by a large standard deviation while a well sorted material demonstrates little standard deviation. Permeability may in some cases be inversely proportional to standard deviation. Spencer (1963) highlights the inappropriateness of using the term *sorting* in a statistical context, as it only serves to describe the result of an actual physical process. Instead the term *dispersion* is suggested as a better fit from a statistical point of view and the terms will therefore be used accordingly in the remainder of this study.

Inclusive Graphic Skewness (Sk_I)

Symmetry of the grain size distribution curve is described by skewness and is the result of concentration of material to either end of the distribution. If the curve is shifted to either side of its center it displays positive or negative skewness. The impact on permeability is analogous to that of M_z in that a concentration of material in the coarser end of the distribution results in raised permeability and a concentration of finer material serves to lower the permeability. Using the phi-scale for grain size, skewness obtains a positive value if there is a concentration of fines and a negative value if the concentration is in the coarser material. Using metric units for grain size reverses the logic of positive and negative values. To avoid this confusion the terms are herein referred to as *fine skewed* or *coarse skewed* for a concentration of material in the finer or coarser interval respectively.

Graphic Kurtosis (K_G)

Kurtosis is a measure of the relation between concentrations of material in the extremes of the distribution to that of the central part, i.e. peakedness. Kurtosis is given the term 'leptokurtic' if the curve is excessively peaked, 'platykurtic' if it is deficiently peaked and 'mesokurtic' if it displays a normal standard deviation. Kurtosis has limited impact on permeability (Masch and Denny, 1966).

Mode

The number of concentrations within a grain size distribution is referred to as 'mode'. A distribution with only one concentration is said to be unimodal while a bimodal soil has two concentrations within the distribution, etc. A multimodal distribution obscures the meaning of skewness and kurtosis, especially the latter in that the focus of the curve, i.e. the peak, can be located between the modes hence in a concave part of the curve.

Thus, it is important to note the mode of a curve in order to correctly interpret the statistical characteristics, especially those of skewness and kurtosis.

1.3 Materials Used

Three materials with different grain size distributions were initially included in the test. These are high quality quartz derivatives with a documented minimum of ca 99 percent SiO₂, products of Dorfner Inc. of Germany. Two of those comprise the *FSG* mixture already available from previous experiments. Each product, including the *FSG*, is presented in one uniform grain size distribution chart for easy comparison between the different products (Fig. 3).

Table 1. Grain size classification.

Grain Size Φ	mm	Descriptive term	
-10	1024	Very Large	Boulder
-9	512	Large	
-8	256	Medium	
-7	128	Small	
-6	64	Very Small	
-5	32	Very Coarse	Gravel
-4	16	Coarse	
-3	8	Medium	
-2	4	Fine	
-1	2	Very Fine	
0	1	Very Coarse	Sand
1	0.500	Coarse	
2	0.250	Medium	
3	0.125	Fine	
4	0.063	Very Fine	
5	0.031	Very Coarse	Silt
6	0.016	Coarse	
7	0.008	Medium	
8	0.004	Fine	
9	0.002	Very Fine	
		Clay	

Information regarding grain size distribution is retrieved from product data sheets provided by the manufacturer (Appendix III). All mass percent ratios are by weight. The products are characterized using Gradistat, a grain size analysis tool (Blott and Pye, 2001). Gradistat employs a modified Wentworth scale for definition of grain size classes (Table 1).

The following are the initial distributions used to compose the soil mixture:

GEBA Weiss

- Well sorted fine sand
- Mode: Unimodal
- Dispersion: Well sorted
- Mean: Fine sand
- Skewness: Coarse skewed
- Kurtosis: Leptokurtic
- $d_{10} = 106 \mu\text{m}$

The *GEBA* constitutes 60 percent of the *FSG* mixture.

Dorosilit 2500

- Very fine sandy very coarse silt
- Mode: Bimodal
- Dispersion: Poorly sorted
- Mean: Coarse silt
- Skewness: Fine skewed
- Kurtosis: Mesokurtic
- $d_{10} = 5.3 \mu\text{m}$

The 2500 constitutes 40 mass percent of the *FSG* mixture.

Dorosilit 4900

- Medium silt
- Mode: Bimodal
- Dispersion: Poorly sorted
- Mean: Coarse silt
- Skewness: Symmetrical
- Kurtosis: Mesokurtic
- $d_{10} = 4.8 \mu\text{m}$

FSG

- Very coarse silty fine sand
- Mode: Bimodal
- Dispersion: Poorly sorted
- Mean: Fine sand
- Skewness: Very fine skewed
- Kurtosis: Platykurtic
- $d_{10} = 8.6 \mu\text{m}$

The *FSG* is herein considered as one discrete soil mixture as it constitutes a product already available for recycling in the large-scale laboratory tests.

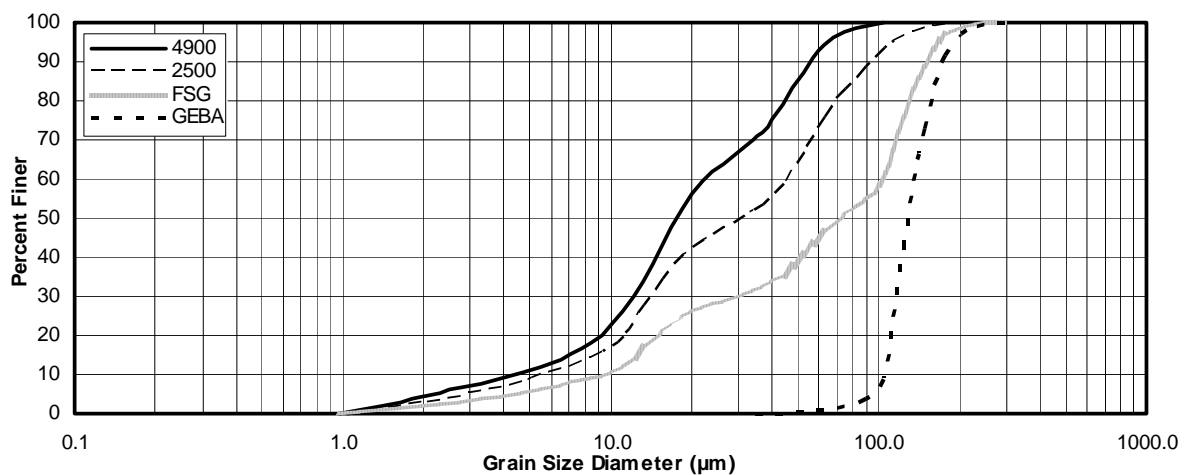


Fig. 3. Grain size distribution of initially provided materials.

1.4 Boundary Conditions

To meet the conditions of the large-scale tests, this study is subject to certain requirements regarding the material properties.

Hydraulic Conductivity

A preferred value of $K_s = 1.0\text{E-}7$ m/s is chosen as it reflects a general condition often encountered in DNAPL source zones not readily addressed with non-thermal in-situ remediation technologies (Baker et al., 2004). This value of hydraulic conductivity is generally considered to be relatively low, although not unusual (USACE, 1986).

Density and Water Content

In determining to what extent a material can be compacted, i.e. the dry bulk density at maximum compaction, a proctor test is often carried out. The proctor test empirically determines maximum attainable density for soils (Dane and Topp, 2002). A sample undergoes static or dynamic compactive effort at a measured water content (w). Its dry bulk density (ρ_d) is recorded and the procedure is repeated at increased water content. ρ_d and w are plotted and the proctor density appears at the point called *optimum moisture* where any further increase in w will result in decreased dry bulk density (Fig. 4) (Fagerström and Wiesel, 1972).

As time is often a limiting factor, this study included, performing proctor tests on the various soil mixtures was beyond the scope of this study. However, VEGAS reported from previous, similar experiments using the *FSG* soil mixture that proctor density has been measured to 1.72 t/m^3 . The *FSG* was compacted to 92 percent of the proctor density at a water content of 10 percent, thus reaching a dry bulk density of 1.58 t/m^3 . Based on this information, an approximation for the new soil mixture was $\rho_d = 1.65 \text{ t/m}^3$ at $10 < w < 12$ percent.

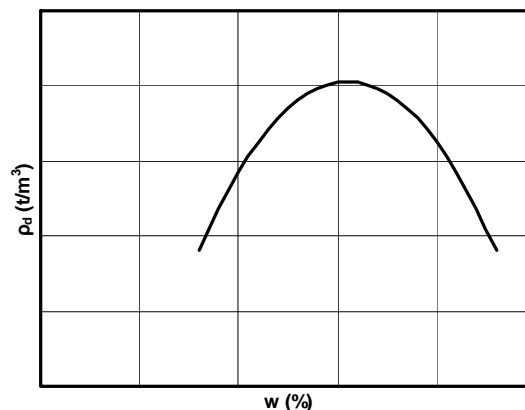


Fig. 4. Schematic exemplification of proctor density.

Recycling of Available Soil Mixture

As a cost efficiency measure, the SERDP project group aims to recycle the soil mixture already available to the greatest possible extent. This material has been used in previous thermal remediation experiments conducted at VEGAS.

Preventing Eluviation

As a means of minimizing possible eluviation (i.e., washing out of the finer particles from the low-permeability layer into adjacent higher-permeability layers during the large-scale experiments), the decision was made to consider adding more of the 2500 in addition to the amount included in the *GEBA*. This results in a wider dispersion theoretically retaining finer particles in the soil matrix (Hillel, 1998).

2 Methods

To facilitate reproducible laboratory conditions, the methodology follows that suggested by the Swedish Standard, Determination of Permeability (SIS, 1989). The flow chart in Fig. 5 shows the order of events, further explained in the following chapters.

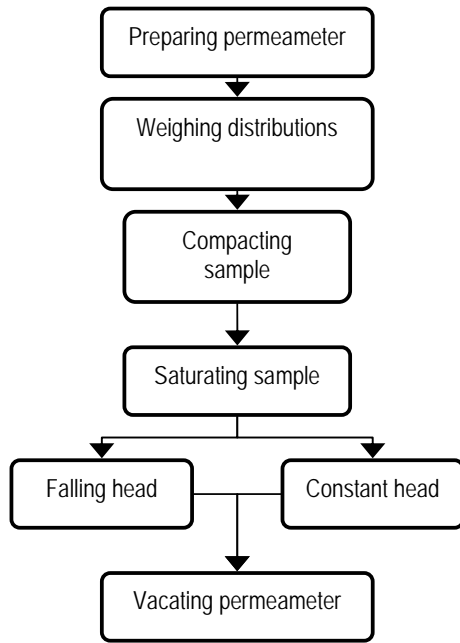


Fig. 5. Flow chart illustrating analysis steps measuring permeability.

2.1 Equipment

The equipment was used according to available standards where applicable. Otherwise, compromises were made to achieve procedures comparable to those advised in literature.

Permeameter

The permeability tests were carried out using a compaction permeameter (Fig. 6), manufactured by Tekno Maskin AB, serial no 14/002. A rigid steel cell ensured constant volume as stress was exerted during compaction and on applying a vacuum to the cell during saturation. Fluid drained into the sample either from the bottom or the top. A vacuum was applied at the evacuation valve on the top lid. The sample rested on a porous plate held in place by a rubber O-ring, which also served to seal the edges around the plate. Fluid drained into or out of the permeameter through a set of grooves in the bottom plate. On top of these grooves lay a wire mesh to ensure even drainage of fluid through the overlaying porous plate. A rubber O-ring held the porous plate in a fixed position, while the steel cell in turn rested on top of the O-ring.

The inside wall of the steel cylinder was coated with grease to prevent fluid from escaping along the sides. The lid had a similar fluid input system as that in the bottom plate with the addition of a concave space above the porous plate. This feature served to provide uniform drainage into the sample.

Permeameter specifications

- Cell length, L ,
0.167 m
- Cell diameter, d_c ,
0.102 m
- Cross sectional cell area, A ,
 $8.17\text{E-}4 \text{ m}^2$
- Pressure head tube diameter, d_t ,
 $8.0\text{E-}3\text{m}$



Fig. 6. Permeameter with vacuum device.

Vacuum Pump

A vacuum pump was connected to the permeameter unit to ensure thorough saturation. It exerted a sub-atmospheric absolute pressure (i.e., vacuum) of 8 mm Hg to the sample.

Compaction Device

A compaction/filling device known as a *tremmie* was made from a 20 mm steel pipe, fitted in the bottom end with a wider bodied cylinder to achieve increased compaction. In the other end a funnel was used to fill the material.

Scale

To ensure the same level of accuracy during the various measurements, the same digital scale was used throughout the tests. The precision of the scale was 1.0E-4 grams.

2.2 Content Composition

As cost efficiency was a main goal of the project, the aim was to recycle the already available soil mixture to the greatest possible extent. Using this available mixture also met the requirement of including the *GEBA* fraction to achieve increased grain size dispersion. Initially at 50 mass percent, the content ratio of the *FSG* was continuously lowered, subsequently increasing the amount of fines for each new test.

2.3 Compaction

Due to time limitations, no complete proctor tests were carried out in this study. Instead, the SERDP project group hypothesized that an increased amount of fines would lead to increased proctor density, hence allowing for an increased dry bulk density (see 1.4.2). The preferred $\rho_d = 1.65 \text{ t/m}^3$ required that 2251 g of material be placed in the permeameter cell.

To fit the measured amount of material into the cylinder, its height was divided into four equal intervals. As each interval was filled, the weight of the residue material was measured to determine whether the following interval needed to be packed more densely or more lightly. It proved easier to achieve the targeted dry bulk density by altering the water content rather than applying different amounts of compactive stress for each new sample. An increased ratio of fines was compensated for by a slight increase in water content, allowing for a static level of energy to be exerted during compaction.

The tremmie was designed to produce an even compaction of the test material throughout the permeameter cell. However, in this particular study, the high content of fines along with the added water congested the pipe. Instead, increments of approximately 150 g of material were placed directly into the cell to undergo compaction through a series of light blows with the compacting device. This procedure was repeated until the cylinder was completely filled. Only after the tests were completed did it become apparent that the problem of congestion could have been avoided by inserting a wire through the pipe and agitating it, keeping the material from becoming stagnant during the filling/compaction process.

2.4 Saturation

As this study intends to measure saturated hydraulic conductivity, the samples had to be completely saturated before the first test run of each new experiment. Since the main aim was to achieve a hydraulic conductivity of $1.0\text{E-}7 \text{ m/s}$, a relatively low value of K_s , it would be overly time-consuming to saturate the sample relying only on capillary forces or by using an elevated pressure head. This issue was resolved by applying a strong vacuum to the top of the permeameter cell while at the same time allowing water to flow upward into the bottom of the permeameter. When fluid had risen up into both the evacuation tube and the inlet tube, the evacuation valve was closed and the vacuum pump switched off. The sample was not yet fully saturated but held a minimum of air, therefore the cell maintained an underpressure. Fluid now entered the sample from the top of the permeameter through the inlet tube. Initially, no fluid drained out of the sample. However, as equilibrium emerged, an equal amount of fluid was collected as that which entered the cell. The sample was then fully saturated.

2.5 Measuring Permeability

Different methods were utilized due to the varying properties of soils. Two different permeameter setups were used to measure hydraulic conductivity in this study: constant head and falling head.

2.5.1 Constant Head

The constant head permeameter setup (Fig. 7) is generally suggested as a suitable method to determine permeability for noncohesive materials (Fetter, 2001; Dane and Topp, 2002). A constant head supplies a steady flow of water. The amount of water that passes through the sample per unit time is measured to calculate the hydraulic conductivity using Eq. 7.

During the course of this study, the constant head method was used only because it allowed the tests to run overnight. Initially, it was also used to verify results from falling head measurements.

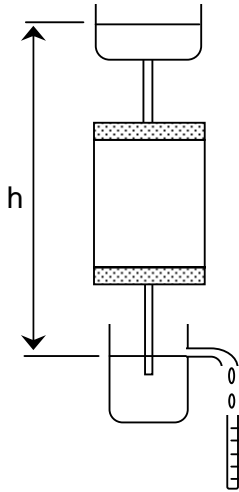


Fig. 7. Constant head permeameter setup.

$$\text{Eq. 7} \quad K = \frac{QL}{Ath}$$

- K , Hydraulic conductivity (L/T)
- Q , Discharge in time (L^3)
- L , Length of sample (L)
- A , Cross-sectional sample area (L^2)
- t , Time elapsed during discharge (T)
- h , Pressure head (L)

Example

1 liter fluid collected during a time period of 1 hour. Pressure head at 1.0 meter.

$$K = \frac{1E-3 * 0.167}{8.17E-4 * 3600 * 1.0}$$

$$K = 5.7E-6 \text{ m/s}$$

2.5.2 Falling Head

This type of permeameter setup (Fig. 8) is generally suitable for cohesive, low permeability materials because it requires a smaller volume of water to pass through the sample to determine the permeability (Fetter, 2001; Dane and Topp, 2002). The initial height of the pressure head is recorded. After some time, the water level is recorded again. This process, along with relevant data on the equipment, makes it possible to calculate the hydraulic conductivity with the use of Eq. 8. Due to the time efficiency of the falling head setup, it became the method of choice throughout this study.

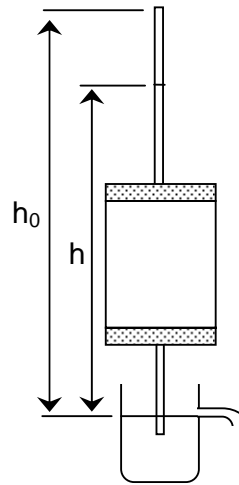


Fig. 8. Falling head permeameter setup.

$$\text{Eq. 8} \quad K = \frac{d_t^2 L}{d_c^2 t} \ln \left(\frac{h_0}{h} \right)$$

- K , Hydraulic conductivity (L/T)
- L , Length of cell (L)
- h_0 , Initial pressure head (L)

- h , Final pressure head (L)
 t , Time elapsed between h_0 and h (T)
 d_i , Inner pressure head tube diameter (L)
 d_c , Inner cell diameter (L)

Example

Initial pressure head at 1.0 m. Pressure head has fallen 0.5 m. in 1 hour.

$$K = \frac{(8.0E - 3)^2 * 0.167}{0.102^2 * 3600} \ln\left(\frac{1.0}{0.5}\right)$$

$$K = 2.0E - 7 \text{ m/s}$$

2.5.3 Vacating the Permeameter Cell

After permeability was determined for each sample, the cell was vacated. Its contents were carefully removed and the total mass weighed.

2.6 Grain Size Analysis

Two sets of samples were analyzed with regard to grain size distribution. The first set of samples consisted of the original soil products as obtained from the manufacturer. The manufacturer's product information constituted the main source of information upon which distribution ratios were estimated. To validate the estimated results, grain size characteristics of this first sample set were analyzed.

The second set contained two samples from the final soil mixture, one from the top and one from the bottom of the sample. These samples were compared to indicate whether the mixture was subject to eluviation.

Grain size distributions of all samples, except for the *GEBA*, were determined by Sedigraph analysis. Prior to testing, each sample was dispersed in a solution containing 0.05M $\text{Na}_4\text{P}_2\text{O}_7$ (Tetrasodium pyrophosphate). The samples were not treated with an ultra-sonic probe. The *GEBA* was sieved in accordance to Swedish Standard, Sieving (SIS, 1978), as it contained particles of excessive size to that processed

by the Sedigraph unit. This sample was not dispersed in any solution or by ultra-sonic probe prior to analysis. Due to the very high content of quartz, ca 99%, no attempts were made to remove organic content.

3 Modeling Permeability

A model was developed to predict mass percent ratios of the available distributions as a function of hydraulic conductivity.

3.1 Model Outline

The process by which suitable content ratios were estimated consisted of a two level procedure (Fig. 9): use of a predictive equation, and use of a grain size distribution model.

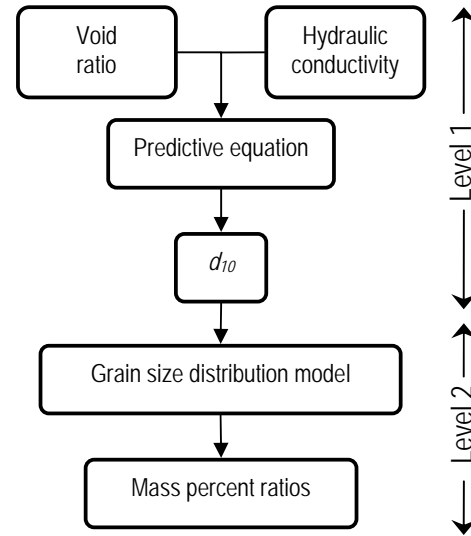


Fig. 9. Flow chart describing the modeling process.

3.1.1 Level 1

In Level 1, an extended version of Hazen's Equation is used. This equation is designed for predicting saturated hydraulic conductivity of nonplastic soils, ranging in grain size between silty sand to coarse sand (Hazen, 1911). The predicting equation (Eq. 11) requires knowledge of void ratio (e) and effective grain size (d_{10}) to determine saturated hydraulic conductivity (K_s). Since void ratio and hydraulic conductivity are known factors in this study, it is possible to rearrange the equation and solve for d_{10} .

3.1.2 Level 2

Level 2 consists of using a grain size distribution model to determine the required ratio of each product to be used in the target mixture. Since the silt distributions do not differ much in the d_{10} interval, it is important that the curves describing these distributions are plotted using a probability scale in the cumulative diagram (Fig. 17). This scale emphasizes the extreme intervals. An existing macro was retrieved from the internet and modified to plot the distribution curves of each material. The macro was modified to automatically produce the resulting grain size distribution curve from the selected mass percent ratios of each distribution (Fig. 17).

The resulting grain size distribution is achieved by performing a series of calculations exemplified in Fig. 10 (Spencer, 1963). The calculations are simple; however, the sheer number of calculations needed to combine four different distributions on a trial and error basis is tremendously facilitated by an automated process, as with the modified macro.

Example

Two distributions, I and II, are mixed at equal mass percent ratios. Point A and B are the results of multiplying the cumulative mass percent, at the respective grain size diameter, of I with the respective mass percent for the new mixed sediment distribution. The same procedure is repeated for II and the resulting terms are added.

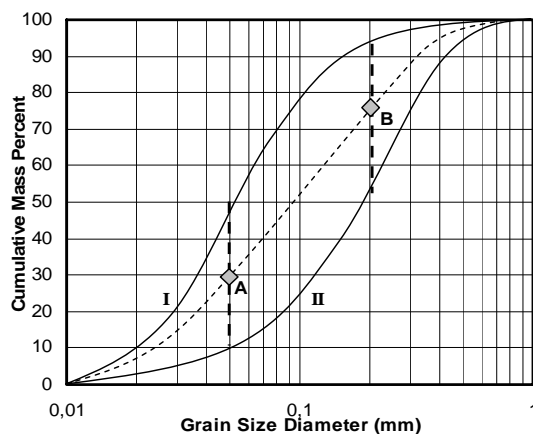


Fig. 10. A mixture containing 50 percent of I and II each is represented by points A and B.

$$A = (0.10 \cdot 0.50) + (0.50 \cdot 0.50) = 30\%$$

$$B = (0.55 \cdot 0.50) + (0.95 \cdot 0.50) = 75\%$$

The model (exemplified with final results in Fig. 17) was based on grain size distributions collected from product information data sheets. The value of d_{10} , estimated in Level 1 was marked into the probability plot. Distribution ratios were then adjusted until the resulting curve cut through the d_{10} mark. This concluded the procedure of estimating distribution mass percent ratios as a function of hydraulic conductivity and void ratio.

4 Results

Applying approximately the same amount of energy during each compaction procedure, it was discovered that a water content of 10 percent resulted in $\rho_d = 1.65 \text{ t/m}^3$. At constant mass percent ratios, increasing the water content to 12 percent increases the density to $\rho_d = 1.70 \text{ t/m}^3$ for the same soil composition. Increasing the water content to 15 percent tends to create fractures in the material during compaction. Since a higher density creates a lower hydraulic conductivity than would a less compacted material at the same content ratios (Dane and Topp, 2002), it seems justified to investigate the hydraulic conductivity at a dry bulk density of $\rho_d = 1.70 \text{ t/m}^3$ in addition to the initially suggested density.

4.1 Measured Hydraulic Conductivity

Initially, permeameter tests were run on 21 different samples. Six samples were tested at $\rho_d = 1.65 \text{ t/m}^3$ and eight at $\rho_d = 1.70 \text{ t/m}^3$. The remaining tests were omitted from further consideration here due to unrepresentative compaction results. Results are presented in Table 2 together with data on distribution ratios, dry bulk density and effective grain size. Complete data on every test are presented in Appendix I.

Table 2. Measured hydraulic conductivities and material properties.

Sample ID	K_s m/s	Ratios GGBA/2500/4900	d_{10} μm	ρ_d t/m^3
B	1.1E-06	30/50/20	5.9	1.65
C	1.0E-06	20/36/30	5.5	1.64
E	7.1E-07	18/42/40	4.9	1.65
F	4.5E-07	12/38/50	4.8	1.64
G	3.1E-07	12/38/50	4.7	1.69
H	3.0E-07	6/34/60	4.6	1.65
I	2.4E-07	0/30/70	4.5	1.65
K	2.3E-07	0/0/100	4.6	1.71
M	3.2E-07	24/16/60	5.0	1.71
N	3.0E-07	12/8/80	4.6	1.69
Q	3.4E-07	9/31/60	4.6	1.70
R	1.8E-07	9/16/75	4.6	1.70
S	2.2E-07	9/6/85	4.5	1.70
U	4.8E-07	24/46/30	5.5	1.70

To illustrate the relationship between permeability and grain size, the measured hydraulic conductivities are plotted as a function of effective grain size at two different dry bulk densities (Figs. 11 & 12). As expected from USACE (1986), the increase in effective grain size progressively declines with increased hydraulic conductivity. This curvature of the trend line is somewhat difficult to perceive in Figs. 11 & 12 due to the narrow intervals of the hydraulic conductivity and the effective grain size. Furthermore, it is also apparent that the importance of effective grain size is subordinate to that of dry bulk density, i.e. compaction has a greater influence on hydraulic conductivity than effective grain size at this range of grain diameters.

Measured results reveal the impossibility of achieving the desired $K_s = 1.0\text{E-}7$ m/s at either dry bulk density. The finest mixture at $\rho_d = 1.65 \text{ t/m}^3$, with content ratio of 6 percent FSG, 34 percent 2500 and 60 percent 4900 yields $K_s = 3.0\text{E-}7$ m/s (sample H). At $\rho_d = 1.70 \text{ t/m}^3$, a content ratio of 100 percent of the 4900, reduced the measured hydraulic conductivity to $K_s = 2.3\text{E-}7$ m/s, in the process disregarding every boundary condition (sample K).

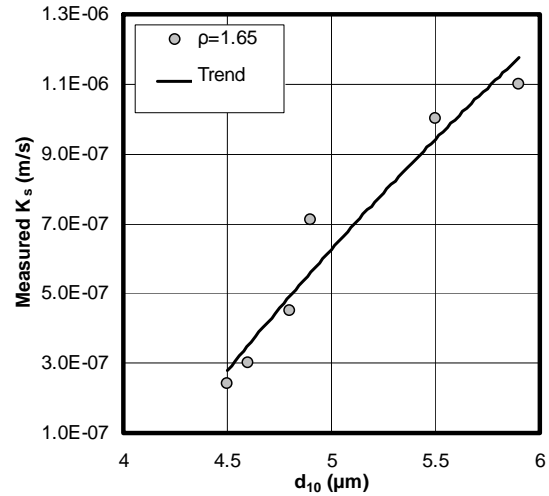


Fig. 11. K_s as a function of d_{10} at $\rho_d = 1.65 \text{ t/m}^3$.

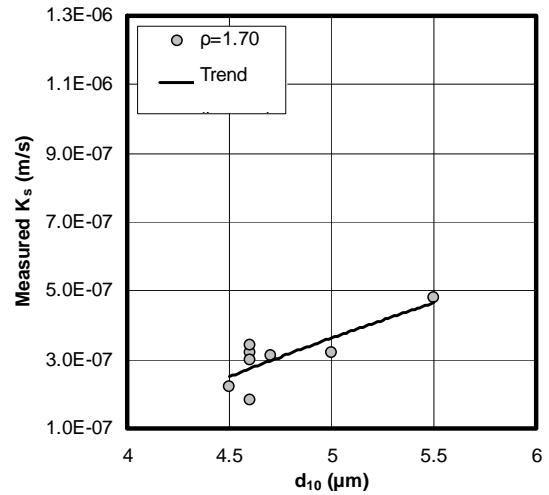


Fig. 12. K_s as a function of d_{10} at $\rho_d = 1.70 \text{ t/m}^3$.

4.2 Estimating Permeability

The compiled measured hydraulic conductivity data make it possible to extrapolate the results and subsequently predict the effective grain size of a soil mixture for a selected hydraulic conductivity. This possibility is pursued to find a suitable soil mixture with hydraulic conductivity beyond the measured results.

4.2.1 Extended Equation of Chapuis

Chapuis developed an equation based on tests performed on various noncohesive materials ranging from silty sands to clean coarse sands (Chapuis, 2004). This equation predicts hydraulic conductivity with good results in the interval of $1\text{E-}7$ m/s to

1E-2 m/s. Chapuis found a relation between parameters from Hazen's Equation (Eq. 6) and the Kozeny–Carman equation (Eq. 5). This relation is quoted below and referred to as Eq. 9.

'According to the Kozeny–Carman equation [Eq. 5], the K value depends linearly on S^{-2} , where S is the specific surface, and on the ratio $e^3/(1+e)$. According to REF EQ, the term d_{10}^2 in the Hazen equation corresponds to $S^2 e^3_{max}/(1+e_{max})$. Thus it was considered that there should be some relationship between an experimental K value and the parameter $x = d_{10}^2 e^3/(1+e)$ [Eq. 9]. Plotting the experimental data reveals that $\log K$ is linearly related to $\log x$. This is a power-law relationship that was determined by a best-fit technique to be

$$[\text{Eq. 10}] \quad K(\text{cm/s}) = 2.4622 \left(\frac{d_{10}^2 e^3}{1+e} \right)^{0.7825}$$

where d_{10} is in mm.' (Chapuis, 2001)

Plotting the measured results against Eq. 10 proves a poor relationship between Chapuis' equation and the measured results (Fig. 13).

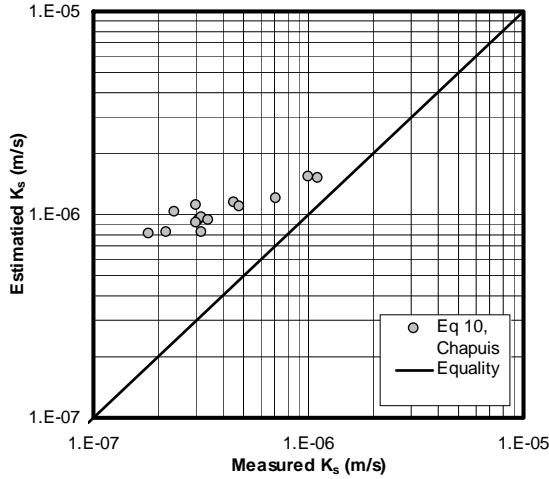


Fig. 13. Measured hydraulic conductivity compared to results estimated by Eq. 10.

4.2.2 New Predictive Equation

Following the procedure quoted in chapter 4.2.1 produced a new equation adapted for the materials used in this study. Plotting the measured hydraulic conductivities as a function of Eq. 9 revealed a linear relationship between $\log K_s$ and x (Fig. 14). This is an exponential relationship

determined by a best fit technique (Eq. 11). The result is different from that of Chapuis in that he found a linear relationship between $\log K_s$ and $\log x$, described by a power-law relationship.

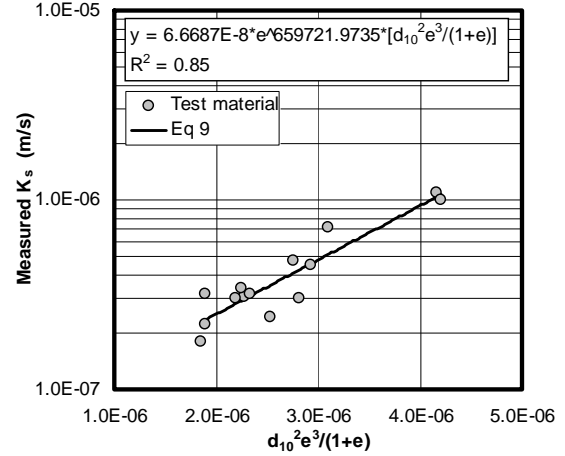


Fig. 14. Measured hydraulic conductivity as a function of Eq. 9.

Eq. 11

$$K_s(\text{m/s}) = 6.6687E-8 \times e^{659721.9735 \left[\frac{d_{10}^2 e^3}{1+e} \right]}$$

Rearranged

Eq. 12

$$d_{10}(\text{mm}) = \sqrt[659721.9735]{\frac{\ln \left(\frac{K_s}{6.6687E-8} \right) \times (1+e)}{e^3}}$$

Plotting measured results as a function of Eq. 11 reveals a considerably improved estimation of hydraulic conductivity (Fig. 15). As a result of this, Eq. 12 is used to predict a value of the effective grain size for a potential soil mixture.

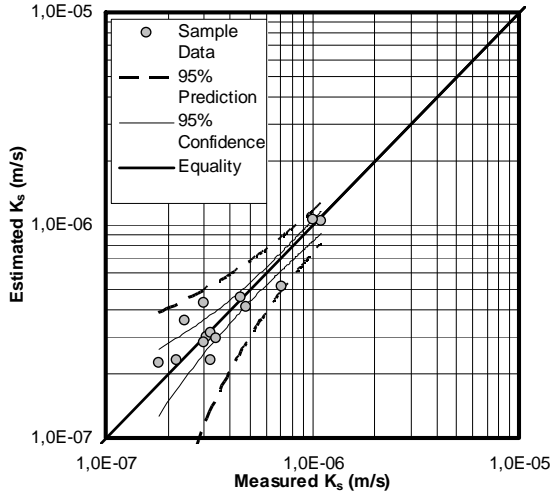


Fig. 15. Measured K_s relative to K_s predicted by Eq. 11.

4.2.3 Predicting Suitable Soil Mixture

A mixture of the *GEBA*, the 2500 and the 4900 did not yield a low enough hydraulic conductivity during the specified conditions. Therefore, distribution ratios of the target mixture needed to be estimated. The following properties were assumed for the target soil mixture:

- $K_s = 1.0E-7$ m/s
- $\rho_d = 1.65$ t/m³
- $e = 0.59$

Rearranging Eq. 11 with respect to d_{10} calculates the effective grain size as a function of hydraulic conductivity and void ratio. Applying the assumed properties to Eq. 12 then yields the following expression:

$$d_{10} = \sqrt[3]{\frac{\ln\left(\frac{1.0E-7}{6.6687E-8}\right) \times (1 + 0.59)}{659721.9735 \times 0.59^3}}$$

$$d_{10} = 0.0022 \text{ mm} = 2.2 \text{ } \mu\text{m}$$

This result agrees with the fact that the effective grain size of the finest fraction, the 4900, is given by the manufacturer to be noted at 4.8 μm . This implies that it is not feasible to reach the desired $K_s = 1.0E-7$ m/s with the original materials provided and the advised parameters. To obtain a mixture where $d_{10} = 2.2 \text{ } \mu\text{m}$, a new distribution must be introduced. This material would need to have an effective grain size of less than 2.2 μm since presence of fine sand, the *GEBA* material, is a required element in the mixture.

A derivative of the *GEBA*, named *Dorosilit 10000*, herein simply referred to as the 10000, and with the following characteristics, was selected for evaluation. The grain size distribution is presented in Fig. 16.

Dorosilit 10000

- Coarse silt
- Skewness: Fine skewed
- Peakedness: Mesokurtic
- $d_{10} = 1.9 \text{ } \mu\text{m}$
- Poorly sorted
- Mean: Medium silt
- Bimodal

The calculated $d_{10} = 2.2 \text{ } \mu\text{m}$ was plotted in the cumulative probability diagram. The mass percent ratios of the four distributions were then adjusted until the resulting distribution curve intersected the plotted d_{10} (Fig. 17).

The determined ratios are:

- *FSG* 15%
- *GEBA* 9%
- 2500 6%
- 2500 5%
- 4900 5%
- 10000 75%

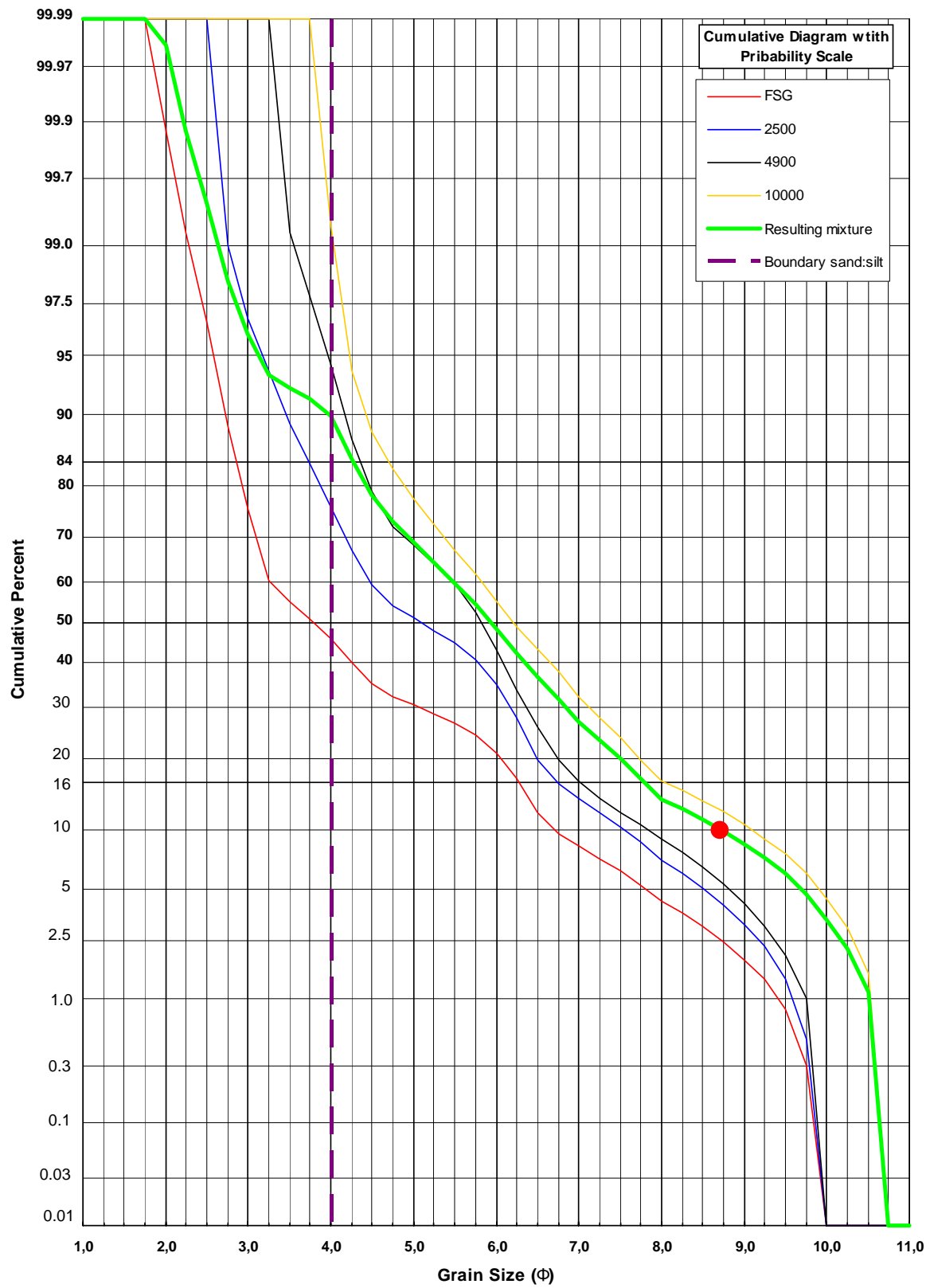


Fig. 16. Grain size distributions and resulting soil mixture at the predicted distribution ratio 15/5/5/75. Note the resulting mixture intersecting the plotted value of d_{10} .

The opportunity arose to validate the estimated results through experiments using a sample of the 10000 product. Applying the predicted distribution ratios in a new soil mixture resulted in a measured hydraulic conductivity of $K_s = 1.7\text{E-}7$ m/s.

○ FSG	5%
GEBA	3%
2500	2%
○ 2500	0%
○ 4900	5%
○ 10000	90%

4.3 Designing the Final Mixture

To attain the boundary condition of $K_s = 1.0\text{E-}7$ m/s, some of the initial conditions have to be compromised. The FSG ratio is kept to a minimum as it contains fine sand that contributes to increased hydraulic conductivity. However, the FSG is not fully omitted. The SERDP project group strongly recommended that it be included to facilitate mixing of the materials during set-up prior to the large-scale test. The additional quantity of the 2500, which was originally added to that amount present in the FSG (see 1.3) and included to avoid eluviation, is removed in the final mixture in favor of the 10000.

Considering the above factors, the closest possible hydraulic conductivity measures $K_s = 1.4\text{E-}7$ m/s at the following mass percent ratios:

4.4 Grain Size Analysis

Grain size analysis was applied to two sets of samples for different purposes: verification of provided grain size distribution curves, and to check for eluviation. Unfortunately, no detailed particle shape analysis could be carried out due to time restrictions. However, the distributions were examined in a 200X magnification microscope. At that magnification the depth of field was very limited, which made it difficult to distinguish separate particles from aggregates. Larger particles were possible to single out at lesser magnification. These appeared to be of high sphericity, sub angular. A scanning electron microscope (SEM) could potentially provide more accurate data on particle shape.

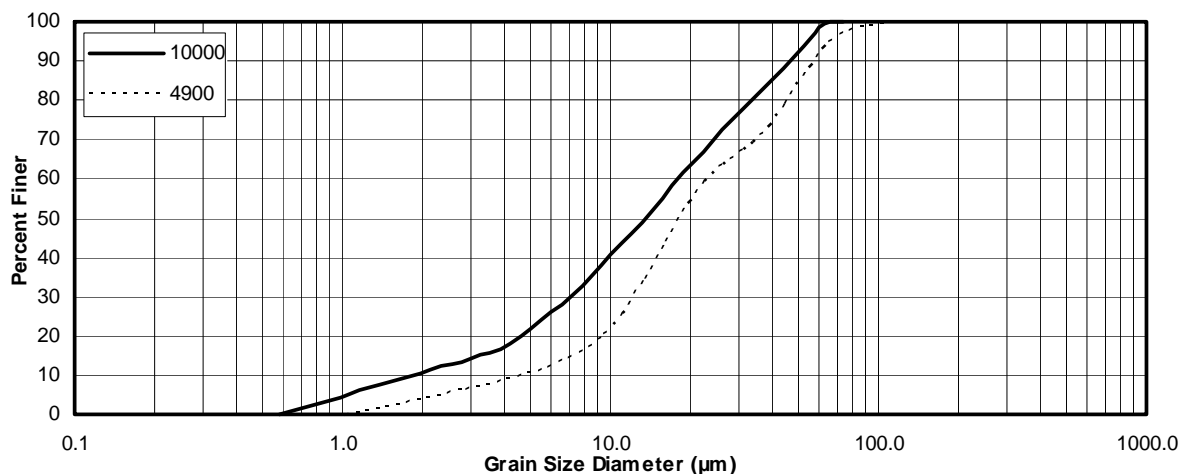


Fig. 17. Grain size distribution of the 10000, derived from manufacturer's data. The 4900 is included for reference.

4.4.1 Verification of Product Data

Each material used in this study was analyzed to verify the product data provided by the manufacturer. Although only the manufacturer's data have been used for the grain size distribution modeling procedure, the verification of size distributions is considered important as background information. The SERDP project group will eventually need to make detailed evaluations of these and other results, including possible sources of error. The measured results for each tested distribution are plotted along with the corresponding product data provided by the manufacturer (Figs. 18-22). The Sedigraph data were also compared to manufacturer's data with respect to the statistical parameters of Folk and Ward (1957) (Table 3).

The measured 2500 (Fig. 18) distribution is notably above the indicated values of the manufacturer's data, by as much as 15 percent. The 4900 (Fig. 19) on the other hand measures slightly lower than the plotted manufacturer's data, at the most 10 percent, although, the overall result appears to be a good match. The measured result of the 10000 (Fig. 20) is a very close match to the product data as is the *GEBA* (Fig. 21). The final soil mixture (Fig. 22) consistently measures slightly higher values, and more so in the coarser grain sizes, than the corresponding calculated data, the latter being a result of the different manufacturer's data.

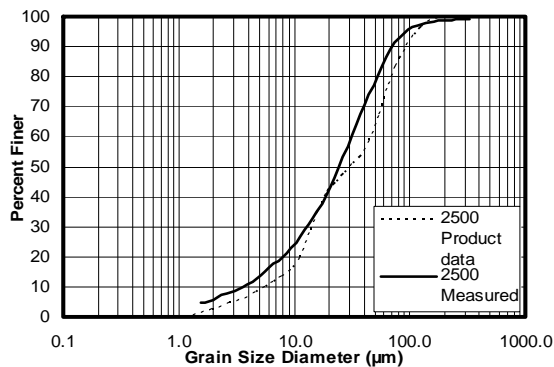


Fig. 18. Sedigraph data of the 2500.

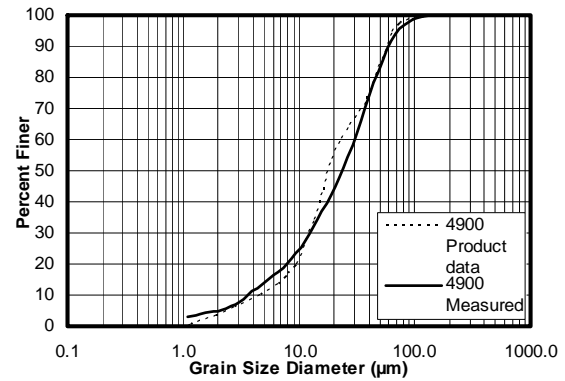


Fig. 19. Sedigraph data of the 4900.

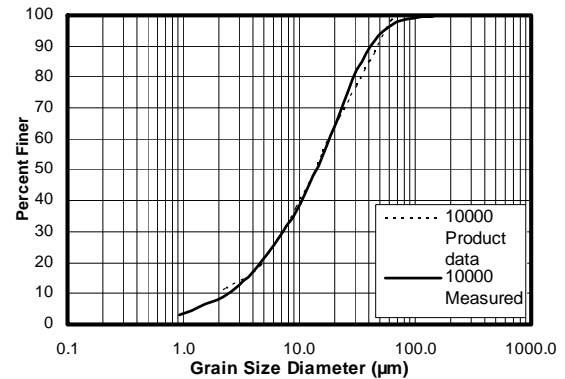


Fig. 20. Sedigraph data of the 10000.

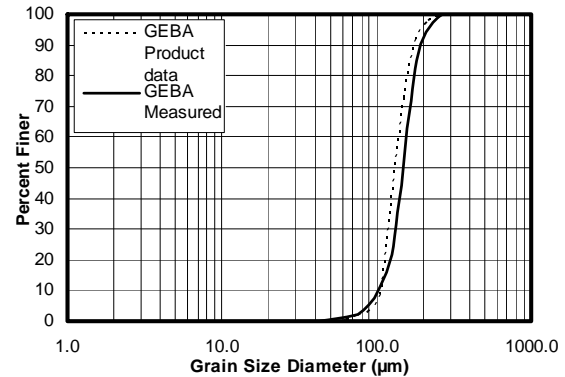


Fig. 21. Sedigraph data of the *GEBA*.

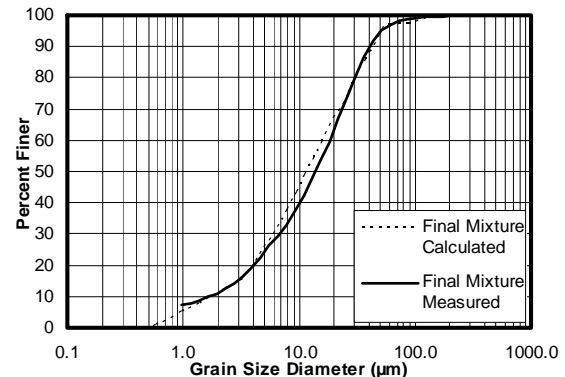


Fig. 22. Sedigraph data of the final soil mixture.

Table 3. Comparison of grain size distribution between product data (upper) and measured data (lower).

Product data	Sediment type	Mean	Modality	Sorting	Skewness	Kurtosis	d_{10} μm
Measured data							
GEBA	Well Sorted Fine Sand	Fine Sand	Unimodal	Well Sorted	Coarse Skewed	Leptokurtic	106
	Well Sorted Fine Sand	Fine Sand	Unimodal	Well Sorted	Fine Skewed	Leptokurtic	99
2500	Very Fine Sandy Very Coarse Silt	Coarse Silt	Bimodal	Poorly Sorted	Fine Skewed	Mesokurtic	5.3
	Very Fine Sandy Very Coarse Silt	Coarse Silt	Unimodal	Poorly Sorted	Fine Skewed	Mesokurtic	5.2
4900	Medium Silt	Coarse Silt	Bimodal	Poorly Sorted	Symmetrical	Mesokurtic	4.8
	Very Coarse Silt	Coarse Silt	Unimodal	Poorly Sorted	Fine Skewed	Mesokurtic	5.1
10000	Coarse Silt	Medium Silt	Bimodal	Poorly Sorted	Fine Skewed	Mesokurtic	1.9
	Coarse Silt	Medium Silt	Unimodal	Poorly Sorted	Fine Skewed	Mesokurtic	3.0
Final Mixture	Medium Silt	Medium Silt	Bimodal	Poorly Sorted	Fine Skewed	Mesokurtic	2.0
	Coarse Silt	Medium Silt	Unimodal	Poorly Sorted	Fine Skewed	Mesokurtic	3.2

4.4.2 Eluviation

During the course of this study, the issue of eluviation in the soil mixture has been raised by the SERDP project group. Therefore, a comparison between the conditions at the top and bottom of the permeameter sample was made, after the testing procedure had been concluded.

The results do not indicate any particle movement as a result of fluid flow within the sample (Fig. 23). The amount of fluid potentially eroding the sample was measured. After saturation of the sample, the under pressure contained within the cell drew another 111 cm³ of water before equilibrium set in and the collected amount of fluid equaled that which drained into the sample per time unit. During the tests runs, a total of 83 cm³ drained into the sample.

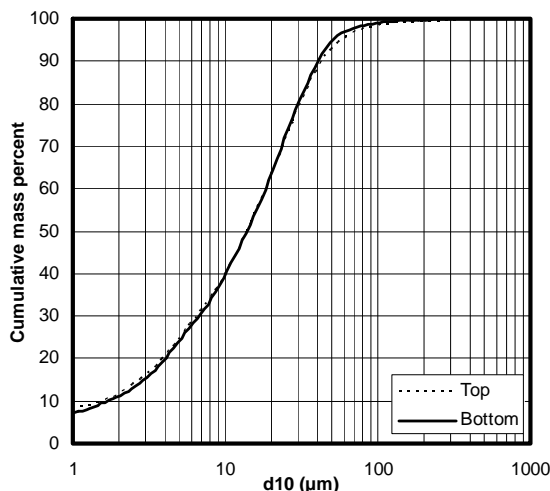


Fig. 18. Comparison of top and bottom section of the final soil mixture.

5 Discussion

It is important to recognize that many parameters affecting hydraulic conductivity interact to create the unique properties of each soil mixture employed in this study. Therefore, no parameter can independently describe the overall effect on hydraulic conductivity (Masch and Denny, 1966).

5.1 Inaccuracies in Manufacturer's Data

As indicated in Figs. 19-22, the grain size distributions appear to vary to some extent between product data and measured results. The 10000 curves are almost identical, as are much of the two distribution curves for the 4900. However, the differences between the 2500 product data and the corresponding measured data are up to 15 percent in the coarser fractions.

Comparing the 2500 and the 4900 reveals another unexpected result; the two distributions appear to be much more similar than indicated by the product data. In fact, they are nearly identical. A closer look at the distribution curves reveals an even more striking difference. Namely, the measured values of the 2500 and the 4900 indicate unimodal distributions in contrast to the corresponding bimodal manufacturer's data. Frequency diagrams clearly illustrate that the measured data contrast with the bimodal product data (Figs. 24-27). According to Masch and Denny (1966), a lower permeability can be expected from a bimodal

distribution than from a unimodal distribution. Only if the materials originally used for product data and those used in this study were to be compared during identical circumstances would the difference in permeability possibly be revealed.

The modality differences can possibly be explained by an effect similar to that used to explain how natural sediments are a product of only a few separate populations (Spencer, 1963). Mixing two distributions which have a small amount of the same sized grains in common (the distribution curves overlap to some degree) results in a bimodal distribution. Suppose that the products used in this study, which show a clear bimodal distribution curves, are the result of mixing together two different industrially manufactured fractions. That would be a possible explanation to the bimodal appearance. In this case, why do the measured Sedigraph results not agree? To answer that question it is necessary to obtain detailed information on the industrial manufacturing process. Available information states that the quartz is ground and then sorted by airflow. Common sense suggests that sorting particles with near perfect reproducibility requires a very uniform airflow. Suppose then that the air flow is not as accurate as desired. For example, the level of air flow may have changed slightly following calibration. Two grain size distribution curves could then overlap to a greater degree than intended. At a certain point, such overlap will be large enough to result in one unimodal curve. This may be of little significance to the manufacturer as these products have their main use in glass industry. From a grain size distribution perspective, however, this discrepancy is far more significant as it could affect the hydraulic conductivity. If these were natural sediments the differences in modality would have provided a false explanation of their implied provenance.

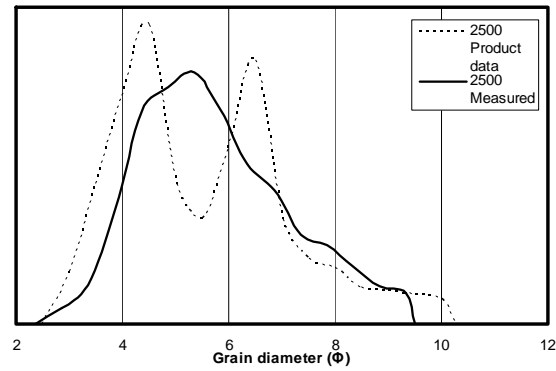


Fig. 19. Comparison of modality, 2500.

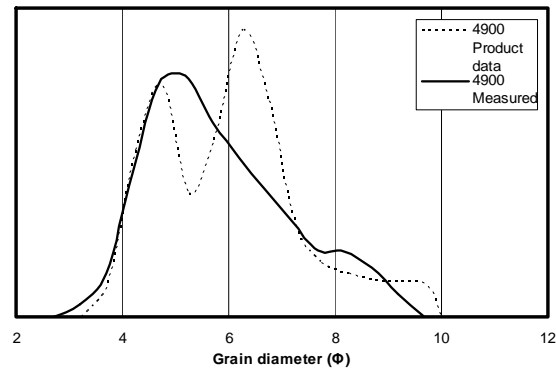


Fig. 20. Comparison of modality, 4900.

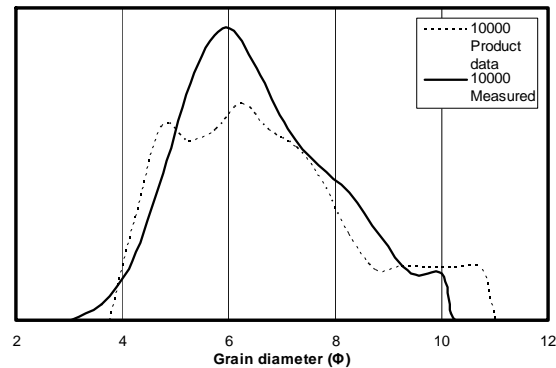


Fig. 21. Comparison of modality, 10000.

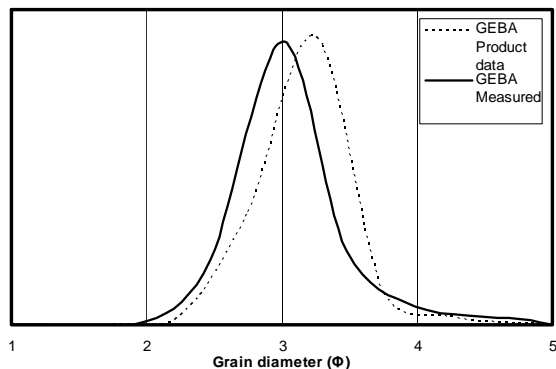


Fig. 22. Comparison of modality, GEBA.

5.2 Method and Measured Results

Ideally, the measured hydraulic conductivity results should demonstrate complete correlation when plotted as a function of Eq. 11. It is evident from Fig. 15 that this is not completely true. There are several possible explanations to this, the most significant being saturation and compaction.

5.2.1 Saturation

During the course of the experiments, saturation of soil samples was obtained using a vacuum pump. This technique was deemed appropriate for the needs of the experiment; however, some variance between the measured results and the calculated hydraulic conductivity values is still apparent. A possible explanation of this variance is that air that may have become trapped in the sample.

Trapped air inside the sample decreases the effective area through which fluid flow can take place, resulting in a lower permeability (Lind, 1999). By applying a negative pressure (suction), air trapped in the pores will be minimized, allowing a greater level of saturation to be achieved. Since this procedure is suggested in Swedish Standard, Determination of Permeability (SIS, 1989), it is assumed that this method satisfactorily saturates the sample.

Fully restoring atmospheric pressure inside the cell after the applied vacuum pressure has been removed is another issue that may affect variance in the results. During the initial phase of the experiments, fluid arose into a tube on the top of the cylinder. After the vacuum pump had been switched off, additional water was poured into the fluid input chamber, yet no water drained from the sample. This indicated there was still a vacuum inside the cell. On average, about 100 cm³ drained into the sample before equilibrium was reached. Failing to correctly measure the input and output amount of fluid could potentially lead to a miscalculation of permeability. However, throughout the experiments carried out in this study, each test run was repeated until the results were consistent.

5.2.2 Compaction

The compaction procedure did not follow a published standard procedure since the equipment required was unavailable. The light hammering of the material, periodically added to the cell as each added amount was fully compacted, allows for a potentially non-uniform compaction throughout the sample column. It is important to note that if $\rho_d = 1.65 \text{ t/m}^3$ is the average density of the entire cylinder, density can vary within each compacted layer. On the other hand, densities close to those of the estimated proctor density were used. Therefore, if the targeted dry bulk density was achieved, a relatively uniform compaction should be ensured throughout the sample. If, however, the target density is not reached, there is no such assurance that that density is representative for each layer in the cylinder.

The significance of density is illustrated in Figs. 28 & 29. Void ratio is thought of as a combined result of density (i.e. compaction) and grain size distribution (represented here by d_{10}). A well compacted material has a lower void ratio than a loose material, the pores of the former being more compressed. However, a grain size distribution containing a larger amount of fines more readily fills the pore space between larger particles, resulting in a lower void ratio than would a coarser distribution (Hillel, 1998). This finding can be interpreted as analogous to that of Mash and Denny. (1966) where the significance of dispersion is explained as having a greater impact on hydraulic conductivity at higher values of d_{50} , where finer grains more readily can fill out the voids between grains. The analogy to Figs. 28 & 29 is that at $\rho_d = 1.65 \text{ t/m}^3$ the pores should be larger and thus more receptive to inter-granular clogging by smaller particles, d_{10} , than would be the case at $\rho_d = 1.70 \text{ t/m}^3$.

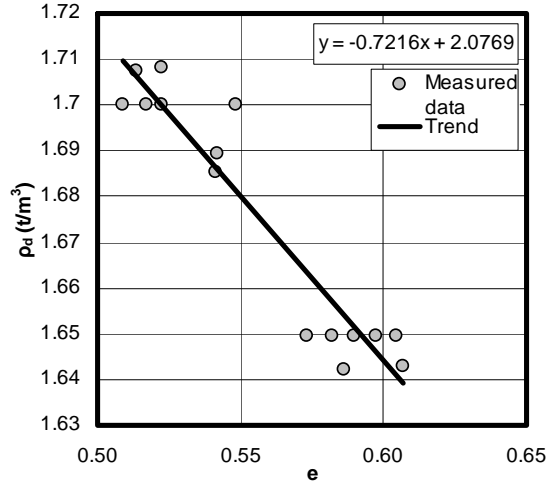


Fig. 23. Void ratio as a function of dry bulk density.

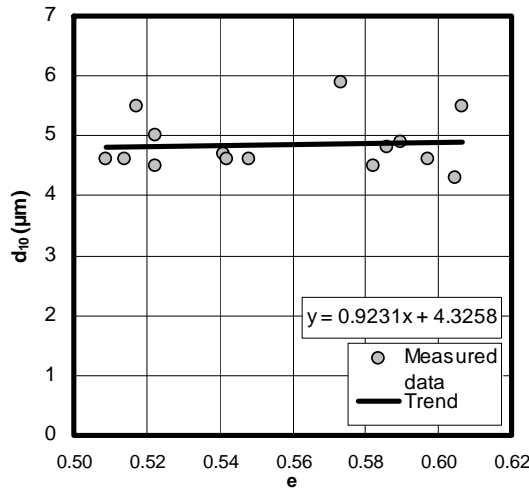


Fig. 24. Void ratio as a function of effective grain size.

5.3 Modeled Results

The modeling procedure in which proper distribution ratios are determined involves several steps. This makes the process vulnerable to cumulative errors. Specifically, the steps that are thought to have a significant impact on the modeled result are firstly the parameters related to measured hydraulic conductivities and secondly the grain size distribution model. In addition, it is likely that focusing on the narrow interval of $1.0\text{E-}7 < K_s < 1.0\text{E-}6$ m/s limits the applicability and accuracy of the predictive results.

5.3.1 Predictive Equation

Since the results measured during the permeability tests serve as the sole source of background information upon which Eq. 11 is based, they play an important role in modeling a potential soil mixture. Even though inconsistency among the results is reduced by excluding unrepresentative data, there is of course a certain degree of variation among the results.

To reach an understanding of how well an equation fits the data that it is meant to describe, one can refer to the R^2 value. R^2 is a dimensionless ratio and varies between 0.0 and 1.0. The goodness-of-fit increases with an increased R^2 value. Perfect correlation is obtained at 1.0 while the opposite, 0.0, indicates a complete lack of correlation (Motulsky and Christopoulos, 2003).

It is also important to consider the 95% confidence intervals. The 95% *confidence interval* confines the area in which there is a 95% chance of finding the regression line. This does not mean that 95% of the measured data is expected to fall within these boundaries. These boundaries are however illustrated by the 95% *prediction interval* (Motulsky and Christopoulos, 2003). These intervals are measures of how well the regression line predicts the results. Consider an R^2 value of 1.0 obtained from only two data points. This situation would create very narrow 95% prediction interval meaning that any added data points would be likely to end up outside that interval, thus the regression line provides a poor prediction. The R^2 value for Eq. 11 is 0.85, which indicates that this equation is an acceptable fit. Plotting K_s calculated from Eq. 11 as a function of measured K_s yields $R^2 = 0.91$, an even better fit than Eq. 11. All of the predicted and measured data values are located within the 95% prediction interval, acceptably excluding the risk for a random distribution of data.

To use Eq. 12 it is essential to input a representative void ratio, e . Since it is a predictive equation, the idea is to input estimated values with ample accuracy. The value of e changes in response to compaction and grain size distribution. As a result of the

moderate changes in grain size distribution for the different mixtures used in this study, the significance of distribution to void ratio was overcome by that of compaction (Figs. 28 & 29). Due to the sensitive response of e as a function of ρ_d , mean values for void ratio are established for narrow intervals of dry bulk density from empirical determinations.

5.3.2 Grain Size Distribution Model

The distribution model used to determine the ratios of the different products is another key feature of the modeling process. This distribution model is based on manufacturer's product data, which has been previously described as a rather questionable match to the measured results of the 2500. Hence, there is some uncertainty regarding its accuracy for determining the proper ratios to obtain the targeted value of hydraulic conductivity.

5.3.3 Introducing a New Distribution

Eq. 11, developed for determining a value of d_{10} , is based on the results of tests carried out on samples containing the *GEBA*, 2500 and 4900. It is prudent to consider the possibility that Eq. 11 is not applicable for mixtures containing other elements than those from which the data originated. Therefore, estimating properties of a mixture containing the 10000, in addition to the original distributions, raises the question of whether the predictive results are reliable. Similarly to results presented in Fig. 15, three mixtures were created from the original distributions and the 10000. Their measured hydraulic conductivities are plotted against those estimated by Eq. 11 (Fig. 30). These results plot slightly farther from equality, indicating a less accurate estimation for samples containing distributions other than those originally included. A possible explanation for this could be the smaller effective grain size of the 10000; fines play a greater role in affecting permeability as they serve to fill out the pore space between larger particles. Also, the 10000 is slightly more poorly sorted; a greater dispersion creates a denser soil matrix subsequently lowering the hydraulic

conductivity. The 2500 and the 4900 are the main distributions in the initial test samples, being the chief distribution in the final mixture. The 10000 could therefore bring unforeseen results.

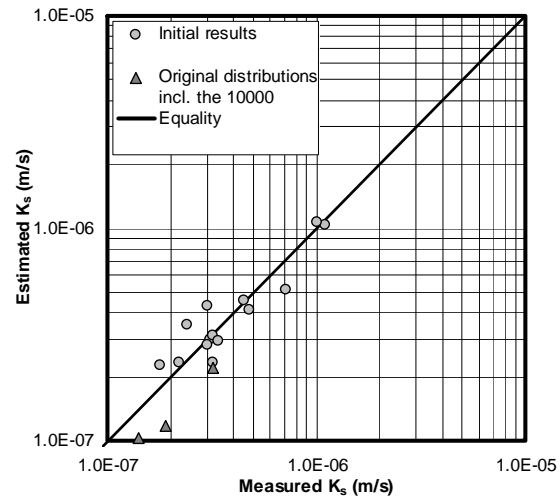


Fig. 25. Original distributions including the 10000 plotted as a function of Eq. 11.

The difference in effective grain size between manufacturer's data and measured results is approximately 1 μm (see 4.4.1), resulting in a notable change in hydraulic conductivity. Herein also lies the reason why the measured results cannot quite reach the preferred hydraulic conductivity. The finest distribution, the 10000, simply does not possess a sufficiently small effective grain size. Manufacturer's data indicates $d_{10} = 2.0 \mu\text{m}$ while measured data point toward $d_{10} = 3.2 \mu\text{m}$, i.e. larger than the predicted effective grain size.

5.4 Eluviation

No attempts were made to estimate eluviation from a mathematical standpoint (Chapuis et al., 1996) as investigation of this issue is not included in the objectives of this study. A rather simplistic test was run to check whether the final soil mixture was prone to eluviation. The negative result should be considered an indication rather than a definite answer. It is possible that the end result would have come out differently if a more substantial amount of fluid had

percolated through the sample. However, the author hypothesizes that the majority of particle transport within the sample occurs at an initial stage of fluid flow. In this case, it is possible that internal erosion would also take place during saturation as an effect of the elevated flow rate due to the applied vacuum. However, it is thought that the overall effect of the wide dispersion in the final soil mixture, spanning from clay sized particles in the 10000 to fine sand in the GEBA, prevents eluviation as smaller particles fill out the pore space between larger ones, hence interlocking the soil matrix.

6 Conclusion

The initial results reveal the impossibility of achieving the preferred $K_s = 1.0\text{E-}7$ m/s at $\rho_d = 1.65$ t/m³. Respecting the boundary conditions, the lowest hydraulic conductivity emerges at a mixture of 6 percent FSG, 34 percent 2500 and 60 percent 4900, measuring $K_s = 3.0\text{E-}7$ m/s. Disregarding the boundary condition concerning cost efficiency and eluviation, a mixture of 100 percent 4900 yields $K_s = 2.3\text{E-}7$ m/s.

Eq. 11 provides a possibility for estimating effective grain size as a function of hydraulic conductivity and void ratio for the materials used in this study with good accuracy. The modeled result indicates that a mixture with $d_{10} = 2.2$ μm would yield the preferred hydraulic conductivity. The modeled result was validated using an actual sample of the 10000. This showed that a slightly smaller effective grain size was needed to achieve the targeted hydraulic conductivity. Even when the new finer distribution was added, the preferred hydraulic conductivity was still slightly out of reach. Eventually, it was found that a mixture containing 5 percent FSG, 5 percent 4900 and 90 percent 10000 resulted in $K_s = 1.4\text{E-}7$ m/s. This mixture compromises the boundary conditions in that the recycled FSG is kept to a minimum. Furthermore, no additional 2500 was included to prevent eluviation as the FSG already contains 40 percent 2500. Also, as the grain size analysis indicated only small differences between the

2500 and the 4900, the latter could be considered to compensate for at least parts of the fractions present in the 2500.

Grain size distributions from the top and bottom of the final mixture were compared and did not indicate signs of eluviation. However, it is still unclear whether this result is fully representative as the volume of percolating fluid was of a limited nature (see 4.4.2).

Regarding the factor of cost efficiency, the fact remains that hydraulic conductivity for silts is expected to range between $1\text{E-}8$ m/s to $1\text{E-}6$ m/s. To recycle a greater amount of the FSG, it would be necessary to add a distribution that has an even higher amount of fines than the 10000. Another possibility for recycling a greater amount of the FSG lies in a more detailed investigation of the proctor density of the final soil mixture. A potential finding of a higher proctor density than that approximated for this study would allow for a higher dry bulk density to be used than $\rho_d = 1.65$ t/m³, set as a boundary condition for this investigation. Subsequently, a coarser grain size distribution, i.e. one containing an increased amount of recycled FSG, would result in the same hydraulic conductivity using a lesser amount of fines.

7 References

- Allaby, A. and Allaby, M., (1999), "Oxford Dictionary of Earth Sciences", Oxford University Press, Oxford, UK.
- Baker, R.S., Heron, G., LaChance, J., Hiester, U., Koschitzky, H.-P., Trötschler, O., Färber, A. and Kuhlman, M. (2004). Large-Scale Physical Models of Thermal Remediation of DNAPL Source Zones in Aquifers. Strategic Environmental Research and Development Program (SERDP) FY2005 Proposal No.05 CU04-009. Submitted to SERDP by TerraTherm, Inc., Fitchburg, MA USA.
- Blott, S.J. and Pye, K., (2001), Gradistat: A Grain Size Distribution and Statistics Package for the Analysis of Unconsolidated Sediments, *Earth Surface Processes and Landforms*, vol. 26, 1237-1248.
- Chapuis, R.P., (2004), Predicting the Saturated Hydraulic Conductivity of Sand and Gravel Using Effective Diameter and Void Ratio, *Canadian Geotechnical Journal*, vol. 41, 787-795.
- Chapuis, R.P. and Aubertin, M., (2003), On the Use of the Kozeny-Carman Equation to Predict the Hydraulic Conductivity of Soils, *Canadian Geotechnical Journal*, vol. 40, 616-628.
- Chapuis, R.P., Contant, A. and Baass, K.A., (1996), Migration of Fines in 0-20 mm Crushed Base During Placement, Compaction and Seepage under Laboratory Conditions. *Canadian Geotechnical Journal*, vol. 33, 168-176.
- Dane, J.H. and Topp, G.C., (2002), "Methods of Soil Analysis, Part 4, Physical Methods", Soil Science Society of America, Inc., Madison, WI, USA.
- Fetter, C.W., (2001), "Applied hydrogeology", Prentice-Hall, Upper Saddle River, New Jersey, USA.
- Fagerström, H. and Wiesel, C.E., (1972), "Permeabilitet och kapillaritet, Förslag till geotekniska laboratorieanvisningar, del 8", Stockholm, Swe.
- Folk, R.L. and Ward, W.C., (1957), Brazos River Bar: A Study in the Significance of Grain Size Parameters, *Journal of Sedimentary Petrology*, vol. 27, 3-26.
- Hazen, A.M., (1911), Discussion on Dams on Sand Foundation, by A.C. Koenig, *Transactions of the American Society of Civil Engineers*, vol. 73, 199-203.
- Hillel, D., (1998), "Environmental Soil Physics", Academic Press, San Diego, CA., USA.
- Lind, B.B., (1999), The Influence of Grain Size and Sediment Sorting on the Hydraulic Conductivity of Some Swedish Tills, *GFF*, vol. 121, 107-111.
- Marshall, T.J., (1958), A Relation Between Permeability and Size Distribution of Pores, *Journal of Soil Science*, vol. 9.
- Masch, F.D. and Denny, K.J., (1966), Grain Size Distribution and its Effect on the Permeability of Unconsolidated Sands, *Water Resources Research*, vol. 2, 665-677.
- Motulsky, H.J. and Christopoulos, A., (2003), "Fitting Models to Biological Data Using Linear and Nonlinear Regression. A Practical Guide to Curve Fitting", GraphPad Software Inc., San Diego, CA, USA.
- Spencer, W.S., (1963), The Interpretation of Grain Size Distribution of Clastic Sediments, *J. Sedimentary Petrology*, vol. 33, 180-190.
- Stegemeier, G.L. and Vinegar, H.J., (2001), "Thermal Conduction Heating for In-Situ Thermal Desorption of Soils." Ch. 4.6, 1-37, In: Chang H. Oh (ed.), Hazardous and Radioactive Waste Treatment Technologies Handbook, CRC Press, Boca Raton, FL., USA.

- SIS, (1994), "SS 02 71 08, Geotekniska provningsmetoder: Packningsegenskaper", Sveriges Standardiseringskommission, Stockholm, Swe.
- SIS, (1989), "SS 02 71 11, Geotekniska provningsmetoder: Bestämning av permeabilitet", Sveriges Standardiseringskommission Stockholm, Swe
- SIS, (1978), "SS 02 71 11, Geotekniska provningsmetoder: Kornfördelning. Siktning.", Sveriges Standardiseringskommission, Stockholm, Swe

Appendix I

Sample Specifications

ID	Amount mixed g	Target sample weight, dry g	Residue, moist g	Residue, dry g	Sample weight, dry g	Sample weight, saturated g	Dry bulk density t/m ³	Void ratio	Hydraulic conductivity m/s	Ratio GEBA/2500/4900 /10000
A	3000	X	154	138	1938	2779	1.42	1.61	6.20E-07	24/56/20
B	2500	2250		X	2250	2747	1.65	0.57	1.10E-07	30/50/20
C	2500	2250	10	X	2241	2756	1.64	0.61	1.00E-07	24/36/30
D	2500	2155	X	X	2188	2685	1.6	0.57	3.30E-07	60/40/0
E	2500	2250	X	X	2250	2756	1.65	0.59	7.10E-07	18/42/40
F	2500	2250	X	10	2240	2744	1.64	0.59	4.50E-07	12/38/50
G	2500	2250	X	X	2299	2778	1.69	0.54	3.10E-07	12/38/50
H	2500	2250	X	X	2250	2760	1.65	0.6	3.00E-07	6/34/60
I	2500	2250	X	X	2250	2752	1.65	0.58	2.40E-07	0/30/70
J	2250	2250	X	X	2250	2764	1.65	0.6	2.30E-07	0/0/100
K	2500	X	136	X	2329	2792	1.71	0.51	3.20E-07	0/0/100
L	2500	X	99	X	2485	2791	1.82	0.29	4.20E-07	12/8/1980
M	2500	X	190	171	2330	2798	1.71	0.52	3.20E-07	24/16/60
N	2500	2319	16	15	2305	2784	1.69	0.54	3.00E-07	12/8/1980
O	2500	2387	x	19	2387	2814	1.75	0.46	8.60E-08	12/8/1980
P	2500	2387	X	X	2387	2800	1.75	0.43	1.40E-07	18/12/70
Q	2500	2319	X	X	2319	2802	1.7	0.55	3.40E-07	9/31/60
R	2500	2319	X	X	2319	2779	1.7	0.51	1.80E-07	9/16/1975
S	2500	2319	X	X	2319	2787	1.7	0.52	2.20E-07	9/6/1985
T	2500	2319	X	X	2319	2785	1.7	0.52	3.70E-07	24/46/30
U	2500	2319	X	X	2319	2784	1.7	0.52	4.80E-07	24/46/30
V	2500	2251	X	X	2251	2736	1.65	0.55	6.90E-07	40/20/40
X	2500	2251	X	X	2251	2758	1.65	0.59	4.90E-07	20/10/70
AA	2500	2251	X	X	2251	2741	1.65	0.56	3.20E-07	30/10/20/40
AB	2500	2251	44	40	2211	X	1.62	X	3.70E-07	20/10/15/55
AC	2500	2251	X	X	2251	2766	1.65	0.61	3.10E-07	20/10/15/55
AD	2500	2251	X	X	2251	2754	1.65	0.58	1.90E-07	20/0/15/65
AE	2500	2251	X	X	2251	2763	1.65	0.6	1.70E-07	15/0/10/75
AF	2500	2251	X	37	2214	2732	1.62	0.61	1.10E-07	0/0/0/100
AG	2500	2251	X	21	2230	2733	1.63	0.58	1.40E-07	5/0/5/90

Appendix II

Permeability Tests

Falling Head	a1	a2	a3	a4	a5	a6
T (s)	630	853	960	940	944	938
h₀ (m)	0.6900	0.6900	0.6900	0.6900	0.6900	0.6900
h (m)	0.3900	0.3900	0.3900	0.3900	0.3900	0.3900
t (m)	0.0080	0.0080	0.0080	0.0080	0.0080	0.0080
c (m)	0.1020	0.1020	0.1020	0.1020	0.1020	0.1020
L (m)	0.1670	0.1670	0.1670	0.1670	0.1670	0.1670
K_s (m/s)	9.3E-07	6.9E-07	6.1E-07	6.2E-07	6.2E-07	6.2E-07

Falling Head	b1	b2	b3	b4
T (s)	511	515	511	512
h₀ (m)	0.6900	0.6900	0.6900	0.6900
h (m)	0.3900	0.3900	0.3900	0.3900
t (m)	0.0080	0.0080	0.0080	0.0080
c (m)	0.1020	0.1020	0.1020	0.1020
L (m)	0.1670	0.1670	0.1670	0.1670
K_s (m/s)	1.1E-06	1.1E-06	1.1E-06	1.1E-06

Falling Head	c1	c2	c3	c4	c5
T (s)	579	584	586	589	592
h₀ (m)	0.6900	0.6900	0.6900	0.6900	0.6900
h (m)	0.3900	0.3900	0.3900	0.3900	0.3900
t (m)	0.0080	0.0080	0.0080	0.0080	0.0080
c (m)	0.1020	0.1020	0.1020	0.1020	0.1020
L (m)	0.1670	0.1670	0.1670	0.1670	0.1670
K_s (m/s)	1.0E-06	1.0E-06	1.0E-06	1.0E-06	9.9E-07

Constant Head	D1	D2	D3
Q (cm³)	214.0000	109.0000	209.0000
T (s)	1680.0000	840.0000	1380.0000
A (m²)	0.0082	0.0082	0.0082
L (m)	0.1670	0.1670	0.1670
h (m)	0.8050	0.8050	0.8050
K_s (m/s)	3.2E-06	3.3E-06	3.8E-06

Falling Head	d1	d2	d3
T (s)	175	174	175
h₀ (m)	0.6900	0.6900	0.6900
h (m)	0.3900	0.3900	0.3900
t (m)	0.0080	0.0080	0.0080
c (m)	0.1020	0.1020	0.1020
L (m)	0.1670	0.1670	0.1670
K_s (m/s)	3.3E-06	3.4E-06	3.3E-06

Constant Head	E1	E2	E3
Q (cm³)	52.0000	53.0000	51.0000
T (s)	1800.0000	1980.0000	1800.0000
A (m²)	0.0082	0.0082	0.0082
L (m)	0.1670	0.1670	0.1670
h (m)	0.8050	0.8050	0.8050
K_s (m/s)	7.3E-07	6.8E-07	7.2E-07

Falling Head	f1	f2	f3	f4	f5	f6	f7
T (s)	924	826	1300	840	1300	870	878
h₀ (m)	0.8200	0.8200	0.9150	0.9150	0.9150	0.9150	0.9150
h (m)	0.5200	0.5200	0.6150	0.6150	0.4980	0.6150	0.6150
t (m)	0.0080	0.0080	0.0080	0.0080	0.0080	0.0080	0.0080
c (m)	0.1020	0.1020	0.1020	0.1020	0.1020	0.1020	0.1020
L (m)	0.1670	0.1670	0.1670	0.1670	0.1670	0.1670	0.1670
K_s (m/s)	5.1E-07	5.7E-07	3.1E-07	4.9E-07	4.8E-07	4.7E-07	4.6E-07

Falling Head	f8	f9	f10	f11	f12	f13	f14
T (s)	882	885	887	892	894	906	986
h₀ (m)	0.9150	0.9150	0.9150	0.9150	0.9150	0.9150	0.9150
h (m)	0.6150	0.6150	0.6150	0.6150	0.6150	0.6150	0.5950
t (m)	0.0080	0.0080	0.0080	0.0080	0.0080	0.0080	0.0080
c (m)	0.1020	0.1020	0.1020	0.1020	0.1020	0.1020	0.1020
L (m)	0.1670	0.1670	0.1670	0.1670	0.1670	0.1670	0.1670
K_s (m/s)	4.6E-07	4.6E-07	4.6E-07	4.6E-07	4.6E-07	4.5E-07	4.5E-07

Falling Head	f15	f16	f17	f18
T (s)	911	911	931	927
h₀ (m)	0.9150	0.9150	0.9150	0.9150
h (m)	0.6150	0.6150	0.6150	0.6150
t (m)	0.0080	0.0080	0.0080	0.0080
c (m)	0.1020	0.1020	0.1020	0.1020
L (m)	0.1670	0.1670	0.1670	0.1670
K_s (m/s)	4.5E-07	4.5E-07	4.4E-07	4.4E-07

Falling Head	g1	g2	g3	g4	g5
T (s)	1855	1332	1331	1329	1329
h₀ (m)	0.9150	0.9150	0.9150	0.9150	0.9150
h (m)	0.5300	0.6150	0.6150	0.6150	0.6150
t (m)	0.0080	0.0080	0.0080	0.0080	0.0080
c (m)	0.1020	0.1020	0.1020	0.1020	0.1020
L (m)	0.1670	0.1670	0.1670	0.1670	0.1670
K_s (m/s)	3.0E-07	3.1E-07	3.1E-07	3.1E-07	3.1E-07

Constant Head	H1
Q (cm³)	618.0000
T (s)	49629.0000
A (m²)	0.0082
L (m)	0.1670
h (m)	0.8500
K_s (m/s)	3.0E-07

Falling Head	h1	h2	h3
T (s)	1410	1349	1353
h₀ (m)	0.9150	0.9150	0.9150
h (m)	0.6040	0.6150	0.6150
t (m)	0.0080	0.0080	0.0080
c (m)	0.1020	0.1020	0.1020
L (m)	0.1670	0.1670	0.1670
K_s (m/s)	3.0E-07	3.0E-07	3.0E-07

Falling Head	i1	i2	i3	i4
T (s)	1810	2130	1830	1736
h₀ (m)	0.9150	0.9150	0.9150	0.9150
h (m)	0.5900	0.5550	0.6000	0.6150
t (m)	0.0080	0.0080	0.0080	0.0080
c (m)	0.1020	0.1020	0.1020	0.1020
L (m)	0.1670	0.1670	0.1670	0.1670
K_s (m/s)	2.5E-07	2.4E-07	2.4E-07	2.4E-07

Constant Head	J1
Q (cm³)	142.0000
T (s)	13260.0000
A (m²)	0.0082
L (m)	0.1670
h (m)	0.9000
K_s (m/s)	2.4E-07

Falling Head	j1	j2	j3	j4
T (s)	2580	2025	1880	3000
h₀ (m)	0.9150	0.9150	0.9150	0.9150
h (m)	0.5140	0.5850	0.6050	0.4730
t (m)	0.0080	0.0080	0.0080	0.0080
c (m)	0.1020	0.1020	0.1020	0.1020
L (m)	0.1670	0.1670	0.1670	0.1670
K_s (m/s)	2.3E-07	2.3E-07	2.3E-07	2.3E-07

Constant Head	K1	K2
Q (cm³)	391.0000	100.5000
T (s)	234900	64500
A (m²)	0.0082	0.0082
L (m)	0.1670	0.1670
h (m)	1.0380	1.0380
K_s (m/s)	3.3E-08	3.1E-08

Falling Head	k1	k2
T (s)	12120	11580
h₀ (m)	1.0380	1.0380
h (m)	0.7180	0.7230
t (m)	0.0080	0.0080
c (m)	0.1020	0.1020
L (m)	0.1670	0.1670
K_s (m/s)	3.1E-08	3.2E-08

Constant Head	L1
Q (cm³)	135.5000
T (s)	58680
A (m²)	0.0082
L (m)	0.1670
h (m)	1.0380
K_s (m/s)	4.5E-08

Falling Head	I1	I2
T (s)	8460	10680
h₀ (m)	1.0380	1.0380
h (m)	0.7380	0.6730
t (m)	0.0080	0.0080
c (m)	0.1020	0.1020
L (m)	0.1670	0.1670
K_s (m/s)	4.1E-08	4.2E-08

Constant Head	M1
Q (cm³)	985.0000
T (s)	54480
A (m²)	0.0082
L (m)	0.1670
h (m)	1.0380
K_s (m/s)	3.6E-07

Falling Head	m1	m2	m3
T (s)	1140	1398	2040
h₀ (m)	1.0380	1.0380	1.0380
h (m)	0.7230	0.6680	0.5580
t (m)	0.0080	0.0080	0.0080
c (m)	0.1020	0.1020	0.1020
L (m)	0.1670	0.1670	0.1670
K_s (m/s)	3.3E-07	3.2E-07	3.1E-07

Falling Head	n1	n2	n3
T (s)	1940	1542	1665
h₀ (m)	1.0380	1.0380	1.0380
h (m)	0.5830	0.6580	0.6380
t (m)	0.0080	0.0080	0.0080
c (m)	0.1020	0.1020	0.1020
L (m)	0.1670	0.1670	0.1670
K_s (m/s)	3.1E-07	3.0E-07	3.0E-07

Falling Head	o1	o2
T (s)	4080	4105
h₀ (m)	1.0380	1.0380
h (m)	0.7380	0.7380
t (m)	0.0080	0.0080
c (m)	0.1020	0.1020
L (m)	0.1670	0.1670
K_s (m/s)	8.6E-08	8.5E-08

Falling Head	p1	p2
T (s)	2659	2541
h₀ (m)	1.0380	1.0380
h (m)	0.7280	0.7380
t (m)	0.0080	0.0080
c (m)	0.1020	0.1020
L (m)	0.1670	0.1670
K_s (m/s)	1.4E-07	1.4E-07

Falling Head	q1	q2	q3	q4
T (s)	1498	1167	1070	1026
h₀ (m)	1.0380	1.0380	1.0380	1.0380
h (m)	0.6380	0.6880	0.7280	0.7380
t (m)	0.0080	0.0080	0.0080	0.0080
c (m)	0.1020	0.1020	0.1020	0.1020
L (m)	0.1670	0.1670	0.1670	0.1670
K_s (m/s)	3.3E-07	3.6E-07	3.4E-07	3.4E-07

Falling Head	r1	r2	r3	r1
T (s)	2520	3020	2320	2520
h₀ (m)	1.0380	1.0380	1.0380	1.0380
h (m)	0.6610	0.6100	0.6880	0.6610
t (m)	0.0080	0.0080	0.0080	0.0080
c (m)	0.1020	0.1020	0.1020	0.1020
L (m)	0.1670	0.1670	0.1670	0.1670
K_s (m/s)	1.8E-07	1.8E-07	1.8E-07	1.8E-07

Falling Head	s1	s2	s3	s4	s5
T (s)	2122	1940	2070	2244	2555
h₀ (m)	1.0380	1.0380	1.0380	1.0380	1.0380
h (m)	0.6480	0.6780	0.6600	0.6390	0.6030
t (m)	0.0080	0.0080	0.0080	0.0080	0.0080
c (m)	0.1020	0.1020	0.1020	0.1020	0.1020
L (m)	0.1670	0.1670	0.1670	0.1670	0.1670
K_s (m/s)	2.3E-07	2.3E-07	2.2E-07	2.2E-07	2.2E-07

Falling Head	t1	t2	t3	t4
T (s)	1093	1182	1045	1065
h₀ (m)	1.0380	1.0380	1.0380	1.0380
h (m)	0.6980	0.6780	0.7130	0.7080
t (m)	0.0080	0.0080	0.0080	0.0080
c (m)	0.1020	0.1020	0.1020	0.1020
L (m)	0.1670	0.1670	0.1670	0.1670
K_s (m/s)	3.7E-07	3.7E-07	3.7E-07	3.7E-07

Falling Head	u1	u2	u3	u4
T (s)	720	780	723	1420
h₀ (m)	1.0380	1.0380	1.0380	1.0380
h (m)	0.7380	0.7180	0.7380	0.5380
t (m)	0.0080	0.0080	0.0080	0.0080
c (m)	0.1020	0.1020	0.1020	0.1020
L (m)	0.1670	0.1670	0.1670	0.1670
K_s (m/s)	4.9E-07	4.9E-07	4.8E-07	4.8E-07

Falling Head	v1	v2	v3
T (s)	507	508	553
h₀ (m)	1.0380	1.0380	1.0380
h (m)	0.7380	0.7380	0.7180
t (m)	0.0080	0.0080	0.0080
c (m)	0.1020	0.1020	0.1020
L (m)	0.1670	0.1670	0.1670
K_s (m/s)	6.9E-07	6.9E-07	6.8E-07

Falling Head	x1	x2	x3	x4
T (s)	844	735	773	716
h₀ (m)	1.0380	1.0380	1.0380	1.0380
h (m)	0.6880	0.7280	0.7180	0.7380
t (m)	0.0080	0.0080	0.0080	0.0080
c (m)	0.1020	0.1020	0.1020	0.1020
L (m)	0.1670	0.1670	0.1670	0.1670
K_s (m/s)	5.0E-07	5.0E-07	4.9E-07	4.9E-07

Falling Head	aa1	aa2	aa3
<i>T (s)</i>	2229	1328	1458
<i>h₀ (m)</i>	1.0380	1.0380	1.0380
<i>h (m)</i>	0.5150	0.6880	0.6680
<i>t (m)</i>	0.0080	0.0080	0.0080
<i>c (m)</i>	0.1020	0.1020	0.1020
<i>L (m)</i>	0.1670	0.1670	0.1670
<i>K_s (m/s)</i>	3.2E-07	3.2E-07	3.1E-07

Falling Head	ab1	ab2	ab3
<i>T (s)</i>	965	997	963
<i>h₀ (m)</i>	1.0380	1.0380	1.0380
<i>h (m)</i>	0.7380	0.7280	0.7300
<i>t (m)</i>	0.0080	0.0080	0.0080
<i>c (m)</i>	0.1020	0.1020	0.1020
<i>L (m)</i>	0.1670	0.1670	0.1670
<i>K_s (m/s)</i>	3.6E-07	3.7E-07	3.8E-07

Falling Head	ac1	ac2	ac3	ac4
<i>T (s)</i>	1127	1735	1185	1410
<i>h₀ (m)</i>	1.0380	1.0380	1.0380	1.0380
<i>h (m)</i>	0.7380	0.6180	0.7280	0.6830
<i>t (m)</i>	0.0080	0.0080	0.0080	0.0080
<i>c (m)</i>	0.1020	0.1020	0.1020	0.1020
<i>L (m)</i>	0.1670	0.1670	0.1670	0.1670
<i>K_s (m/s)</i>	3.1E-07	3.1E-07	3.1E-07	3.0E-07

Falling Head	ad1	ad2	ad3	ad4
<i>T (s)</i>	1870	1876	1880	1181
<i>h₀ (m)</i>	1.0380	1.0380	1.0380	1.0380
<i>h (m)</i>	0.7380	0.7380	0.7380	0.8380
<i>t (m)</i>	0.0080	0.0080	0.0080	0.0080
<i>c (m)</i>	0.1020	0.1020	0.1020	0.1020
<i>L (m)</i>	0.1670	0.1670	0.1670	0.1670
<i>K_s (m/s)</i>	1.9E-07	1.9E-07	1.9E-07	1.9E-07

Falling Head	ae1	ae2	ae3
<i>T (s)</i>	2018	1640	1791
<i>h₀ (m)</i>	1.0380	1.0380	1.0380
<i>h (m)</i>	0.7380	0.7880	0.7680
<i>t (m)</i>	0.0080	0.0080	0.0080
<i>c (m)</i>	0.1020	0.1020	0.1020
<i>L (m)</i>	0.1670	0.1670	0.1670
<i>K_s (m/s)</i>	1.7E-07	1.7E-07	1.7E-07

Falling Head	af1	af2	af3
<i>T (s)</i>	2387	2314	3220
<i>h₀ (m)</i>	1.0380	1.0380	1.0380
<i>h (m)</i>	0.7960	0.8030	0.7280
<i>t (m)</i>	0.0080	0.0080	0.0080
<i>c (m)</i>	0.1020	0.1020	0.1020
<i>L (m)</i>	0.1670	0.1670	0.1670
<i>K_s (m/s)</i>	1.1E-07	1.1E-07	1.1E-07

Falling Head	ag1	ag2	ag3	ag4	ag5	ag6	ag7
<i>T (s)</i>	3887	1911	4236	3647	5000	2780	2660
<i>h₀ (m)</i>	1.0380	1.0380	1.0380	1.0380	1.0830	1.0830	1.0830
<i>h (m)</i>	0.6580	0.8280	0.6330	0.6480	0.5610	0.7380	0.7380
<i>t (m)</i>	0.0080	0.0080	0.0080	0.0080	0.0080	0.0080	0.0080
<i>c (m)</i>	0.1020	0.1020	0.1020	0.1020	0.1020	0.1020	0.1020
<i>L (m)</i>	0.1670	0.1670	0.1670	0.1670	0.1670	0.1670	0.1670
<i>K_s (m/s)</i>	1.2E-07	1.2E-07	1.2E-07	1.3E-07	1.4E-07	1.4E-07	1.5E-07

Appendix III

Manufacturer's Data

GEBA® weiß

Feinstkristallquarzsand 0,063 - 0,3 mm



200309

Charakterisierung

GEBA® weiß ist ein Feinstkristallquarzsand, der speziell für den Einsatz in bauchemischen Produkten aufbereitet wird.

Lieferung

lose oder verpackt in 25 kg Papiertüten

Chemische Analyse

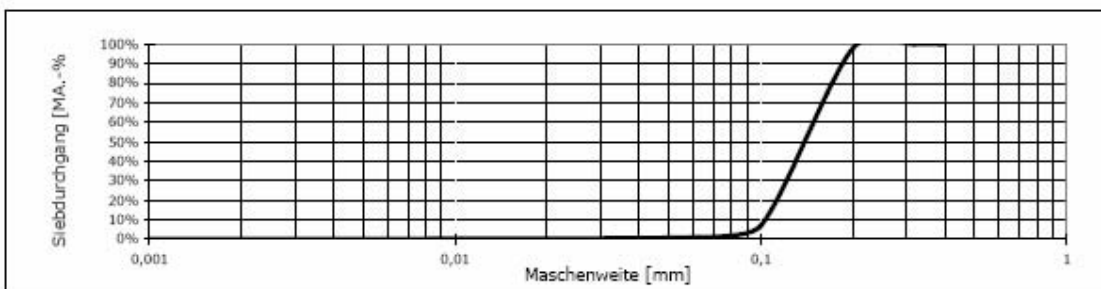
Oxide	SiO ₂	Al ₂ O ₃	Fe ₂ O ₃	TiO ₂	K ₂ O	Na ₂ O	CaO	MgO			Glühverlust
MA.-%	98,8	0,20	0,10	0,24	< 0,01	< 0,01	< 0,01	< 0,01			0,10

Analyse nach DIN 51001 mit RFA

Physikalische Daten				Kornaufbau (Sedigraph 5100)					
Feuchtigkeit	< 1	MA.-%	DIN ISO 787 Teil 2	0,2	>	0,315	mm	Spur	
Dichte	2,65	g/ml	DIN ISO 787 Teil 10	0,1	-	0,315	mm	2 MA.-%	
Schüttdichte	1,35	g/ml		0,063	-	0,2	mm	91 MA.-%	
					-	0,1	mm	6 MA.-%	
					<	0,063	mm	1 MA.-%	

Mineralogische Zusammensetzung			
Quarz		99,2	MA.-%
Tonminerale		0,3	MA.-%
Restbestandteile		0,5	MA.-%

Mittlere Korngröße:	0,13 mm
---------------------	---------



Basis: Produktionsdurchschnittswerte 2003

Wichtiger Hinweis:

Wir weisen ausdrücklich darauf hin, daß es sich bei den vorliegenden Produkten um Naturprodukte handelt, die veredelt und/oder gemischt sein können (auch mit synthetischen Produkten). Alle angegebenen Daten und Werte sind daher lediglich als Richtwerte zu verstehen. Unser Vertragspartner bleibt verpflichtet, die Tauglichkeit des Produktes für seine Einsatzzwecke zu prüfen und konkrete Auskünfte über Toleranzbreiten und anwendungstechnische Erfahrungen aufgrund der naturgegebenen sowie produktions- und lagerstättenbedingten Toleranzen für den konkreten Verwendungszweck zu erfragen. Im übrigen gelten unsere "Allgemeinen Verkaufs- und Lieferbedingungen."

DORSILIT® 2.500 MI



Kristallquarzmehl 0-125 µm

200309

Charakterisierung

DORSILIT® - und MIKRO-DORSILIT® - Kristallquarzmehle werden durch eisenfreie, trockene Vermahlung von aufbereitetem Quarzsand und nachfolgender Windsichtung hergestellt. Sie zeichnen sich durch einen hohen SiO₂ - Gehalt von über 99 MA.-% aus und enthalten nur geringe Mengen an Nebenbestandteilen. Sie werden in mehreren Mahlfineinheiten geliefert.

Lieferung

lose oder verpackt in 25 kg Papiersäcken

Chemische Analyse

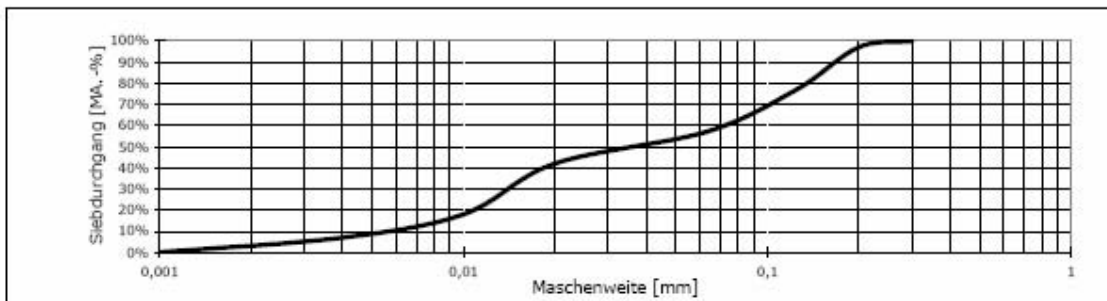
Oxide	SiO ₂	Al ₂ O ₃	Fe ₂ O ₃	TiO ₂	K ₂ O	Na ₂ O	CaO	MgO	P ₂ O ₅	BaO	Glühverlust
MA.-%	99,10	0,45	0,016	0,04	0,01	0,01	0,02	0,01	-	-	0,20

Analyse nach DIN 51001 mit RFA

Physikalische Daten				Kornaufbau (Sedigraph 5100)			
Weißgrad R457 abs	75	%			>	125	µm
Spezifische Oberfläche (BET)	0,61	m ² /g	DIN 66132	63	-	125	µm
Dichte	2,63	g/ml		40	-	63	µm
Schüttdichte	1,05	g/ml		20	-	40	µm
Stampfvolumen	0,60	ml/g	DIN ISO 787, Teil 11	10	-	20	µm
Ölzahl	18	g/100 g	DIN ISO 787, Teil 5	4	-	10	µm
pH-Wert 100 g/l	6		DIN ISO 787, Teil 9		<	4	µm
							3 MA.-%
							20 MA.-%
							20 MA.-%
							15 MA.-%
							24 MA.-%
							11 MA.-%
							7 MA.-%

Mineralogische Zusammensetzung			
Quarz		99,0	MA.-%
Feldspat		0,5	MA.-%
Restbestandteile		0,5	MA.-%

Mittlere Korngröße:	39 µm
---------------------	-------



Basis: Produktionsdurchschnittswerte 2003

Wichtiger Hinweis:

Wir weisen ausdrücklich darauf hin, daß es sich bei den vorliegenden Produkten um Naturprodukte handelt, die variiert und/oder gemischt sein können (auch mit synthetischen Produkten). Alle angegebenen Daten und Werte sind daher lediglich als Richtwerte zu verstehen. Unser Vertragspartner bleibt verpflichtet, die Tauglichkeit des Produktes für seine Einsatzzwecke zu prüfen und konkrete Auskünfte über Toleranzbreiten und anwendungstechnische Erfahrungen aufgrund der naturgegebenen sowie produktions- und lagerstättenbedingten Toleranzen für den konkreten Verwendungszweck zu erfragen. Im übrigen gelten unsere "Allgemeinen Verkaufs- und Lieferbedingungen."

DORSILIT® 4.900



Kristallquarzmehl 0-90 µm

200309

Charakterisierung

DORSILIT® - und MIKRO-DORSILIT® - Kristallquarzmehle werden durch eisenfreie, trockene Vermahlung von aufbereitetem Quarzsand und nachfolgender Windsichtung hergestellt. Sie zeichnen sich durch einen hohen SiO₂ - Gehalt von über 99 MA.-% aus und enthalten nur geringe Mengen an Nebenbestandteilen. Sie werden in mehreren Mahfeinheiten geliefert.

Lieferung

lose oder verpackt in 25 kg Papiertüten

Chemische Analyse

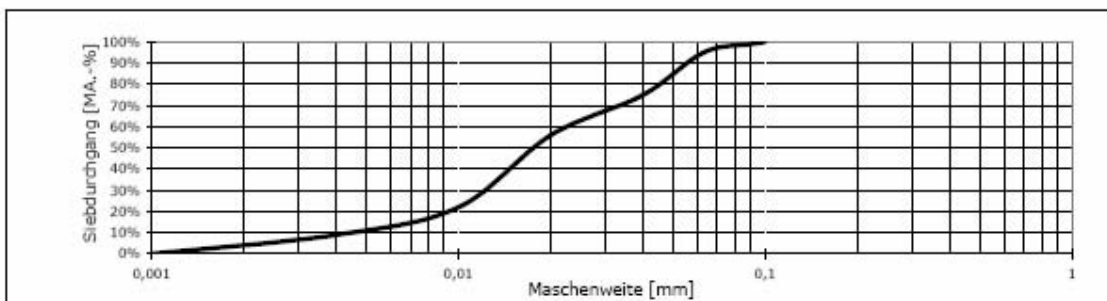
Oxide	SiO ₂	Al ₂ O ₃	Fe ₂ O ₃	TiO ₂	K ₂ O	Na ₂ O	CaO	MgO	P ₂ O ₅	BaO	Glühverlust
MA.-%	99,10	0,48	0,017	0,04	0,01	0,01	0,02	0,01	-	-	0,20

Analyse nach DIN 51001 mit RFA

Physikalische Daten				Kornaufbau (Sedigraph 5100)			
Weißgrad R457 abs	79	%			>	90	µm
Spezifische Oberfläche (BET)	0,83	m ² /g	DIN 66132	63	-	90	µm
Dichte	2,63	g/ml		40	-	63	µm
Schüttdichte	0,94	g/ml		20	-	40	µm
Stampfvolumen	0,66	ml/g	DIN ISO 787, Teil 11	10	-	20	µm
Ölzahl	19	g/100 g	DIN ISO 787, Teil 5	4	-	10	µm
pH-Wert 100 g/l	6		DIN ISO 787, Teil 9		<	4	µm
							1 MA.-%
							4 MA.-%
							20 MA.-%
							19 MA.-%
							34 MA.-%
							13 MA.-%
							9 MA.-%

Mineralogische Zusammensetzung			
Quarz		99,0	MA.-%
Feldspat		0,5	MA.-%
Restbestandteile		0,5	MA.-%

Mittlere Korngröße:	21 µm
---------------------	-------



Basis: Produktionsdurchschnittswerte 2003

Wichtiger Hinweis:

Wir weisen ausdrücklich darauf hin, daß es sich bei den vorliegenden Produkten um Naturprodukte handelt, die veredelt und/oder gemischt sein können (auch mit synthetischen Produkten). Alle angegebenen Daten und Werte sind daher lediglich als Richtwerte zu verstehen. Unser Vertragspartner bleibt verpflichtet, die Tauglichkeit des Produktes für seine Einsatzzwecke zu prüfen und konkrete Auskünfte über Toleranzen und anwendungstechnische Erfahrungen aufgrund der naturgegebenen sowie produktions- und lagerstättenbedingten Toleranzen für den konkreten Verwendungszweck zu erfragen. Im übrigen gelten unsere "Allgemeinen Verkaufs- und Lieferbedingungen."

DORSILIT® 10.000

Kristallquarzmehl 0-63 µm



200309

Charakterisierung

DORSILIT® - und MIKRO-DORSILIT® - Kristallquarzmehle werden durch eisenfreie, trockene Vermahlung von aufbereitetem Quarzsand und nachfolgender Windsichtung hergestellt. Sie zeichnen sich durch einen hohen SiO₂-Gehalt von über 99 MA.-% aus und enthalten nur geringe Mengen an Nebenbestandteilen. Sie werden in mehreren Mahlfractions geliefert.

Lieferung

lose oder verpackt in 25 kg Papiertüten

Chemische Analyse

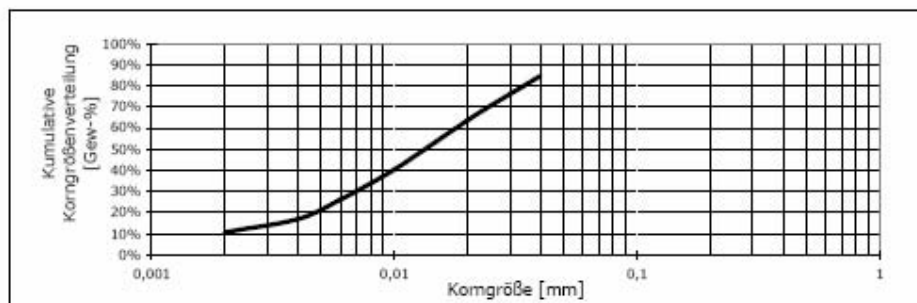
Oxide	SiO ₂	Al ₂ O ₃	Fe ₂ O ₃	TiO ₂	K ₂ O	Na ₂ O	CaO	MgO	P ₂ O ₅	BaO	Glühverlust
MA.-%	99,00	0,61	0,016	0,04	0,02	0,01	0,02	0,01	-	-	0,19

Analyse nach DIN 51001 mit RFA

Physikalische Daten				Kornaufbau (Sedigraph 5100)			
Weißgrad R457 abs	80,5	%			>	63	µm
Spezifische Oberfläche (BET)	0,97	m ² /g	DIN 66132	40	-	63	µm
Dichte	2,63	g/ml		30	-	40	µm
Schüttdichte	0,91	g/ml		20	-	30	µm
Stampfvolumen	0,68	ml/g	DIN ISO 787, Teil 11	10	-	20	µm
Ölzahl	20	g/100 g	DIN ISO 787, Teil 5	6	-	10	µm
pH-Wert 100 g/l	5,7		DIN ISO 787, Teil 9	4	-	6	µm
				2	-	4	µm
					<	2	µm
							0,7 MA.-%
							14,7 MA.-%
							8,5 MA.-%
							12,5 MA.-%
							23,3 MA.-%
							14,2 MA.-%
							9,2 MA.-%
							6,3 MA.-%
							10,6 MA.-%

Mineralogische Zusammensetzung			
Quarz		99,0	MA.-%
Feldspat		0,5	MA.-%
Restbestandteile		0,5	MA.-%

Mittlere Korngröße:	18 µm
---------------------	-------



Wichtiger Hinweis:

Wir weisen ausdrücklich darauf hin, daß es sich bei den vorliegenden Produkten um Naturprodukte handelt, die veredelt und/oder gemischt sein können (auch mit synthetischen Produkten). Alle angegebenen Daten und Werte sind daher lediglich als Richtwerte zu verstehen. Unser Vertragspartner bleibt verpflichtet, die Eignung des Produktes für seine Einsatzzwecke zu prüfen und konkrete Auskünfte über Toleranzen und anwendungstechnische Erfahrungen aufgrund der naturgegebenen sowie produktions- und lagerstättenbedingten Toleranzen für den konkreten Verwendungszweck zu erfragen. Im übrigen gelten unsere "Allgemeinen Verkaufs- und Lieferbedingungen."

Appendix B: Supporting Data: MKTS, 2009 Simulation Modeling Report

**Simulations of Small- and Large-Tank, Conductive-Heating and
Remediation Experiments – SERDP Project: ER 1423 –“*Large
Scale Physical Models of DNAPL Source Zones in Aquitards*”**

Myron Kuhlman – MK Tech Solutions, Inc

January 2006 – May 2008



MK Tech Solutions
Houston, Texas

INDEX

Summary	1
Background	1
Purpose of Current Study	1
Experimental Details	2
2D Flume Experiments (Thin Box)	2
Tank Heating and Remediation Experiments	3
Details of Simulations	4
Results of Simulations	9
2D Flume Heating Experiments	9
First Large-Tank-Heating Experiment	12
Large-Tank TCE Remediation Predictions	14
Small-Tank Heating Experiment	17
2D-Flume Remediation Experiment	24
Small- and Large-Tank-Remediation Experiments	32
Discussion	39
Effect of Capillary Pressure and Dispersion	40
Conduction versus Convection:	41
Migration of DNAPL	42
Evidence of Azeotropes	43
Lessons Learned	44
Conclusions	45
References	47

Summary

Simulations of several 2-D flume and large-tank heating and remediation experiments were conducted with the Computer Modeling Group's simulator, STARS. Both the temperature distribution in the containers and production rate of vaporized perchloroethylene (PCE) were modeled well. However, migration of the PCE from the lenses where it had been placed was very important in several of the experiments. This migration was not predicted well, since flow of dissolved DNAPL countercurrent to upwardly flowing water is difficult, if not impossible, to model. This is because it is not practicable to make the grid blocks in the simulations small enough or heterogeneous enough.

Capillary pressure, DNAPL relative permeability, and dilation of the unconsolidated sand were the most important variables controlling heating of the containers and migration of the DNAPL in all of the experiments. The capillary pressures used in these simulations are significantly lower than measured capillary pressures because numerical dispersion in simulations affects movement of fluids in the same way as capillary pressure does. Dilation of the unconsolidated sand was important because pressures rise enough, due to evaporation of water in the 2-D flume experiments, to part sand grains and temporarily increase the sand's permeability.

In the tank experiments, the aquifer-influx rate was also very important because high aquifer-influx rates seemed to be associated with migration upward and horizontally of DNAPL constituents, both as a separate-phase liquid and as a component dissolved in the water. Although not obvious in the physical experiments, the simulations predicted that low aquifer-influx rates would allow the DNAPL constituents to migrate downward as both a free liquid and in the vapor phase, or to condense from the vapor outside the edges of the heated zone. In either case, if DNAPL were to migrate from the heated zone, the models indicate that it can only be recovered slowly at a low concentration in the aqueous and vapor phases. The ideal aquifer-influx rate for the large-scale tank experiments appeared to be 0.55 m/day (2 m³/day in a 6x6 meter tank). This enabled a rapid steaming of the target treatment zone (TTZ) with a PCE mass recovery of about 90% in two weeks, while preventing migration of the DNAPL.

Migration of a DNAPL and the difficulty of recovering DNAPL that is flushed or condensed outside of the small heated zone in these experiments are artifacts of these experiments that are not important in field thermal conduction heating (TCH) projects. This is in part because in field practice, the SVE wells are placed inside (not outside) the heater arrays. In addition, in the field, migration of the DNAPL has occurred over years and did not begin when the experiment started. This study showed that simulation is a versatile tool for modeling and explaining a variety of phenomena, e.g., prediction of the re-condensation of steamed contaminant at the steam front.

Background

Purpose of Current Study: The overall purpose of this study was to evaluate the mechanisms that control in-situ thermal desorption (ISTD) of DNAPL in aquitards beneath the water table with an active underlying aquifer. Experiments were conducted in large tanks at the Universität Stuttgart, Germany. MK Tech Solutions' portion of this study was to help quantify important

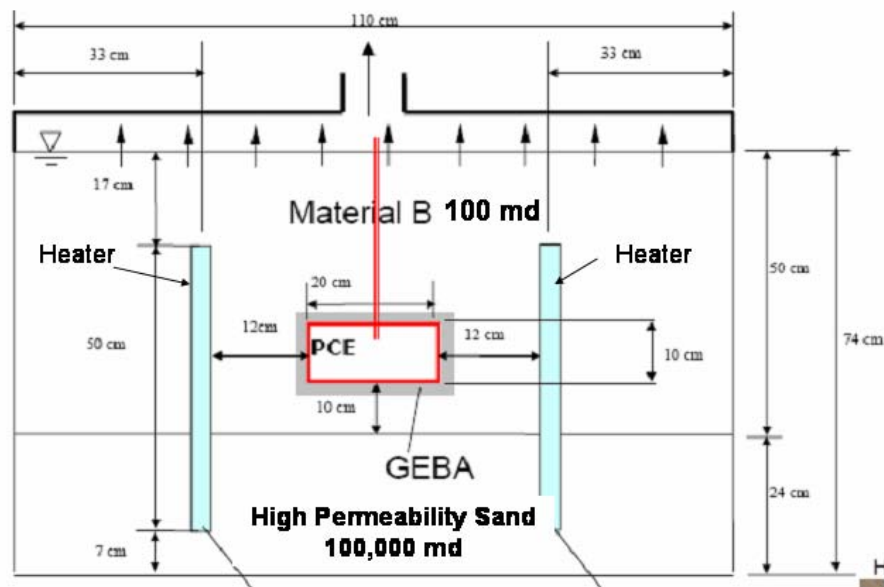
mechanisms by simulating the several experiments with STARS, a thermal simulator developed and marketed by the Computer Modeling Group of Calgary, Alberta.

STARS has been under development for approximately 25 years, is perhaps the best, advanced-process, thermal simulator in the world and is used by several thousand engineers in academia and the oil industry. It has been used for projects as diverse as surfactant floods of oil fields and industrial sites; thermal production or recovery with steam injection of up to several million-centipoise tars below the permafrost or at former industrial sites; gas hydrate production; CO₂ sequestration; production of oil from western US oil shales; and assisting in the design of approximately 20 ISTD projects conducted by Shell Technology Ventures in the 1990s and TerraTherm, Inc. since 2000.

Experimental Details: Two types of experiments were conducted: These were a) small (approximately 1 meter) experiments conducted in less than 24 hours by heating thin boxes filled with sands that could have a lens filled with perchloroethylene (PCE) and b) large (up to 162 cubic meter) tanks filled with high- and lower-permeability sand and two lenses saturated with PCE. In the tank experiments water was allowed to flow across the bottom and to imbibe upward into a lower-permeability aquitard.

2D Flume Experiments (Thin Box): Five experiments were conducted and four were modeled in this study. All of the flumes had the dimensions shown in Figure 1. The interior dimensions of the equipment were 110 cm wide, 74 cm high and 8.5 cm deep. The back, sides and top of the boxes were insulated stainless steel, while the front of the box was reinforced Pyrex™ that was also insulated during much of the experiment. Of the five experiments conducted, three were heating only without contaminants; two were heating and remediation experiments with contaminants.

Figure 1 – Face View of Equipment in 2D Remediation Experiment



The configuration in the heating-only experiments differed from that in Figure 1 in that a) one heater was used and b) the overflow was on the upper left of the box and a constant head inflow screen was on the right hand side. Whereas there was no influx of water into the equipment in

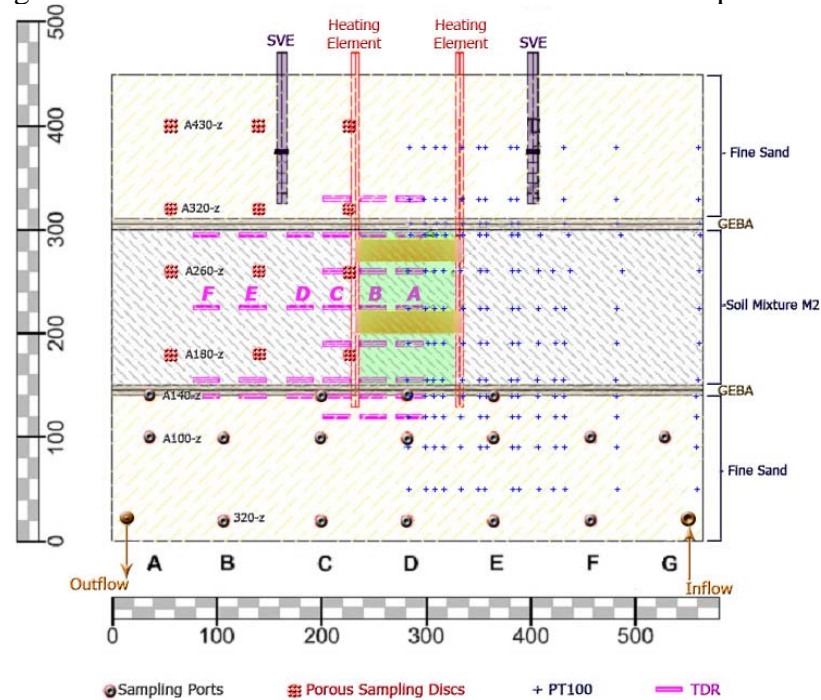
Figure 1, so water had to evaporate in the experiment through the outlet at the top of the box in the heating-only experiments. As Figure 1 shows, it was necessary in the heating and remediation experiments to use two heaters in the configuration shown since the lens that was saturated with PCE was in the center of the box.

Three heating experiments were conducted and modeled, while only one of two remediation experiments was modeled. The experiments were

- Fine sand (30 Darcy) heating experiment – modeled.
- Medium sand (470 Darcy) heating experiment – modeled.
- Coarse sand (4,600 Darcy) heating experiment – modeled.
- Mixed sand remediation experiment with two heaters (Figure 1) – the upper two thirds of the sand in this experiment had a permeability of approximately 100 md, while the lower sand had a permeability of approximately 100 Darcies. These results are summarized in this report.
- Mixed sand remediation experiment with slanted heater – described in Sec. 7.4 but not modeled.

Tank Heating and Remediation Experiments: Five experiments were conducted and three were simulated in this study. The general description of a tank is shown in Figure 2. This figure is a side view of a “small” tank. All tanks were 4.5 meters deep and 6 meters long. The “small”

Figure 2 – Side View of Small-Tank 3D Remediation Experiment



tanks were only 3 meters wide whereas the “large” tanks were 6 meters wide. The heaters supplied 1.2 to 1.5 kW each. In both heating-only experiments, as well as in the beginning of the first remediation experiment, four heaters were operated in a 1 m x 1 m square. During the first remediation experiment, this distance was at first increased to a 1.25 m x 1.25 m

square. Finally, the heater set-up was changed to a third constellation of eight operating heaters, four at a distance of 1 m x 1 m and four at a distance of 1.25 m x 1.25 m.

The small tank had two soil vapor extraction (SVE) wells, whereas the large tank had four SVE wells spaced 3 meters apart. The SVE wells were completed in the fine (10 to 100 Darcy) upper-sand layer above the water table (above three meters elevation – but still within the capillary fringe). The heaters were placed so that their tops were below the top of the M2 soil mixture shown in Figure 2 and penetrated a short distance into the lower sand layer. The permeability of the middle layer was approximately 35 md for the M2 mixture but up to one Darcy in other experiments.

Water mimicking an aquifer entered from the bottom right and exited from the bottom left in the tanks. Each tank was equipped with numerous thermocouples, sampling ports and equipment for measuring water saturations (i.e., Time Domain Reflectometers, TDRs). Water could imbibe through the GEBA layers to replace water that was removed in the vapor at the SVE wells. Because the aquifer flow was from right to left and the SVE wells were placed outside the heated region, it was easy for a contaminant to migrate towards the left side of the tank if the aquifer rate was high enough and only be produced by flowing down to the outflow well or migrating in water towards two of the SVE wells.

As noted above, five tank experiments were conducted as part of this study. These were

- A large-tank heating experiment conducted at the beginning of the project with no water influx. After the water level reached the lower coarse sand layer, water influx started and continued until water reached the original water level. This experiment was modeled and is reported herein.
- Small-tank heating experiment with aquifer influxes ranging from 4 m³/day to 0.03 m³/day. This experiment continued for approximately 150 days and was modeled extensively. What was learned about the relationship between capillary pressure and numerical dispersion on water movement was very useful.
- A large-tank heating experiment that was not modeled.
- A small-tank remediation experiment in which the two lenses shown in Figure 2 were filled with PCE. The first 42 days of this experiment were modeled and the results are reported herein.
- A final, large-tank remediation experiment. This specific experiment was not modeled because aquifer influx was low enough that the PCE did not disperse throughout the tank and 90% could be recovered as expected within two weeks as predicted by other simulations.

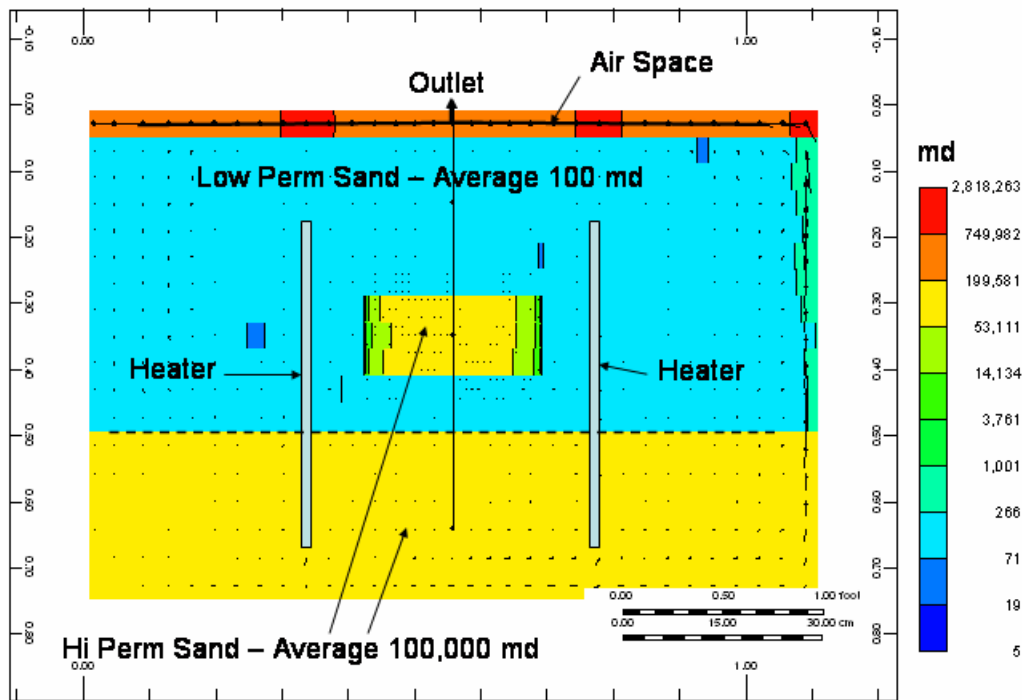
Details of Simulations: As noted above, the simulations reported here were conducted with STARS. STARS is an advanced-process, compositional simulator and is perhaps the most widely used thermal simulator in the world. It is the simulator of choice for oil field applications but is not widely used for environmental work because it is expensive to lease. However, MKTS and TerraTherm have been using STARS or its predecessor Therm since 1989 for numerous thermal conduction projects including at least 20 TerraTherm or other thermal conduction projects. The Computer Modeling Group donated a STARS lease for this project and it was used on one or two machines for a total of 30 man-months to conduct these simulations.

A short summary of the simulations is that heating is easy to model, but flow of fluids is determined by conditions which must be learned from history matches of the experiments. The most important of these variables are permeability distribution, relative permeability and capillary pressure since they control where the fluids move. Now, in heating experiments, capillary pressure and water relative permeability are very important, while in remediation experiments three-phase, relative permeability of the DNAPL also becomes important because it controls the movement of low concentrations of DNAPL into the unheated zones. This in turn controls the initial rates of remediation.

Likewise, while the low-saturation end of the water-NAPL capillary pressure curve is very important in heating experiments because it controls movement of water towards the heaters and into the vadose zone, the high-saturation end of the water-capillary pressure curve is also very important in the remediation experiments because it is part of the resistance to movement of the DNAPL constituents into the unheated zone. In other words, much of the movement of the DNAPL constituents is controlled by their movement in water and at DNAPL saturations of less than 0.002. The characteristics of the curves used in these experiments will be discussed in subsequent sections.

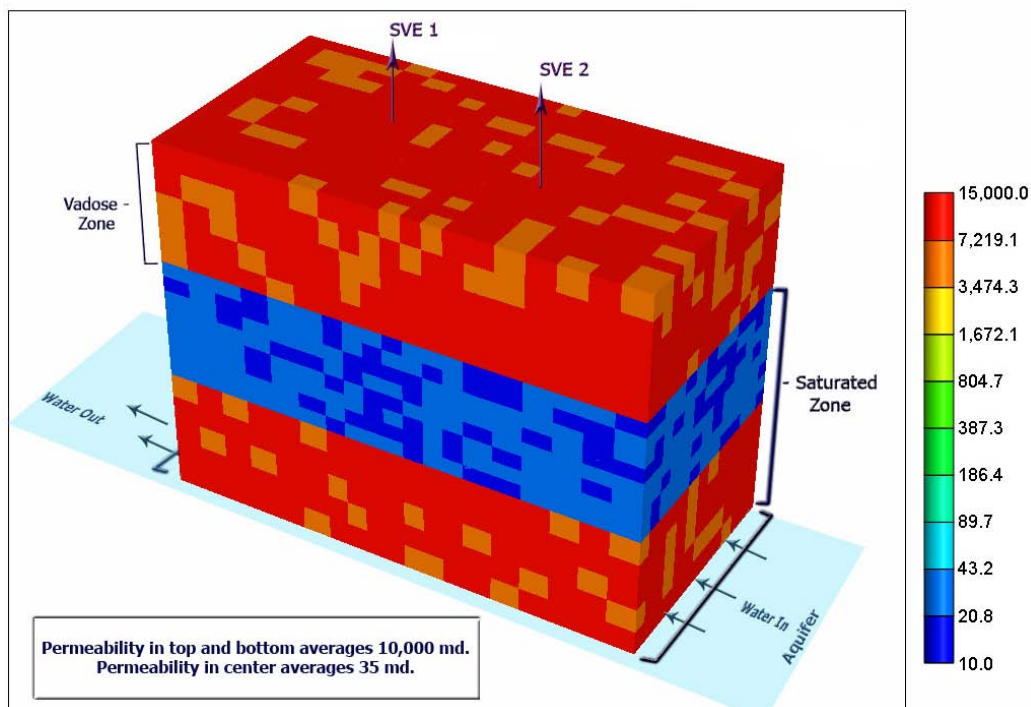
The permeability distribution of two 2D and 3D experiments are shown in Figures 3 and 4. The grid block orientation is not shown in these figures but will be evident later. As shown in Figure 3, the 2D-remediation experiment had three distinct sand units and a void space at the top. The basic grid was 35 wide by 21 tall by 5 deep. The outer boundaries on all six sides were stainless

Figure 3 – Permeability in 2D Remediation Simulation.



steel or Pyrex™ walls. The interior layers were sand; the sand-filled blocks had dimensions of 3.33 cm, 3.89 cm and 2.83 cm with a pore volume of 14.2 cm³, i.e., 39 % porosity. Blocks around and below the high-permeability lens in the center of the model were subdivided into 25 smaller blocks with pore volumes of 0.57 cm³. The void at the top of the flume was modeled as a several million millidarcy (md) space with porosity of 99.9 %. The low-permeability sand mixture had an average permeability of 100 md, but a range of 50 to 150 md. The lower, high-permeability sand in Figure 3 had an average permeability of 100,000 md with a ± 50 % range.

Figure 4 Permeability Distribution in 3D Tank Experiments



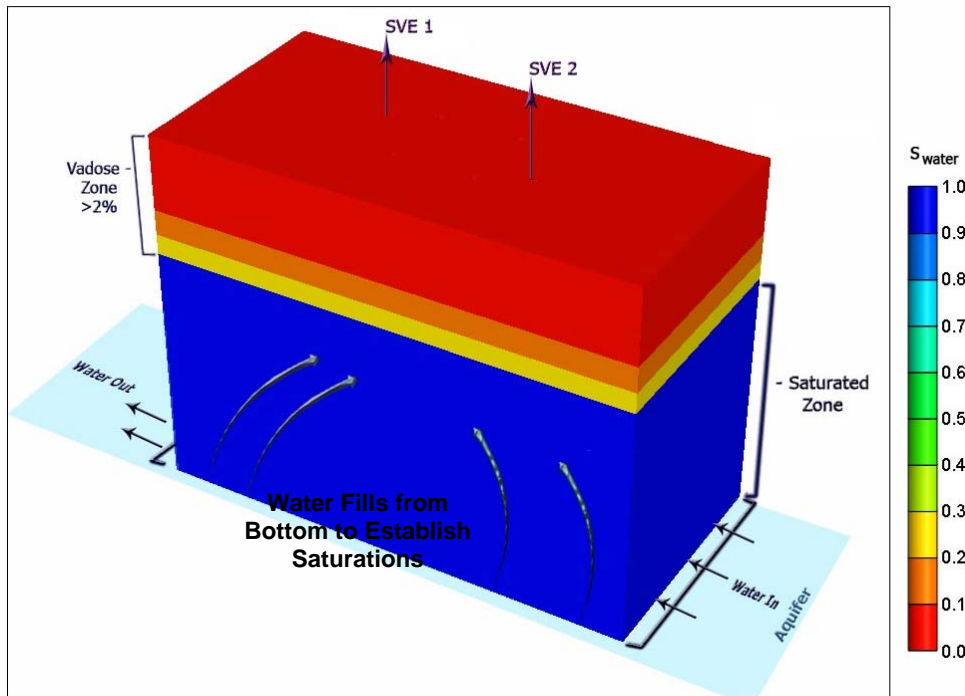
The temperatures in these experiments were measured in two ways: The first was directly with approximately 100 evenly spaced thermocouples entering the sand through the solid back wall. The other method was with infrared imaging. The results differ somewhat since the thermocouples measure the temperature in the center of the box, while the infrared method measures the temperature of the Pyrex™ window on the front of the box. The 2D heating and remediation experiments lasted between 90 minutes and 27 hours since the power used at the heaters ranged from 1.5 kW to 0.24 kW. As can be imagined, much of this energy was lost from the boundaries of the flume.

As noted above, five experiments were conducted in two 3D tanks. Both of the tanks were 6 m long and 4.5 m tall, but the widths of the small and large tanks were 3 m and 6 m, respectively. Each experimental tank was part of a group of four adjacent tanks, so that each experimental tank had three tanks as neighbors. Thus, the tank shown in Figure 4 had another tank on the front and two ends. Only the back wall was free standing (lab atmosphere of approx. 20°C) without soil on the other side. None of the tanks was insulated, and a significant amount of heat was lost through the sealed top, back side and to the adjacent three tanks.

The tanks were filled with two types of sand separated by a very fine sand (“GEBA”) transition layer as shown in Figures 2 and 4. They were also equipped with 15 thermocouples at each of twelve layers, for a total of 180 thermocouples. These temperature data were the primary data being modeled, since aquifer injection rates and SVE extraction rates were constant for long periods of time. For the first of the two remediation experiments, 10 kg of PCE (and 2 kg of a tracer) were placed in each of the two DNAPL release lenses shown in Figure 2. The production of PCE and the two tracers in the aquifer water from the bottom of each tank and the SVE in the vadose zone were monitored. Since one tracer (1,4-DCB) was added to the upper DNAPL release lens and another (1,2-DCB) to the lower lens, the production rates of the two tracers were used to identify the lens that produced the PCE. A short summary of the performance of the simulations is that STARS did a good job of predicting production of PCE in the vapor, but it did not predict how much PCE was produced from the bottom of the tank since no simulator can predict the movement of water or NAPL in a countercurrent direction to the movement of water upwards from the aquifer into the aquitard.

Figures 5 and 6 illustrate the initial water and PCE saturations in the model. As Figure 5 shows, water saturation was established with gravity-capillary equilibrium by filling the model with water from the bottom until the saturated zone reached 3 m from the bottom. Because of the very high permeability and very low capillary pressure in the vadose zone, there was a small capillary fringe and the water saturation in the top blocks of the model was approximately 2%. It was necessary to establish a low vadose-zone water saturation in order for it to dry out as quickly as it did in the heating experiments.

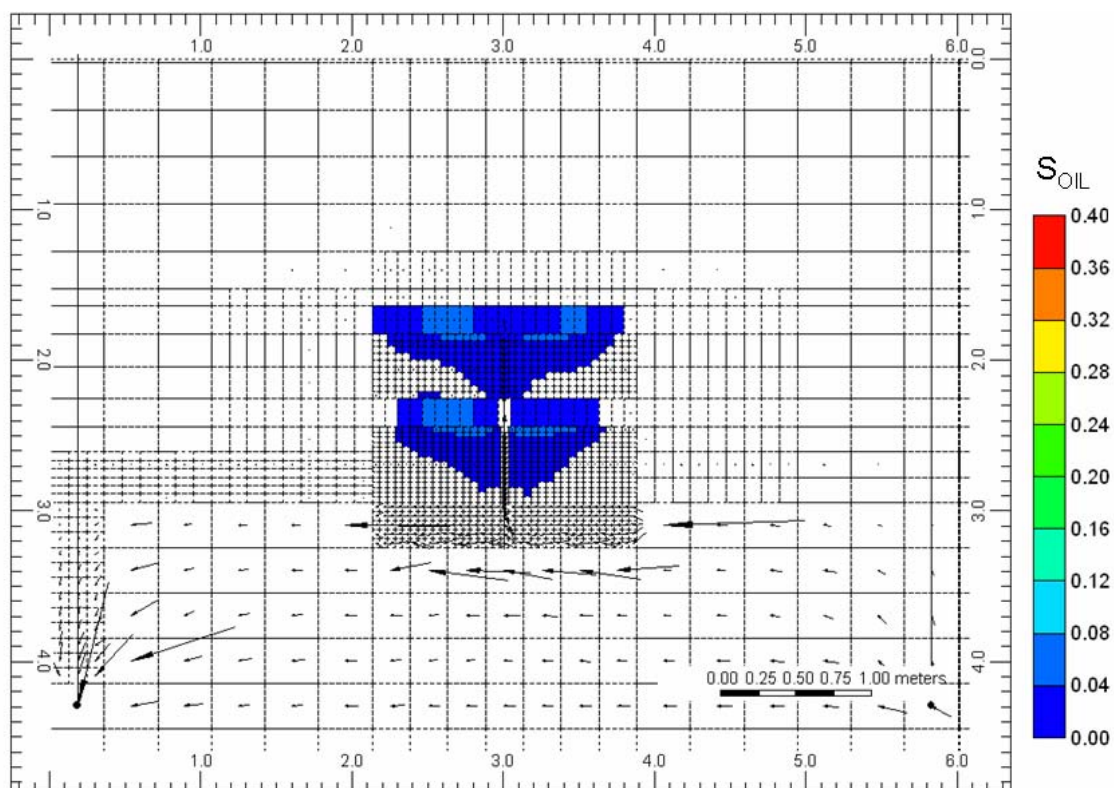
Figure 5 – Initial Water Saturations in Small-Tank 3D Model



Also, the vadose zone would not dry out and exceed 200°C next to the canisters (termed “cans”) containing the heaters at the top of the model unless convection of heated air inside the cans was assumed. This was simulated by borrowing power from the portion of the cans with heating elements and pretending that 20% of the power was used in the vadose zone, i.e., the temperature outside the can cannot be above 200°C unless the can is that hot and steam moving upwards outside of the can only has a temperature of approximately 100°C. The heater cans themselves were modeled as highly refined grids with negligible horizontal permeability, high conductivity and high vertical permeability, e.g. approximations to impermeable metal cans. In contrast, the heaters were immersed in the sand in the 2D flume experiments and modeled as elongated heat sources with direct contact to water and soil. Attempting to model the details of the heaters without a more complex (Computational Fluid Dynamics) simulator was one of the challenges of this research.

Figure 6 shows the distribution of PCE at the start of aquifer influx in a 3D tank-remediation experiment. The PCE was placed in the two DNAPL release lenses five days earlier and allowed to drain. In the simulation, a small amount of PCE reached the aquifer before aquifer influx and heating began. However, this PCE was immediately flushed away and movement of water into the heated zone limited movement of PCE downward. The relative permeabilities and capillary pressures in the remediation experiments were optimized to promote movement of PCE since migration affected the results of the experiments more than heating of the region between the heaters.

Figure 6 – Grid Sizes around DNAPL Release Lenses and PCE Distribution at Start of Aquifer Influx, 3D Remediation Experiment



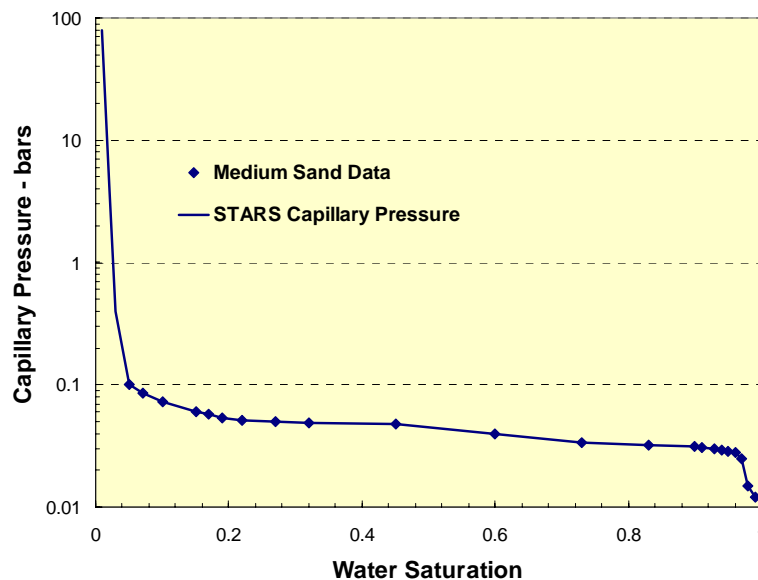
Results of Simulations

Most of the experiments listed above were modeled and are discussed below. The distribution of heat in the tanks was largely determined by the capillary pressure at low water saturation and also in the large-tank experiments by the distribution of energy transfer from the cans containing the heaters. The initial rate of recovery of PCE was determined by the NAPL-water capillary pressure at the high water-saturation end of the capillary curve by the critical DNAPL saturation, i.e., the saturation at which the DNAPL would migrate downward or outward under a pressure or density gradient. The simulations reported below largely chronicle the improved understanding of this relationship and are discussed in the order in which they were done.

2D Flume Heating Experiments: Three 2D flume heating experiments were modeled. All of these experiments had permeability like that found in the high-permeability zones of the large 3D tank.

The first of these experiments was called the fine-sand heating experiment and had a permeability of 30 Darcies. The power applied to the heater in this experiment was 0.24 kW. A partial capillary pressure curve (above 5% water saturation) had been generated by *VEGAS* for the medium-sand experiment and is shown in Figure 7. When used in *STARS* for the fine-sand experiment, these capillary pressure data were extended exponentially towards higher saturations and increased by the square of the permeability ratio. This is important because capillary pressure is the driving force that imbibes water back into the hot zone and prevents desiccation of the steam zone (which did not dry out in any of these experiments).

Figure 7 – Capillary Pressure Used in Medium-Sand 2D Flume Experiment Simulations

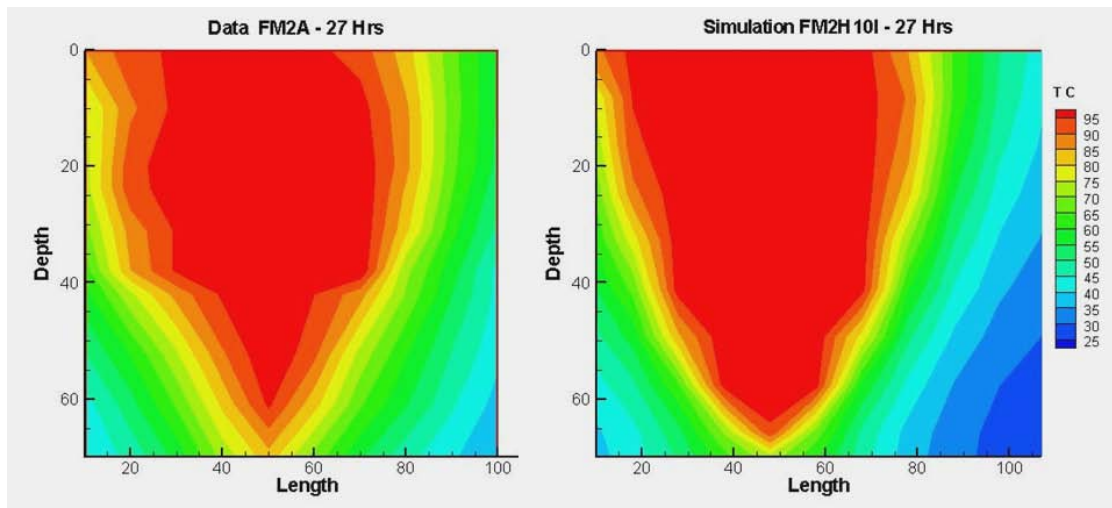


For the lower- or higher-permeability experiments, the capillary pressure shown in Figure 7 was increased or decreased by the inverse of the square root of the permeability ratio. The gas and water relative permeabilities used were simple Brooks-Corey type curves with an exponent of

1.25 since the permeability in all experiments is high. The permeability of the top layer of sand in this experiment (and the other experiments) was increased by 100X since packing of the porous medium was assumed to be imperfect there.

Figure 8 compares the final temperature distribution reported for the fine-sand experiment with that predicted by STARS. The agreement is reasonable. The temperature distribution is

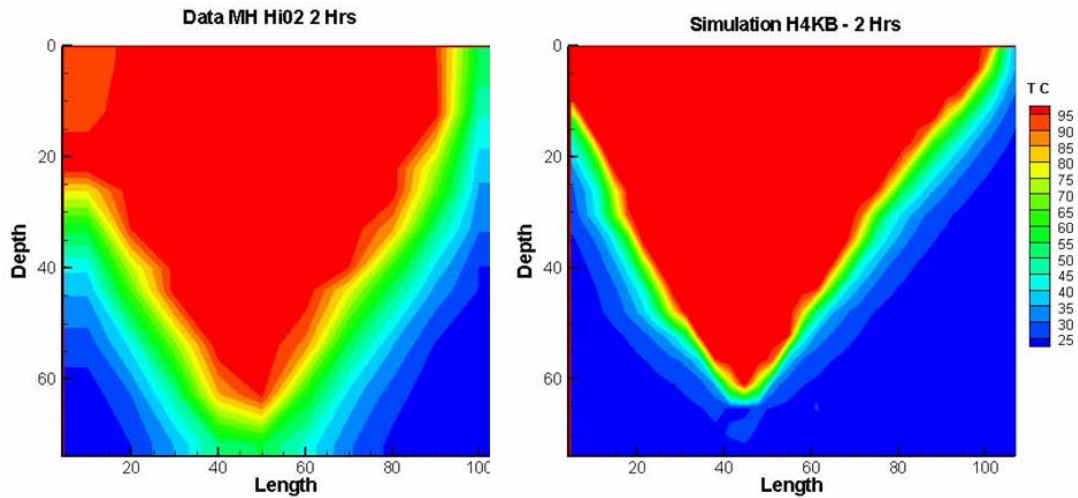
Figure 8 – Temperatures in Fine-Sand 2D Flume at 27 Hours



asymmetric and skewed towards the expansion overflow of the flume. The asymmetry is most apparent at the top of the physical model, i.e., in the higher-permeability, more-loosely-packed zone. With 0.24 kW of power most of the water in the model was heated in 27 hours. This is much longer than in the coarser-sand experiments (where more power was used) because higher capillary forces in the lower-permeability sand cause more water to imbibe back towards the heater.

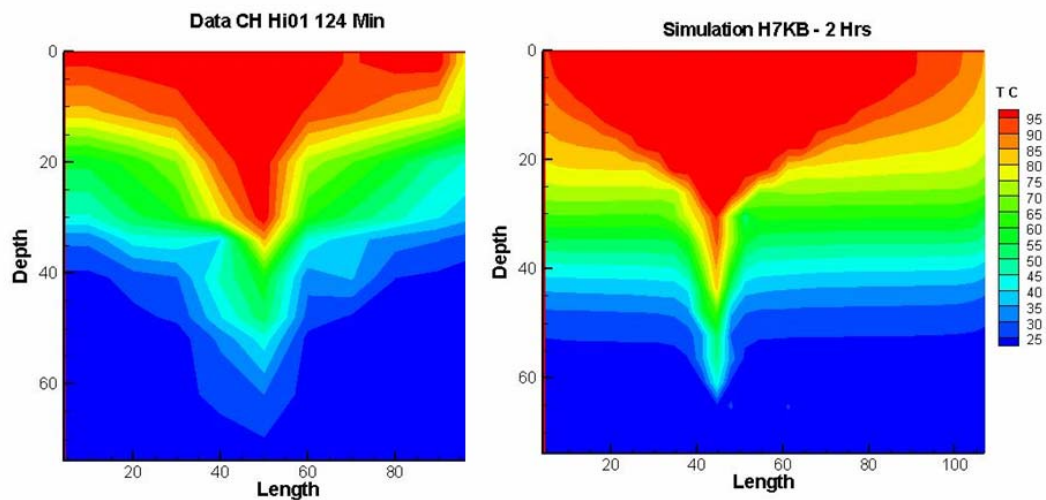
The second experiment was conducted with a medium-permeability, 470-Darcy sand. The power, 1.5 kW, applied to the heater was over six times as high and the capillary pressure in the sand was 25% of that in the fine-sand experiment. As might be expected with so much more power, the water in the flume was heated to over 100°C in a fraction (7.4%) of the time required in the fine-sand experiment. Figure 9 shows the temperature distributions in the experiment and simulation at the end of the experiment (120 minutes). As in the fine-sand experiment, the steam tends to flow towards the expansion overflow of the model. Again, the actual and predicted temperatures are similar. While the hot zone has the same general shape as in Figure 8, the bottom of the tank is not hot because hot water rises faster in this higher-permeability sand experiment and the experiment was completed in a much shorter time because the heating rate is higher.

Figure 9 – Temperatures in Medium-Sand 2D Flume at 2 Hours



The final, 2D-heating experiment was conducted with 4,600-Darcy sand in the box. The power applied at the heater in this very-coarse sand experiment was 1.5 kW. Because the permeability is so high, gravity is very important and the steam zone segregates to the top of the flume. Figure 10 shows that after 90 minutes the water at the bottom of the flume has not been heated. While the behavior of hot vapors in this very coarse material may be interesting, it is clear that very coarse material such as deposited by a mountain stream is not appropriate for conductive heating experiments below a water table. This permeability is so high that capillary forces are less than 8% of those in the low-permeability sand experiment and relative permeability curves have lost their curvature. Flow behavior in this material is closer to what is observed in fractured shales, for instance, than what is observed in sand. As a result of the permeability being so high, steam which forms near the bottom of the heater does not spread out but flows upward and collects at the top of the model.

Figure 10 – Temperatures in Coarse-Sand 2D Flume at 90 Minutes



First Large-Tank 3D Heating Experiment: Prior to the actual start of this project, VEGAS had conducted a large-tank heating experiment with no aquifer influx until late in the experiment. The initial lessons that were learned about relative shapes of capillary pressure curves and design of the heater cans were unlearned in this experiment.

After over 100 simulations of this experiment, our understanding of the differences between the initial prediction of results and the actual experimental data are as follows:

1. Low power input was caused by the controllers on the heaters. The actual power input is approximately one half of the maximum power that the heaters could have delivered.
2. In this simulation with coarser cells, the end point of the capillary pressure curve cannot be as high as in the 2D simulation because numerical dispersion also helps move water towards the heaters. Thus, the lesson learned from the 2D flume simulations had to be unlearned in a model with larger cells.
3. Another new technique has been developed in these simulations. In earlier models of TerraTherm projects, cells were larger and often the permeability was lower. That being the case, the heaters could be treated as a heat source in the continuous porous media. Now, primarily due to the higher permeability of the lower-permeability soil layer (i.e., the aquitard) that is the subject of these experiments, cross flow of water prevented high temperatures at the heater and the heaters always operated at full power. This was corrected by enclosing the heater in impermeable metal cans (as they actually are in reality). Now, energy input into the model can be more accurate, and the flow of fluids and modification by capillary pressure and relative permeability can be studied.
4. The K_v/K_h (anisotropy) of the soils in the large tank could be higher than that determined by history matching the 2D-flume experiments. Since these experiments were conducted in packed containers, rather than in sediments deposited by falling out of water, packing tends to be more random than in nature and K_v/K_h is four or more times higher than the 0.1 ratio often found in natural sediments.

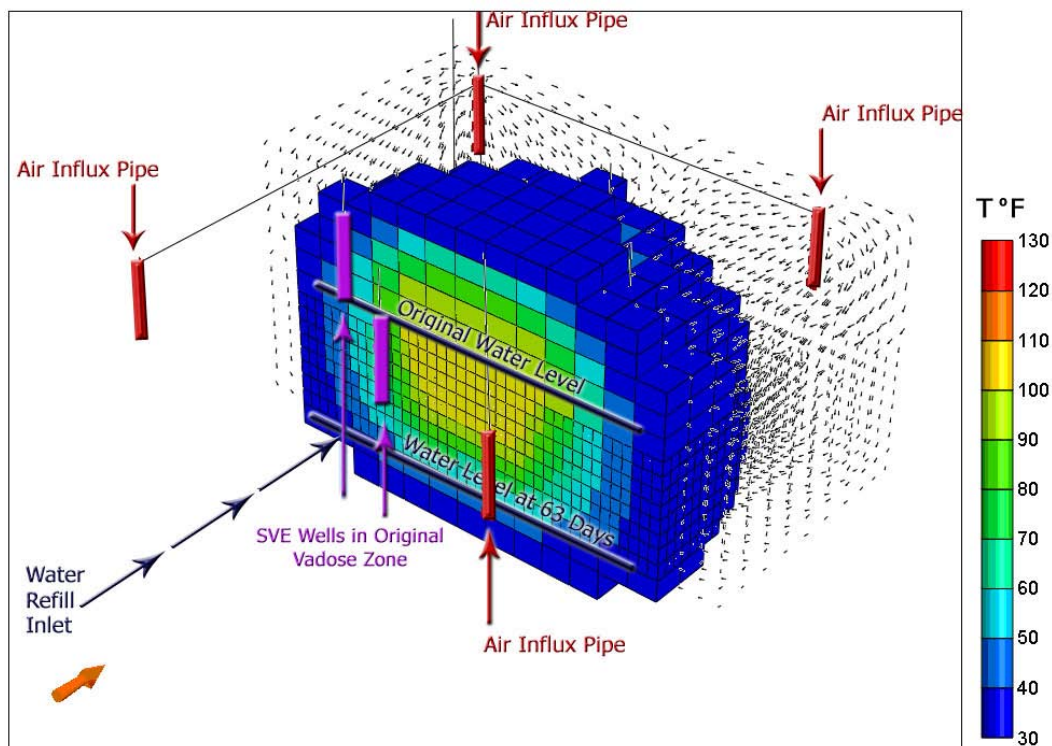
After these modifications were made, the water levels and temperatures recorded in the 3D experiment were more closely modeled. Again, as noted above, the capillary pressures of both the high- and low-permeability soils were the factors that controlled movement of water into the heated zone and, therefore, the temperatures in that region.

The heat lost at the boundaries (walls and surface) of the 3D tanks was also important. Most simulations that also matched the temperature and saturation profiles lost over 20% of the power input to the tank through convection to the atmosphere and conduction into surrounding tanks. All of this heat is lost by conduction through the sides and sealed top of the box and then convection into the atmosphere or into another tank. The temperature increases at the metal sides of the tank exposed to the atmosphere are approximately 1.6 to 1.7°C; the increase is 15°C at the sealed top of the tank and 5°C at the wall of a neighboring tank.

Figure 11 illustrates the complexity of the flow field and temperature distribution. The figure shows that the heated zone ($> 30^\circ\text{C}$ [$> 86^\circ\text{F}$]) reaches to the top of the box but does not reach the sides or bottom of the box. However, mass and energy are circulating through the vadose zone (and also the remainder of the saturated zone) in the mobile gas and water phases. Since the temperature in one half of the tank is being displayed, only half of the SVE wells, but all of the

air-inlet pipes, are visible. Air is sucked into the tank by the SVE wells, but gas circulates wherever a gas phase has been created by heating or imbibition. Thus, convection dominates heat transfer as it eventually does in all ISTR projects, and capillary pressure prevents drainage of water from the lower-permeability (100 md) soil.

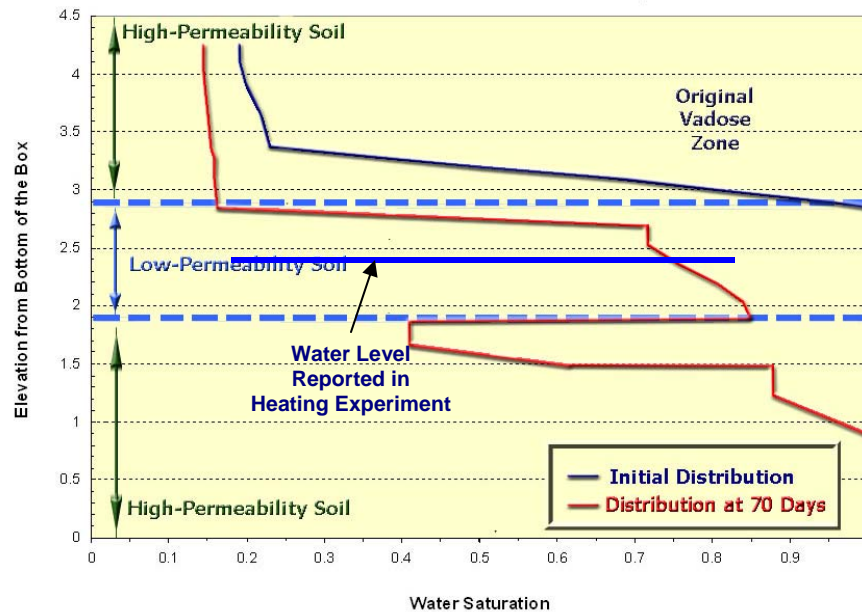
Figure 11 - 3D Cross-Sectional View of the Temperature Distribution at 63 Days in the Large, 3D-Heat-Transfer Experiment in the Original Setup with Gas-Velocity Vectors



Typical vertical water-saturation distributions at the start of a simulation and after 70 days of heating are shown in Figure 12. The nominal bottom of the vadose zone is initially at 3.0 m, but the water-saturated zone extends some distance above that due to capillary rise. After heating for 70 days, water has imbibed from the underlying, high-permeability soil region (aquifer) into the higher-capillary-pressure, lower-permeability soil layer (aquitard).

The nominal, final water level in the simulation is approximately 1.5 m from the bottom in the center of the tank. This is below the level reported for the experiment at that time (2.1 m at the wall). However, the water level measured near the wall of the tank is slightly higher because the internal pressure in the center of the tank is raised by the energy added by the heaters. This pushes water towards the walls and raises the pressure at the bottom of the tank. This higher pressure is reflected in higher measured water levels in external gauges and the high pressure in the center of the tank can raise the externally-measured, apparent water level by 0.5 m when the capillary pressures are as low as were needed to model this experiment.

Figure 12 - Initial Water-Saturation Distribution and Simulated, Saturation Distribution after 10 Weeks of Heating in the 3D-Heat-Transfer Experiment in the Original Setup



While differences still exist between the observations from the experiment and predictions over a range of parameters, the following controlling phenomena had been identified:

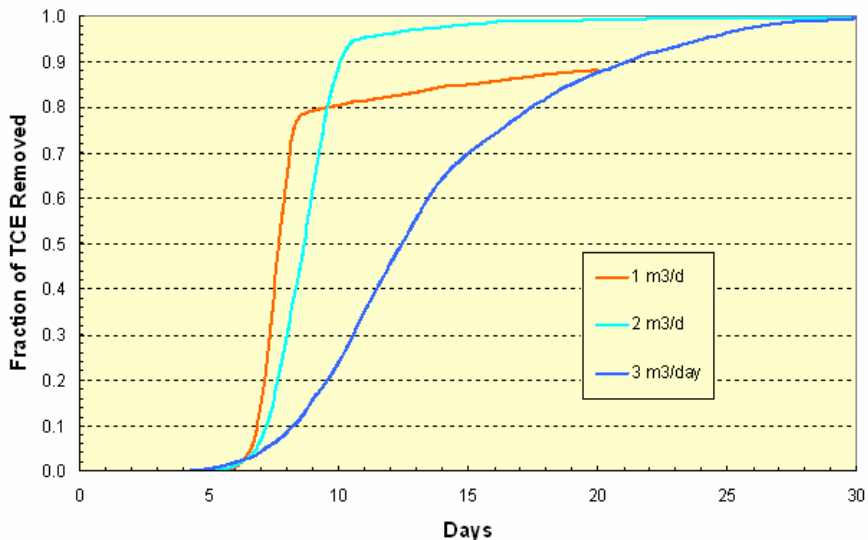
- Capillary pressure causes imbibition into higher capillary-pressure regions such as the lower-permeability soil and near the heaters;
- The water saturations are nearly level; and
- Gas moves freely throughout the enlarged, but cooler, unsaturated zone. Removal of the contaminants from a cooler zone will occur much more slowly and therefore their movement into such zones should be avoided.

Table 10 of Section 7 summarizes the variables that most affect temperature and water distribution in the heating experiments and their possible effect on remediation. The factors listed in the table suggest that the water level difference noted above, in Figure 12, is likely to be the result of lower power delivery by the heaters or even lower capillary pressure than was used in the model.

3D Large-Tank TCE Remediation Predictions: The calibrated, large-tank simulation was next used to predict remediation of TCE (BP = 90°C) from a DNAPL release lens placed 2 m from the bottom of a tank. Figure 13 shows that aquifer influx has a dramatic effect on removal of TCE from the lower lens of the tank. With an aquifer influx of 1 m³/day, 80% of the TCE is recovered quickly (prediction), but the remainder is recovered slowly. This is because the TCE has migrated outside of the heated region and even into the high-permeability (10 Darcy) lower zone. When the aquifer influx rate is 2 m³/d, the predicted recovery rate is not quite as fast but over 95% is recovered within 15 days. If the rate is raised even higher (3 m³/d) the TCE is not recovered as quickly because the heated zone is cooler. So, the aquifer influx rate is predicted to be a very critical factor controlling remediation in these experiments. As will be shown later,

really high aquifer influx rates disperse a contaminant far enough that it is very difficult to recover, e.g., once the PCE migrates outside of the heated region it cannot be easily recovered by vaporization.

Figure 13 – Effect of Aquifer Influx on Removal of TCE from a Large-Tank 3D Experiment



Figures 14 and 15 show that the gas rate at the SVE extraction wells has little impact on TCE removal but has a large impact on the actual water saturation in the tank in a simulation with two m^3/day aquifer influx. As Figure 14 shows, the effect of increasing the SVE extraction rate by a factor of three has negligible impact on TCE recovery when the aquifer influx rate is $2 \text{ m}^3/\text{day}$. Figure 15 shows the same increase in the SVE gas rate has an insignificant affect on the apparent water level in the tank. This level is assumed by assessing the level of water in the inlet and overflow lines. Here, it is calculated from the pressure at the water inlet well located in the bottom right corner of the drawing in Figure 2.

Figure 14 – Effect of SVE Gas Rate on Recovery of TCE from Large Tank

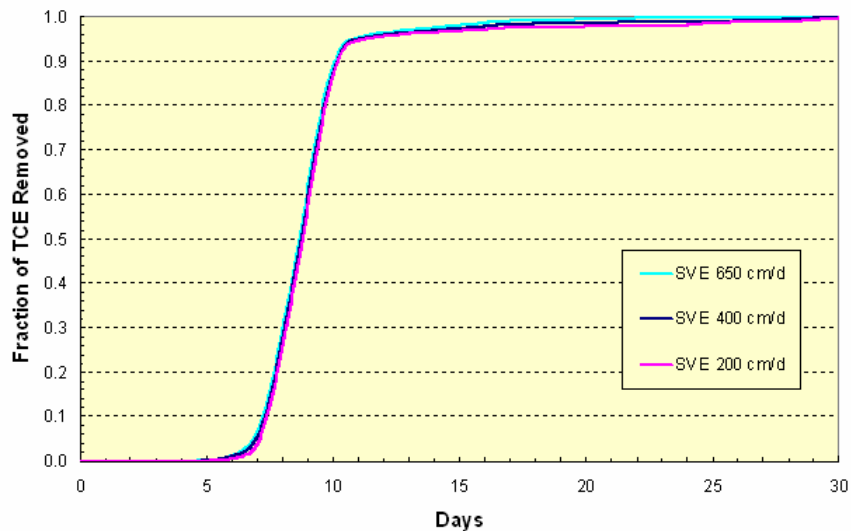
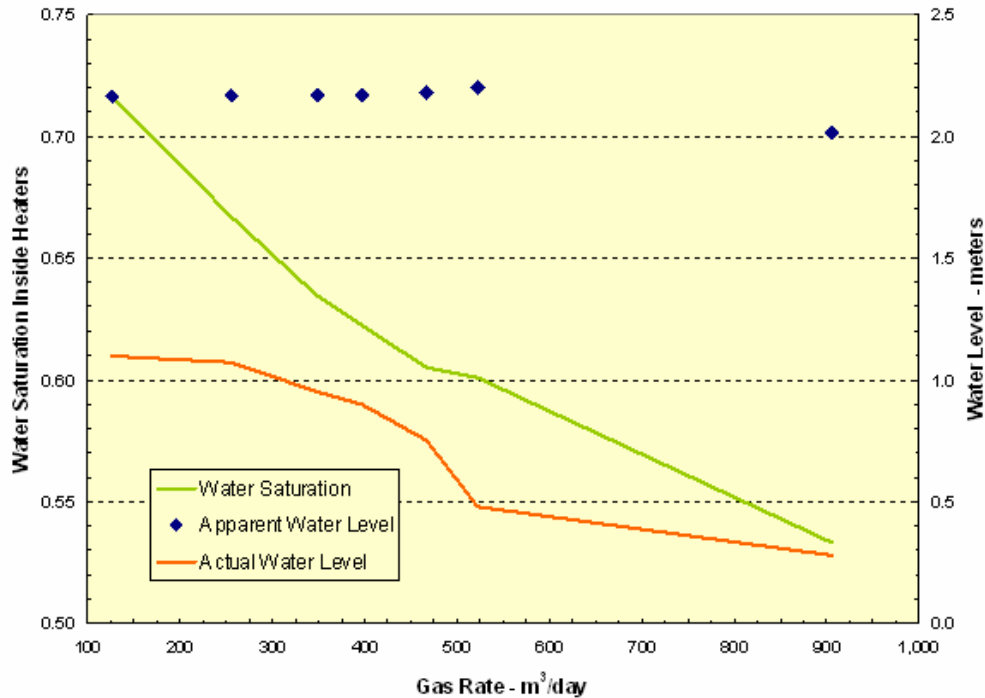


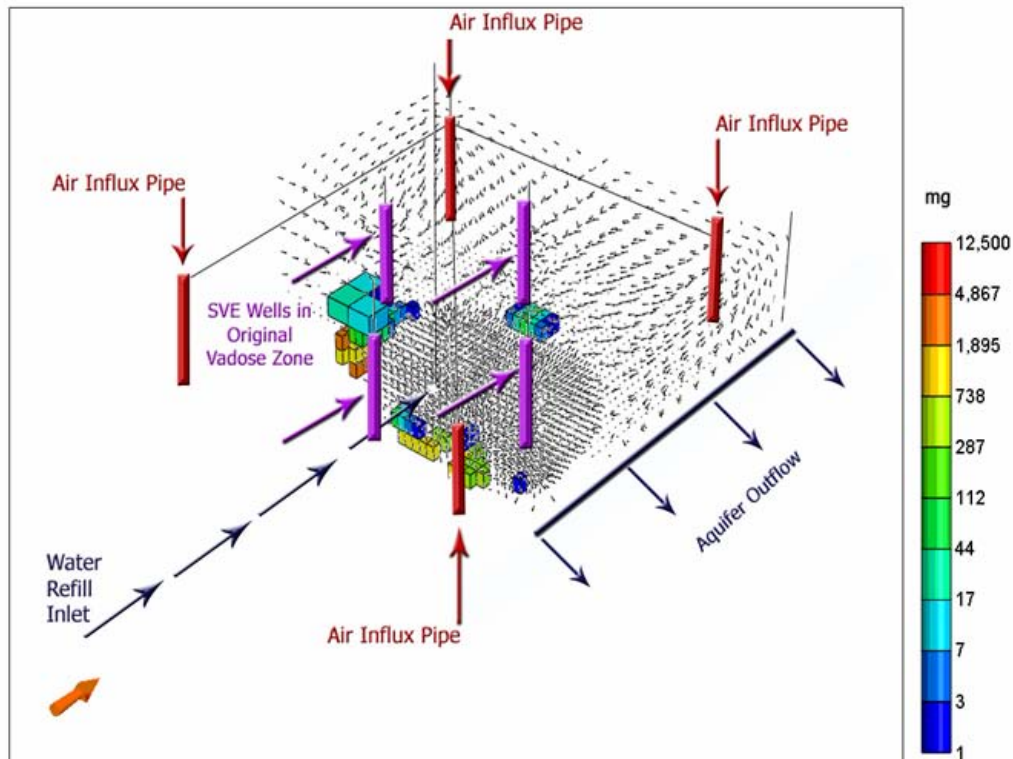
Figure 15 – Effect of SVE Gas Rate on Apparent and Predicted Water Levels between Heaters



However, Figure 15 also shows that the average water saturation and actual water level in the tank are both strongly affected by the SVE extraction rate at a fixed aquifer influx rate. The SVE extraction rate reduces water saturation almost linearly with rate because it reduces water's partial pressure and promotes evaporation of water. This evaporation reduces the water level in the tank and also cools the tank with the result that TCE stripping does not increase with SVE extraction rate. However, the difference between the actual and apparent water level in the tank increases. This tells us that the water level in the tank can be far below what is assumed from external measurements and that TCE in the vapor can condense into that cooler, un-steamed aquitard region at the boundary between coarse and fine sands. In this unheated region the TCE will not be recovered by vaporization.

Figure 16 shows the predicted locations of the residual TCE after heating with low SVE extraction rate and higher water table. The residual TCE is all outside of the SVE wells or at the actual water level, i.e., where the TCE can condense from the vapor. This indicates that lateral migration of TCE outside the TTZ prevents TCE recovery and that the tank experiments should be designed to limit lateral migration of the DNAPL constituents in either the gas or water phase. But in the 3D tank experiments, lateral, gaseous contaminant migration in the aquitard cannot be avoided completely because (in sharp contrast to field applications) no SVE wells were installed in the lower permeable layer. Thus, processes like the heat-pipe effect (Udell and Fitch, 1985) would enable a transport of steamed contaminant in the gaseous phase to the boundary (steam condensation) and a transport of dissolved contaminant in the liquid phase including a re-steaming.

Figure 16 – Locations of Residual Saturations of TCE in 3D Tank Remediation Simulation



Small-Tank 3D Heating Experiment: The modeling of the first large-tank experiment with no aquifer influx has been described previously. The small-tank 3D heating experiment was conducted in a tank that was half as wide as the large tank. Aquifer influx was held at 1 m³/day for 67 days (with low and high heater power), 0.67 m³/day for 14 days, 0.5 m³/day for 8 days and finally 0.03 m³/day for 12 days. The experiment continued beyond this point with increased aquifer flow rates, but these phases of the experiment were not modeled.

Ninety percent of the work done to model this experiment was expended in modeling heating of the vadose zone. Some of the techniques used to model this, such as approximating convection inside of the heater cans are described below. The experimental results clearly show that the vadose zone began to dry out near the heaters a few weeks after heating began and that the rest of the vadose zone between the heaters gradually dried out during the rest of the experiment. The temperature at the heater cans - 1 m above the heaters - exceeded 150°C after a few weeks of heating and reached 230°C by 101 days. Most of the modeling effort was spent trying to reach these temperatures by convection of hot steam upwards from the heaters (Single-Convection Model). However, that proved impossible to accomplish. It was, however, relatively easy to reach those temperatures and dry out the vadose zone if approximately 20 % of the power of the heaters was transferred from the heater cans into the vadose zone. This means that heat was moving by convection inside of the heater cans. Since some upward convection of steam outside of the can was retained, we call this the dual-convection model.

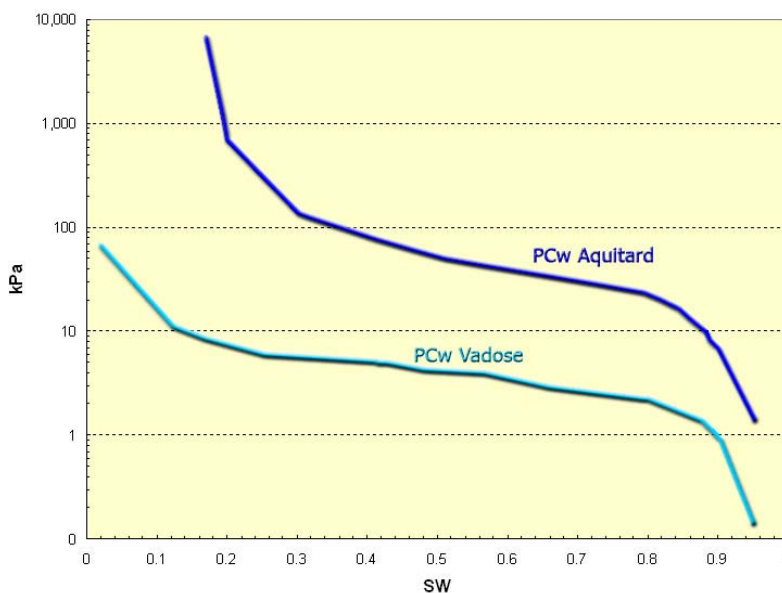
In the single-convection method of modeling the high temperatures, heating was assumed to be limited to the locations of the heaters. The steam that was generated outside of the cans then

could move upward, around the can. This method has two flaws. The first is that moving steam upwards prevents the top of the tank from drying out and limits the temperature there to around 100°C. The second flaw is that ridiculously high vertical permeabilities are needed to effect significant heating by this method.

The dual-convection method is much simpler. Since the interior of the can had infinite vertical permeability, convection would occur. Now, STARS is a simulator meant to model movement of energy and fluids in soil and rock, not natural convection in air. So, in the absence of a convenient computational fluid dynamics model in STARS, some of the energy from the heaters was borrowed and dispersed fairly uniformly within a meter above each heater can. Then the temperature could rise above 100°C as soon as the water was evaporated.

As a result of using the dual-conduction model, the ratio of the capillary pressures in the aquifer and aquitard could be increased. The NAPL-water capillary pressure curves used in the final simulation of the small-tank 3D heating experiment are shown in Figure 17. The important characteristic of these capillary pressure curves is that the capillary pressure in the aquitard is always at least an order of magnitude larger than the capillary pressure in the aquifer. The ratio increases with decreasing water saturation. This draws more water into the aquitard as it starts to dry out. The movement of water upward to be evaporated in turn accelerates movement of DNAPL constituents upward and slows migration of DNAPL constituents downward.

Figure 17 – Capillary Pressure-Saturation Relationships Used in Final Small-Tank 3D Heating Experiment Simulations



Figures 18 through 20 show the temperature distribution in a cross section through the center of the tank at 67 days (aquifer influx 1 m³/d), 89 days (aquifer influx 0.5 m³/d) and 101 days (aquifer influx 0.03 m³/d), respectively. Figure 18 shows that the region around the tops of the heaters is hotter than 135°C (actually 160°C). The regions where the DNAPL release lenses are located (1.8 m and 2.2 m from the top of the tank and 2.7 and 2.3

Figure 18 – Temperature Distribution across the Center of 3D Tank after 67 Days of Heating

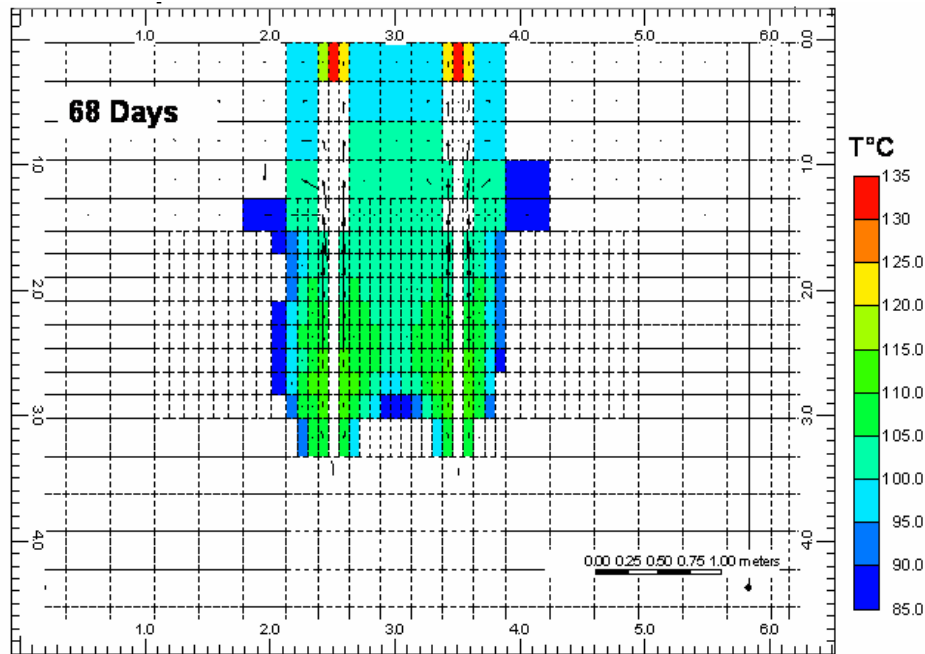
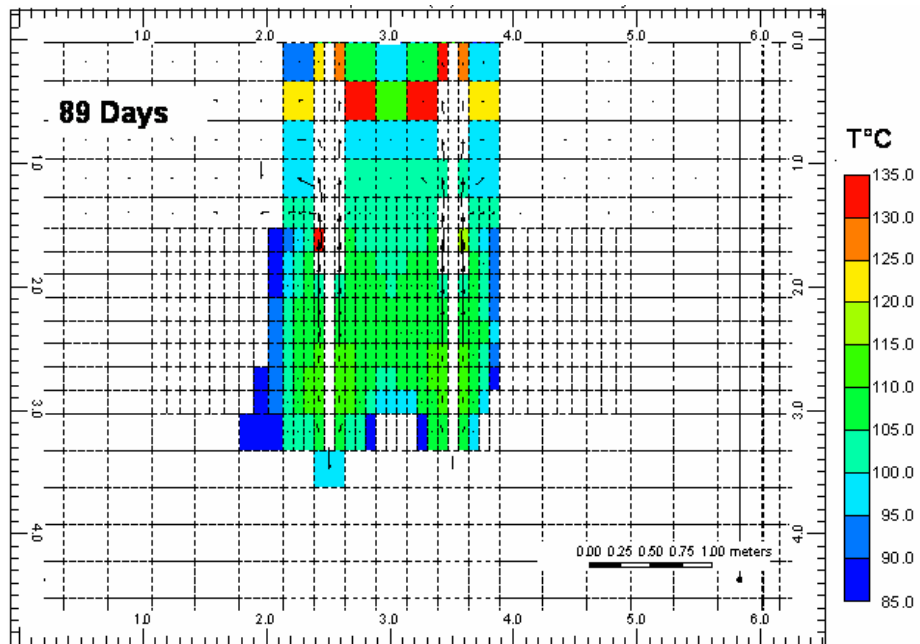


Figure 19 – Temperature Distribution across Center of 3D Tank after 89 Days of Heating



m from the bottom) are between 100°C and 105°C. This is below the boiling point of PCE but subsequent simulations show that any PCE in the lenses is gone by then. Figure 19 shows the temperatures after 89 days (end of 0.5 m³/d aquifer influx). Now, the vadose zone is starting to dry out and the average temperature in the vadose zone is 110°C as is the region between the

heaters in the aquitard. The tops of the heater cans are again even hotter. The final figure of this group (Figure 20) shows temperatures at 101 days (end of 0.03 m³/d aquifer influx). Now, the

Figure 20 – Temperature Distribution across Center of 3D Tank after 101 Days of Heating

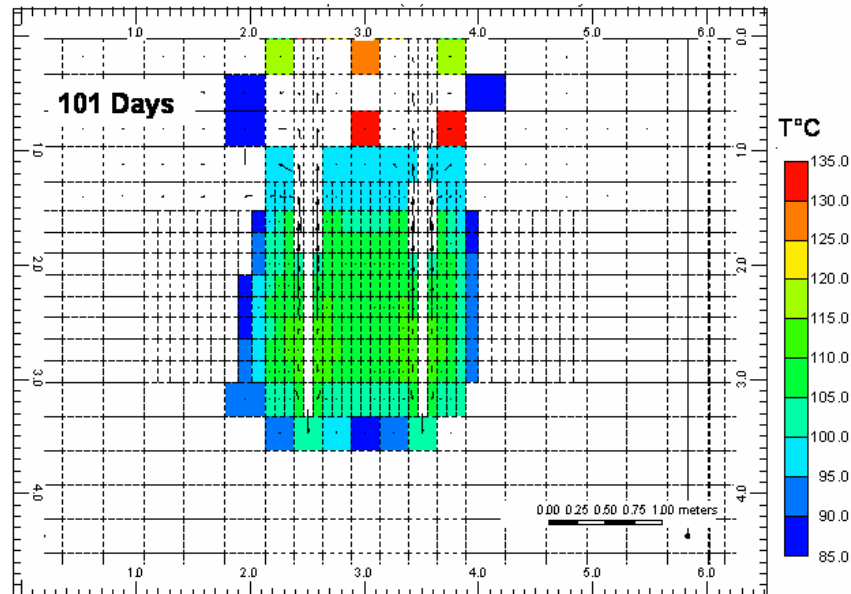
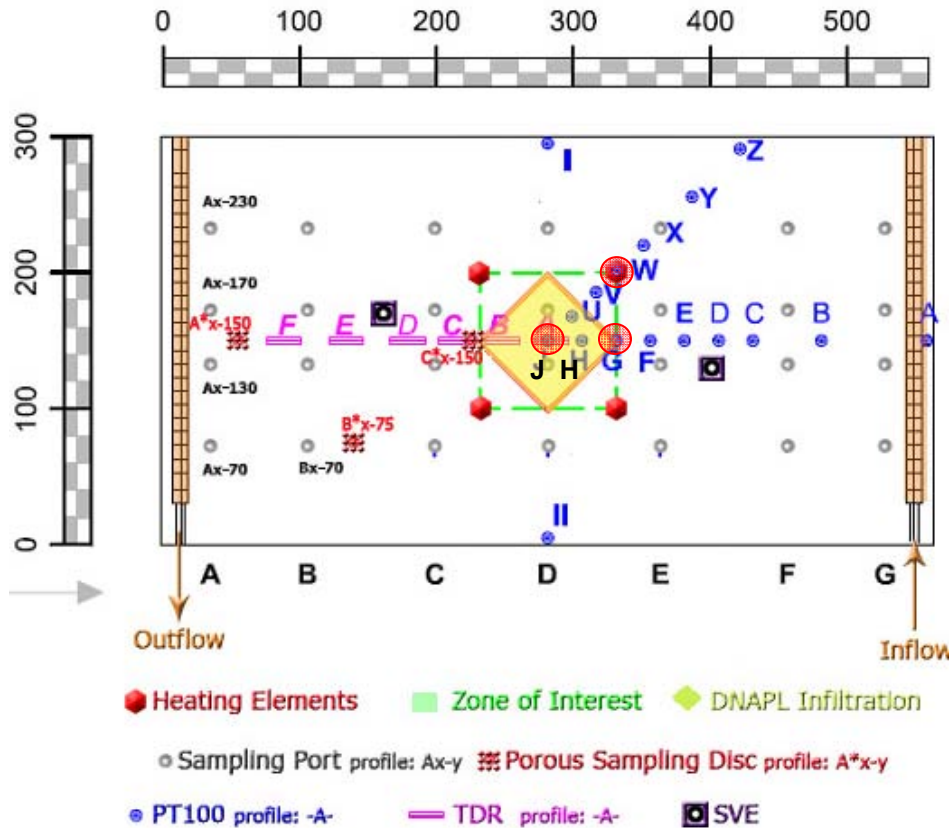


Figure 21 – Plan View of Small 3D Tank Showing Locations of Thermocouple Profiles A to Z



vadose zone is very hot and completely dry, yet the temperature between the heaters in the aquitard is approximately the same as it was in the previous two slides.

The next group of figures shows the history match of the temperatures along three sets of vertical thermocouple arrays (“profiles”). These are thermocouple profile W at a heater can, thermocouple profile J, in the centroid of the tank, and thermocouple profile G, midway between two heaters. The locations of these thermocouple profiles are shown in Figure 21 (large red circles). The matches between actual and predicted temperatures at thermocouple profiles W, J and G are shown in Figures 22 through 24, respectively.

The temperature match at the heater can is shown in Figure 22. The figure shows steadily increasing temperature in the aquifer below the heaters, a broad plateau of relatively constant temperature around the heaters, and a region of steadily increasing temperature in the vadose zone (after 1.2 kW was applied at each heater after 24 days). The temperature at 24 days could be matched by saying that 40% of the heaters power convected upward. When the heaters were placed on full power, approximately 20% of the power convected upward inside of the cans. Then, the temperatures in the vadose zone 0.5 m below the top of the sand next to the can reach 200°C because the heater cans are that hot. The temperatures of the portions of the heater cans protruding above the box, however, were < 37°C, as measured from infrared photographs.

In contrast, the temperature at the centroid of the model shown in Figure 23 remains around 107°C in the aquitard and vadose zone until the aquifer flux is reduced to 0.03 m³/d (between 89 and 101 days). Then, the centroid dries out completely and the temperature reaches 140°C. As in the previous figure, the centroid temperature at 24 days could only be matched by allowing 20% of the heater’s power to convect upwards inside of the heater can. Finally, Figure 24 shows the temperature between two heaters at thermocouple G, which remains fairly constant around 107°C before 81 days.

Figure 22 – Predicted and Actual Temperatures at Thermocouple Profile W – at Heater Can

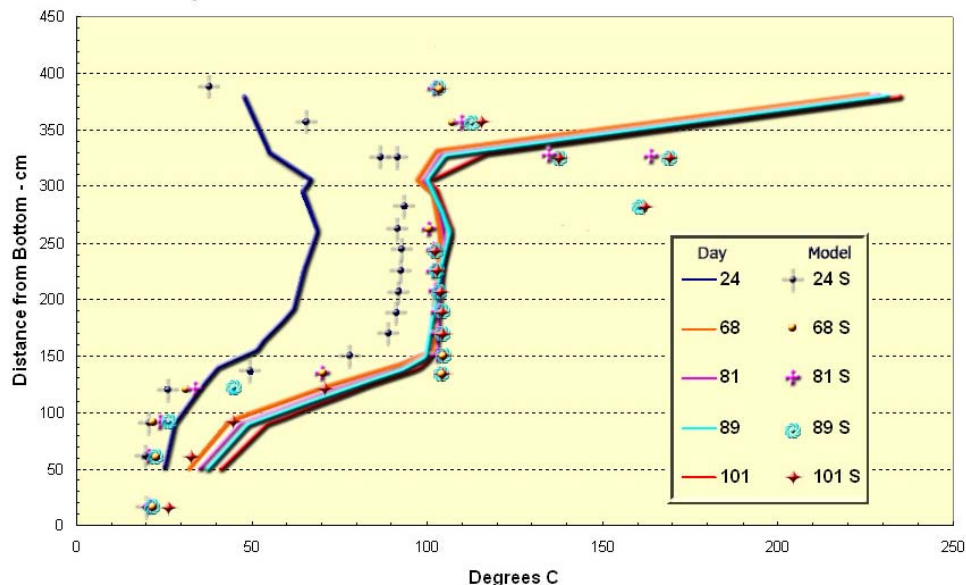


Figure 23 – Predicted and Actual Temperatures at Thermocouple Profile J – at Centroid

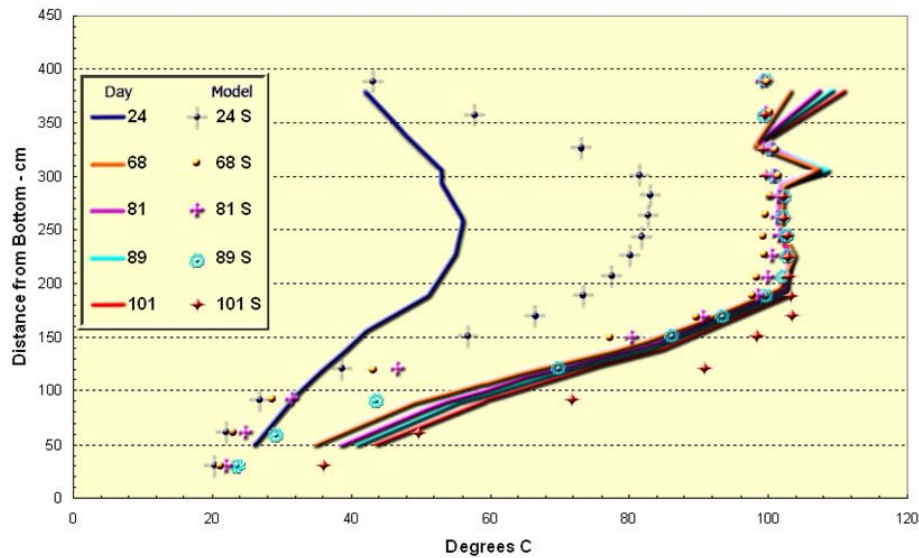
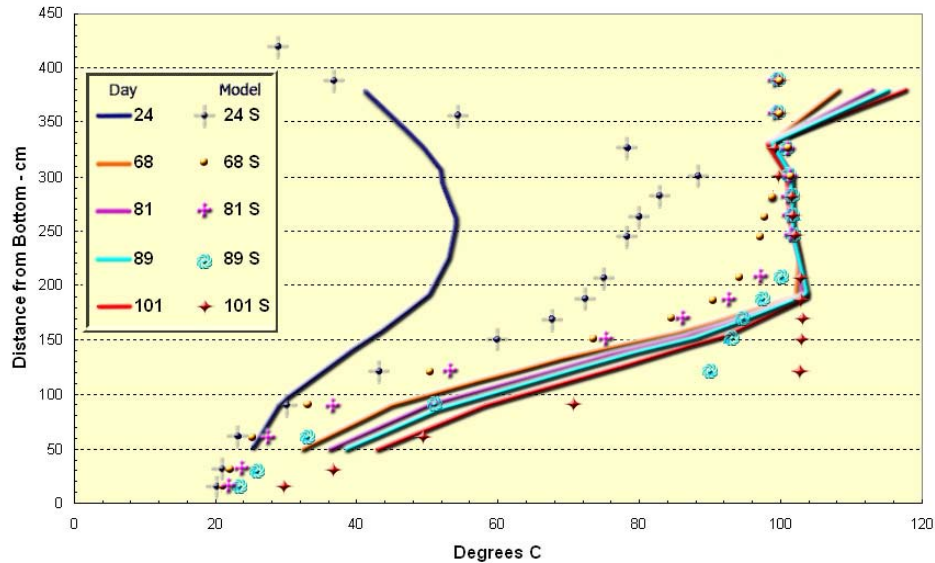


Figure 24 – Predicted and Actual Temperatures at Thermocouple Profile G – Between Heaters



The next three figures illustrate the advantage of the dual convection model. Figure 25 shows a 3D image of the predicted temperature and gas velocity in the front half of the tank at 101 days. The hot spots above two of the heaters can be identified, and the hot, drying part of the vadose zone between the heaters is visible at the level of the well screens. There is a cooler, wetter zone above the heaters in the capillary fringe at the bottom of the vadose zone, and the region between the heaters in the aquitard has a fairly uniform temperature. The temperatures shown in Figure 26 where the vadose zone is heated by convection of steam upwards outside of the heater cans (i.e., the single convection model) is a stark contrast to Figure 25 where heat can convect both inside and outside of the heater can. In

Figure 25 – 3D View of Temperature and Gas Vectors with Dual Convection at Heaters

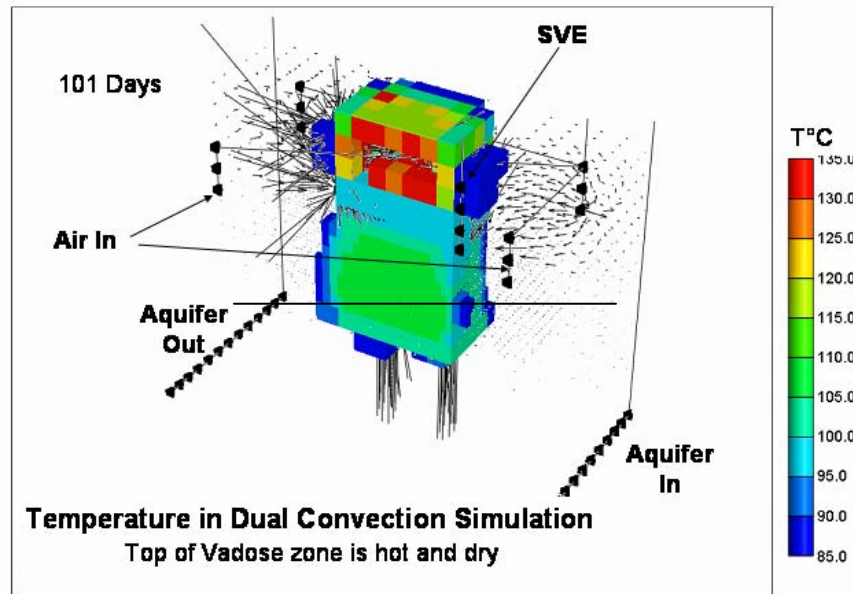


Figure 26 with single convection the entire vadose zone is cooler than the aquitard and the aquitard is cooler than with dual convection. The temperature is lower because more energy can be stored in hot water than in dry air and more energy is lost from the tank when the vadose zone is wet. Finally, Figure 27 shows the water saturations with dual convection. Now, the vadose zone is dry between the four air inlet wells and the steam zone (< 80 % water saturation) ends at about the top of the aquitard. With single convection, the center of the vadose zone between the heaters is still wet and the steam zone has moved into the aquifer.

Figure 26 – 3D View of Temperature and Gas Vectors with Convection Outside of Heaters (Single Convection Model)

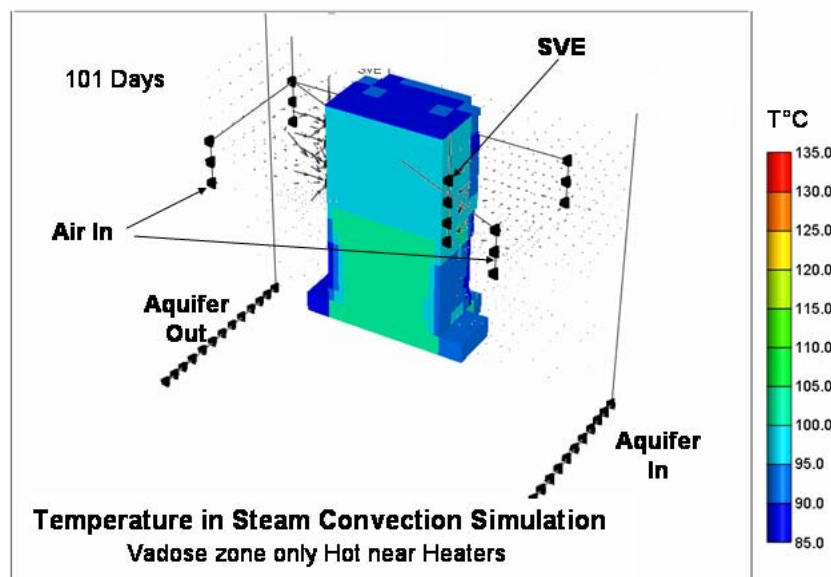
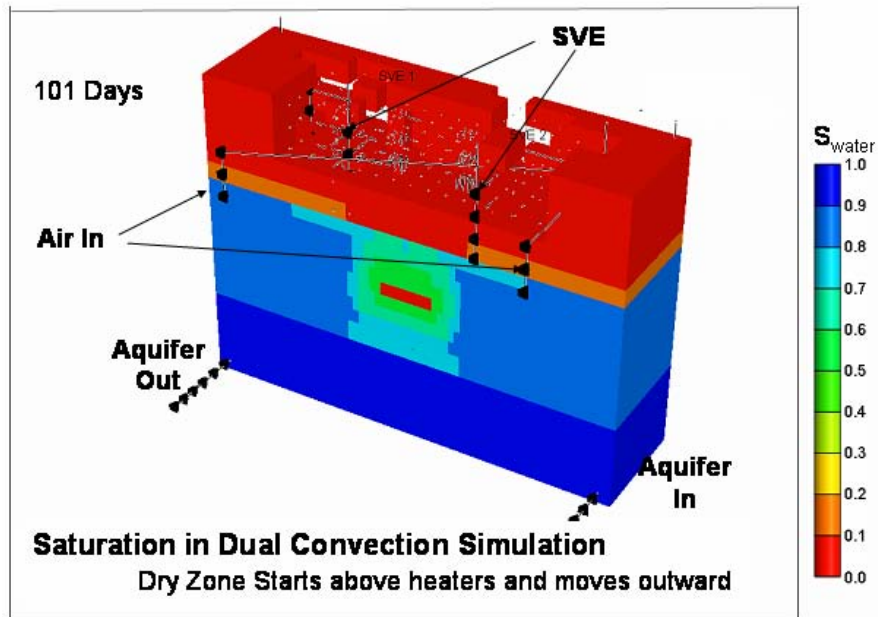


Figure 27 – 3D View of Water Saturation with Dual Convection at Heaters



2D-Flume Remediation Experiment: The flume in this experiment contained two types of sand as shown in Figure 3. The top 2/3rds of the box was filled with nominal 100-md sand, while the bottom of the box was filled with nominal 100-Darcy sand. During the remediation experiment the PCE began to drain from the DNAPL release lens in the center of the flume within minutes of being injected, as evident in photographs in which small amounts of the dyed PCE entered the GEBA transition layer adjacent to the lens. It is not known from the laboratory data whether or how much PCE drained further downward.

Modeling of this experiment was divided into two portions. At first, only the temperature in the box was modeled. This allowed the upper end of the capillary pressure curves and heat losses from the box to be established. Then, the recovery of PCE was modeled. Most of that portion of the simulations was directed towards enhancing movement of PCE from the lens so that it could be produced as early as it was produced from the experiment.

Figures 28 through 32 highlight the details of the history match of temperature. The temperature after 3 and 6 hours is shown in Figures 28 and 29. The important feature in Figure 28 is that the temperature in the high-permeability zone at 3 hrs is higher under the lens than the temperature of the lens. The maximum temperature around the lens is 85°C, and the temperature inside the lens is less than 60°C. The PCE in the lens is not volatile at these temperatures, so any PCE that was produced must have migrated into a hotter zones, i.e., towards the heaters and/or into the “Grossand” zone (because its pressure is higher). Figure 29 shows that at 6 hrs the lens is now hotter than that in the high-permeability sand under the lens (because the pressure in the low-permeability sand is higher). By this time, 90% of the PCE had been vaporized and recovered.

Figures 30 and 31 show the predicted water saturation in the model at 3 hours and 6 hours, respectively. As with the temperature at 3 hours, the water saturation is lower under the lens

Figure 28 – Temperature in Model after 3 Hours of Heating

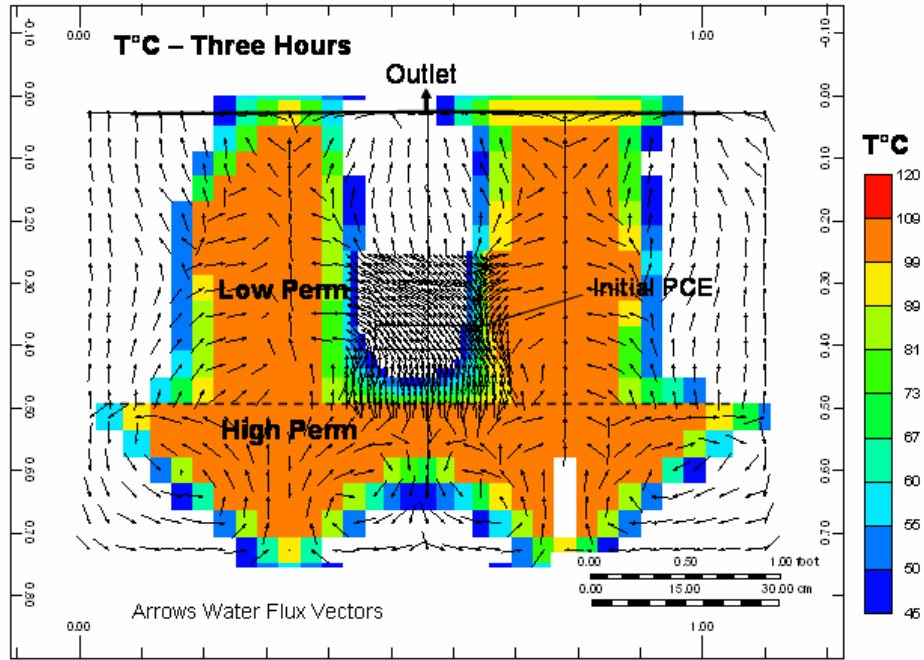


Figure 29 – Temperature in Model at End of Heating at 6 Hours

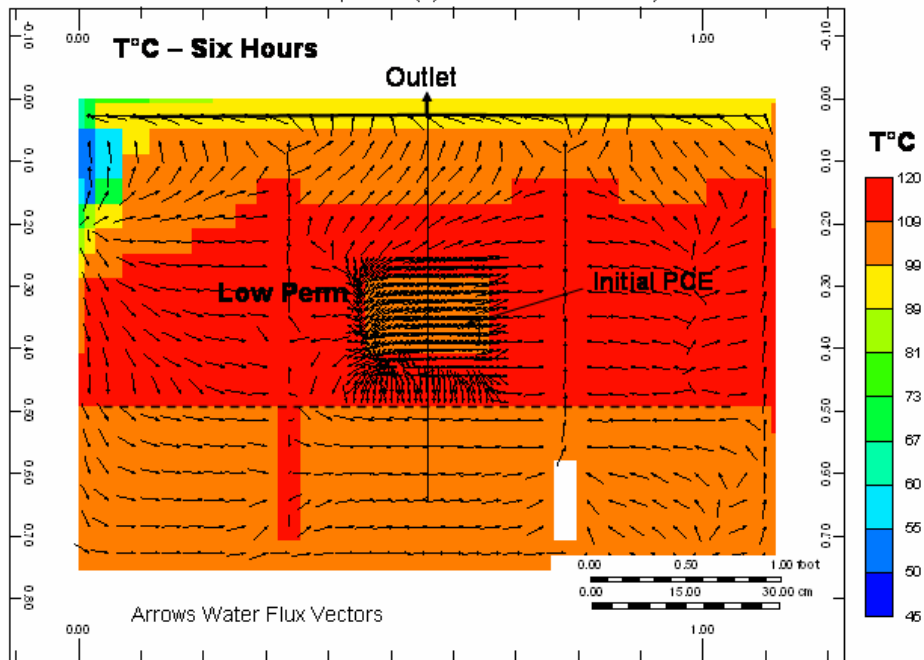


Figure 30 – Water Saturation in the Model after 3 Hours

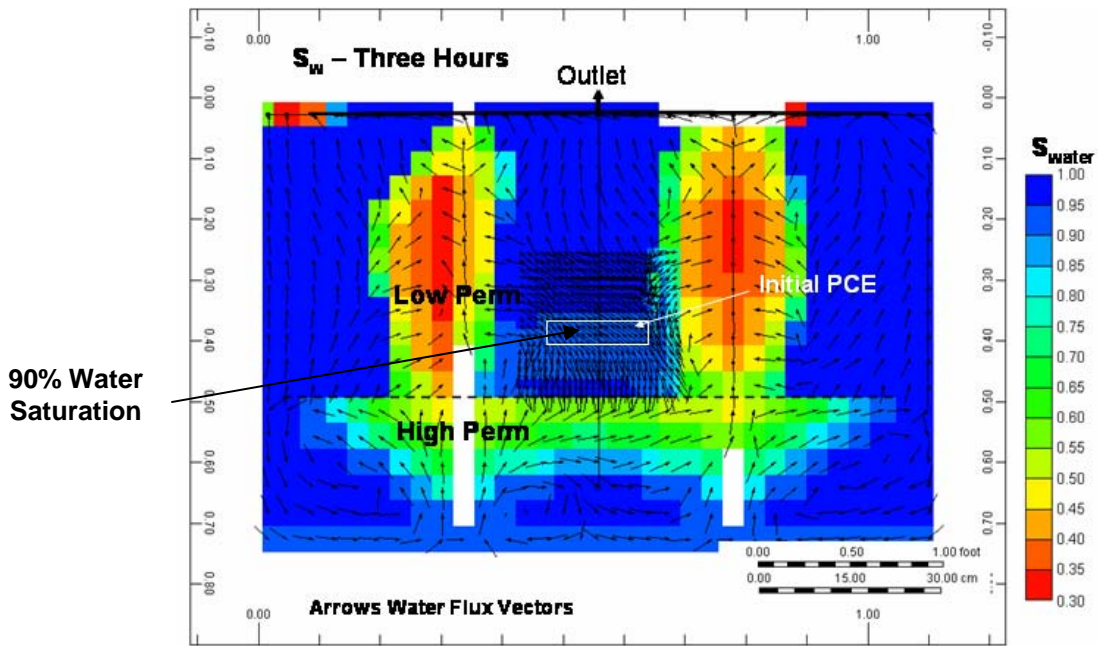
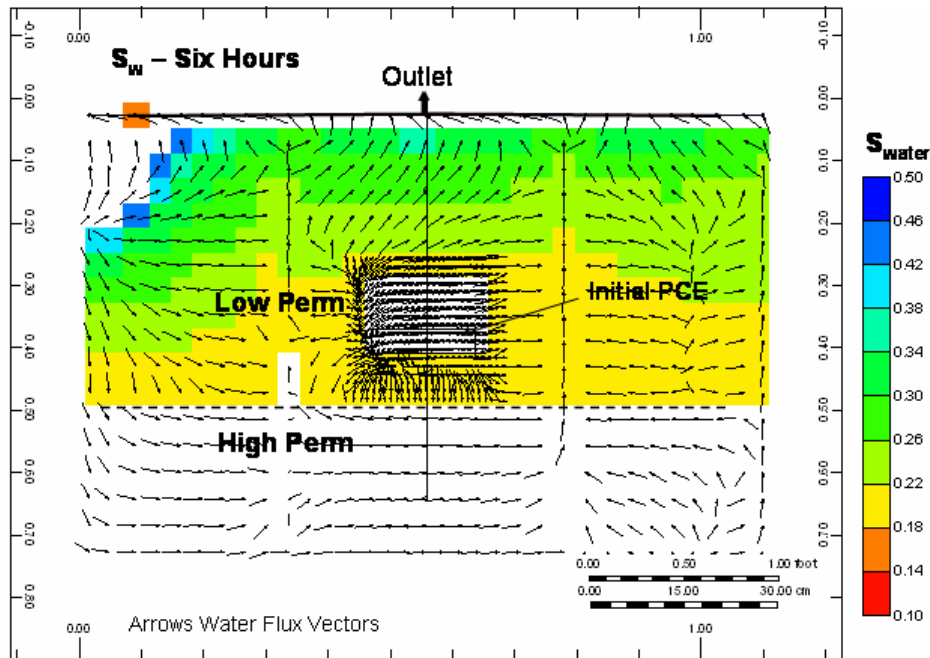


Figure 31 – Water Saturation after 6 Hours



than it is in the lens. This means that PCE that will move into this area will be vaporized before the PCE in the lens is vaporized. Now, Figure 31 shows that at the end of the experiment the lower, high-permeability sand is nearly dry, while the lens still has a water saturation of 20% and the area above the lens has a water saturation over 30%, i.e., it is cooler. Both Figures 32 and 33 show how the flux of water in the model could affect movement of the PCE. The flux of

water in the model is upwards from the hot, “Grossand” layer and then towards the left heater. This will move PCE from the lens to be vaporized before the lens is hot.

Figure 32 shows the predicted water production. Significant water production starts at about 2 hours and rises dramatically after 4 hours as the high-permeability sand dries out. Water production decreases again after 5 hours when water has been removed from the lower-permeability soil. In this example, 70% of the water in the model is removed.

Figure 32 – Estimated Water Production Rate from Experiment

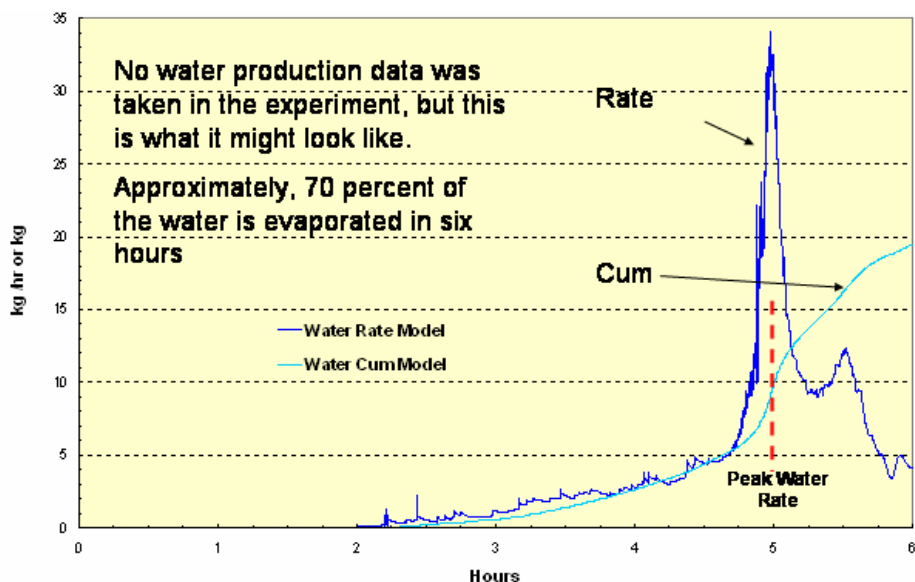
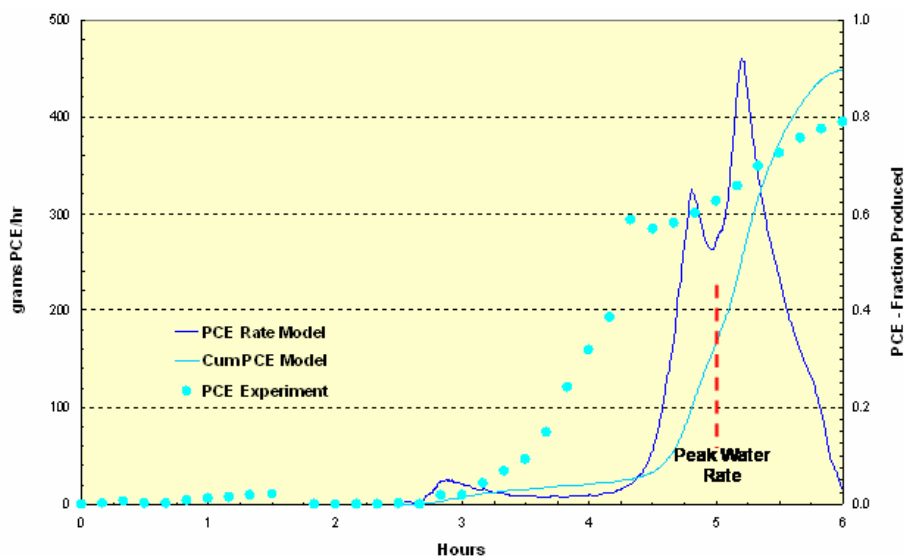


Figure 33 compares predicted and actual PCE production. The figure shows that predicted, cumulative PCE production eventually exceeds actual cumulative production, but the simulations do not predict the high production rate of PCE at approximately 4 hours.

Figure 33 – Predicted and Actual PCE Production Rates from 2D Remediation Experiment



While the simulations didn't completely track the PCE migration rate, they can be useful to show where the PCE could have moved. Figures 34, 35 and 37 through 40 show the predicted distribution of PCE as a DNAPL and PCE that is dissolved in the water. The simulation starts when PCE was injected into the lens over a 2-hour period. The PCE saturation distribution at the end of injection is shown in Figure 34. Most of the PCE remains in the lens but small amounts have migrated in all directions. Heating did not start until the next morning. By that

Figure 34 – Predicted PCE Saturation after Lens Filling

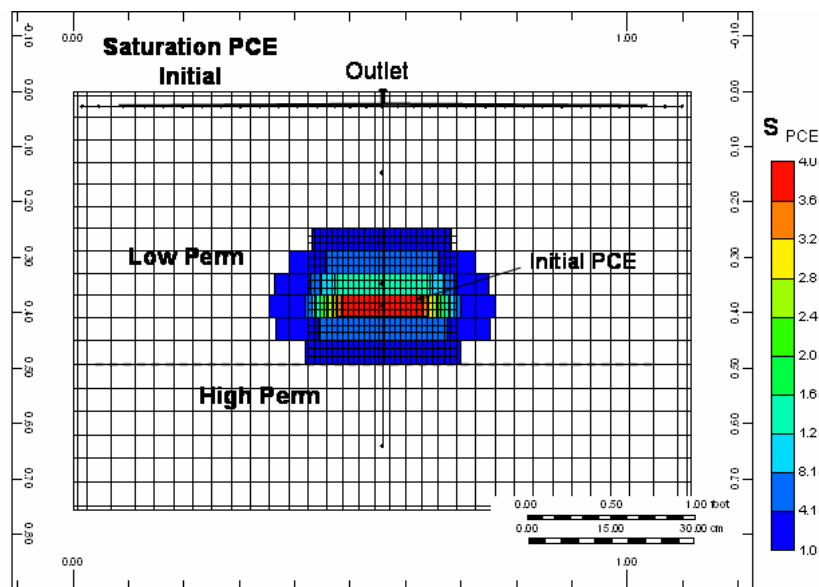
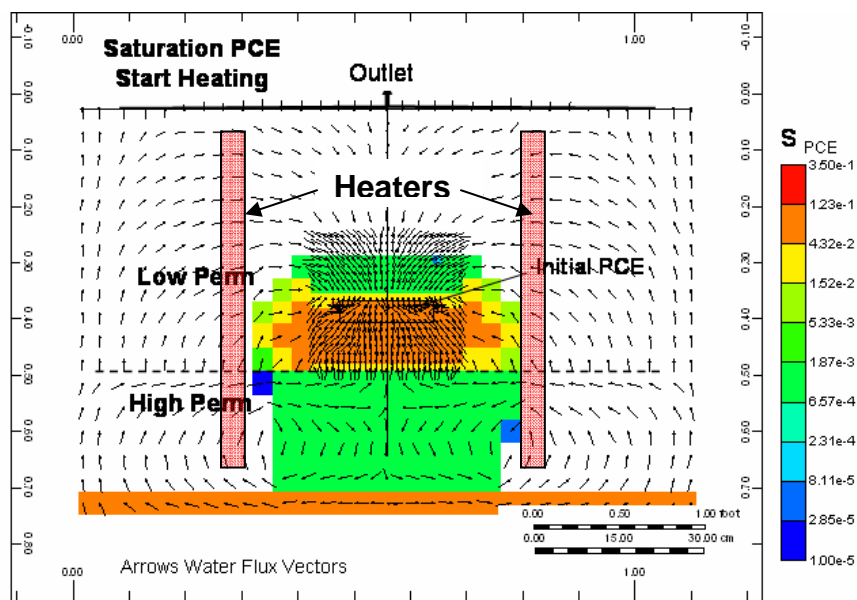


Figure 35 – Predicted PCE Distribution at Start of the Heating



time, although not observed in the experiment, some PCE was predicted to have drained to the bottom of the flume, Figure 35. In addition, some PCE has migrated to the heaters, shown in

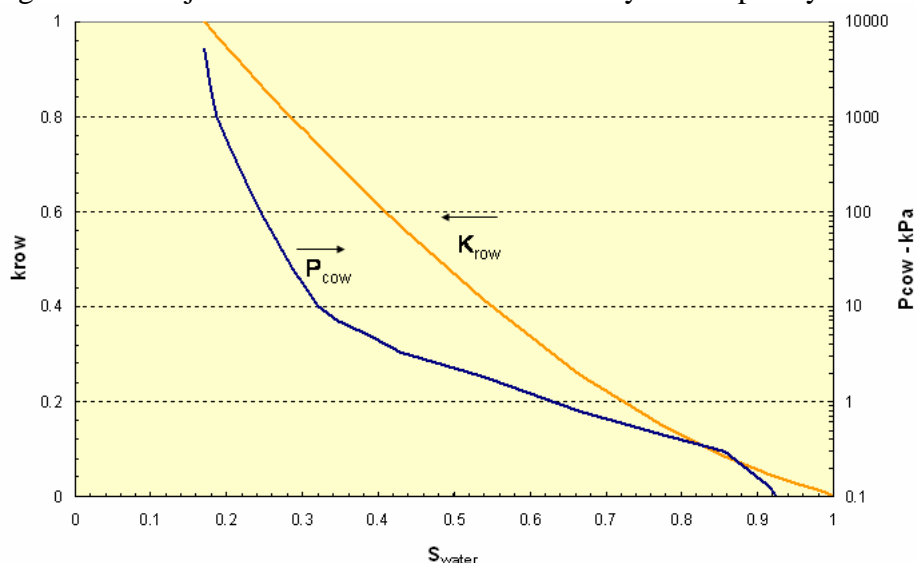
transparent red in Figure 35. Such PCE would probably be produced immediately upon turning on the heaters. However, the mass of the initial production is predicted to be small.

Modeling of the heating was not a problem. However, modeling how rapidly the PCE was produced did prove to be difficult. Three factors were important: Relative permeability of the NAPL at low saturations, the vertical permeability, and dilation of unconsolidated sand to relieve the pressure caused by boiling of water.

The relative permeability and capillary pressure were modified extensively in order to promote this migration of PCE. Normally, the water-NAPL curve of a simulator like STARS is an imbibition curve and reflects how NAPL is trapped when the water saturation is increasing. However, this process is a drainage process in which small saturations of PCE move through the soil in a few pore channels. Thus, the water-NAPL curve is more like a normal relative-permeability curve for injection of a gas or oil, i.e., it is non-zero at low saturations, and the NAPL relative-permeability curve shown in Figure 36 is non-zero for all saturations greater than 0.1 % (approximately 400 ppm on a dry weight basis).

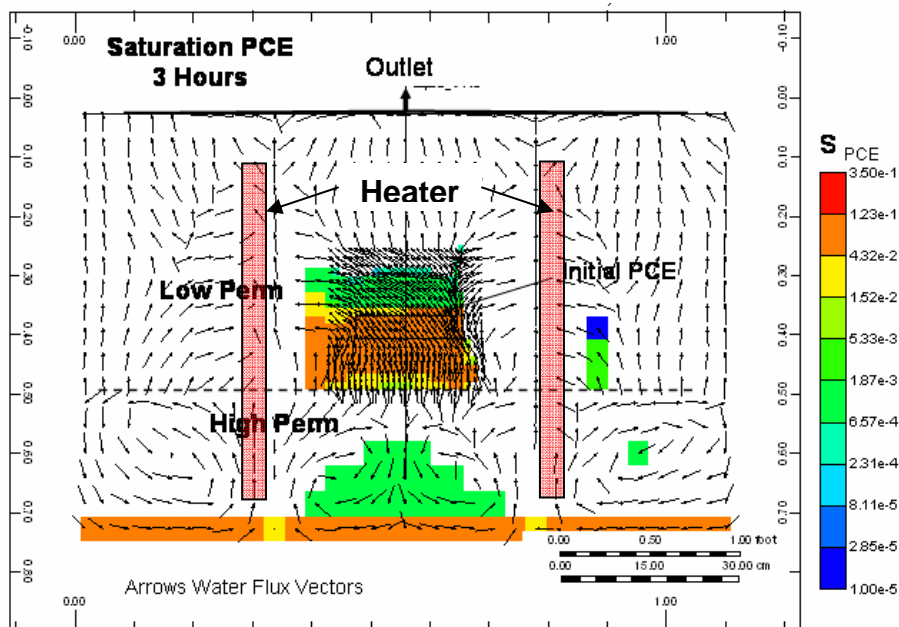
There are several forces affecting how the DNAPL moves: Gravity causes the DNAPL to move downward into the zone which is heated first. Bouyancy, (of the DNAPL vapors) which increases as the DNAPL is heated and more vaporizes, can cause it to move upward. The regional pressure gradient causes the DNAPL to move in one direction or another and quickly opposes the movement of PCE downward. Figures 30 and 31, for example, show that the movement of water is upwards. Finally, capillary forces can oppose the movement of the DNAPL if the DNAPL is nonwetting. Then the DNAPL must be forced into a pore. For that reason, the NAPL-water capillary pressures used in these simulations and shown in Figure 36 are negative (by 0.01 psig) below a NAPL saturation of two volume percent. The high end of the capillary pressure curve is similar to that shown in Figure 17 and controls imbibition of water to the heaters and into the low-permeability zone.

Figure 36 – Adjusted NAPL Relative Permeability and Capillary Pressure



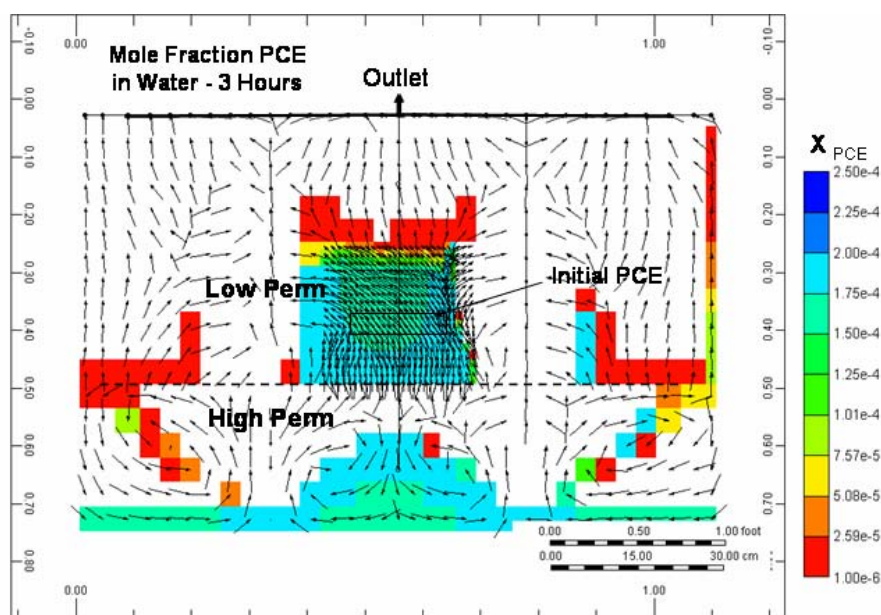
The saturations of PCE as a DNAPL and concentrations of PCE dissolved in the water phase after three hours of heating are shown in Figures 37 and 38, respectively. Figure 37 shows that the PCE near the heaters and in the hot zones of Figure 28 has evaporated. Unfortunately, some of this PCE may have condensed in cooler regions since the gas velocity vectors move away

Figure 37 - Predicted PCE Distribution after 3 Hours of Heating



from the heaters as well as upwards to the void space. The concentration of PCE in the water phase is shown in Figure 38. This figure shows that the concentration is high everywhere there is a free NAPL phase and low in most other places.

Figure 38 – Predicted PCE Distribution in Water after 3 Hours of Heating



Figures 39 and 40 show the distribution of PCE after 4.5 and 6 hours, respectively. At 4.5 hours, the PCE is clearly moving (via distillation and convection) towards the heater on the left side of the flume. The simulation predicts a low saturation of PCE (around 400 ppm) in the hot lower zone because convection is lower there after most of the water has evaporated.

Figure 39 – Predicted PCE Distribution after 4.5 Hours of Heating

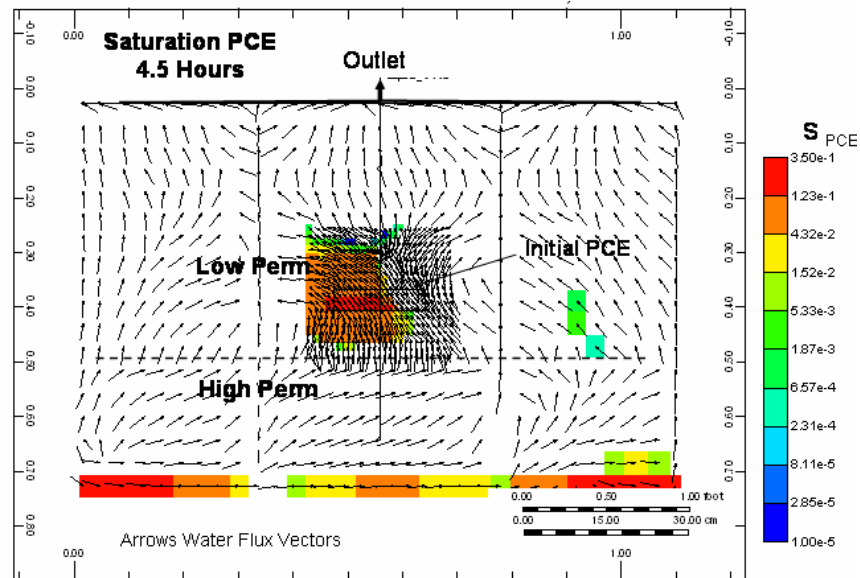


Figure 40 – Predicted PCE Distribution after 6 Hours

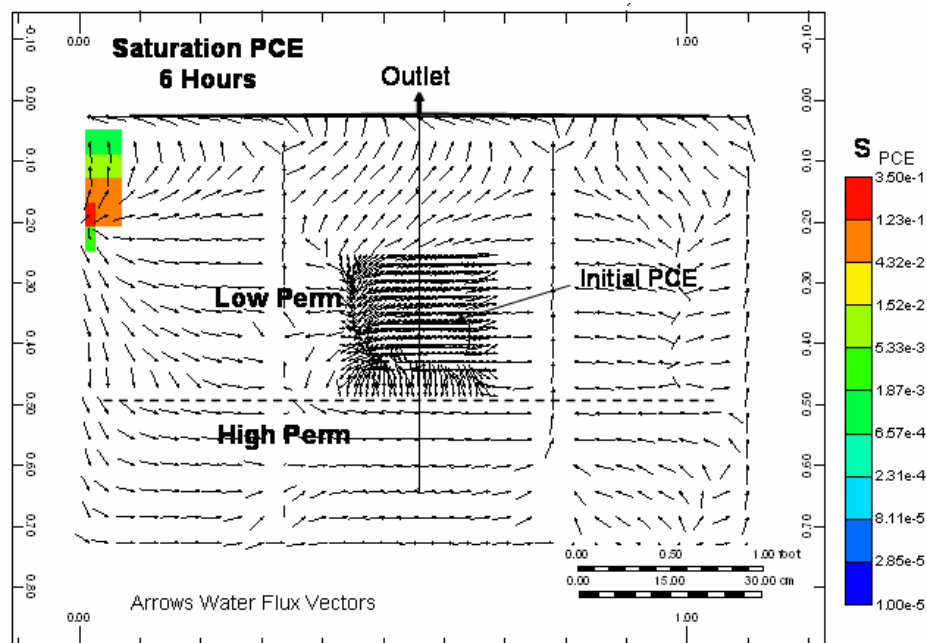
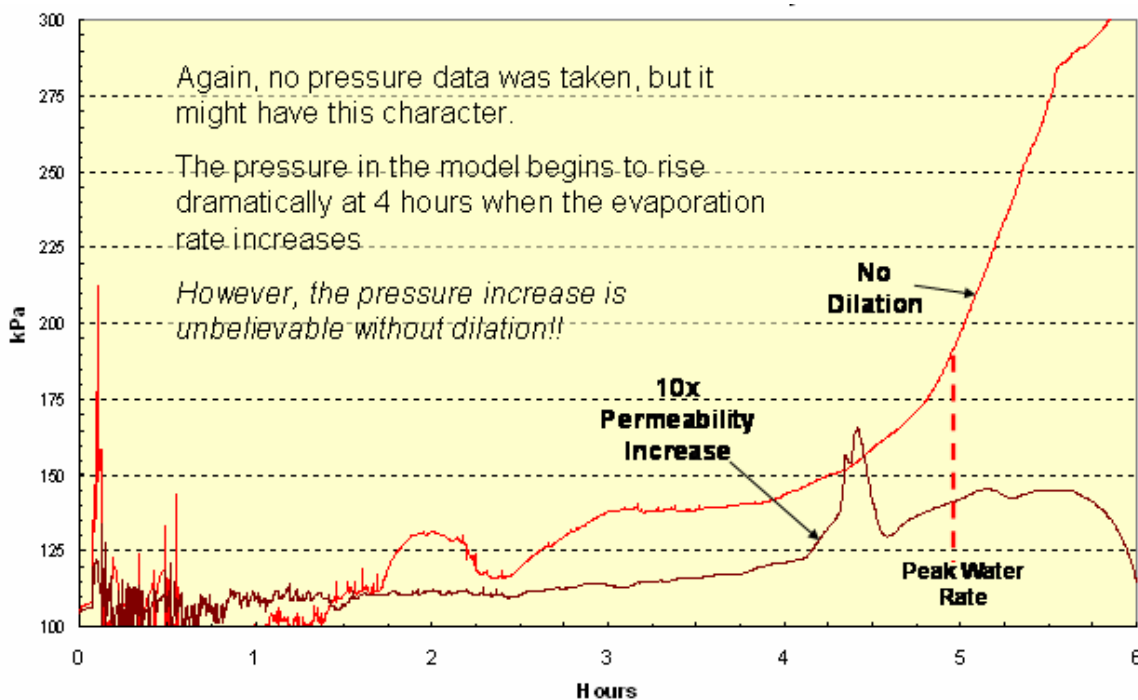


Figure 40 shows the distribution of PCE at 6 hours. The only PCE that remains in the water or as a free DNAPL is predicted to be in the upper left corner of the flume where the flow vectors reverse and heating by convection is ineffective.

As noted above, the most important factors in predicting movement of PCE and the temperature in the model were:

- Dilation of the unconsolidated sand as pressure in the sand increases. This allows steam and water to move from and through the lens easily and reduces the pressure in the model. The temperature in the sand is another clue. The reported temperature does not exceed 107°C. This means that the pressure could not have exceeded 130 kPa. If the sand had not dilated and its permeability temporarily increased at least a factor of 10 the pressures would have been as high as 300 kPa in the model, as shown in Figure 41, and the temperature could reach 133°C.
- A vertical permeability at least half that of the horizontal permeabilities. This is similar to the K_v/K_h ratio of 0.4 reported for the flume heating experiments in a previous section. It is predicted that this higher K_v/K_h facilitated movement of water upwards, movement of PCE upwards into cooler regions of the model, and also may have allowed the PCE to initially move downward into the higher permeability sand.
- The low critical saturations for DNAPL and vapor, discussed above, as well as the slightly negative capillary pressures for the DNAPL near the critical saturations. Both the relative permeability and the capillary pressure allowed the PCE to move with the water and steam that begin circulating through the area of the lens.

Figure 41 – Pressure Predictions with and without Dilation of the Unconsolidated Sand



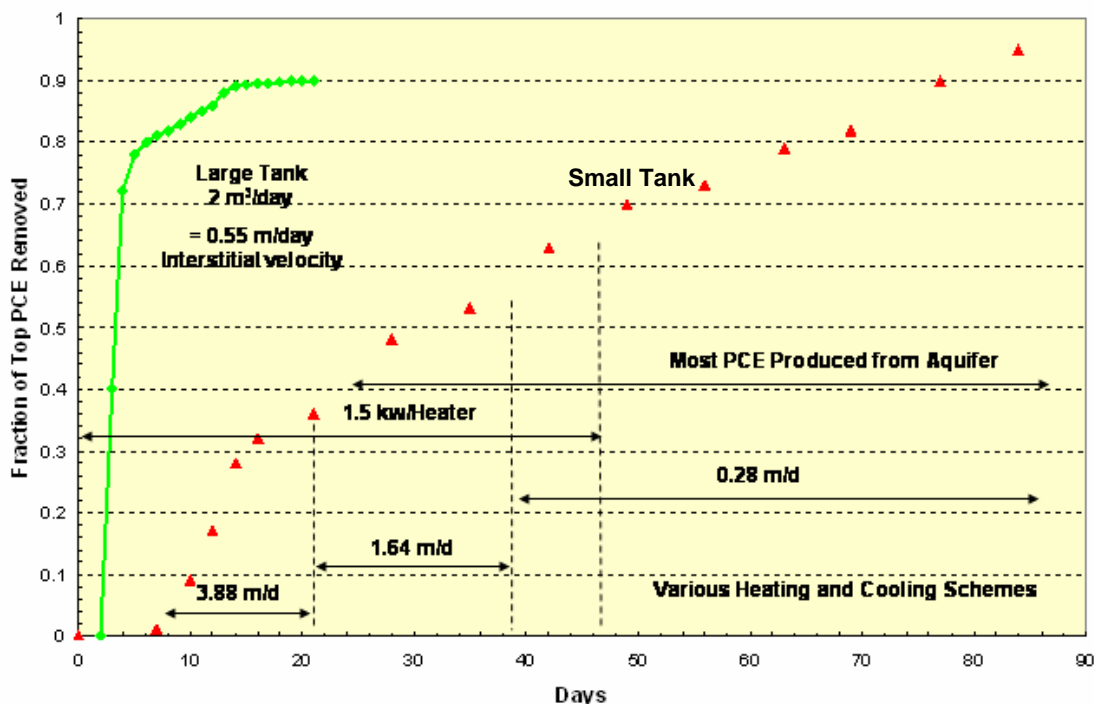
Small- and Large-Tank 3D Remediation Experiments: The contrasting results of these two experiments and their simulations highlight conditions under which the PCE could be remediated

very slowly (small tank) and quickly (large tank). The simulation results shown in Figure 13 suggested that an aquifer rate in a large tank of 2 m³/day was ideal for recovery of TCE from the lower lens in the simulation. Less TCE was recovered with a lower rate because the TCE was predicted to enter the aquifer, and the TCE was recovered slowly when the rate was higher because the tank was cool and TCE could be dispersed in the water. As the results presented below show, this appears to be what happened in the small- and large-tank remediation experiments.

The front view of the tank is shown in Figure 2, while the plan view of the 3-meter wide (small) tank is shown in Figure 21. Each DNAPL release lens in the large tank was filled with 3.48 kg of PCE (and a tracer with a similar boiling point), while each lens in the small tank was filled with 10 kg of PCE. The small- tank experiment was conducted first. This tank was flooded with 7 m³/d of water for 21 days (3.88 m/d interstitial velocity), 3 m³/d of water for 18 days (1.64 m/d interstitial velocity) then 0.5 m³/d for 8 days (0.25 m/d interstitial velocity) while it was heated with four heaters delivering 1.5 kW each. The large tank was flooded with 1 m³/d of water (0.25 m/d interstitial velocity).

Figure 42 compares the PCE recovery from the large- and small-tank experiments. As shown in Figure 13, recovery of PCE is rapid when the interstitial velocity is low and recovery is low when interstitial velocity is high, or in other words, high aquifer influx both slows the heating and disperses the PCE so that it can't be recovered by heating. The results for the large tank are very similar to that reported for extraction of TCE with 2 m³/d aquifer influx from the lower lens shown in Figure 13.

Figure 42 – Recovery of PCE from the Small- and Large-Tank 3D Remediation Experiments

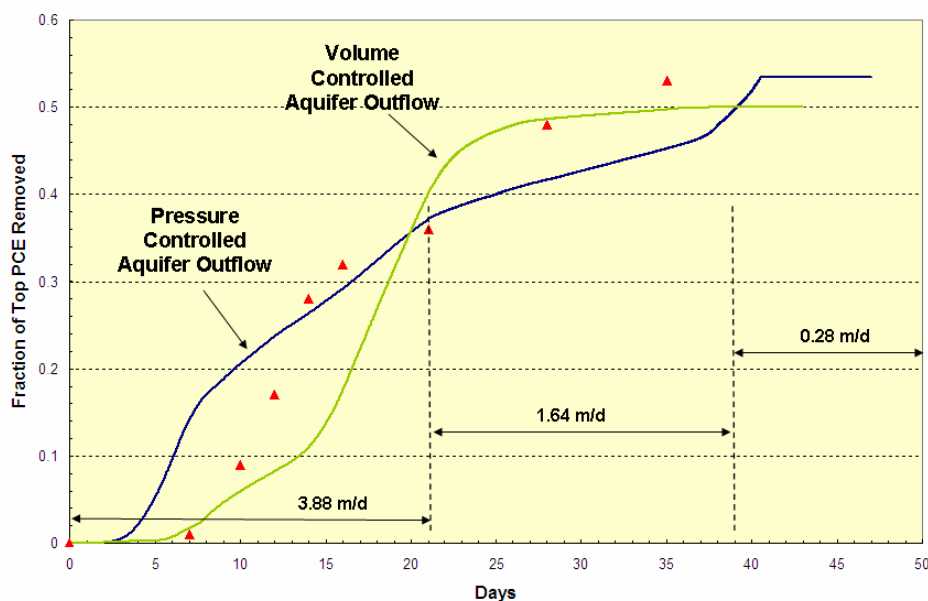


In contrast, 35% and 6% of the PCE in the upper and lower lenses, respectively, were recovered in 21 days from the small-tank experiment where the interstitial velocity was 7 times higher.

The notes for the small-tank experiment indicate that half of the PCE was being produced with the aquifer water after 21 days. After that time, the aquifer influx was lowered in stages until 47 days when various heater schemes like turning the heaters off to collapse the steam chest and switching from heaters spaced 1 meter apart to heaters spaced 1.25 meters apart were tried. As Figure 42 shows, recovery of PCE gradually increased; however, after 21 days most of the PCE was being produced from the aquifer, i.e., it was moving down rather than up. It is likely that the PCE first moved horizontally in this experiment along small preferential pathways, then downward along the side of the tank since PCE was detected very quickly at a sampling port on the side of the tank.

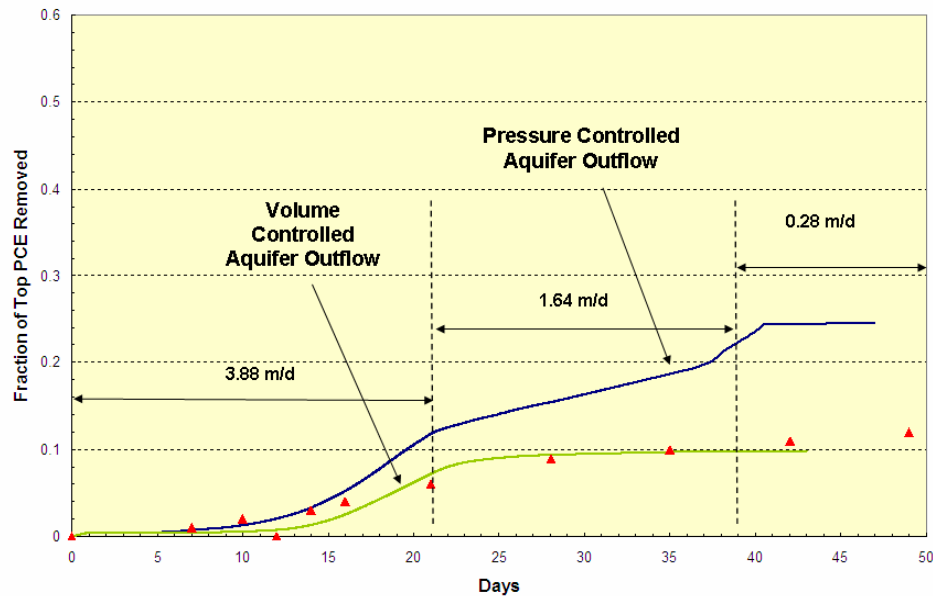
Thus, modeling the small-tank remediation experiment was a similar exercise to modeling the flume remediation experiment, i.e., “How to get the PCE to migrate?” Figure 42 shows that most of the PCE was being produced from the aquifer in the small-tank experiment after 21 days. Attempts to model movement of PCE into the aquifer of the small-tank experiment were unsuccessful because there is a steady flow of water upward into the aquitard; Figures 43 and 44 show where STARS was capable of predicting PCE recovery and where it wasn’t.

Figure 43 – Predicted Recovery of PCE from the Upper Lens at the SVE Wells



Both figures show that STARS could predict that approximately the right amount of PCE was being recovered in the first 38 days of heating. However, all of this PCE is being produced from the SVE wells and none is being produced from the aquifer, as it was in the experiment. Two types of simulations are presented in each figure. In one, the aquifer outflow was controlled by the bottomhole pressure (head of water) in the outflow well. This tended to force too much water upwards and produce the PCE too quickly. The other method was to simply give the aquifer well an allowable production rate of water. The second method worked better because less water entered the aquitard and less PCE was pushed upward into the vadose zone to be vaporized.

Figure 44 – Predicted Recovery of PCE from the Lower Lens



The difficulty in this experiment was the very high ground water influx during the first experimental stage. This is predicted to push PCE out of the bottom lens and disperse it horizontally and vertically throughout the tank. In the simulation this will push PCE upwards during the high-velocity, early phase of the experiment. That PCE will be vaporized in the hotter, shallower portions of the aquitard. This also means that the production of PCE would stop in these simulations when the water injection rate was reduced.

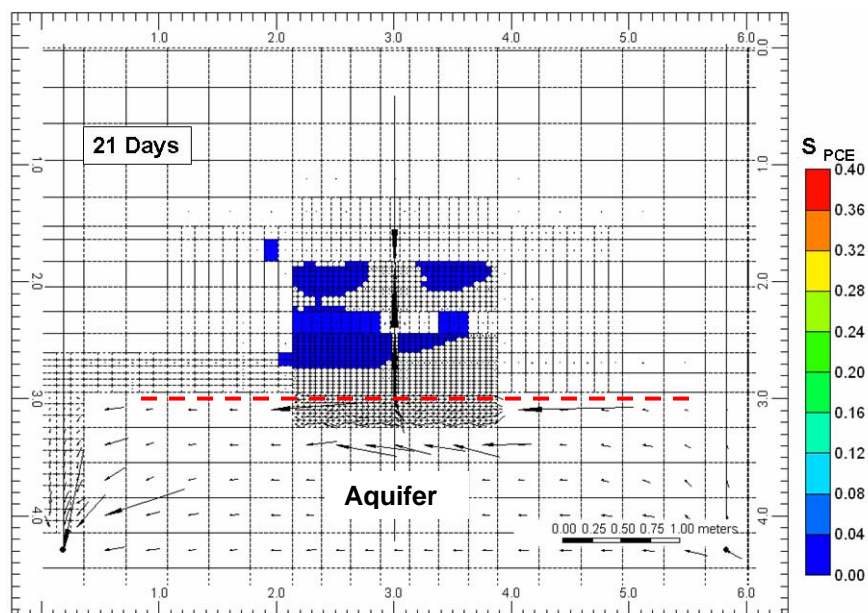
Unfortunately, countercurrent flow is very difficult to model in a simulation unless the cells are extremely small. So, the dissolved PCE won't migrate downward in the simulations against a current of rising water, and STARS would not predict production of PCE in the water from the aquifer within the first 50 days of heating as was observed in the experiment.

Figures 45 through 46 illustrate how the PCE was dispersed in the simulations. In the experiment it was dispersed over a much larger volume than is shown in these figures, but no finite-difference simulator is good at predicting movement of low flow rates of a nonwetting phase or a miscible phase like PCE in water because the cells are too large. As these figures show, the cells below the lenses appear to be small. Their pore volume is 10.8 cm^3 . However, this volume is still not small enough to model countercurrent flow of PCE downward in one group of blocks and water upwards in another group of blocks.

Figures 6 and 45 show the distribution of PCE at the start of the heating phase and after 21 days of heating. Figure 6 shows that PCE had migrated to the bottom of the tank in the absence of aquifer influx. That PCE was immediately flushed from the tank. Then the rest of the PCE began to move upward and outward. Figure 45 shows that most of the free PCE has been removed from the upper lens and the PCE in the lower lens is moving to the left with the flow of water. Figure 46 shows that dissolved PCE has migrated upward in the water. Figures 6 and 45 also show that there is a high flow rate of water upwards along thermocouple profile J. This is

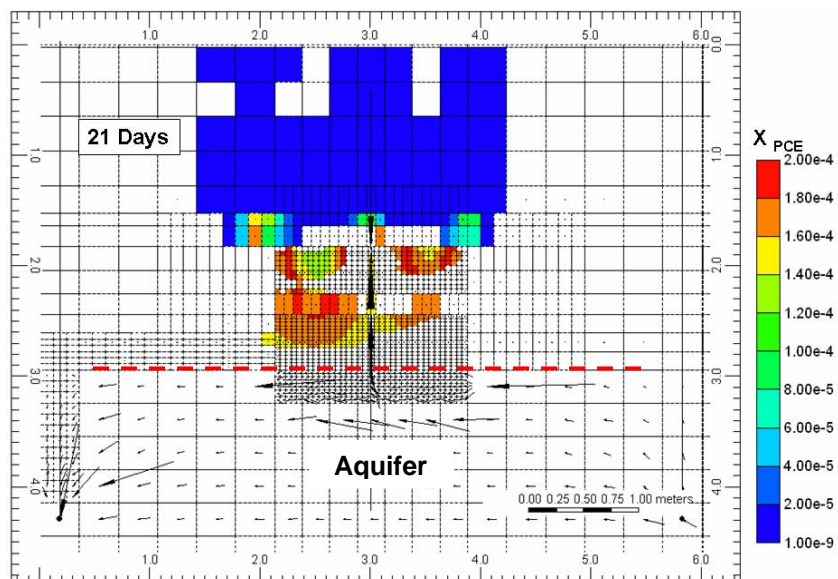
because the vertical permeability was increased by a factor of ten there. That was done because the best method to make PCE move downward was to cause an uneven flow of water upward.

Figure 45 – DNAPL Distribution at the End of 21 Days of High Aquifer Influx



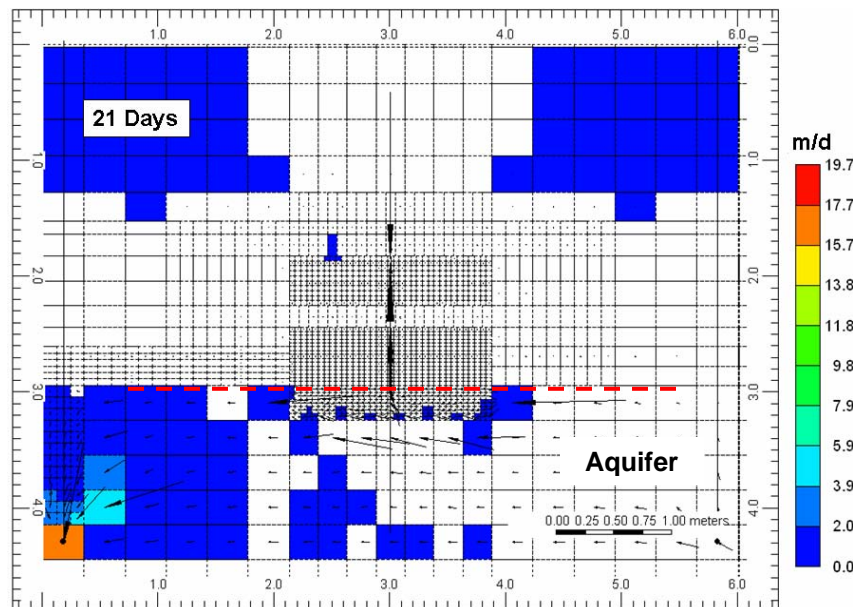
The predicted mole fraction of PCE in water at the end of the high aquifer influx phase of the experiment is shown in Figure 46. The maximum value on the scale (0.0002) is equal to 1,840 ppm of PCE in the water. The concentration of PCE in the vadose zone is less than 180 ppm, but the figure shows that no PCE is moving into the aquifer or to the left side of the tank where it was observed in the experiment, i.e., it was not possible to predict as much movement of PCE as occurred with the very high aquifer influx in this experiment.

Figure 46 – Predicted Mole Fraction of PCE in Water at the End of High Aquifer Influx Phase



The difficulty of making the PCE move into the aquifer is shown by the vertical water velocity in Figure 47. The figure shows that the water is moving downwards (positive values) in small portions of the model but that the water moves upward almost everywhere in the aquitard. So, if water is moving upward dissolved PCE cannot move downward and cannot be produced from the aquifer unless it reaches the aquifer at the left side of the model. It will certainly take very detailed models with smaller cells and a wider permeability distribution than were used in these models to generate countercurrent flow of dissolved PCE down and fresh water upwards.

Figure 47 – Predicted Vertical Water Velocity at the End of High Aquifer Influx Phase



It should also be noted that the PCE has not moved very far to the left. This is because the simulator is predicting that the primary direction of water movement is upward. The predicted horizontal water velocity in the aquitard is approximately 0.01 m/day. This would move dissolved PCE approximately 0.2 meters in 21 days. In the actual experiment significant concentrations of PCE were detected over a meter from the lenses within a few days of the start of aquifer influx. The probable reason for this failure is that the cells were too large and fingering of the dissolved or free PCE could not occur.

Figures 45 through 47 can be contrasted with the distributions of velocity, DNAPL and dissolved PCE at the end of one low aquifer influx phase of the experiment at 47 days as shown in Figures 48 through 50. Figure 48, for instance, shows that water velocity is flowing downward in most of the volume of the tank. The velocity is especially high at the boundary between the aquitard and aquifer under the lens. Figure 49 shows that there is no DNAPL in either lens. The distribution of dissolved PCE is shown in Figure 50. The PCE has moved approximately a meter from the lens at the top of the aquitard and has reached the aquifer below the lenses as did the DNAPL. However, the PCE had not migrated to the left edge of the tank as it had in the experiment. From this point on, dissolved PCE moves into the aquifer and will be produced. However, the movement is still slow and many weeks later than it was actually produced. It is

clear that a much more refined model of flow outside of the heater zone is needed to completely model this experiment.

Figure 48 – Predicted Vertical Water Velocity at the End of Low Aquifer Influx Phase

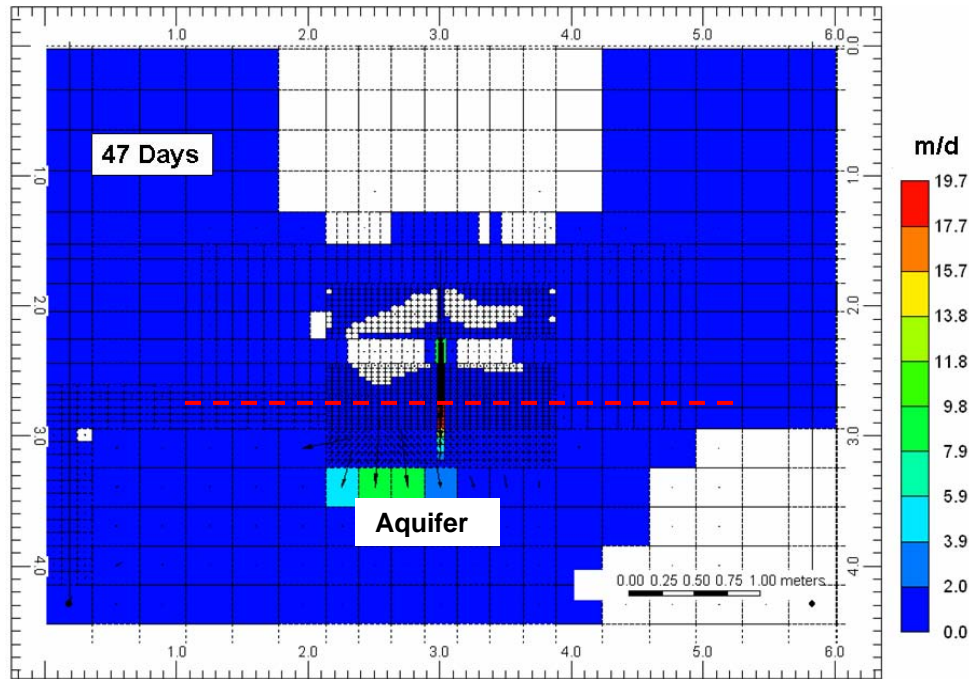


Figure 49 – Predicted DNAPL Distribution at the End of Low Aquifer Influx Phase

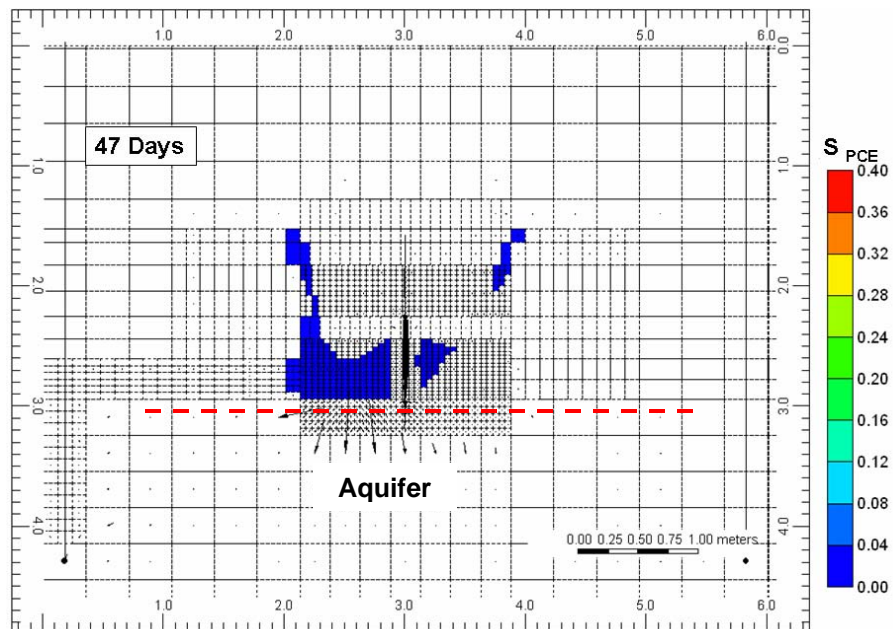
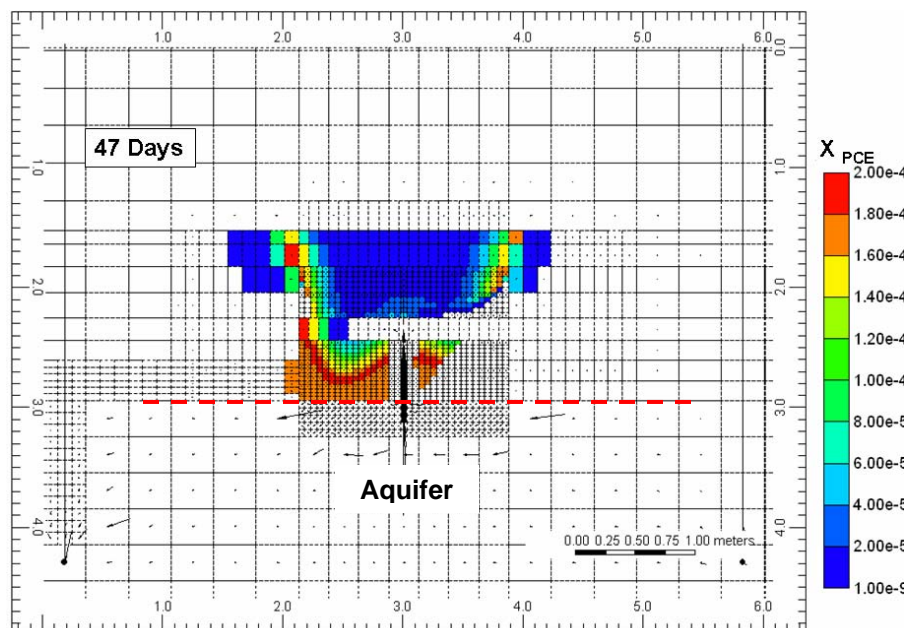


Figure 50 – Predicted Mole Fraction of PCE in Water at the End of Low Aquifer Influx Phase



As noted above, the large-tank remediation experiment with PCE was not modeled. Frankly, its performance was so close to that predicted in Figure 13 (the large-tank remediation experiment modeled with TCE) that little might have been learned by modeling it.

Discussion

Several factors appear to strongly affect heating and remediation in these experiments. They are:

- How capillary pressure and numerical dispersion affect fluid mobility and heat transfer
- When convection is important in the aquitard
- Migration of the DNAPL from the lenses – Migration as a vapor that condenses in cooler regions appears to be modeled well and is easy to understand. However, migration as a miscible component of water appears to be caused by countercurrent flow of small quantities of fluids. This may in turn be affected by volume changes in solution that are not modeled well in general-purpose simulators.
- Recovery of PCE by vaporization appeared to be routine, with no evidence of a significant affect of the PCE-water azeotropes. The early recovery of PCE from experiments occurred when the lenses were quite cool, so the DNAPL may have migrated into hotter regions to be vaporized as strongly suggested by the flow vectors shown for the 2D experiment.
- It is important to recognize that both the 2D and 3D experiments were conducted in packed unconsolidated sands with high compressibility and little resistance to dilation and a temporary increase in permeability. This appears to have been very important in the 2D experiment, but was not modeled due to time constraints in the 3D tanks.

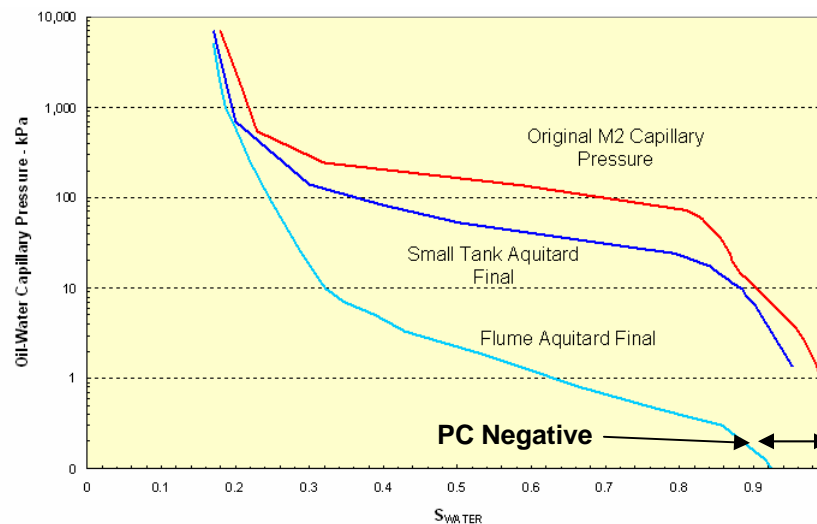
The evidence supporting these statements will be presented in subsequent sections.

Effect of Capillary Pressure and Numerical Dispersion: The point has been made several times that numerical dispersion affects the results of simulations and that this acts in concert with other dispersive forces such as capillary pressure. Numerical dispersion is the equivalent of solving the convection-dispersion equation below (1)³.

$$\text{Diffusive Term} \rightarrow D_{\text{numerical}} \frac{\partial^2 u}{\partial x^2} - v f' \cdot \frac{\partial u}{\partial x} = \frac{\partial u}{\partial t} \quad 1)$$

This means that capillary pressure is a history-matching parameter and must be smaller than the capillary pressure that is actually measured. For example, in coarse-grid simulation of a large volume it is very common to not use capillary pressure because numerical dispersion diffuses fluids between blocks. Thus, Figure 51 shows that the aquitard capillary pressure used for water and gas in the small-tank heating experiment is significantly lower than the actual data and that the NAPL-water capillary pressure used in the flume-remediation simulation and small-tank remediation simulations are even lower.

Figure 51 – Final Capillary Pressures Used in 2D Flume and Small-Tank Heating Experiment



The primary reasons that the NAPL-water capillary pressures used in the flume- and small-tank simulations are so much lower than the gas-water is that

- a) PCE has significant solubility in water, and therefore, its NAPL-water capillary pressure will be lower and
- b) mixed wettability was invoked in order to promote movement of PCE from the lenses into the aquifer of the small-tank remediation experiment and high-permeability, lower zones of the flume-remediation experiment.

After all, the positive capillary pressures shown in the original and small-tank aquitard curves of Figure 50 mean that pressure is needed to force a DNAPL into a pore; whereas the slightly negative capillary pressures below 8% DNAPL saturation in the flume and small-tank

remediation experiments implies neutral or hydrophobic conditions, meaning that there will be no resistance for movement by imbibition of small saturations of the non-wetting DNAPL into a pore.

Convection versus Conduction: Thermal conductive heating is advertised as a means to heat low permeability soil because thermal conduction is not affected much by barriers such as buried walls or low-permeability soil. However, convective heat transfer can be much higher than conductive heat transfer. So, it is useful to show when convection becomes important in a thermal heating experiment.

Figures 52 and 53 compare the ratio of convective heat transfer to conductive heat transfer calculated for the small-tank heating experiment along the loci of thermocouple profiles J and G (centroid and between heaters). This ratio is negative, and implies that convection opposes the movement of heat by conduction in some locations. While the ratio is calculated for the aquifer in both figures, it doesn't mean much there because there is so little conductive heat transfer. In the aquitard and vadose zone, however, the ratio is meaningful. At the centroid (Figure 52) the ratio is low at 24 and 68 days. Figure 23 shows that the temperature is low at 24 days. That should not be surprising. However, Figure 23 also shows that the temperature is 104°C at the centroid at 68 days yet the ratio is still low. The ratio climbs above one after that even though the temperature does not rise. The ratio reaches two and three at the centroid in the high-permeability vadose zone as it dries out.

Figure 52 – Ratio of Convective to Conductive Heat Transfer at Centroid (J) Thermocouples

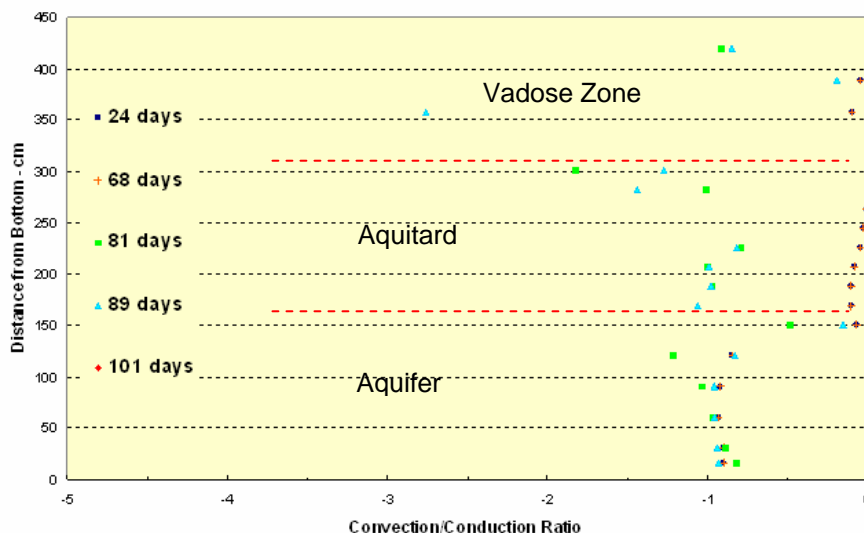
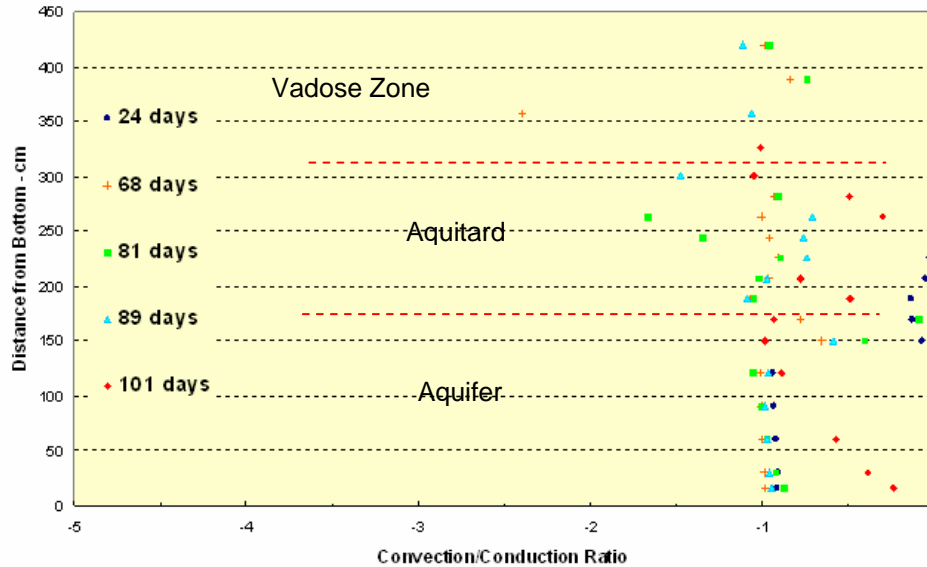


Figure 53 – Ratio of Convective to Conductive Heat Transfer Between Heaters



In contrast, Figure 53 shows that the convection is almost as high as conduction by 68 days in the aquitard. Yet, Figure 24 shows that the temperature is lower between the heaters than at the centroid in Figure 23. This can only be true if the pressure there is lower. The ratio of convection to conduction is always around one between the heaters in the vadose zone since water is evaporating there much earlier than it does at the centroid. Thus, convection is generally at least as large as conduction in the low-permeability aquitard and generally as large, or larger than conduction in the high-permeability vadose zone.

The ratio of convection to conduction in the 2D-flume experiment is even higher than in the tank experiments. Conduction is higher than convection in the first three hours of the remediation experiment because the flume isn't hot and the pressure gradients are still low. However, after three hours the ratio of convection to conduction becomes as high as 10:1 at 4.5 hours and is still 3:1 at the end of the simulation. Again, this ratio is generally negative and means that convection opposes horizontal conduction, but may enhance vertical conduction of heat into the lens from the hotter, lower sand in the 2D-flume experiment.

Migration of DNAPL: The tank experiments were purposefully set up to prevent easy remediation of the DNAPL because the SVE wells were placed outside of the heated volume. A field project would never be set up like this since the goal is to capture DNAPL not move it around. In spite of this, the tanks could be remediated quickly if migration of the DNAPL outside of the heated zone was prevented.

Several mechanisms contribute to migration of DNAPL to cool areas. They include

- The SVE wells drawing the vaporized DNAPL into cool zones where it condenses and cannot be easily recovered as was observed in all tank remediation simulations.
- Expansion of the steam chamber into the aquifer where vaporized DNAPL condenses as was shown in the large-tank heating and remediation simulations. Then, the DNAPL is

more likely to dissolve in the water and be removed in the aquifer than to be vaporized again and collected at the SVE wells.

- Downward movement of DNAPL from the lens to the aquifer where it is slowly produced as a dissolved plume as observed in the 2D-flume and small-tank remediation experiments. This could have happened in the first few hours of the 2D-flume experiment and was observed after several weeks in the small-tank remediation experiment.
- Flushing of DNAPL from the lens horizontally outside of the heated zone, where production by any method is difficult as observed in the small-tank remediation experiment.
- Flushing of DNAPL upwards into the vadose zone where it could be vaporized as in the small-tank remediation experiment.

As has been noted, a large amount of the work required for remediation modeling was really learning how to model migration of DNAPL. As shown in Figure 13, the primary method of migration prevention in a tank was to control the aquifer influx. We recognize that this is not a controlled variable in any field operation, so areas with high aquifer influx should be avoided or treated with combined remedies that include steam injection, not only because it is difficult to heat the aquifer and vaporize the DNAPL using electrical heating methods alone, but because a large quantity of DNAPL has probably already been flushed out of the zone that is to be heated.

The observations presented previously show that the DNAPL must have been able to move at low saturations in order for it to have been flushed as far as it was in just a few days. This means that the critical saturation (point where relative permeabilities become non-zero) must be very low. A critical saturation of 0.1% was used in these simulations. This allowed the DNAPL to drain in the absence of upward water flux and migrate easily as convection increased. That is probably not unreasonable since large amounts of DNAPL are known to migrate into aquifers.

The values of the NAPL-water capillary pressure used in this work are a history matching parameter that enhanced migration of PCE. They do not reflect the known PCE-water interfacial tension of 44 dynes per cm. For example, an interfacial tension of 44 dynes per cm means that the DNAPL-water capillary pressure curve in Figure 50 should be 12 kPa at a water saturation of 86%. The capillary pressures used are much lower and needed to be negative at low saturations in the simulation for the PCE to migrate quickly as a separate phase. Migration as a dissolved liquid just couldn't move enough DNAPL.

Evidence for Azeotropes: Perchloroethylene and water form an azeotrope containing 82.8% PCE at 88.5°C. The simulation models do not suggest that a PCE-water azeotrope accelerated remediation in these experiments significantly. For example, Figures 33, 43 and 44 all predict that PCE was being produced long before the edges of the lenses reached 88.5°C. However, the 2-D remediation experimental data, for example (refer to Figure 31 in the Final Report) clearly show that temperatures in the PCE lens rose above 88°C (the PCE-water azeotrope) at 3 hours, which is when PCE first began to be recovered as a vapor.

It may be an artifact of the numerical simulations that they did not indicate an azeotropic affect. It is well known, however, from laboratory studies (Udell, 1996) and from data obtained from

many field remediation projects (e.g., Heron et al. 2008) that significant vapor recovery first begins when temperatures within the DNAPL zone achieve the azeotrope.

Lessons Learned: There are two types of lessons to be learned from these simulations:

First the general lessons are that:

Capillary pressure is not used directly in simulations because numerical dispersion during the simulation affects movement of fluids and energy in the same way as does capillary pressure and thermal or mass diffusivity. It is beyond the scope of this study to recommend what should be done in every circumstance. In general, capillary pressure should be 10 to 20% of the measured value or can even be zero in large oil reservoirs or regional scale simulations.

Also, capillary pressures (and relative permeabilities) deduced from small scale laboratory experiments cannot be used directly in larger scale modeling because numerical dispersion (and mixing of energy or fluids in large cells) affect the results of the simulation so strongly. This issue is relatively well known among experienced numerical modelers. Unfortunately, there is no universal answer for this dilemma other than to adjust the model to a) reduce capillary pressure, b) increase NAPL saturations trapped by imbibition and c) reduce the saturation at which NAPL becomes mobile during drainage.

A corollary of the previous observations is that small scale laboratory experiments do not represent field scale phenomena very well. The extreme example would be the flume experiment where the heating rate had to be high relative to the volume of the experiment or most of the power input would be lost to the surroundings. Then, convection totally dominated movement of heat or mass and the pore pressure became high enough that dilation of the unconsolidated sand was a major factor, whereas it was not a factor in the tank experiments.

Also, in general, the permeability anisotropy of freshly-packed, unconsolidated sands is not like the permeability anisotropy in most lower-energy, natural-deposition environments. We believe that the ratio of vertical to horizontal permeability in these experiments was 0.4 to 0.5 or higher. This represents random mixing. In low-energy natural sediments, K_v/K_h is approximately 0.1 because layering is important.

Finally, in general, aquifer influx will be much less important in field applications simply because thermal conduction or electrical heating remediation probably won't be conducted in 100-md to 1-D sands that could be steam flooded. Instead, both are predominantly applied, below the water table, to treatment of lower- and moderate permeability media.

The specific lessons that can be applied to future laboratory modeling are:

Numerical dispersion will be conquered by computer power. This modeling study was conducted in 2005 and 2006 with dual-processor workstations having just 4 GB of RAM. They were very powerful for that time period, but are less powerful than many entry-level computers are now. Current workstations could process four to eight times as many cells so that capillary pressure doesn't have to be reduced as much and be heterogeneous enough for migration of NAPL at low concentrations to be studied.

The heterogeneity of permeability in these simulations was modeled by imposing random permeabilities on a uniform permeability field. This tends to disperse NAPL, not allow it to move long distances. It would be better to generate the permeability distribution by geostatistical modeling. This would create small, high-permeability regions and perhaps allow the PCE migration to the boundaries of the tank to occur more easily.

Migration of DNAPL in aquifers has certainly been studied for decades, so the advice that could be given to future researchers is to be very familiar with those studies and the lessons learned. The migration in these experiments was an experimental artifact caused by relatively-high, 100-md permeability where movement of DNAPL can occur faster than heating.

These three issues could be addressed in the advanced modeling work requested in a White Paper² for this project.

Capture of DNAPL was an issue in these experiments. That can simply be corrected by heating the contaminated zone from outside the SVE wells, not inside them. TerraTherm has already conducted successful field-scale remediation projects where SVE wells were placed in coarse fill above contaminated mud or in glacial till sandwiched between an aquifer and the cement floor of a dry cleaning plant.

Conclusions

Several heating and remediation experiments have been modeled as part of SERDP project ER-1423. The results show the following:

1. Capillary pressure is the most important variable affecting both heating and remediation experiments because it controls imbibition of water into the aquitard and vadose zone, and migration of the DNAPL into cooler or hotter regions of the tanks.
2. The capillary pressures used in these models are lower than the capillary pressures measured for the aquitard material because numerical dispersion in the simulations has the same affect on movement of water as does capillary pressure.
3. Dilation of freshly packed, unconsolidated sand appeared to be very important in the flume experiment because the evaporation rates were relatively high compared to the volume of the box, but aren't as likely to be important in the tank experiments because the relative heating rate is lower and expanding fluids can move into quite a large volume.

4. While PCE is vaporizing at a high rate at approximately 90°C, the models suggest it may not be due to boiling of an azeotrope, and may instead be due to steam distillation of PCE by vaporizing water.
5. Migration of PCE was the variable that affected the remediation experiments most. Migration can be the result of
 - a. The SVE wells drawing vaporized DNAPL into cooler regions of the model where it condenses
 - b. Expansion of the steam chamber into the aquifer where the DNAPL will be flushed away by water or condensed and immobilized.
 - c. Downward movement of PCE when the upward flux of water is low. In the 2D-flume experiment the PCE migrated into a hot zone where it could be produced by steam distillation. In the small-tank 3D remediation experiment the PCE migrated laterally along preferential pathways, after which it migrated into the aquifer and was flushed away in the water.
 - d. Horizontal migration caused by high, aquifer-flushing rates into cooler regions where the only recovery mechanism can be extraction as a dissolved component in water.
 - e. Upward flushing with water into the vadose zone where the DNAPL could be stripped and produced by air drawn into the SVE wells.
6. In the tank experiments an aquifer flux of approximately 0.55 m/day (2 m³/d in a 6 m x 6 m tank) controlled most of these migration mechanisms and resulted in remediation of 90% of the PCE within two weeks.
7. The migration mechanisms listed above are mostly artifacts of the experiments conducted in this project because in field ISTD projects the SVE wells are inside the heaters and not outside. Moreover, migration of DNAPL has invariably occurred in a time frame of years and seldom at the beginning of a remediation project lasting a few months.
8. The heat transfer in the tank experiments appeared to be strongly affected by convection of heat inside the heater cans, and 20% of the energy from the heated zone appeared to have migrated upward by this mechanism.
9. STARS proved to be a relatively robust simulator for this project. The problems encountered in this project were generally those related to history matching of poorly known variables, such as the amount of heat that conducts upward inside of the heater cans in the tank experiments or the balance between capillary forces and numerical dispersion.
10. It is clear that the grids used in these experiments were not fine enough, nor were the permeability differences between refined blocks large enough to model either the fingering of dissolved DNAPL constituents or the countercurrent fingering of DNAPL and dissolved DNAPL constituents that transferred some of the PCE into the aquifer in the small-tank-remediation experiment.
11. If future modeling of these experiments is conducted, it should be done with models that include geostatistically-generated permeability distributions and all that is known about DNAPL migration using more powerful computers than were available when this modeling study started.

References

- 1) SERDP Project ER-1423, White Paper, "Large Scale Physical Models of DNAPL Source Zones in Aquifers," June 29, 2007.
- 2) Peaceman, Donald W. "Fundamentals of Numerical Reservoir Simulation," pp 68-75, Elsevier Scientific, New York, 1977.
- 3) Udell, K.S. AND J.S. Fitch. 1985. "Heat and Mass Transfer in Capillary Porous Media Considering Vaporisation, Condensation and Non-Condensable Gas Effects." Paper presented at 23rd ASME/AIChE *National Heat Transfer Conference*, Denver, CO.
- 4) Udell, K.S. 1996. "Heat and mass transfer in clean-up of underground toxic wastes." In *Annual Reviews of Heat Transfer*, Vol. 7, Chang-Lin Tien, Ed.; Begell House, Inc.: New York, Wallingford, UK, pp. 333-405.

Appendix C: List of Technical Publications:

Peer-Reviewed Journals or Papers:

- HIESTER, U., H.-P. KOSCHITZKY, O. TRÖTSCHLER, A. FÄRBER, R. S. BAKER, J. C. LACHANCE, G. HERON AND M. KUHLMAN. 2006. *Thermal well operation in the saturated zone - new options for DNAPL remediation*. J. Land Contamination and Reclamation, 14(2):615-619.

Technical Reports:

- JOHANNES MARK: *Permeability and Grain Size Relationships*, M.S. Thesis, Earth Science Department, Göteborg University, Sweden 2005.
- MARTINA MÜLLER: *Experimentelle Untersuchungen auf technischer Skala zum Einsatz fester Wärmequellen bei der In-situ-Reinigung geringdurchlässiger, gesättigter Böden*; M.S. Thesis, VEGAS, Universität Stuttgart 2008
- PHILIPP LEUBE: *Experimentelle Untersuchungen der Prozesse auf technischer Skala bei der In-situ-Reinigung geringdurchlässiger, gesättigter Böden mit festen Wärmequellen*; M.S. Thesis, VEGAS, Universität Stuttgart 2008
- UWE HIESTER: *Technologieentwicklung zur In-situ-Sanierung der ungesättigten Bodenzone mit festen Wärmequellen*, Mitteilungen Heft 178, Institut für Wasserbau, Universität Stuttgart, Diss. 2008, ISBN 3-933761-82-8. 2009

Conference/Symposium Proceedings Papers:

- UWE HIESTER, HANS-PETER KOSCHITZKY, OLIVER TRÖTSCHLER, ARNE FÄRBER, RALPH BAKER, GORM HERON, JOHN LACHANCE, MYRON KUHLMAN: *Feste Wärmequellen zur In-situ-Grundwasserreinigung bei DNAPL-Schäden – Erste Ergebnisse einer U.S.-geförderten Forschungskooperation*, in Braun, Koschitzky, Müller (Eds.) Ressource Untergrund, 10 Jahre VEGAS: Forschung und Technologieentwicklung zum Schutz von Grundwasser und Boden, Institut für Wasserbau, Universität Stuttgart, 2005, ISBN 3-933761-48-4 pp 109-112.
- UWE HIESTER, ARNE FÄRBER, HANS-PETER KOSCHITZKY, OLIVER TRÖTSCHLER, RALPH BAKER, GORM HERON, JOHN LACHANCE, MYRON KUHLMAN: *Use of thermal wells to remove DNAPL from the saturated zone – options and risks*, Conference CD, p 2273, ConSoil 2005, Bordeaux, France, 03.-07. October 2005.
- BAKER, R.S., J.C. LACHANCE, G. HERON, U. HIESTER, H.-P. KOSCHITZKY, O. TRÖTSCHLER, A. FÄRBER, AND M. KUHLMAN. 2006. *DNAPL Removal from the Saturated Zone using Thermal Wells*. Remediation of Chlorinated and Recalcitrant Compounds: Proceedings of the Fifth International Conference (May 22-25, 2006). Battelle, Columbus, OH.

- HIESTER, U., H.-P. KOSCHITZKY, O. TRÖTSCHLER, A. FÄRBER, R. BAKER, G. HERON, J. LACHANCE AND M. KUHLMAN. 2006. *In-situ Sanierung von Schadstoffen im Grundwasser mit Festen Wärmequellen – Erweiterung der Einsatzbereiche des THERIS-Verfahrens*. Mitteilungen 150:49-59. Institut für Wasserbau, Universität Stuttgart, Germany.
- UWE HIESTER, HANS-PETER KOSCHITZKY, OLIVER TRÖTSCHLER, MARTINA MÜLLER, ARNE FÄRBER, LI YANG, RALPH BAKER, GORM HERON, JOHN LACHANCE, MYRON KUHLMAN: *THERIS-Verfahren zur Reinigung von Aquitarden – Einflussfaktoren und Betriebsparameter* –, in Braun, Koschitzky, Stuhmann (Eds.) VEGAS Kolloquium 2007, Institut für Wasserbau, Universität Stuttgart, 2007, ISBN 3-933761-69-7 pp 41-51.
- RALPH BAKER, GORM HERON, JOHN LACHANCE, ARNE FÄRBER, LI YANG, UWE HIESTER: *2-D Physical Models of Thermal Conduction Heating for Remediation of DNAPL Source Zones in Aquitards*. Conference proceedings, ConSoil 2008, Milano, Italy, 03.-06. June 2008.
- UWE HIESTER, MARTINA MÜLLER, OLIVER TRÖTSCHLER, HANS-PETER KOSCHITZKY, RALPH BAKER, JOHN LACHANCE, GORM HERON, MYRON KUHLMAN: *Dominating processes during DNAPL removal from the saturated zone using thermal wells*. Conference proceedings, ConSoil 2008, Milano, Italy, 03.-06. June 2008.
- UWE HIESTER, HANS-PETER KOSCHITZKY, OLIVER TRÖTSCHLER, MARTINA MÜLLER, ARNE FÄRBER, LI YANG, RALPH BAKER, GORM HERON, JOHN LACHANCE and MYRON KUHLMAN: *Dominating Processes during DNAPL Removal from the Saturated Zone Using Thermal Wells*. Remediation of Chlorinated and Recalcitrant Compounds: Proceedings of the Sixth International Conference, (May 19-22, 2008). Battelle, Columbus, OH.

Published Technical Abstracts:

- RALPH BAKER, UWE HIESTER, GORM HERON, JOHN LACHANCE, MYRON KUHLMAN, ARNE FÄRBER, HANS-PETER KOSCHITZKY AND OLIVER TRÖTSCHLER: *Large-Scale Physical Models of Thermal Remediation of DNAPL Source Zones in Aquifers*, Poster paper presented at 21st Annual International Conference on Soils, Sediments and Water, University of Massachusetts at Amherst, 17-20 October 2005.
- RALPH BAKER, GORM HERON, JOHN LACHANCE, UWE HIESTER, HANS-PETER KOSCHITZKY, OLIVER TRÖTSCHLER, ARNE FÄRBER AND MYRON KUHLMAN: *Large-Scale Physical Models of Thermal Remediation of DNAPL Source Zones in Aquifers*, Poster paper presented at SERDP-ESTCP Partners in Environmental Technology Technical Symposium and Workshop, Washington, DC, Nov. 29-Dec. 1, 2005.
- HIESTER, U., H.-P. KOSCHITZKY, O. TRÖTSCHLER, A. FÄRBER, R. BAKER, G. HERON, J. LACHANCE AND M. KUHLMAN. 2006. *The Use of Thermal Wells to Remove DNAPL from the Saturated Zone*. EC-DNAPL1: The First European Conference on DNAPL Characterization and Remediation – Abstracts. pp. 53-54. Göttingen, Germany.

- BAKER, R.S., U. HIESTER, G. HERON, J.C. LACHANCE, M. KUHLMAN, A. FÄRBER, H.-P. KOSCHITZKY AND O. TRÖTSCHLER. 2006. *Heat Flow and Desaturation in Large-Scale Experiments of Thermal Remediation of DNAPL Sources in Aquifers*. Abstracts, 22nd Annual International Conference on Soils, Sediments and Water, Oct. 16-19, 2006, Univ. of Massachusetts, Amherst, MA.
- BAKER, R.S., G. HERON, J.C. LACHANCE, U. HIESTER, H.-P. KOSCHITZKY, O. TRÖTSCHLER, A. FÄRBER, AND M. KUHLMAN. 2006. *Large-Scale Physical Models of Thermal Conduction Heating for Remediation of DNAPL Source Zones in Aquifers*. Poster abstract. SERDP-ESTCP Partners in Environmental Technology Technical Symposium & Workshop, Nov. 28-30, 2006, Washington, DC.
- BAKER, R.S., J.C. LACHANCE, G. HERON, U. HIESTER, H.-P. KOSCHITZKY, O. TRÖTSCHLER, AND M. KUHLMAN. 2007. *Improved Understanding of Thermal Mechanisms obtained during Meter-Scale Experiments Simulating DNAPL Sources in Aquifers*. Poster abstract. SERDP-ESTCP Partners in Environmental Technology Technical Symposium & Workshop, Dec. 4-6, 2007, Washington, DC.
- BAKER, R.S., J.C. LACHANCE, G. HERON, U. HIESTER, O. TRÖTSCHLER, H.-P. KOSCHITZKY, AND M. KUHLMAN. 2008. *Dominating Processes during DNAPL Removal from the Saturated Zone Using Thermal Wells*. Poster abstract. SERDP-ESTCP Partners in Environmental Technology Technical Symposium & Workshop, Dec. 2-4, 2008, Washington, DC.
- KUHLMAN, M. 2008. *Simulation of Laboratory In Situ Thermal Desorption of DNAPLs*. Poster abstract. SERDP-ESTCP Partners in Environmental Technology Technical Symposium & Workshop, Dec. 2-4, 2008, Washington, DC.

Published Text Books or Book Chapters: None